NATIONAL TECHNICAL UNIVERSITY OF ATHENS

SCHOOL OF CIVIL ENGINEERING

INSTITUTE OF STRUCTURAL ANALYSIS & ASEISMIC RESEARCH

Modeling Reinforced Concrete Structures under Severe Cyclic Loading Incorporating Plasticity and Damage Models

DOCTORAL DISSERTATION

for the title of Doctor of Philosophy in Engineering submitted in the School of Civil Engineering, National Technical University of Athens

Ilias A. Gkimousis

Diploma in Civil Engineering N.T.U.A

Master of Science in Civil Engineering N.T.U.A

Athens 2017

ΕΘΝΙΚΟ ΜΕΤΣΟΒΙΟ ΠΟΛΥΤΕΧΝΕΙΟ

ΣΧΟΛΗ ΠΟΛΙΤΙΚΩΝ ΜΗΧΑΝΙΚΩΝ

ΕΡΓΑΣΤΗΡΙΟ ΣΤΑΤΙΚΗΣ & ΑΝΤΙΣΕΙΣΜΙΚΩΝ ΕΡΕΥΝΩΝ

Ανάλυση Κατασκευών Οπλισμένου Σκυροδέματος Υποβαλλόμενων σε Ισχυρές Ανακυκλιζόμενες Φορτίσεις με Ομαλά Κατασταστικά Προσομοιώματα

ΔΙΔΑΚΤΟΡΙΚΗ ΔΙΑΤΡΙΒΗ

για τον Επιστημονικό Τίτλο του Διδάκτορα Μηχανικού υποβληθείσα στη Σχολή Πολιτικών Μηχανικών του Εθνικού Μετσοβίου Πολυτεχνείου

Ηλίας Α. Γκιμούσης

Διπλωματούχος Πολιτικός Μηχανικός Ε.Μ.Π.

Μεταπτυχιακό Δίπλωμα Ειδίκευσης Ε.Μ.Π.

Αθήνα 2017

NATIONAL TECHNICAL UNIVERSITY OF ATHENS

School of Civil Engineering

Institute of Structural Analysis & Aseismic Research

Modeling Reinforced Concrete Structures under Severe Cyclic Loading Incorporating Plasticity and Damage Models

DOCTORAL DISSERTATION

for the title of Doctor of Philosophy in Engineering submitted in the School of Civil Engineering, National Technical University of Athens

Ilias A. Gkimousis

M.Sc., Diploma in Civil Engineering N.T.U.A

ADVISORY COMMITTEE

1. Vlasis Koumousis
   Professor N.T.U.A
2. Charis Gantes
   Professor N.T.U.A
3. Vissarion Papadopoulos
   Associate Professor N.T.U.A

EXAMINATION COMMITTEE

1. Vlasis Koumousis
   Professor N.T.U.A
2. Charis Gantes
   Professor N.T.U.A
3. Vissarion Papadopoulos
   Associate Professor N.T.U.A
4. Stefanos Dritsos
   Professor UPatras
5. Konstantinos Spiliopoulos
   Professor N.T.U.A
6. Christos Zeris
   Associate Professor N.T.U.A
7. Michalis Fragiadakis
   Assistant Professor N.T.U.A

Athens 2017

This doctoral thesis was financially supported by the National Technical University of Athens

Acknowledgments

Although these words are the last to be written, they are the most important as the conduct of this dissertation would be impossible without the contribution of the following people.

First and foremost, I would like to thank my advisor, Professor Vlasis Koumousis for his continuous support, guidance and confidence he has shown to me. His contribution to this dissertation exceeds his outstanding academic role and for this reason I will always be grateful.

I would also like to thank Professor Charis Gantes and Associate Professor Vissarion Papadopoulos for serving on my doctoral committee and for contributing valuable insight to my thesis work through their individual comments. Special thanks are also due to Professor Stefanos Dritsos, Professor Konstantinos Spilliopoulos, Associate Professor Christos Zeris and Assistant Professor Michalis Fragiadakis for serving on the defense committee of my dissertation. Their individual comments and constructive remarks essentially improved this dissertation.

This work was accomplished through the financial support from the National Technical University of Athens. This support is greatly acknowledged.

I want to thank also Charalampos Andriotis for working together along the same research path during the period I co-supervised his diploma thesis. The result of this journey isn't only a joined journal paper but also a reminder that although Phd thesis is mainly an individual sport, every obstacle can be surpassed through teamwork. Also, special thanks are due to Savvas Triantafyllou, Assistant Professor at Nottingham University, for setting the foundations for my dissertation to evolve and grow. Many thanks go to my friends and members of the research group Christos Sofianos and Argyris Moysidis for their valuable comments and support during the preparation of this thesis. I would also like to thank my sister Dimitra for her valuable help with the language editing of this dissertation.

Most of all, I would like to thank my parents. I would never have reached this milestone in my life without their selfless support, continuous encouragement and personal sacrifices.

Last but not least, it would be an omission not to mention the special person of mine, my companion Stefania for her love, affection, continuous support and tolerance throughout the course of this dissertation.

ΠΕΡΙΛΗΨΗ ΣΤΗΝ ΕΛΛΗΝΙΚΗ ΓΛΩΣΣΑ

Ανάλυση Κατασκευών Οπλισμένου Σκυροδέματος Υποβαλλόμενων σε Ισχυρές Ανακυκλιζόμενες Φορτίσεις με Ομαλά Κατασταστικά Προσομοιώματα

I. Εισαγωγή

Οι κατασκευές από Οπλισμένο Σκυρόδεμα (ΟΣ) αποτελούν τη μεγάλη πλειοψηφία του δομικού ιστού σε σεισμογενείς περιοχές. Μία έκρηξη στην κατασκευή πολυώροφων κτιρίων από ΟΣ συνέβη τις δεκαετίες του 60 και 70, συνεπώς αυτές οι κατασκευές έχουν ήδη ξεπεράσει ή πλησιάζουν σήμερα την αρχική εκτίμηση για το χρόνο ζωής τους. Είναι, λοιπόν, επιτακτική η ανάγκη της σεισμικής αποτίμησης και της ενίσχυσης αυτών των κατασκευών ώστε να εναρμονιστούν με τις σύγχρονες απαιτήσεις του αντισεισμικού σχεδιασμού. Για να επιτευχθεί κάτι τέτοιο, είναι αναγκαία η προσομοίωση των κατασκευών ΟΣ με μη-γραμμικές μεθόδους οι οποίες αναδεικνύουν την πραγματική συμπεριφορά του ΟΣ σε επιβαλλόμενες σεισμικές διεγέρσεις. Η ρεαλιστική σεισμική αποτίμηση έχει εξάλλου σημαντικές επιπτώσεις στη γενικότερη οικονομία της κοινωνίας, καθώς οδηγεί στη χρήση τεχνολογιών επισκευών και ενισχύσεων το κόστος των οποίων θα επιβαρύνει εν τέλει μεγάλο μέρος του κοινωνικού συνόλου.

Σε αυτό το πλαίσιο οι σύγχρονοι κανονισμοί παρέχουν οδηγίες για τον προσδιορισμό των μη γραμμικών ιδιοτήτων των μελών από ΟΣ και για την εκτίμηση της μη-γραμμικής συμπεριφοράς τους. Στον πυρήνα των σύγχρονων κανονισμών βρίσκεται ο σχεδιασμός με βάση την επιτελεστικότητα ο οποίος απαιτεί μία δεδομένη κατασκευή να είναι σε θέση να αναλάβει σεισμικά φορτία διαφορετικών εντάσεων μέσω της εμφάνισης ελεγχόμενων βλαβών, χωρίς ωστόσο να κινδυνεύσει με ολική κατάρρευση. Είναι, συνεπώς, άμεση η ανάγκη της προσομοίωσης των κατασκευών όχι μόνο στα αρχικά στάδια της μη-γραμμικής συμπεριφοράς τους, αλλά σε περιοχές που εκτείνονται μέχρι τη θραύση και την ολική βλάβη των επιμέρους μελών τους.

Γενικά οι μορφές αστοχίας υποστυλωμάτων ΟΣ κατηγοριοποιούνται στις εξής κατηγορίες (Berry et al. 2004).

- Καμπτική μορφή αστοχίας
- Διατμητική μορφή αστοχίας
- Καμπτο-διατμητική μορφή αστοχίας

Επίσης, τα είδη των βλαβών σε υποστυλωμάτων από ΟΣ εξαιτίας ανακυκλιζόμενων φορτίσεων εντοπίζονται στα εξής:

- Σύνθλιψη πυρήνα
- Σημαντική αποφλοίωση επικάλυψης

- Λυγισμός διαμηκών ράβδων
- Θραύση διαμηκών ράβδων
- Απώλεια ικανότητας ανάληψης αξονικού φορτίου

Κατά τη διάρκεια των τελευταίων 50 χρόνων πληθώρα αριθμητικών προσομοιωμάτων και τεχνικών Πεπερασμένων Στοιχείων έχουν προταθεί για την ανάλυση της συμπεριφοράς κατασκευών από ΟΣ. Τα στοιχεία δοκού-υποστυλώματος που έχουν προταθεί μπορούν να κατηγοριοποιηθούν σε τρεις κύριες κατηγορίες, στα συγκεντρωμένης πλαστικότητας, κατανεμημένης πλαστικότητας και στα λεπτομερή προσομοιώματα πεπερασμένων στοιχείων.

Στην πρώτη κατηγορία η μη-γραμμικότητα εκφράζεται σε όρους εντατικών μεγεθών, ενώ περιορίζεται σε προκαθορισμένες θέσεις στα άκρα των μελών, σχηματίζοντας τις λεγόμενες πλαστικές αρθρώσεις. Σε αυτές τις περιοχές χρησιμοποιούνται στροφικά ελατήρια για την προσομοίωση της μη-γραμμικής συμπεριφοράς σε όρους ροπών-καμπυλοτήτων. Γενικά, τα φαινομενολογικά προσομοιώματα πλαστικών αρθρώσεων εξαρτώνται από ένα πλήθος προκαθορισμένων παραμέτρων όπως η γεωμετρία της διατομής και οι συνθήκες φόρτισης που επηρεάζουν αισθητά την απόκριση της κατασκευής. Επιπλέον, η παρουσία της διαξονικής κάμψης με αξονική δύναμη αντιμετωπίζεται με την έννοια της επιφάνειας διαρροής και της πλαστικής ροής, τα οποία έχουν αναπτυχθεί για την περίπτωση μεταλλικών διατομών, έχοντας έτσι περιορισμένη εφαρμογή σε διατομές οπλισμένου σκυροδέματος. Παρ’ όλα αυτά το σημαντικό μειονέκτημα τους είναι ότι περιορίζουν την ανελαστική συμπεριφορά σε προκαθορισμένες θέσεις χωρίς να μπορούν να παρακολουθήσουν την εξάπλωση της στο εσωτερικό του στοιχείου.

Η δεύτερη κατηγορία αφορά στα προσομοιώματα κατανεμημένης πλαστικότητας τα οποία ελέγχουν την ανελαστική συμπεριφορά σε περισσότερες από μία θέσεις στο εσωτερικό του στοιχείου. Οι διατομές ελέγχου επιμερίζονται σε ίνες οι οποίες ενσωματώνουν τα μονοαξονικά καταστατικά προσομοιώματα της ράβδου οπλισμού και των ινών του σκυροδέματος. Η διακριτοποίηση σε ίνες παρουσιάζει το πλεονέκτημα της προσαρμογής του ουδέτερου άξονα συναρτήσει της καμπυλότητας και αξονικής δύναμης, αναπαριστώντας άμεσα την αλληλεπίδραση της κάμψης με αξονική δύναμη. Ο προσδιορισμός των επικόμβιων εντατικών μεγεθών και της δυσκαμψίας του μέλους πραγματοποιείται είτε με βάση την κλασική μέθοδο των μετακινήσεων, είτε με τη μέθοδο των δυνάμεων βασιζόμενη σε ενεργειακές μεθόδους του λογισμού των μεταβολών (Hjelmstad and Taciroglu 2003; Taylor et al. 2003; Alemdar and White 2005; Alsafadie et al.

2011; Correia et al. 2015). Η δεύτερη διατύπωση έχει το πλεονέκτημα της ικανοποίησης της ισορροπίας στο εσωτερικό του στοιχείου και συνεπώς δεν απαιτείται η διακριτοποίηση του μέλους σε περισσότερα στοιχεία.

Το βασικό μειονέκτημα των στοιχείων κατανεμημένης πλαστικότητας είναι η αδυναμία τους να ενσωματώνουν άμεσα τριαξονικές καταστατικές σχέσεις σκυροδέματος ώστε να περιγράφουν το φαινόμενο της περίσφιγξης λόγω της αλληλεπίδρασης με τους συνδετήρες. Επιπλέον, ενώ εντάσσονται τέλεια στην καμπτική θεωρία δοκού Euler-Bernoulli, η επέκταση τους ώστε να συμπεριλάβουν διατμητικά φαινόμενα δεν μπορεί να είναι άμεση. Τέλος, ειδική μεταχείριση απαιτείται ώστε να ενσωματωθούν στο προσομοίωμα οι συνθήκες συνάφειας των διεπιφανειών των ράβδων οπλισμού και του περιβάλλοντος σκυροδέματος στις θέσεις των κόμβων δοκού-υποστυλώματος και υποστυλώματος-πεδίλου.

Αντίθετα, στη λεπτομερή προσομοίωση του μέλους με πεπερασμένα στοιχεία το χωρίο του σκυροδέματος διακριτοποιείται με τρισδιάστατα στοιχεία, ενώ οι ράβδοι οπλισμού προσομοιώνονται με μονοδιάστατα στοιχεία δικτυώματος ως ένθεμα στα στοιχεία σκυροδέματος (Hartl and Ch 2002; Spiliopoulos and Lykidis 2006). Παρ΄ όλα αυτά, αν και η λεπτομερής προσομοίωση φαίνεται να προσφέρει την πιστότερη δυνατή προσομοίωση, απαιτεί τεράστιο υπολογιστικό χρόνο και παρουσιάζει αδυναμία αριθμητικής σύγκλισης εξαιτίας των πολύπλοκων τριαξονικών καταστατικών προσομοιωμάτων (Markou and Papadrakakis 2012).

Ο στόχος της διατριβής είναι να προτείνει ένα στοιχείο δοκού-υποστυλώματος ινών ικανού να προσομοιώνει πλαισιωτές κατασκευές από ΟΣ υποβαλλόμενων σε ισχυρά ανακυκλιζόμενα φορτία. Η θεώρηση ινών συνδυάζει την υπολογιστική ταχύτητα και ευστάθεια με την ικανοποιητική ακρίβεια να περιγράψει το φυσικό πρόβλημα μέχρι το στάδιο στο οποίο η καταπόνηση γίνεται έντονα τρισδιάστατη. Το ενδιαφέρον της μελέτης επικεντρώνεται στην αριθμητική προσομοίωση των καμπτικών μορφών αστοχίας μελών ΟΣ δηλαδή της σύνθλιψης πυρήνα, αποφλοίωσης της επικάλυψης και λυγισμού των ράβδων οπλισμού. Πιο συγκεκριμένα στόχος της διατριβής είναι:

- Να αναπτύξει ένα μονοαξονικό ανακυκλιζόμενο προσομοίωμα χάλυβα που να ενσωματώνει μη-γραμμική κινηματική και ισοτροπική κράτυνση μαζί με την περιγραφή του πλατό διαρροής και του φαινομένου Bauschinger.

- Να περιγράψει το φαινόμενο του ανελαστικού λυγισμού των ράβδων οπλισμού ικανοποιώντας την ισορροπία στην παραμορφωμένη κατάσταση.

- Να αναπτύξει ένα μονοαξονικό προσομοίωμα σκυροδέματος που να συνδυάζει τη θεωρία πλαστικότητας και μηχανικής των βλαβών, έτσι ώστε να περιγράψει τα φαινόμενα της σύνθλιψης πυρήνα και της αποφλοίωσης της επικάλυψης. Η αποφλοίωση καθορίζει την απαρχή ενεργοποίησης του μηχανισμού λυγισμού των ράβδων.

- Να αναπτύξει ένα πεπερασμένο στοιχείο δοκού βασιζόμενο στην ενεργειακή θεωρία μεταβολών δύο πεδίων. Το στοιχείο αυτό ενσωματώνει τα καταστατικά προσομοιώματα σκυροδέματος και χάλυβα ενώ η επίλυση των εξισώσεων ισορροπίας και συμβιβαστότητας θα πραγματοποιηθεί με τη μέθοδο της γραμμικοποίησης.

II. Προσομοίωση Ράβδων Οπλισμού

Ο σκοπός αυτού του κεφαλαίου είναι διττός, πρώτα να αναπτύξει το μονοαξονικό προσομοίωμα του χάλυβα σε ανακυκλιζόμενες φορτίσεις και έπειτα να το χρησιμοποιήσει στην περιγραφή του λυγισμού των ράβδων οπλισμού. Το μοντέλου του λυγισμού βασίζεται στις εργασίες των Massone και Moroder (2009) και Urmson και Mander (2012) και επεκτείνεται στην περίπτωση της ανακυκλικής φόρτισης. Η ράβδος οπλισμού προσομοιώνεται ως αμφίπακτη δοκός ανάμεσα στους δύο γειτονικούς συνδετήρες και το αριθμητικό πρόβλημα του λυγισμού καταλήγει σε μία επαυξητική διαδικασία όπου η καμπυλότητα στο μέσον της ράβδου ανανεώνεται, έως ότου επιτευχθεί η ισορροπία στην παραμορφωμένη κατάσταση.

Παρακάτω περιγράφεται αναλυτικά η εξαγωγή του μοναξονικού προσομοιώματος του χάλυβα. Βασιζόμενοι στην κλασική θεωρία πλαστικότητας, ο ρυθμός μεταβολής της τάσης εκφράζεται σύμφωνα με τον κανόνα της αποσύζευξης ως:

$$\dot{\sigma} = E\left(\dot{\varepsilon} - \dot{\varepsilon}^{p}\right) \tag{2.1}$$

όπου σ είναι η τάση, ε είναι η συνολική παραμόρφωση και ε^{p} είναι η πλαστική παραμόρφωση. Η συνάρτηση διαρροής θεωρώντας κινηματική και ισοτροπική κράτυνση διατυπώνεται ως εξής:

$$\Phi(\sigma,b,r)=|\sigma-b|-r\le 0 \tag{2.2}$$

όπου, b είναι η τάση της κινηματικής κράτυνσης (back stress) και r είναι το απόθεμα (reserve) ανάμεσα στο b και την τάση διαρροής του οποίου ο ρυθμός εξέλιξης δίνεται από τη σχέση:

$$\dot{r}=m\cdot H\cdot\dot{\lambda} \tag{2.3}$$

όπου $\dot{\lambda}\ge 0$ είναι ο πλαστικός πολλαπλασιαστής, ο οποίος είναι πρακτικά το μέγεθος του ρυθμού πλαστικής παραμόρφωσης. Η βαθμωτή μεταβλητή m είναι το ποσοστό της ισοτροπικής κράτυνσης, ενώ $(1-m)$ είναι το απομένον ποσοστό της κινηματικής κράτυνσης. Επίσης, ο νόμος της πλαστικής ροής δίνει το ρυθμό μεταβολής της πλαστικής παραμόρφωσης $\dot{\varepsilon}^p$ ως εξής:

$$\dot{\varepsilon}^p=\dot{\lambda}\cdot\frac{\partial\Phi}{\partial\sigma}=\dot{\lambda}\cdot sgn(\sigma-b) \tag{2.4}$$

Υιοθετώντας το μη-γραμμικό νόμο κράτυνσης των Armstrong-Frederick (1966) λαμβάνεται η παρακάτω σχέση για το ρυθμό μεταβολής της κινηματικής τάσης κράτυνσης:

$$\begin{aligned}\dot{b}&=(1-m)\left(H_0\cdot\dot{\varepsilon}^p-q\cdot\left|\dot{\varepsilon}^p\right|\cdot b\right)\\&=(1-m)\cdot\ q\cdot\dot{\varepsilon}^p\cdot\left[\frac{H_0}{q}-\mathrm{sgn}(\dot{\varepsilon}^p)\cdot b\right]=\ (1-m)\cdot H\cdot\dot{\varepsilon}^p\ =\ (1-m)\cdot H\cdot\dot{\lambda}\cdot sgn(\sigma-b)\end{aligned} \tag{2.5}$$

όπου, H είναι το μη-γραμμικό μέτρο κράτυνσης που εξαρτάται από τη θετική παράμετρο q, με αρχική τιμή H_0.

$$H=H_0-q\cdot\mathrm{sgn}(\dot{\varepsilon}^{pl})\cdot b \tag{2.6}$$

Το μέτρο κράτυνσης μπορεί να εκφραστεί με βάση τον λόγο των εφαπτομενικών μέτρων ελαστικότητας μετά και πριν τη διαρροή $a=E_t/E$ ως εξής:

$$H=\frac{E_t}{1-E_t/E}=\frac{a}{1-a}\cdot E \tag{2.7}$$

Επιπρόσθετα, εφαρμόζοντας συνθήκες Karush-Kuhn-Tucker (ΚΚΤ) καταλήγουμε στην ακόλουθη σχέση:

$$\dot{\lambda}\cdot\Phi(\sigma,b,r)=0 \tag{2.8}$$

Κατά τη διάρκεια της πλαστικής παραμόρφωσης ($\dot{\lambda}>0$, $\Phi(\sigma,b,r)=0$) η παραγώγιση της σχέσης (2.8) δίνει την κατάσταση της συνέπειας (consistency condition):

$$\dot{\Phi}(\sigma,b,r)=0\Rightarrow\left(\dot{\sigma}-\dot{b}\right)\cdot sgn\left(\sigma-b\right)-\dot{r}=0 \tag{2.9}$$

Αντικαθιστώντας τις σχέσεις (2.1), (2.3) and (2.5) στην εξίσωση (2.9) λαμβάνεται η παρακάτω έκφραση του πλαστικού πολλαπλασιαστή:

$$\dot{\lambda}=sgn(\sigma-b)\cdot\frac{E}{E+H}\cdot\dot{\varepsilon}=(1-a)\cdot sgn(\sigma-b)\cdot\dot{\varepsilon} \tag{2.10}$$

Επίσης, αντικαθιστώντας τη σχέση (2.10) στη (2.4) η έκφραση της πλαστικής παραμόρφωσης εξάγεται ως εξής:

$$\dot{\varepsilon}^{p}=(1-a)\cdot\dot{\varepsilon} \tag{2.11}$$

όπου, ο λόγος των μέτρων ελαστικότητας μετά και πριν τη διαρροή δίνεται από την έκφραση (2.12) σύμφωνα με τις σχέσεις (2.6) και (2.7) :

$$a=\frac{E_{pl}}{E}=\frac{H}{E+H}=\frac{H_0-q\cdot\mathrm{sgn}(\dot{\varepsilon}^{pl})\cdot b}{E+H_0-q\cdot\mathrm{sgn}(\dot{\varepsilon}^{pl})\cdot b} \tag{2.12}$$

Η έκφραση (2.11) αφορά την περίπτωση πλαστικής ροής μόνο. Για να είναι δυνατή η έκφραση όλων των σταδίων φόρτισης εισάγονται δύο συναρτήσεις τύπου Heaviside οι οποίες δρουν ως διακόπτες ενεργοποιώντας την ελαστική/πλαστική συμπεριφορά:

$$\dot{\varepsilon}^{p}=H_1\cdot H_2\cdot(1-a)\cdot\dot{\varepsilon} \tag{2.13}$$

Η συνάρτηση H_1 ελέγχει τη διαρροή, ενώ η H_2 ελέγχει τη φάση φόρτισης/αποφόρτισης.

$$H_1=\begin{cases}0, & \text{ελαστική παραμόρφωση } \left(\dot{\varepsilon}^{p}=0\right)\\ 1, & \text{πλαστική παραμόρφωση } \left(\dot{\varepsilon}^{p}=H_2\cdot(1-a)\cdot\dot{\varepsilon}\right)\end{cases} \tag{2.14}$$

$$H_2=\begin{cases}0, & \text{αποφόρτιση}\left(\dot{\varepsilon}^{p}=0\right)\\ 1, & \text{φόρτιση}\left(\dot{\varepsilon}^{p}=H_1\cdot(1-a)\cdot\dot{\varepsilon}\right)\end{cases} \tag{2.15}$$

Ο «διακόπτης» H_1 προκύπτει από την ομαλοποίηση της συνάρτησης διαρροής ως εξής:

$$H_1=\left|\frac{\sigma-b}{r}\right|^{n}=\left|\frac{\sigma_h}{r}\right|^{n} \tag{2.16}$$

Η παράμετρος n ελέγχει τη μορφή μετάβασης από την ελαστική στην πλαστική περιοχή, η οποία γίνεται ομαλότερα για μικρές τιμές της παραμέτρου ενώ για μεγαλύτερες προσεγγίζεται απότομα η διγραμμική συμπεριφορά.

Επιπρόσθετα, ο «διακόπτης» H_2 στοχεύει στο να ελέγξει τη συνθήκη φόρτισης/αποφόρτισης ελέγχοντας το πρόσημο του ρυθμού μεταβολής της συνάρτησης διαρροής ως εξής:

$$H_2 = 0.5 \cdot \left(1 + sgn\left(\frac{d\Phi}{d\sigma} \cdot \dot{\sigma} \right) \right) = 0.5 + 0.5 \cdot sgn\left((\sigma - b) \cdot \dot{\varepsilon} \right) \tag{2.17}$$

Τέλος, αντικαθιστώντας τις συναρτήσεις (2.16) και (2.17) αρχικά στη σχέση (2.13) και έπειτα στη σχέση (2.1) η τελική ελαστοπλαστική καταστατική έκφραση είναι η ακόλουθη:

$$\dot{\sigma} = \left[1 - (1-\alpha) \cdot H_1 \cdot H_2 \right] \cdot E \cdot \dot{\varepsilon} \; = \; E_t \cdot \dot{\varepsilon} \tag{2.18}$$

όπου E_t είναι το εφαπτομενικό μέτρο Young του χάλυβα.

Στη συνέχεια το βασικό καταστατικό προσομοίωμα τροποποιείται ώστε να ενσωματώσει το φαινόμενο Bauschinger. Η αρχική διγραμμική συμπεριφορά της πρώτης διαρροής περιγράφεται με μια μεγάλη τιμής της παραμέτρου n $\left(n_1 \geq 8 \right)$, ενώ η μετέπειτα ομαλή επαναφόρτιση στην αντίθετη διεύθυνση περιγράφεται αν η αρχική τιμή n μειωθεί σε μια μικρότερη για τους επόμενους κύκλους $\left(n_2 \leq 2 \right)$.

Παρομοίως, το πλατό διαρροής ενσωματώνεται στο προτεινόμενο προσομοίωμα θέτοντας μία τιμή κατωφλίου ε_{plat} όπου ο λόγος *a* λαμβάνει την τελική τιμή του. Πιο συγκεκριμένα, ο λόγος *a* ratio αρχικοποιείται σε μηδενική τιμή που αντιστοιχεί σε ελαστική απολύτως πλαστική συμπεριφορά και τη στιγμή που η πλαστική παραμόρφωση ε^p ξεπερνά την τιμή ε_{plat} σηματοδοτείται η έναρξη του κλάδου κράτυνσης $\left(a > 0 \right)$.

Μία ακόμα τροποποίηση αφορά τη συμβατότητα του μοντέλου με τα αξιώματα της πλαστικότητας των Drucker και Ilyushin όταν εμφανίζεται κλάδος μερικής αποφόρτισης/επαναφόρτισης. Αυτό επιτυγχάνεται αν ο δείκτης H_2 λάβει την παρακάτω μορφή:

$$\overline{H}_2 = H_2 \cdot (1 - R) \tag{2.19}$$

όπου $R\left(\sigma_h ,\, \varepsilon ,\, \sigma_{y0} \right)$ είναι ο παράγοντας που ελέγχει την ανάκτηση της δυσκαμψίας στο στάδιο της επαναφόρτισης:

$$R = 0.5 \cdot \left[1 + sgn(\sigma_h - \sigma_r) \cdot sgn(\sigma_h) \right] \cdot \left(\frac{\varepsilon_r - \varepsilon_c}{\varepsilon_r - \varepsilon} \right) \tag{2.20}$$

Στη σχέση (2.20) σ_h είναι το υστερητικό μέρος της τάσης $\left(\sigma_h = \sigma - b\right)$, σ_r και ε_r είναι η τάση και η παραμόρφωση στο σημείο αποφόρτισης και ε_c είναι η τροποποιημένη παραμόρφωση στον κλάδο αποφόρτισης για το αντίστοιχο επίπεδο έντασης της υστερητικής τάσης σ_h :

$$\varepsilon_c = \left(\frac{\sigma_h - \sigma_r}{\sigma_{y0}} \right) \cdot \varepsilon_{y0} + \varepsilon_r \cdot sgn(\sigma_h) \tag{2.21}$$

Καταλήγοντας, το προτεινόμενο προσομοίωμα του χάλυβα παρουσιάζεται στο Σχήμα 2.1 όπου επίσης παρατίθενται η ακολουθία των σημείων εναλλαγής της έντασης, το πλατό διαρροής και το φαινόμενο της ισοτροπικής κράτυνσης. Η καμπύλη τάσεων-παραμορφώσεων του χάλυβα προκύπτει με την επιβολή της χρονοϊστορίας αξονικής παραμόρφωσης του Πίνακα 2.1.

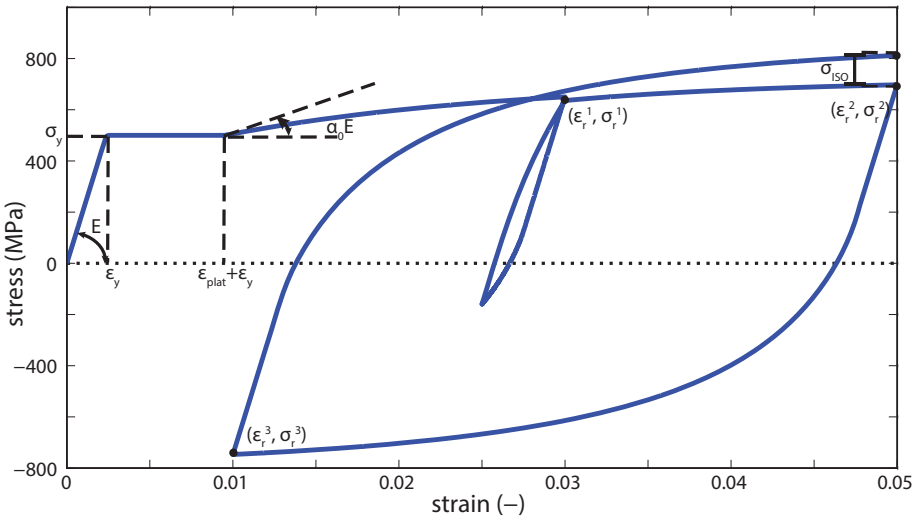

Σχήμα 2.1. Προτεινόμενο προσομοίωμα χάλυβα

Ψευδοχρόνος (sec)	**Παραμόρφωση (-)**
0	0
1	0.03
2	0.025
3	0.05
4	0.01
5	0.05

Πίνακας 2.1. Χρονοϊστορία επιβαλλόμενων παραμορφώσεων

Η τεκμηρίωση του προτεινόμενου προσομοιώματος γίνεται με τη σύγκριση με πειραματικά δεδομένα των Ma et al. (1976). Τα αποτελέσματα της σύγκρισης παρουσιάζονται στο Σχήμα 2.2, ενώ οι παράμετροι που χρησιμοποιήθηκαν στο προτεινόμενο προσομοίωμα παρατίθενται στον Πίνακα 2.2. Είναι γενικά εμφανές ότι ο εξαγόμενος καταστατικός νόμος είναι αρκετά ικανός να περιγράψει όλα τα στάδια της ανελαστικής συμπεριφοράς, δηλ. το πλατό διαρροής, τη μη γραμμική κράτυνση και το φαινόμενο Bauschinger.

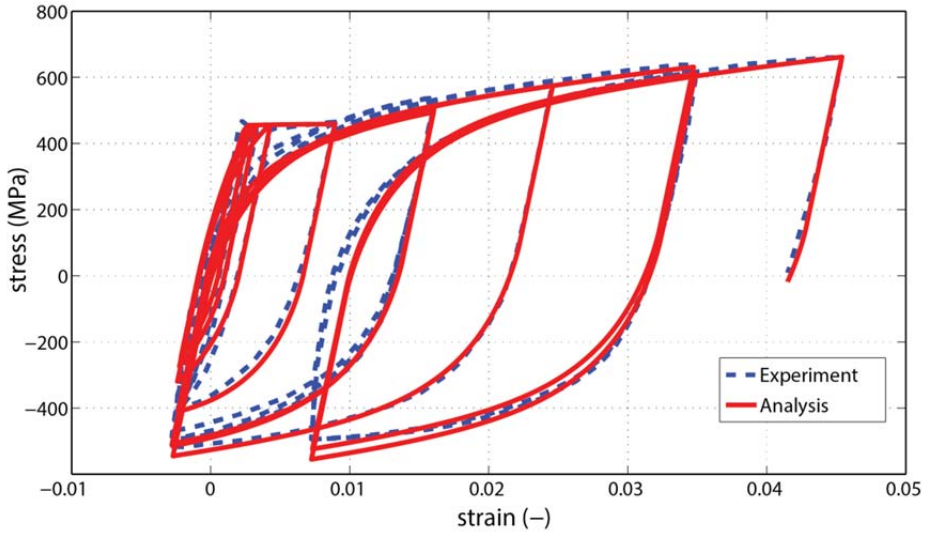

(a)

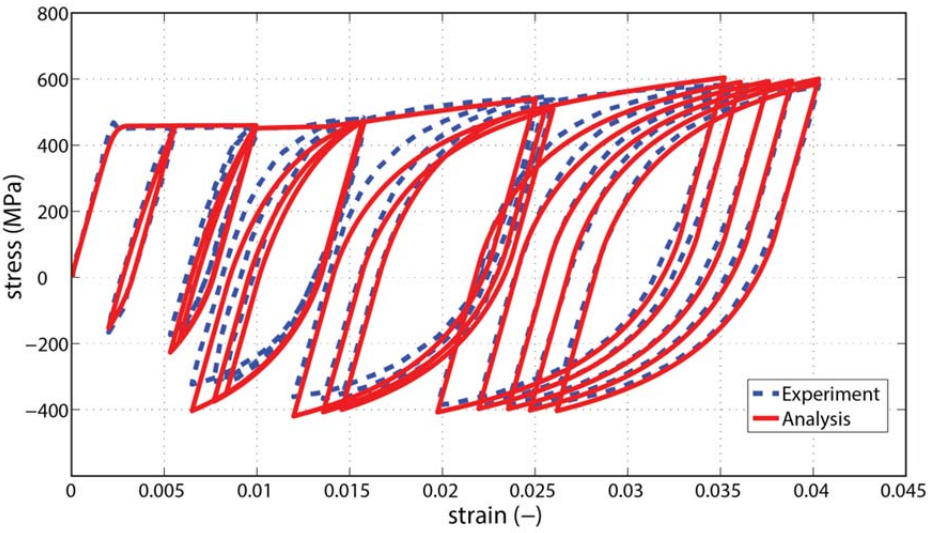

(b)

Σχήμα 2.2. Σύγκριση με τα πειραματικά αποτελέσματα των Ma et al. (a) Δοκίμιο 3 (b) Δοκίμιο 2

σ_y (MPa)	α	n_1	n_2	ε_{plat}	m	q
460	0.035	10	0.5	$4\varepsilon_y$	0.03	10

Πίνακας 2.2. Παράμετροι προσομοιώματος χάλυβα για τη σύγκριση με τα πειραματικά αποτελέσματα των Ma et al.

Όσον αφορά τη μεθοδολογία υπολογισμού του λυγισμού των διαμήκων ράβδων οπλισμού, αυτή βασίζεται στην υπόθεση των απαραμόρφωτων συνδετήρων, συνεπώς η ράβδος οπλισμού θεωρείται αμφίπακτη υπό την επιβολή αξονικού φορτίου (Σχήμα 2.3).

Σύμφωνα με την ελαστική θεωρία λυγισμού Euler, η ράβδος παραμορφώνεται πλευρικά, εκδηλώνοντας πλευρικές μετακινήσεις υπό την μορφής συνημιτονοειδούς καμπύλης:

$$y(x) = \frac{e}{2} \cdot \left(1 - \cos\left(\frac{2\pi x}{L} \right) \right) \tag{2.22}$$

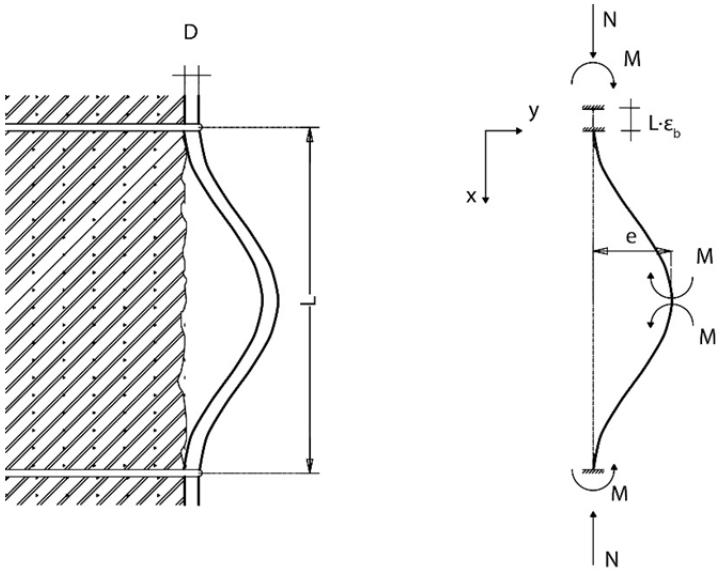

Σχήμα 2.3. Φυσικό και υπολογιστικό προσομοίωμα λυγισμού των ράβδων οπλισμού

Επίσης, η καμπυλότητα κατά μήκος της ράβδου προκύπτει από τη διπλή παραγώγιση της εξίσωσης μετακινήσεων:

$$\varphi(x) = \frac{2e\pi^2}{L^2} \cdot \cos\left(\frac{2\pi x}{L} \right) \tag{2.23}$$

Με μέγιστη τιμή στο μέσον:

$$\varphi(L/2) = \frac{2e\pi^2}{L^2} \tag{2.24}$$

Η συνολική μέση αξονική παραμόρφωση ε_{av} της ράβδου μπορεί να θεωρηθεί ως το άθροισμα της παραμόρφωσης $\varepsilon_{0,}$ η οποία συμμετέχει στην εσωτερική ενέργεια παραμόρφωσης της ράβδου και στη δευτερογενή παραμόρφωση λυγισμού ε_b η οποία οφείλεται στην επιπρόσθετη βράχυνση εξαιτίας του αυξημένου μήκους τόξου που προκαλεί η πλευρική παραμόρφωση.

$$\varepsilon_{av} = \varepsilon_0 + \varepsilon_b \tag{2.25}$$

Το μήκος τόξου της παραμορφωμένης ράβδου υπολογίζεται αναλυτικά μέσω της σχέσης που πρότειναν οι Dhakal και Maekawa (2002):

$$L = \int_0^{L(1-\varepsilon_b)} \sqrt{1+\left(\frac{dy}{dz}\right)^2}\,dx = 2\cdot \int_0^{\frac{L(1-\varepsilon_b)}{2}} \sqrt{1+\left(\frac{e\pi}{L(1-\varepsilon_b)}\sin\frac{2\pi x}{L(1-\varepsilon_b)}\right)^2}\,dx \tag{2.26}$$

Η σχέση (2.26) αναπτύσσεται σε σειρά Taylor αμελώντας τους όρους ανωτέρας τάξης δίνοντας εν τέλει την παρακάτω έκφραση της δευτερογενούς παραμόρφωσης λυγισμού:

$$\varepsilon_b = \frac{1}{2}\left(1-\sqrt{1-e^2\pi^2}\right) \tag{2.27}$$

Η τεκμηρίωση του προσομοιώματος λυγισμού πραγματοποιείται μέσω της σύγκρισης με τα πειραματικά αποτελέσματα των Monti and Nuti (1992). Σε αυτή την σύγκριση εφαρμόζεται συμμετρική χρονοϊστορία παραμορφώσεων στο εύρος (-0.03-0.03), ενώ ο λόγος μήκους προς διάμετρο της εξεταζόμενης ράβδου είναι L/D=11. Επίσης, οι παράμετροι που χρησιμοποιήθηκαν για το προσομοίωμα του χάλυβα παρατίθενται στον Πίνακα 2.3

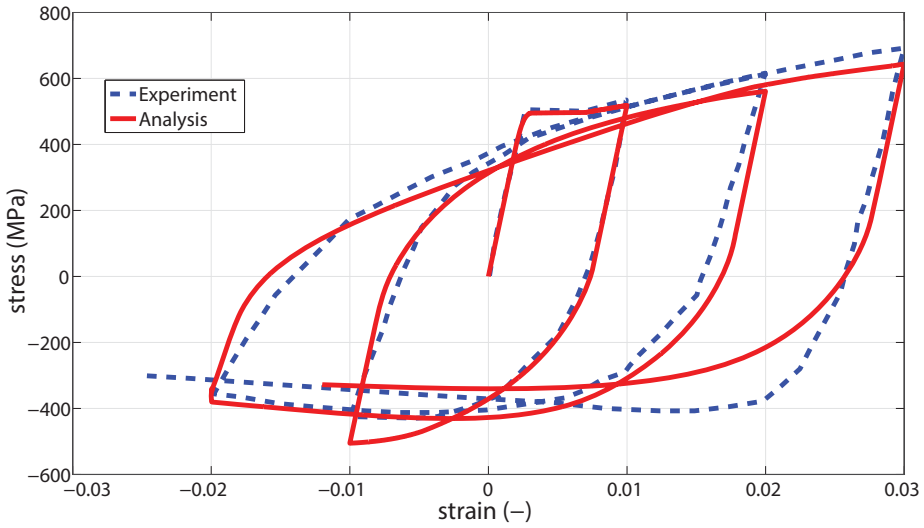

Σχήμα 2.4. Σύγκριση με τα πειραματικά αποτελέσματα των Monti and Nuti (S series, L/D=11)

σ_y (MPa)	α	n_1	n_2	ε_{plat}	m	q
500	0.035	10	0.3	$1.8\varepsilon_y$	0.05	10

Πίνακας 2.3. Παράμετροι του προσομοιώματος χάλυβα για την ανάλυση με τα πειράματα Monti και Nuti (S series, L/D=11).

Η τελευταία σύγκριση αφορά στην επιβολή μη συμμετρικής αλληλουχίας παραμορφώσεων ενώ η σύγκριση με τα αριθμητικά αποτελέσματα παρουσιάζεται στο Σχήμα 2.5. Οι παράμετροι της προτεινόμενης μεθοδολογίας παρατίθενται στον Πίνακα 2.4.

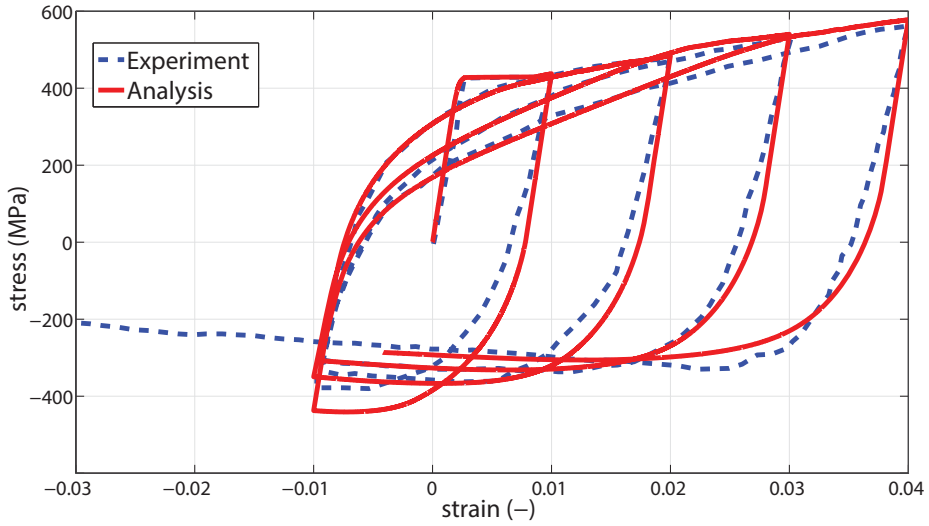

Σχήμα 2.5. Σύγκριση με τα πειραματικά αποτελέσματα των Monti and Nuti (C5 specimen, L/d=11)

σ_y (MPa)	α	n_1	n_2	ε_{plat}	m	q
430	0.03	10	0.4	$3\varepsilon_y$	0.05	10

Πίνακας 2.4. Παράμετροι του προσομοιώματος χάλυβα για την ανάλυση με τα πειράματα Monti και Nuti (C5 specimen, L/D=11).

Είναι πρόδηλο από τα αποτελέσματα των συγκρίσεων ότι το προσομοίωμα των ράβδων οπλισμού αποδίδει ικανοποιητικά τους βρόχους υστέρησης και ειδικά την περιοχή του έντονου στενέματος των βρόχων στη θλιπτική περιοχή, όπου εξαιτίας του έντονου λυγισμού παρουσιάζεται κλάδος αρνητικής δυσκαμψίας.

III. Προσομοίωση Σκυροδέματος

Σε αυτό το κεφάλαιο αναπτύσσεται ένα ομαλό, μονοαξονικό προσομοίωμα σκυροδέματος το οποίο συνδυάζει την πλαστικότητα με τη μηχανική των βλαβών. Το προσομοίωμα είναι ικανό να περιγράψει την ασύμμετρη θλιπτική και εφελκυστική συμπεριφορά, ενώ αντιμετωπίζει επιτυχώς ανακυκλιζόμενα φαινόμενα όπως η μη-γραμμική αποφόρτιση και το φαινόμενο του κλεισίματος/ανοίγματος των ρωγμών.

Το σκυρόδεμα όταν υποβάλλεται σε χαμηλού επιπέδου ένταση εμφανίζει ελαστική συμπεριφορά η οποία εξελίσσεται γρήγορα σε μη-γραμμική με την εμφάνιση των πρώτων ρωγμών. Η τριβή ανάμεσα στις ρωγμές εμποδίζει το περαιτέρω άνοιγμα των ρωγμών χωρίς αντίσταση. Κατά τη διαδικασία αυτή αναπτύσσεται υστερητική ενέργεια και ως συνέπεια εμφανίζεται μακροσκοπικά υστερητική συμπεριφορά η οποία μπορεί να περιγραφεί ως ελαστοπλαστική συμπεριφορά με μη-γραμμικό νόμο ισοτροπικής κράτυνσης. Συνεπώς, ο μη-γραμμικός καταστατικός νόμος τάσεων-παραμορφώσεων λαμβάνει την ακόλουθη μορφή:

$$\dot{\bar{\sigma}}_c = E_C \cdot \dot{\varepsilon}_c^{el} = E_c \cdot \left(\dot{\varepsilon}_c - \dot{\varepsilon}_c^{p} \right) \tag{3.1}$$

όπου $\bar{\sigma}_c$ είναι η τάση του σκυροδέματος χωρίς βλάβες και $\varepsilon_c, \varepsilon_c^p$ είναι η συνολική και πλαστική παραμόρφωση αντίστοιχα. Η πλαστική παραμόρφωση δίνεται σε ενοποιημένη μορφή χρησιμοποιώντας τις συναρτήσεις τύπου «διακόπτη» ελαστικής/πλαστικής H_{c1} φόρτισης και φόρτισης/αποφόρτισης H_{c2} ως εξής:

$$\dot{\varepsilon}_c^{p} = H_{c1} \cdot H_{c2} \cdot (1-\alpha_c) \cdot \dot{\varepsilon}_c \tag{3.2}$$

$$H_{c2} = 0.5 \cdot \left[1 + \text{sgn}(\bar{\sigma}_c \cdot \dot{\varepsilon}_c) \right] \tag{3.3}$$

$$H_{c1} = \left| \frac{\bar{\sigma}_c}{\sigma_{yc}} \right|^{n_c} \tag{3.4}$$

όπου η μεταβλητή $\alpha_{c,i}$ ορίζει το λόγο της μετελαστικής προς την ελαστική δυσκαμψία και η παράμετρος n_c ελέγχει την ομαλότητα της καμπύλης μετάβασης από την ελαστική στην πλαστική περιοχή. Στην παρούσα διατύπωση του προσομοιώματος δεν απαιτείται ομαλή μετάβαση, οπότε $n_c \geq 10$. Επίσης, σ_{yc} είναι η τρέχουσα τάση διαρροής η οποία εξελίσσεται σύμφωνα με τον ακόλουθο μη-γραμμικό νόμο ισοτροπικής κράτυνσης:

$$\dot{\sigma}_{yc} = H_{c1} \cdot H_{c2} \cdot \alpha_c \cdot \text{sgn}(\bar{\sigma}_c) \cdot E_c \cdot \dot{\varepsilon}_c \tag{3.5}$$

όπου ο λόγος α_c δίνεται από τη σχέση:

$$a_c = \frac{E_{c,pl}}{E_c} = \frac{H_c}{H_c + E_c} = \frac{H_{c0} - q_C \cdot \left(\sigma_{yc} - \sigma_{yc0}\right)}{E_c + H_{c0} - q_c \cdot \left(\sigma_{yc} - \sigma_{yc0}\right)} \tag{3.6}$$

με H_c και q_c να ορίζονται το μέτρο κράτυνσης και η παράμετρος μη-γραμμικής κράτυνσης αντίστοιχα. Τελικά με τη χρήση των σχέσεων (3.1), (3.2), (3.5) και (3.6) καταλήγουμε στην έκφραση της τάσης του σκυροδέματος χωρίς βλάβη:

$$\dot{\bar{\sigma}}_c = \left(1 - (1 - \alpha_c) \cdot H_{c1} \cdot H_{c2}\right) \cdot E_c \cdot \dot{\varepsilon}_c \tag{3.7}$$

Επίσης, διαφορετική αρχική τάση διαρροής θεωρείται σε εφελκυσμό και θλίψη καθώς οι εφελκυστικές ρωγμές εμφανίζονται σε πολύ χαμηλότερα επίπεδα έντασης από ότι στη θλίψη:

$$\sigma_{\mathrm{yc}0,i} = \left(1 - H_{c3}\right) \cdot \sigma^{+}_{\mathrm{yc}0} + H_{c3} \cdot \sigma^{-}_{\mathrm{yc}0} \tag{3.8}$$

όπου $\sigma^{+}_{\mathrm{yc}0}$ είναι η αρχική τάση διαρροής στον εφελκυσμό, $\sigma^{-}_{\mathrm{yc}0}$ είναι η αρχική τάση διαρροής στη θλίψη και η συνάρτηση τύπου Heaviside H_{c3} ορίζει την κατάσταση φόρτισης (0: εφελκυσμός, 1: θλίψη) και λαμβάνει την ακόλουθη μορφή:

$$H_{c3} = 0.5\left(1 - \mathrm{sgn}(\bar{\sigma}_c)\right) \tag{3.9}$$

Σύντομα μετά την εμφάνιση των αρχικών ρωγμών με τη συνεχόμενη επιβολή του φορτίου η εξέλιξη και το άνοιγμα τους έχουν ως συνέπεια τη μείωση του όγκου αναφοράς στην κρίσιμη περιοχή του μέλους ΟΣ. Το φαινόμενο αυτό της βλάβης προκαλεί την απομείωση και την αρνητική τιμή δυσκαμψίας και αναπαρίσταται στο παρόν προσομοίωμα από τη θεωρία βλάβης συνεχούς μέσου (damage mechanics) (Kachanov 1986). Πιο συγκεκριμένα, γίνεται χρήση της έννοιας της ενεργού τάσης και η θεώρηση ότι η παραμόρφωση αναφοράς είναι η ίδια στην αρχική κατάσταση και στην κατάσταση που έχει επέλθει η βλάβη. Αντίθετα, η πραγματική τάση είναι μειωμένη στην κατάσταση με βλάβη καθώς ο όγκος αναφοράς έχει αυξηθεί λόγο των κενών που οφείλονται στην εξάπλωση των ρωγμών. Ωστόσο, η θεωρία βλαβών από μόνη της δεν μπορεί να περιγράψει τις παραμένουσες παραμορφώσεις στο σκυρόδεμα έπειτα από αποφόρτιση λόγω του μερικού κλεισίματος των ρωγμών. Συνεπώς, είναι αναγκαίος ο συνδυασμός τόσο της πλαστικότητας όσο και της συμπεριφοράς με ενσωμάτωση της βλάβης (Σχήμα 3.1)

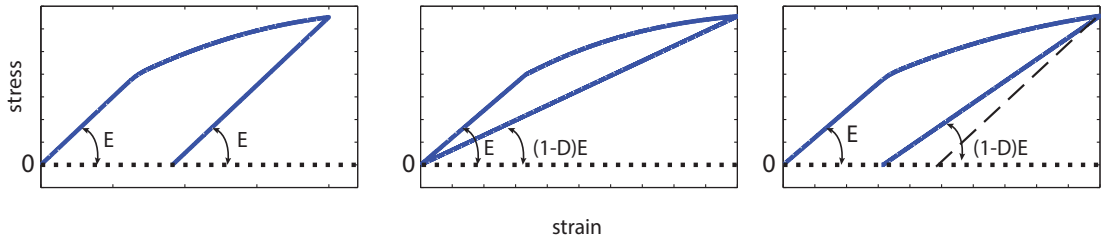

(a) (b) (c)

Σχήμα 3.1. Συνδυασμός θεωριών πλαστικότητας και βλαβών

Η πραγματική τάση του σκυροδέματος υπολογίζεται από την ενεργή τάση μέσω της παραμέτρου βλάβης που ποσοτικοποιεί τη βλάβη σε θλίψη και εφελκυσμό σύμφωνα με τη σχέση (3.11).

$$\sigma_c = (1-D)\cdot\bar{\sigma}_c \tag{3.10}$$

$$(1-D) = (1-H_{c3}D_-)\cdot\left[1-(1-H_{c3})D_+\right] \tag{3.11}$$

Ο ρυθμός μεταβολής της σχέσης (3.11) προκύπτει ως εξής:

$$\dot{D} = H_{c3}\dot{D}_-\left[1-(1-H_{c3})D_-\right]+(1-H_{c3})\dot{D}_+\left[1-H_{c3}D_-\right] \tag{3.12}$$

ενώ ο ρυθμός μεταβολής της (3.10) δίνεται από την παρακάτω σχέση:

$$\dot{\sigma}_c = (1-D)\dot{\bar{\sigma}}_c - \dot{D}\bar{\sigma}_c \tag{3.13}$$

Η παράμετρος βλάβης είτε σε θλίψη είτε σε εφελκυσμό $D_i = D_i\left(k_i\left(\varepsilon_i\right)\right)$ ελέγχεται από τη μεταβλητή εξέλιξης της βλάβης k_i και δίνεται αναλυτικά από την έκφραση:

$$D_i = 1-e^{-\left(\frac{k_i-k_{0,i}}{b_i k_{0,i}}\right)^{p_i}} \tag{3.14}$$

όπου b_i και p_i είναι παράμετροι του μοντέλου που ελέγχουν την εξέλιξη της βλάβης και οι τιμές τους μπορούν να προσδιοριστούν από πειραματικά δεδομένα. Η μεταβλητή εξέλιξης της βλάβης k_i είναι συνάρτηση της διακριτής παραμόρφωσης ε_i σε θλίψη ή εφελκυσμό ενώ αρχίζει να εξελίσσεται πέρα ενός ορίου $k_{0,i}$ το οποίο ορίζει την εκκίνηση της βλάβης.

$$\dot{k}_i = H_{c4}\cdot H_{c2}\cdot\dot{\varepsilon}_{c,i} \tag{3.15}$$

όπου $\varepsilon_{c,i}$ είναι η διακριτή τιμή της παραμόρφωσης του σκυροδέματος σε θλίψη/εφελκυσμό και η συνάρτηση «διακόπτης» H_{C4} ενεργοποιεί την εξέλιξη της βλάβης (0: κατάσταση χωρίς βλάβη, 1: κατάσταση με βλάβη):

$$H_{C4} = \left| \frac{\varepsilon_{c,i}}{k_i} \right|^m \tag{3.16}$$

Η παράμετρος m ελέγχει την ομαλή μετάβαση από την αρχική κατάσταση στην κατάσταση βλάβης προτείνοντας μεγάλες τιμές ($m \geq 10$) καθώς η απότομη μετάβαση είναι επιθυμητή.

Εφαρμόζοντας των κανόνα αλυσιδωτής παραγώγισης για την παράμετρο D_i, λαμβάνεται η εξέλιξη της ως εξής:

$$\dot{D}_i = \frac{dD_i}{dk_i} \dot{k}_i \tag{3.17}$$

Έπειτα αντικαθιστώντας τη σχέση (3.15) στη σχέση (3.17) παράγεται η ακόλουθη εξίσωση του ρυθμού μεταβολής της παραμέτρου βλάβης:

$$\dot{D}_i = \frac{dD_i}{dk_i} \dot{k}_i = H_{c4} \cdot H_{c2} \cdot \frac{dD_i}{dk_i} \cdot \dot{\varepsilon}_{c,i} \tag{3.18}$$

Τέλος, η αντικατάσταση των σχέσεων (3.7) και (3.18) στη σχέση (3.13) έχει ως αποτέλεσμα τις ακόλουθες συνοπτικές εξισώσεις οι οποίες περιγράφουν το μοντέλο σκυροδέματος και συνδυάζουν πλάστιμη και φθίνουσα συμπεριφορά λόγω βλάβης:

$$\dot{\sigma}_c = E_{c,t} \, \dot{\varepsilon}_c \tag{3.19}$$

$$E_{c,t} = \left\{ (1-D)\left[1-(1-a_c)\cdot H_{c1}\cdot H_{c2}\right] - \left(H_{c4}\cdot H_{c2}\cdot \frac{dD_i}{dk_i}\cdot \frac{\bar{\sigma}_c}{E_c} \right) \right\} E_c \tag{3.20}$$

Επιπρόσθετα, είναι προφανές από πειραματικά δεδομένα ανακυκλιζόμενης συμπεριφοράς δοκιμίων σκυροδέματος ότι ο κλάδος αποφόρτισης στη θλίψη είναι μη-γραμμικός. Το φαινόμενο αυτό ενσωματώνεται στο προσομοίωμα σύμφωνα με τη σχέση:

$$r_{un} = \left(c_1 \left| \frac{\bar{\sigma}_c}{\bar{\sigma}_{c,r}} \right| + c_2 \right)^{1-H_{c2}} \tag{3.21}$$

όπου r_{un} αποτελεί τι συνάρτηση μη-γραμμικής αποφόρτισης που ορίζεται από το σημείο εναλλαγής της έντασης $\bar{\sigma}_{c,r}$ έως την πλήρη μείωση της ενεργούς τάσης στο μηδέν, ενώ ο εκθέτης $1-H_{c2}$ ενεργοποιεί τη συνάρτηση μόνο όταν ανιχνεύεται αποφόρτιση και c_1, c_2

είναι παράμετροι. Συνεπώς το εφαπτομενικό μέτρο του σκυροδέματος διαμορφώνεται ως εξής:

$$E_{c,t} = \left\{ (1-D)\left[1-(1-a_c)\cdot H_{c1}\cdot H_{c2}\right] - \left(H_{c4}\cdot H_{c2}\cdot \frac{dD_i}{dk_i}\cdot \frac{\bar{\sigma}_c}{E_c} \right) \right\} \cdot r_{un}\cdot E_c \tag{3.22}$$

Επίσης, όταν συμβαίνει αποφόρτιση από τον εφελκυστικό κλάδο, εμφανίζονται ομοίως παραμένουσες παραμορφώσεις οι οποίες οφείλονται στην ατελή γεωμετρία των ρωγμών. Όταν η φόρτιση συνεχιστεί στη θλιπτική περιοχή η επαναφορά της δυσκαμψίας γίνεται σταδιακά ακολουθώντας το κλείσιμο των ρωγμών. Το φαινόμενο αυτό ενσωματώνεται επίσης στο προτεινόμενο προσομοίωμα μέσω της συνάρτησης επαναφοράς δυσκαμψίας $r_{rec}(\varepsilon_{rec}, \varepsilon_c^-)$:

$$r_{rec} = 1 - \left(1 - \frac{E_c}{E_{c,t}^+}\right)\cdot \left|\frac{\varepsilon_c^-}{\varepsilon_{rec}}\right|^{n_{rec}} \tag{3.23}$$

$$\dot{\varepsilon}_c^- = \left(1 - \left|\frac{\varepsilon_c^-}{\varepsilon_{rec}}\right|^{n_{rec}}\right)\cdot \left|\dot{\varepsilon}_c\right| \tag{3.24}$$

όπου $E_{c,t}^+$ είναι η εφαπτομενική εφελκυστική δυσκαμψία, ε_C^- είναι η θλιπτική παραμόρφωση και ε_{rec} είναι η παραμόρφωση όπου οι ρωγμές κλείνουν εντελώς όταν το φαινόμενο αγνοείται. Επίσης, η παράμετρος n_{rec} ελέγχει την ομαλότητα του κλεισίματος των ρωγμών τείνοντας στην εξαφάνιση του φαινομένου για μεγάλες τιμές.

Τέλος, συνδιάζοντας όλα τα φαινόμενα, το συνολικό καταστατικό προσομοίωμα του σκυροδέματος εκφράζεται μέσω των παρακάτω σχέσεων:

$$\begin{aligned} \dot{\sigma}_c &= E_{c,t}\cdot \dot{\varepsilon}_c \\ E_{c,t} &= \begin{cases} \left\{ (1-D)\cdot\left[1-(1-a)\cdot H_{c1}\cdot H_{c2}\right] - \left(H_{c4}\cdot H_{c2}\cdot \frac{dD_i}{dk_i}\cdot \frac{\bar{\sigma}_c}{E_i} \right) \right\} \cdot r_{un}\cdot E_c \\ r_{rec}\cdot E_{c,t}^+ \end{cases} \end{aligned} \tag{3.25}$$

Στο Σχήμα 3.2 παρουσιάζεται γραφικά η μονοαξονική συμπεριφορά του σκυροδέματος, ενώ οι τιμές των παραμέτρων που χρησιμοποιήθηκαν παρατίθενται στον Πίνακα 3.1.

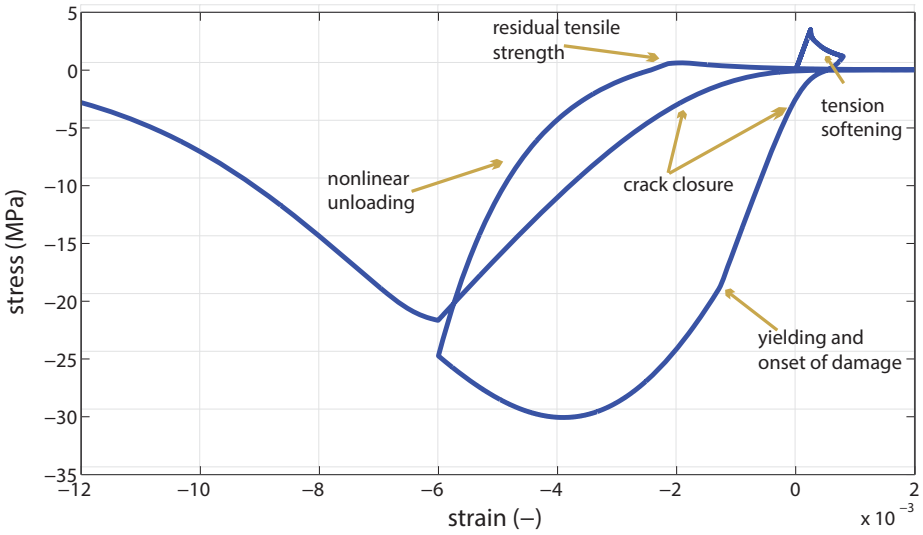

Σχήμα 3.2. Σχηματική αναπαράσταση του προσομοιώματος σκυροδέματος

	E_c (GPa)	σ_y (MPa)	a_c	q_c	$k_{0,i}$	b_i	p_c	c_1	c_2	n_{rec}
Θλίψη	30	25.0	0.5	1000	0.000833	6.5	1.0	3.0	0.2	10
Εφελκυσμός		5.0	-	-	0.000167	0.5	0.5	3.0	0.2	-

Πίνακας 3.1. Παράμετροι του προσομοιώματος σκυροδέματος

Η τεκμηρίωση της θλιπτικής συμπεριφοράς του προτεινόμενου προσομοιώματος πραγματοποιείται με τη σύγκριση με τα πειραματικά δεδομένα των Sinha et al. (1964), Bahn and Hsu (1998) και Muguruma et al. (1983). Τα αποτελέσματα των συγκρίσεων παρουσιάζονται στα Σχήματα 3.3 έως 3.5, ενώ οι παράμετροι που χρησιμοποιήθηκαν παρατίθενται σε αδιάστατη μορφή στον Πίνακα 3.2.

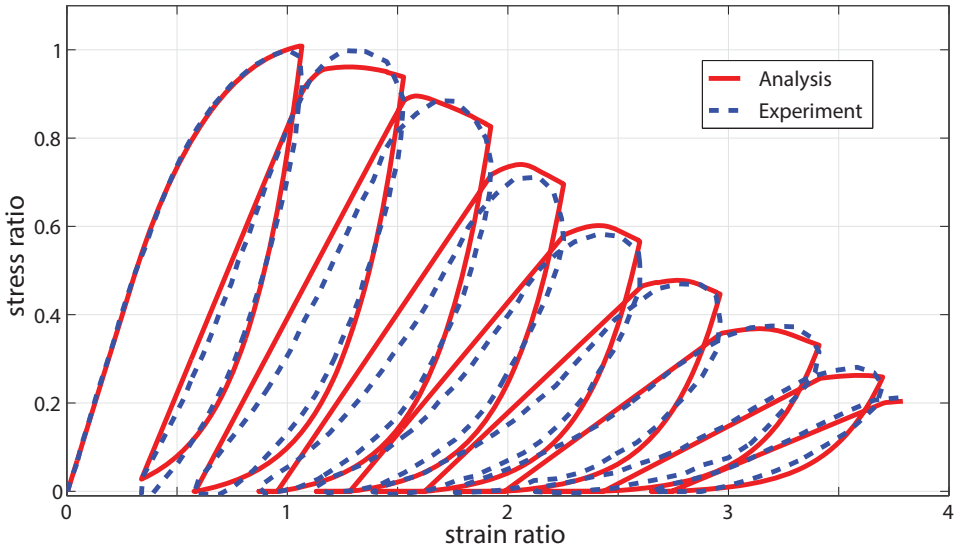

Σχήμα 3.3. Σύγκριση με τα πειραματικά δεδομένα των Sinha et al.

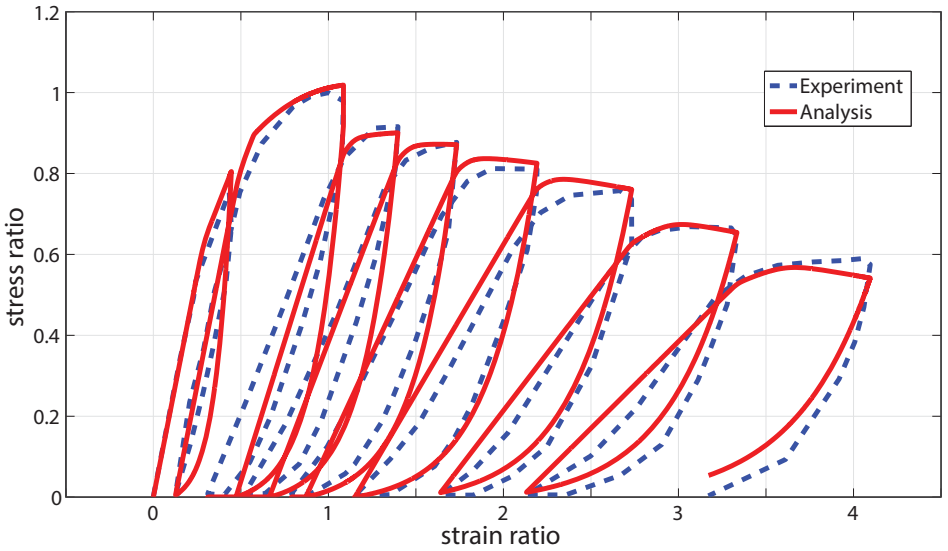

Σχήμα 3.4. Σύγκριση με τα πειραματικά δεδομένα των Muguruma et al.

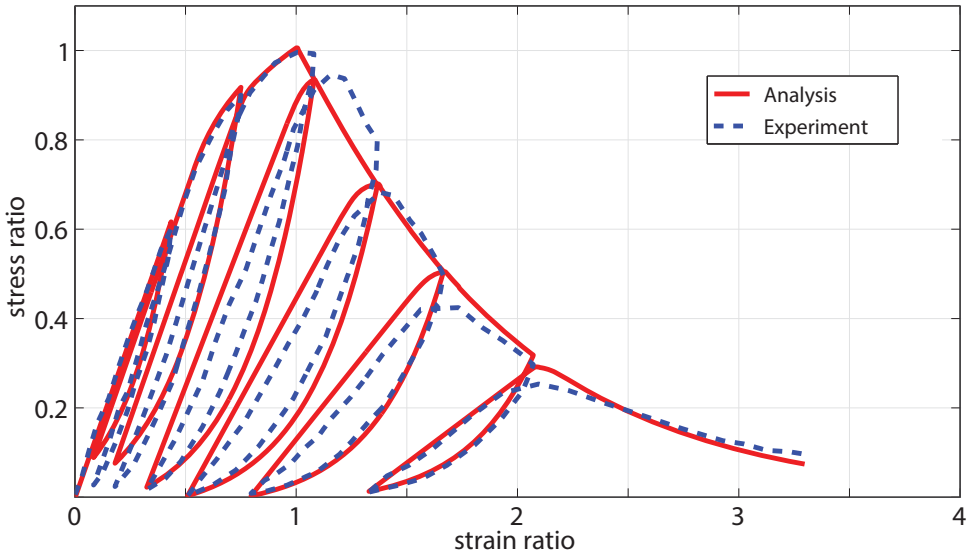

Σχήμα 3.5. Σύγκριση με τα πειραματικά δεδομένα των Bahn και Hsu

Αδιάστατες παράμετροι	Sinha et al.	Muguruma et al.	Bahn-Hsu
$\sigma_{yc}/\sigma_{c,max}$	0.7	0.6	0.75
$\varepsilon_{yc}/\varepsilon_{co}$	0.4	0.29	0.5
α_c	0.5	0.5	0.7
q_c	10	10	12
k_o/ε_o	0.4	0.57	1.0
b_c	4.5	2.5	0.9
p_c	1.4	0.75	1.0
c_1	3.8	4.0	3.5
c_2	0.1	0.1	0.1

Πίνακας 3.2. Θλιπτικές παράμετροι σκυροδέματος.

Παρομοίως, όσον αφορά την εφελκυστική συμπεριφορά, η σύγκριση γίνεται με τα πειραματικά αποτελέσματα των Reinhardt και Cornelissen (1984), όπου το δοκίμιο σκυροδέματος φορτίζεται στη θλίψη και εφελκυσμό και συνεπώς αναπαράγεται το φαινόμενο του κλεισίματος/ανοίγματος των ρωγμών. Επίσης, οι παράμετροι του μοντέλου που χρησιμοποιήθηκαν παρουσιάζονται στον Πίνακα 3.3.

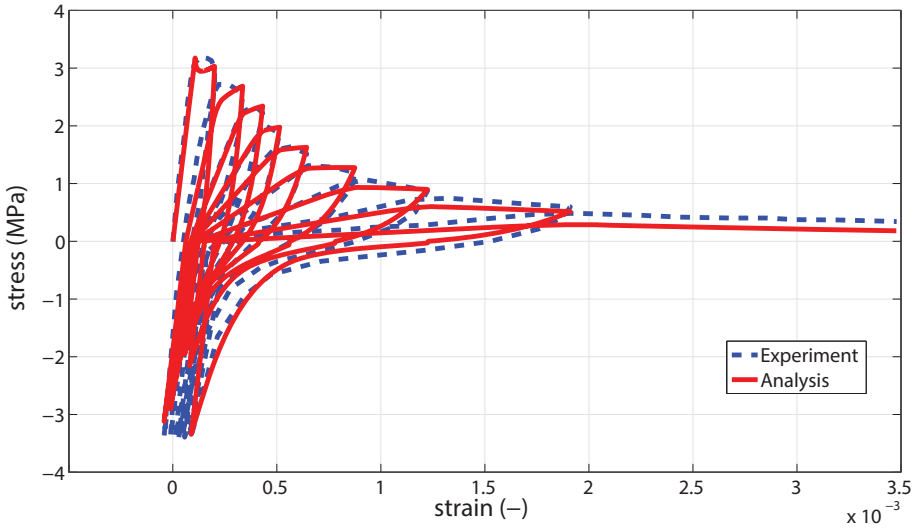

Σχήμα 3.6. Σύγκριση με τα πειραματικά δεδομένα των Reinhardt και Cornelissen

E_C (GPa)	σ_{yt} (MPa)	$\alpha_{c,t}$	$q_{c,t}$	$k_{0,t}$	b_t	p_t	c_1	c_2	n_{rec}
30	3.2	0.6	0	0.00011	3.0	0.7	3.5	0.8	5.0

Πίνακας 3.3. Εφελκυστικές παράμετροι σκυροδέματος

Είναι γενικά εμφανές από τις συγκρίσεις ότι τη προτεινόμενη μεθοδολογία μπορεί να αναπαράγει επιτυχώς τα πειραματικά δεδομένα τόσο στη θλίψη όσο και στον εφελκυσμό αναπαριστώντας ρεαλιστικά κάθε μορφή των βρόχων υστέρησης.

IV. Προσομοίωμα δοκού-υποστυλώματος ινών

Σε αυτό το κεφάλαιο αναπτύσσεται η διατύπωση του πεπερασμένου στοιχείου δοκού στο πλαίσιο της θεώρησης κατανεμημένης πλαστικότητας. Γενικά, η καθολική διατύπωση του στοιχείου και η επίλυση ολόκληρης της κατασκευής βασίζεται σε τέσσερα επίπεδα (Σχήμα 4.1).

1. Επίπεδο ίνας, όπου με δεδομένη την αξονική παραμόρφωση και των εσωτερικών καταστατικών μεταβλητών, προσδιορίζονται οι τάσεις του σκυροδέματος και του χάλυβα οπλισμού και τα εφαπτομενικά τους μέτρα.
2. Επίπεδο διατομής, όπου οι τάσεις και τα εφαπτομενικά μέτρα των ινών αθροίζονται και προκύπτουν τα εντατικά μεγέθη και το μητρώο δυσκαμψίας της διατομής.
3. Επίπεδο στοιχείου, όπου διενεργείται ο προσδιορισμός των επικόμβιων εσωτερικών δυνάμεων του στοιχείου και του μητρώου δυσκαμψίας του μέσω της ολοκλήρωσης των εντατικών μεγεθών των επιμέρους διατομών ελέγχου.

4. Επίπεδο κατασκευής, όπου ελέγχεται η συνολική ισορροπία μέσω της ισότητας των εσωτερικών και εξωτερικών δράσεων.

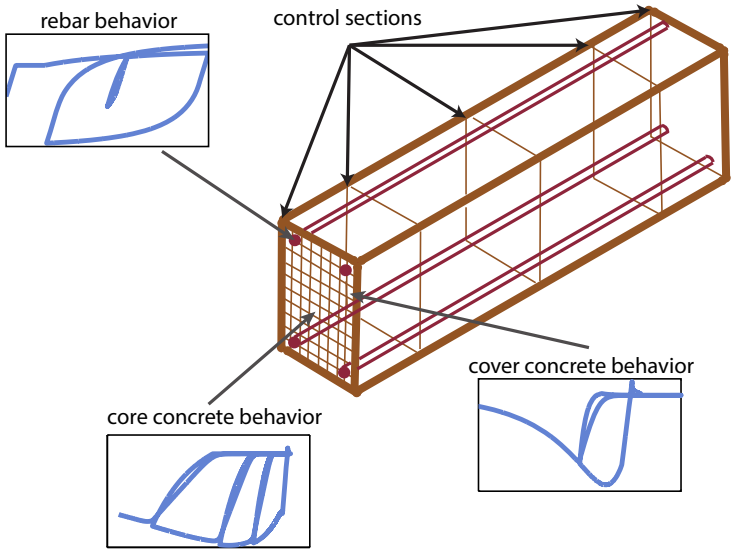

Σχήμα 4.1. Σχηματική αναπαράσταση του στοιχείου δοκού ινών

Αρχικά, γίνεται η κινηματική θεώρηση ότι οι διατομές παραμένουν επίπεδες μετά την παραμόρφωση και κάθετες στον άξονα της ελαστικής γραμμής. Βασιζόμενοι σε αυτή την παραδοχή η αξονική μετακίνηση σε κάθε σημείο της διατομής εκφράζεται από τη σχέση:

$$u_x(x,y) = u(x) - y \cdot \frac{\partial w(x)}{\partial x} \tag{4.1}$$

όπου $u(x)$ και $w(x)$ είναι η αξονική και η κάθετη μετακίνηση της διατομής στον άξονα αναφοράς. Επίσης, παρόμοια σχέση ισχύει και για την αξονική παραμόρφωση:

$$\varepsilon(x,y) = \varepsilon_0(x) - y \cdot \varphi(x) = \begin{bmatrix} 1 & -y \end{bmatrix} \cdot \boldsymbol{d}(x) = \boldsymbol{l}^T \cdot \boldsymbol{d}(x) \tag{4.2}$$

όπου το πεδίο των παραμορφώσεων $\boldsymbol{d}(x) = \left\{ \varepsilon_0(x),\ \varphi(x) \right\}^T$ αποτελείται από την αξονική παραμόρφωση $\varepsilon_0(x)$ και την καμπυλότητα $\varphi(x)$ στον άξονα αναφοράς. Επιπρόσθετα, διατυπώνονται οι εξισώσεις ισορροπίας της διατομής στην περίπτωση της θεωρίας δοκού Euler-Bernoulli.

$$N(x) = \int_A \sigma(x,y) dA \quad , \quad M(x) = -\int_A y \cdot \sigma(x,y) dA \tag{4.3}$$

$$\boldsymbol{D}(x) = \int_A \begin{bmatrix} 1 & -y \end{bmatrix}^T \cdot \sigma(x,y) dA \tag{4.4}$$

όπου $\boldsymbol{D}(x) = \left\{ N(x), M(x) \right\}^T$. Επίσης, ο ρυθμός της ορθής τάσης εκφράζεται ως:

$$\dot{\sigma}(x,y) = E_t \cdot \dot{\varepsilon}(x,y) \tag{4.5}$$

Αντικαθιστώντας τις εξισώσεις (4.5) και (4.2) στην εξίσωση (4.4) εκφρασμένη σε ρυθμό μεταβολής, παράγεται η παρακάτω καταστατική εξίσωση της διατομής:

$$\dot{\boldsymbol{D}}(x) = \boldsymbol{k}(x) \cdot \dot{\boldsymbol{d}}(x) \tag{4.6}$$

με δυσκαμψία:

$$\begin{aligned} \boldsymbol{k}(x) &= \int_A \begin{bmatrix} 1 & -y \end{bmatrix}^T \cdot E_t \cdot \begin{bmatrix} 1 & -y \end{bmatrix} dA \\ &= \begin{bmatrix} \sum_{i=1}^{n(x)} \left(E_{\mathrm{t}} \cdot A\right)_i & -\sum_{i=1}^{n(x)} \left(E_{\mathrm{t}} \cdot A\right)_i \cdot y_i \\ -\sum_{i=1}^{n(x)} \left(E_{\mathrm{t}} \cdot A\right)_i \cdot y_i & \sum_{i=1}^{n(x)} \left(E_{\mathrm{t}} \cdot A\right)_i \cdot y_i^2 \end{bmatrix} \end{aligned} \tag{4.7}$$

όπου $n(x)$ είναι ο αριθμός των ινών σε μία διατομή τοποθετημένη σε "x" απόσταση από τον κόμβο αρχής του στοιχείου. Τέλος, το μητρώο ευκαμψίας της διατομής προσδιορίζεται απλά ως το αντίστροφο του μητρώου δυσκαμψίας της.

$$\boldsymbol{f}(x) = \boldsymbol{k}(x)^{-1} \tag{4.8}$$

Όσον αφορά το στοιχείο δοκού δύο διαστάσεων, θεωρούνται οι τυπικοί έξι βαθμοί ελευθερίας $\bar{\boldsymbol{u}} = \{u_1, u_2, r_1, u_4, u_5, r_2\}^T$ και οι σχετικές τρεις παραμορφώσεις στα άκρα $\boldsymbol{q} = \{\delta, \theta_1, \theta_2\}^T$ δηλ. η αξονική παραμόρφωση δ και οι δύο στροφές χορδής οι οποίες δίνουν τα τρία ανεξάρτητα εντατικά μεγέθη $\boldsymbol{Q} = \{N, M_1, M_2\}^T$. Η σχέση που συνδέει τις επικόμβιες μετατοπίσεις με τις παραμορφώσεις διαμορφώνεται με τη χρήση του μητρώου μετασχηματισμού $\boldsymbol{T}$ το οποίο αφαιρεί την κίνηση στερεού σώματος της δοκού (Σχήμα 4.2).

$$\boldsymbol{q} = \boldsymbol{T} \cdot \bar{\boldsymbol{u}}, \quad \boldsymbol{T} = \begin{bmatrix} 1 & 0 & 0 & -1 & 0 & 0 \\ 0 & 1/L & 1 & 0 & -1/L & 0 \\ 0 & 1/L & 0 & 0 & -1/L & 1 \end{bmatrix} \tag{4.9}$$

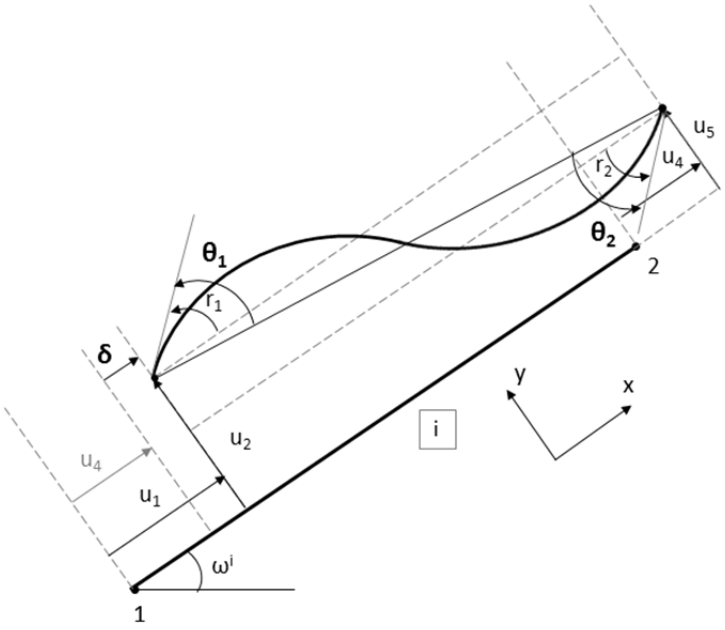

Σχήμα 4.2. Επικόμβιες μετακινήσεις και παραμορφώσεις του στοιχείου δοκού

Επίσης, η ισορροπία του στοιχείου υπό την επιβολή των κατανεμημένων φορτίων $\boldsymbol{b(x)} = \left[b_x(x), b_y(x) \right]^T$ στις δύο διευθύνσεις x, y εκφράζεται ως:

$$\begin{aligned} \frac{\partial^2 M(x)}{\partial x^2} - b_y(x) &= 0 \\ \frac{\partial N(x)}{\partial x} - b_x(x) &= 0 \end{aligned} \tag{4.10}$$

Η διατύπωση του στοιχείου δοκού βασίζεται στην αρχή μεταβολής δύο πεδίων η οποία θεωρεί τόσο το πεδίο μετακινήσεων όσο και το πεδίο των δυνάμεων αρχικά ως ανεξάρτητα. Συνεπώς, για μία παραμορφώσιμη δοκό με ορθή ένταση σ, αξονική μετακίνηση u και παραμόρφωση ε σε κάθε σημείο της, το συναρτησιακό των Hellinger-Reissner (1950) εκφράζεται συναρτήσει των δύο ανεξάρτητων πεδίων ως εξής:

$$\Pi_{HR}(\sigma, u) = \int_V \{ \varepsilon(u) \cdot \sigma - \chi(\sigma) \} dV - \Pi_{ext}(u) \tag{4.11}$$

όπου $\chi(\sigma)$ είναι η συμπληρωματική συνάρτηση της πυκνότητας ενέργειας μέσω της οποίας οι παραμορφώσεις προκύπτουν από τις τάσεις, $\Pi_{ext}(u)$ είναι το συναρτησιακό των εξωτερικών δυνάμεων και η ολοκλήρωση γίνεται στον απαραμόρφωτο όγκο του στοιχείου. Ειδικότερα, το συναρτησιακό των Hellinger-Reissner είναι ένα ενεργειακό συναρτησιακό η ύπαρξη του οποίου προϋποθέτει το υλικό να είναι υπερελαστικό. Αυτό σημαίνει ότι

υπάρχει μία ενεργειακή συνάρτηση τάσεων $\chi(\sigma)$ όπου οι παραμορφώσεις προκύπτουν από τις τάσεις ως εξής:

$$\varepsilon = \frac{\partial \chi(\sigma)}{\partial \sigma} \tag{4.12}$$

Το παραπάνω συναρτησιακό μπορεί να εκφραστεί, επίσης, σε όρους εντατικών και αντίστοιχων παραμορφωσιακών μεγεθών από τη σχέση:

$$\Pi_{HR}(\boldsymbol{D},\boldsymbol{u}) = \int_0^L \left\{ \boldsymbol{d}(\boldsymbol{u})^T \cdot \boldsymbol{D} - \chi(\boldsymbol{D}) \right\} dx - \Pi_{ext}(\boldsymbol{u}) \tag{4.13}$$

Η συμπληρωματική ενέργεια εκφράζεται σε αυτή την περίπτωση ως:

$$d(\boldsymbol{D}) = \frac{\partial \chi(\boldsymbol{D})}{\partial \boldsymbol{D}} \tag{4.14}$$

ενώ το συναρτησιακό των εξωτερικών επικόμβιων φορτίων $\boldsymbol{F_n}$ και κατανεμημένων φορτίων $\boldsymbol{b}(x) = \left[b_x(x), b_y(x) \right]^T$ λαμβάνει τη μορφή:

$$\Pi_{ext} = \overline{\boldsymbol{u}} \cdot \boldsymbol{F_n} + \int_0^L \boldsymbol{u}^T \cdot \boldsymbol{b}\, dx \tag{4.15}$$

Η ισορροπία του στοιχείου δοκού απαιτεί τη στασιμότητα του συναρτησιακού Hellinger-Reissner. Αυτό επιτυγχάνεται θέτοντας την πρώτη μεταβολή του συναρτήσει των δύο ανεξάρτητων μεταβλητών ίση με το μηδέν.

$$\delta\Pi_{HR} = \int_0^L \left(\delta \boldsymbol{d}(\boldsymbol{u})^T \cdot \boldsymbol{D} \right) dx + \int_0^L \delta \boldsymbol{D}^T \cdot \left(\boldsymbol{d}(\boldsymbol{u}) - \boldsymbol{d}(\boldsymbol{D}) \right) dx - \delta \overline{\boldsymbol{u}}^T \cdot \boldsymbol{F_n} - \int_0^L \delta \boldsymbol{u}^T \cdot \boldsymbol{b}\, dx \; = 0 \tag{4.16}$$

Τότε για όλες τις μεταβολές $\delta\boldsymbol{u}(x)$ και $\delta\boldsymbol{D}(x)$ κάθε κατάσταση που ορίζεται από το πεδίο των μετακινήσεων και δυνάμεων $\left(\boldsymbol{u}(x), \boldsymbol{D}(x)\right)$ ικανοποιεί τις κλασικές εξισώσεις της ισορροπίας (4.17) και συμβιβαστότητας (4.18).

$$\int_0^L \left(\delta \boldsymbol{d}(\boldsymbol{u})^T \cdot \boldsymbol{D} \right) dx - \delta \overline{\boldsymbol{u}}^T \cdot \boldsymbol{F_n} - \int_0^L \delta \boldsymbol{u}^T \cdot \boldsymbol{b}\, dx \; = 0 \tag{4.17}$$

$$\int_0^L \delta \boldsymbol{D}^T \cdot \left(\boldsymbol{d}(\boldsymbol{u}) - \boldsymbol{d}(\boldsymbol{D}) \right) dx = 0 \tag{4.18}$$

Στη συνέχεια τα ανεξάρτητα πεδία εκφράζονται ως γραμμικός συνδυασμός συναρτήσεων σχήματος και αντίστοιχων επικόμβιων μεγεθών. Πιο συγκεκριμένα, για το πεδίο

μετακινήσεων θεωρούνται τα κλασικά κυβικά πολυώνυμα, ενώ το πεδίο των παραμορφώσεων προκύπτει από την παραγώγιση του πεδίου μετακινήσεων:

$$\begin{aligned} &\boldsymbol{u}(x) = \boldsymbol{N}_u(x)\cdot\bar{\boldsymbol{u}} \\ &\boldsymbol{d}\left(\boldsymbol{u}(x)\right) = \partial\left(\boldsymbol{N}_u(x)\right)\cdot\bar{\boldsymbol{u}} = \boldsymbol{N}_d(x)\cdot\boldsymbol{q} = \boldsymbol{N}_d(x)\cdot\boldsymbol{T}\cdot\bar{\boldsymbol{u}} \end{aligned} \tag{4.19}$$

Το πεδίο των δυνάμεων εκφράζεται βασιζόμενο στη θεώρηση της ισορροπίας κατά μήκος του στοιχείου. Συνεπώς, οι εξισώσεις ισορροπίας (4.10) ολοκληρώνονται απευθείας και εφαρμόζοντας τις συνοριακές συνθήκες παράγεται η ακόλουθη σχέση παρεμβολής .

$$\boldsymbol{D}(x) = \boldsymbol{N}_D(x)\cdot\boldsymbol{Q} + \boldsymbol{D}_p \ , \quad \boldsymbol{N}_D(x) = \begin{bmatrix} 1 & 0 & 0 \\ 0 & \dfrac{x}{L} - 1 & \dfrac{x}{L} \end{bmatrix} \tag{4.20}$$

όπου, $\boldsymbol{D}_p$ είναι οι εσωτερικές εντάσεις που προκύπτουν από τα κατανεμημένα φορτία.

Αντικαθιστώντας τις σχέσεις (4.19) και (4.20) στο συναρτησιακό (4.16), προκύπτει η ακόλουθη διακριτή μορφή του:

$$\begin{aligned} \delta\Pi_{HR} = \delta\bar{\boldsymbol{u}}^T \cdot \left\{ \boldsymbol{T}^T \cdot \int_0^L \boldsymbol{N}_d{}^T \cdot \left(\boldsymbol{N}_D\cdot\boldsymbol{Q} + \boldsymbol{D}_p\right) dx - \int_0^L \boldsymbol{N}_u{}^T \cdot \boldsymbol{b}\ dx - \boldsymbol{F}_n \right\} + \\ + \delta\boldsymbol{Q}^T \cdot \left\{ \int_0^L \boldsymbol{N}_D{}^T \cdot \left(\boldsymbol{N}_d\cdot\boldsymbol{T}\cdot\bar{\boldsymbol{u}} - \boldsymbol{d}(\boldsymbol{D})\right) dx \right\} = 0 \end{aligned} \tag{4.21}$$

Καθώς η εξίσωση (4.21) ισχύει για κάθε δυνατή μεταβολή των δύο ανεξάρτητων πεδίων και οι δύο όροι του αθροίσματος λαμβάνονται με βάση το λήμμα του λογισμού των μεταβολών ίσοι με το μηδέν. Επιπρόσθετα, οι συναρτήσεις σχήματος που επιλέχθηκαν είναι ορθογώνιες μεταξύ τους καθώς $\int_0^L \boldsymbol{N}_d{}^T \cdot \boldsymbol{N}_D\ dx = \boldsymbol{I}$. Συνεπώς, έπειτα από κάποιες αλγεβρικές πράξεις προκύπτουν οι ακόλουθες εξισώσεις που περιγράφουν την κατάσταση του στοιχείου σε επιβαλλόμενο εξωτερικό φορτίο.

$$\boldsymbol{T}^T\cdot\left(\boldsymbol{Q} + \boldsymbol{Q}_p\right) - \boldsymbol{P}_{ext} = 0 \tag{4.22}$$

$$\boldsymbol{T}\cdot\bar{\boldsymbol{u}} - \int_0^L \boldsymbol{N}_D^T\cdot\boldsymbol{d}(\boldsymbol{D})\ dx = 0 \tag{4.23}$$

όπου το διάνυσμα των ισοδύναμων επικόμβιων εξωτερικών δράσεων έχει τη μορφή:

$$\boldsymbol{P}_{ext} = \boldsymbol{F}_n + \int_0^L \boldsymbol{N}_u^T\cdot\boldsymbol{b}\ dx \tag{4.24}$$

και $\boldsymbol{Q_p}$ είναι το διάνυσμα των επικόμβιων εσωτερικών δυνάμεων που προκύπτει από τις επιπλέον εσωτερικές δράσεις κατά μήκος του στοιχείου λόγω των κατανεμημένων φορτίων:

$$\boldsymbol{Q_p} = \int_0^L \boldsymbol{N_d^T} \cdot \boldsymbol{D_p}\, dx \tag{4.25}$$

Η εξίσωση (4.22) αντιπροσωπεύει την εξίσωση ισορροπίας ενώ η εξίσωση (4.23) τη συνθήκη συμβιβαστού των παραμορφώσεων. Η συνέχεια ανάμεσα στα στοιχεία εξασφαλίζεται αντιστοιχίζοντας τις καθολικές μετακινήσεις της κατασκευής στις τοπικές, επικόμβιες μετακινήσεις $\bar{\boldsymbol{u}}$ του εκάστοτε μέλους.

Η εξαρτημένη μεταβλητή, δηλ. το πεδίο των παραμορφώσεων μπορεί να προκύψει τόσο από την παρεμβολή των επικόμβιων δράσεων κατά μήκος του στοιχείου, όσο και από την ολοκλήρωση των καταστατικών σχέσεων στις ίνες της διατομής. Για το διαχωρισμό των δύο εννοιών, οι παρεμβαλόμενες δυνάμεις συμβολίζονται με $\boldsymbol{D}(x)$ ενώ οι δυνάμεις που προέρχονται από τις καταστατικές σχέσεις συμβολίζονται με $\hat{\boldsymbol{D}}(x)$. Η ισότητα των δύο διατυπώσεων σε γραμμικοποιημένη μορφή δίνει την ακόλουθη σχέση:

$$\boldsymbol{D}^{i+1} = \hat{\boldsymbol{D}}^{i+1} \Rightarrow \Delta \boldsymbol{d}^i = \boldsymbol{f}^i \cdot \left(\boldsymbol{D}^{i+1} - \hat{\boldsymbol{D}}^i \right) \tag{4.26}$$

Συνεπώς, οι τρέχουσες παραμορφώσεις στη διατομή προκύπτουν ως:

$$\boldsymbol{d}^{i+1} = \boldsymbol{d}^i + \boldsymbol{f}^i \cdot \left(\boldsymbol{D}^{i+1} - \hat{\boldsymbol{D}}^i \right) \tag{4.27}$$

Αντικαθιστώντας την εξίσωση (4.27) στην (4.23) καταλήγουμε στις εξής γραμμικοποιημένες εξισώσεις της ισορροπίας και συμβιβαστότητας:

$$\boldsymbol{T}^T \cdot \left(\boldsymbol{Q}^{i+1} + \boldsymbol{Q_p}^{i+1} \right) - \boldsymbol{P_{ext}}^{i+1} = 0 \tag{4.28}$$

$$\boldsymbol{T} \cdot \bar{\boldsymbol{u}}^{i+1} - \boldsymbol{F}^i \cdot \Delta \boldsymbol{Q}^i - \boldsymbol{q}^i - \boldsymbol{c}^i = 0 \tag{4.29}$$

όπου, το μητρώο ευκαμψίας, οι επικόμβιες παραμορφώσεις και το παραμένον υπόλοιπο των παραμορφώσεων προκύπτουν από την ολοκλήρωση κατά μήκος του στοιχείου ως εξής:

$$\boldsymbol{F}^i = \int_0^L \left(\boldsymbol{N_D^T} \cdot \boldsymbol{f}^i \cdot \boldsymbol{N_D} \right) dx \tag{4.30}$$

$$\boldsymbol{q}^i = \int_0^L \boldsymbol{N_D^T} \cdot \boldsymbol{d}^i \left(\boldsymbol{D}^i \right) dx \tag{4.31}$$

$$\boldsymbol{c}^i = \int_0^L \boldsymbol{N}_D^T \cdot \boldsymbol{f}^i \cdot \left(\boldsymbol{D}^i - \hat{\boldsymbol{D}}^i + \Delta \boldsymbol{D}_p^i \right) dx \tag{4.32}$$

Η ολοκλήρωση των παραπάνω σχέσεων γίνεται με την αριθμητική ολοκλήρωση Gauss-Lobatto η οποία θέτει διατομές ελέγχου στα άκρα του στοιχείου όπου αναμένεται και η σημαντικότερη μη-γραμμική συμπεριφορά.

Επαυξητικές σχέσεις θεωρούνται επίσης για τις επικόμβιες δυνάμεις και μετακινήσεις $\boldsymbol{Q}^{i+1} = \boldsymbol{Q}^i + \Delta \boldsymbol{Q}^i$, $\overline{\boldsymbol{u}}^{i+1} = \overline{\boldsymbol{u}}^i + \Delta \overline{\boldsymbol{u}}^i$. Στη συνέχεια πραγματοποιείται η απαλοιφή των επαυξητικών δυνάμεων στις σχέσεις (4.28) και (4.29) και οι επαυξητικές επικόμβιες μετακινήσεις μπορούν να υπολογιστούν από τη σχέση (4.33) με την προϋπόθεση ότι το μητρώο ευκαμψίας του μέλους είναι αντιστρέψιμο.

$$\boldsymbol{K}^i \cdot \Delta \overline{\boldsymbol{u}}^i = \boldsymbol{P}_{ext}{}^{i+1} - \overline{\boldsymbol{Q}}_{int}{}^i \tag{4.33}$$

$$\overline{\boldsymbol{Q}}_{int}{}^i = \boldsymbol{K}^i \cdot \overline{\boldsymbol{u}}^i + \boldsymbol{T}^T \cdot \left[\boldsymbol{Q}^i - (\boldsymbol{F}^i)^{-1} \cdot \left(\boldsymbol{q}^i + \boldsymbol{c}^i \right) + \boldsymbol{Q}_p^{i+1} \right] \tag{4.34}$$

V. Αριθμητικό Παράδειγμα

Σε αυτό το παράδειγμα το αριθμητικό προσομοίωμα ελέγχεται και τεκμηριώνεται με τα πειραματικά αποτελέσματα των Ghannoum και Moehle (2008, 2012a) σε ένα τριώροφο πλαίσιο από ΟΣ τριών ανοιγμάτων, στο οποίο πραγματοποιήθηκε πειραματική δοκιμή στη σεισμική τράπεζα του Πανεπιστημίου Berkeley, California. Το πλαίσιο κατασκευάστηκε σε κλίμακα 1/3 και αναπαριστά τον συνήθη σχεδιασμό της δεκαετίας του 1960 ισχυρής δοκού, ασθενούς υποστυλώματος. Οι διαστάσεις και οι λεπτομέρειες όπλισης της κατασκευής παρουσιάζονται στο Σχήμα 5.1. Πιο συγκεκριμένα, τα υποστυλώματα της αριστερής πλευράς (C1-C3, D1-D3) έχουν σχεδιαστεί σύμφωνα με σύγχρονους κανονισμούς (ACI 318-08), ενώ τα υποστυλώματα της δεξιά μισής πλευράς (A1-A3, B1-B3) είναι σχεδιασμένα ώστε να αναπαριστάνουν τυπικούς σχεδιασμούς της δεκαετίας του 1960 με κύριο χαρακτηριστικό τους πολύ αραιούς συνδετήρες.

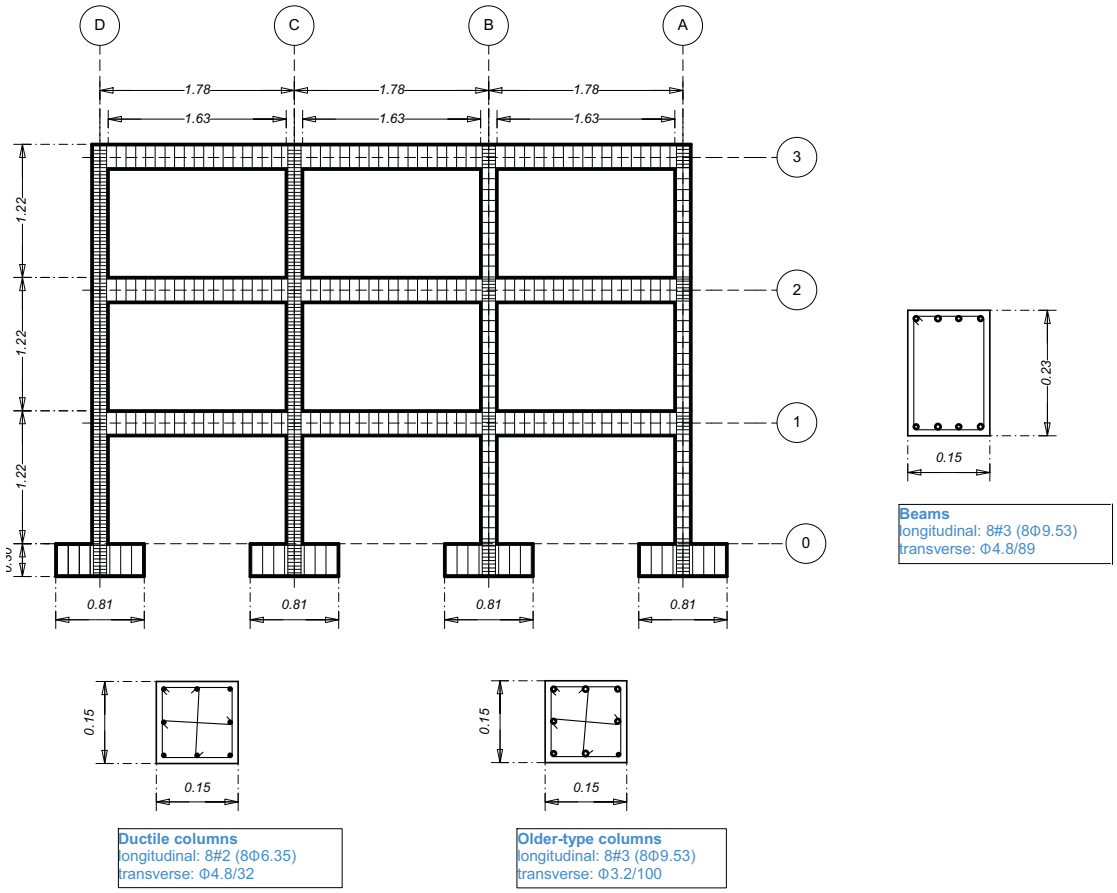

Σχήμα 5.1. Διαστάσεις και λεπτομέρειες όπλισης του τριώροφου πλαισίου τριών ανοιγμάτων

Το πλαίσιο από ΟΣ διεγείρεται δυναμικά με τη σεισμική καταγραφή που συνέβη στις 3 Μαρτίου, 1985 στο σεισμό της Χιλής (Llolleo Station, Component 100), η οποία παρουσιάζεται στο Σχήμα 5.2. Το αρχικό επιταχυνσιογράφημα πολλαπλασιάζεται με τον επαυξητικό συντελεστή 4.06 έτσι ώστε το πλαίσιο να ξεπεράσει την αντοχή του και να επέλθουν σημαντικές βλάβες στα υποστυλώματα του.

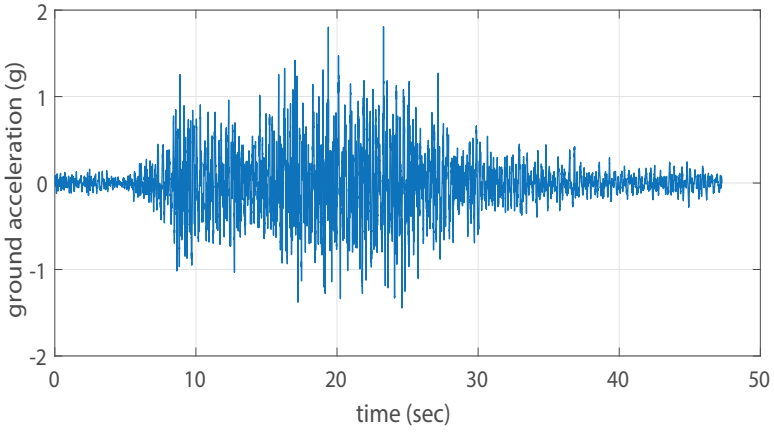

Σχήμα 5.2. Επιβαλλόμενη σεισμική διέγερση (Chile Valparaio 1985 Llolleo x 4.06)

Οι παράμετροι του χάλυβα που χρησιμοποιήθηκαν παρατίθενται στον Πίνακα 5.1. Η τάση διαρροής είναι $\sigma_{sy} = 475\ MPa$ και δίνεται στα πειραματικά δεδομένα.

σ_y (MPa)	α	n_1	n_2	ε_{plat}	m	q
475	0.03	10	0.5	$3\varepsilon_y$	0.02	20

Πίνακας 5.1. Παράμετροι του προσομοιώματος των ράβδων οπλισμού

Παρομοίως, οι παράμετροι του σκυροδέματος αναφέρονται στον Πίνακα 5.2 όπου διαχωρίζονται οι παράμετροι που χρησιμοποιήθηκαν για την προσομοίωση του περισφιγμένου πυρήνα και της απερίσφιγχτης επικάλυψης. Η αντοχής του σκυροδέματος δίνεται στα $\sigma_c = 24.6\ MPa$ και το μέτρο ελαστικότητας σε επίπεδο έντασης $0.4\sigma_c$ δίνεται στα $E_c = 19\ GPa$. Η μεταβολή της αντοχής λόγω περίσφιγξης έγινε με βάση το προσομοίωμα των Mander et al. (1988). Συνεπώς, ο συντελεστής περίσφιγξης k λαμβάνει την τιμή $k = 1.9$ για τα υποστυλώματα νεότερου τύπου $\left(\sigma_{cc} = k \cdot \sigma_{c0} = 46.7\ MPa\right)$ και $k = 1.1$ για τα παλαιότερου τύπου $\left(\sigma_{cc} = k \cdot \sigma_{c0} = 27.1\ MPa\right)$.

	E_C (GPa)	σ_y (MPa)	α_C	q_C	k_0	b	p	c_1	c_2
Περισφιγμένα υποστυλώματα (C1-C3,D1-D3)									
Πυρήνας	20	18	0.9	0	0.0009	5	0.7	2	0.35
Επικάλυψη	20	18	0.7	0	0.0009	3	1.2	4	0.1
Παλαιού-τύπου υποστυλώματα (A1-A3,B1-B3)									
Πυρήνας	20	18	0.8	0	0.0009	3.7	0.8	2	0.35
Επικάλυψη	20	18	0.7	0	0.0009	3	1.2	4	0.1
Beams									
Πυρήνας	20	18	0.7	0	0.0009	3	1.2	4	0.1

Πίνακας 5.2. Παράμετροι περισφιγμένου και απερίσφιχτου σκυροδέματος

Κάθε άνοιγμα αναλαμβάνει επίσης κατανεμημένο φορτίο *16.67 KN/m* το οποίο συμμετέχει και ως ισοδύναμη μάζα. Επίσης, η ευκαμψία των πεδίλων ενσωματώθηκε στο προσομοίωμα με στροφικά ελατήρια. Η βαθμονόμηση τους πραγματοποιήθηκε με τέτοιο τρόπο ώστε η θεμελιώδης ιδιοπερίοδος (T_1*=0.34 sec*) του πλαισίου να συμπίπτει με την ιδιοπερίοδο που προσδιορίστηκε πειραματικά (K_{spring}*=6500 KNm/rad)*.

Η ανάλυση χρονοϊστορίας πραγματοποιείται χρησιμοποιώντας την αριθμητική ολοκλήρωση Newmark των εξισώσεων κίνησης με $\beta = 0.25$ και $\gamma = 0.50$. Θεωρήθηκε, επίσης, ιξώδης απόσβεση Rayleigh με βάση τις δύο πρώτες ιδιομορφές και λόγους απόσβεσης όπως αυτοί μετρήθηκαν πειραματικά. Έτσι, για την πρώτη ιδιοπερίοδο $\left(T_1 = 0.34 \text{ sec}\right)$ ο λόγος απόσβεσης είναι *1.93,* ενώ για τη δεύτερη $\left(T_2 = 0.12\ sec\right)$ είναι *1.85.*

Το στοιχείο δοκού-υποστυλώματος διακριτοποιείται σε 4 διατομές ελέγχου, οι οποίες αντιστοιχούν σε μία ζώνη συγκέντρωσης της έντασης (localization zone) εύρους *83 mm* σε κάθε άκρο. Η διακριτοποίηση της διατομής σε λωρίδες περιλαμβάνει 12 λωρίδες για την επικάλυψη και 30 λωρίδες για τον πυρήνα των διατομών. Τέλος, αποφλοίωση της επικάλυψης θεωρείται ότι επέρχεται όταν η παράμετρος βλάβης ξεπεράσει τη συμβατική τιμή $D_{sp} = 0.7$.

Αρχικά, η σύγκριση γίνεται σε όρους καθολικών μεγεθών όπως η σχετική μετακίνηση ορόφων και η τέμνουσα βάσης. Στο Σχήμα 5.3 και Σχήμα 5.4 παρουσιάζεται η σύγκριση των χρονοϊστοριών των σχετικών μετακινήσεων ορόφων και των τεμνουσών βάσης για τη

χρονική διάρκεια του σεισμού από 10 έως 35 sec όπου παρατηρείται η σημαντική μη-γραμμική συμπεριφορά.

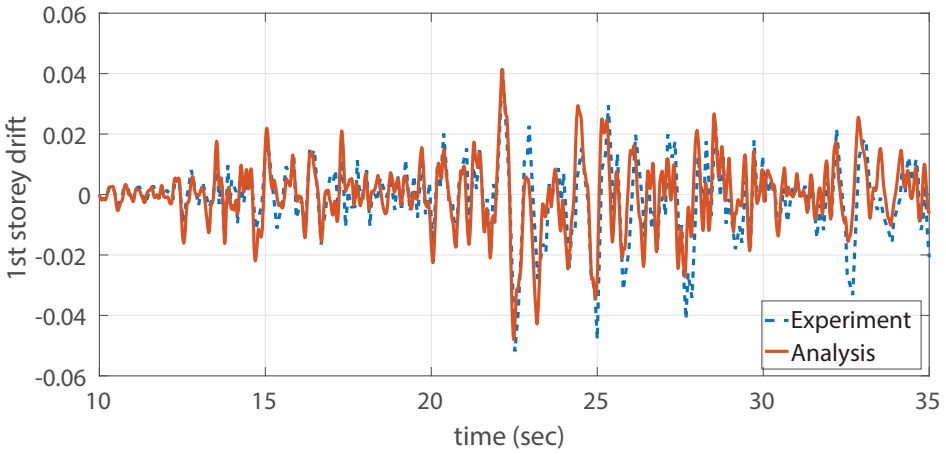

Σχήμα 5.3. Σύγκριση σχετικής μετακίνησης πρώτου ορόφου

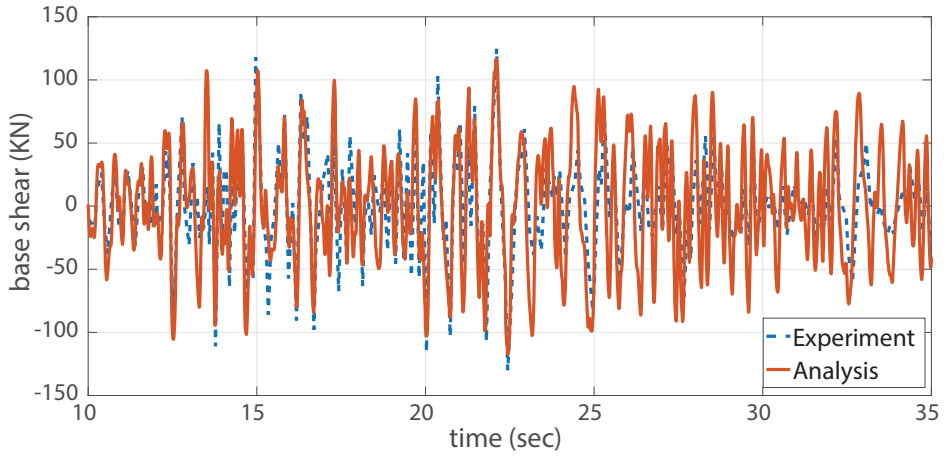

Σχήμα 5.4. Σύγκριση τεμνουσών βάσεως

Η αρχική ελαστική συμπεριφορά μέχρι τη διαρροή του εσωτερικού παλαιότερου τύπου υποστυλώματος περίπου στα 13 sec συμπίπτει και στις δύο περιπτώσεις. Στη συνέχεια παρατηρείται διαρροή του εξωτερικού υποστυλώματος A1 και από το σημείο αυτό εμφανίζονται μερικές διαφοροποιήσεις ανάμεσα στο αριθμητικό προσομοίωμα και στο πείραμα. Η απόκλιση γίνεται εντονότερη μετά το 22^{o} δευτερόλεπτο όπου συμβαίνει σημαντική και μη-αναστρέψιμη βλάβη στο υποστύλωμα B1. Κατά τη διάρκεια του ισχυρού τμήματος της σεισμικής διέγερσης το πλαίσιο διεγείρεται με ένα ισχυρό κύκλο έντασης όπου η σχετική γωνία σχετικής μετακίνησης του $1^{ου}$ ορόφου φτάνει στο 5%. Όσον αφορά τις τέμνουσες βάσης, το αριθμητικό προσομοίωμα προβλέπει μεγαλύτερες τέμνουσες βάσης

καθώς η παραμένουσα αντοχή του υποστυλώματος B1 μετά την αστοχία υπερεκτιμάται. Παρ' όλα αυτά η ικανοποιητική σύγκριση σε όρους σχετικών μετακινήσεων εξακολουθεί να ισχύει. Σε κάθε περίπτωση, οι διαφορές των αποτελεσμάτων οφείλονται σε μεγάλο βαθμό σε φαινόμενα που ξεπερνούν το αντικείμενο αυτής της διατριβής, όπως η ολίσθηση οπλισμού στην αγκύρωση του στα πέδιλα, η εμφάνιση διαγώνιων ρωγμών στους κόμβους και το ανασήκωμα του υποστυλώματος D1.

Στη συνέχεια η σύγκριση πραγματοποιείται σε επίπεδο μέλους και πιο συγκεκριμένα αφορά στα υποστυλώματα A1 και B1. Στο Σχήμα 5.5 παρουσιάζεται η σύγκριση σε όρους τέμνουσας ως προς τη σχετική μετακίνηση κορυφής. Το αριθμητικό προσομοίωμα είναι ικανό να αποτυπώσει επαρκώς τους αρχικά σταθερούς υστερητικούς βρόχους και το εύρος των σχετικών μετακινήσεων και στα δύο υποστυλώματα. Η σύγκριση είναι καλύτερη στην περίπτωση του ακραίου υποστυλώματος A1, ενώ απόκλιση παρατηρείται όταν το υποστύλωμα B1 εμφανίζει σημαντικές βλάβες τρισδιάστατης καταπόνησης. Είναι, επίσης, ενδιαφέρον ότι το υποστύλωμα B1 εκδηλώνει συμμετρικούς βρόχους, ενώ αντίθετα η μέγιστη αντοχή του υποστυλώματος A1 εμφανίζεται μειωμένη στην αρνητική διεύθυνση εξαιτίας της ανάπτυξης εφελκυστικού φορτίου που μειώνει τη θλιβόμενη ζώνη του.

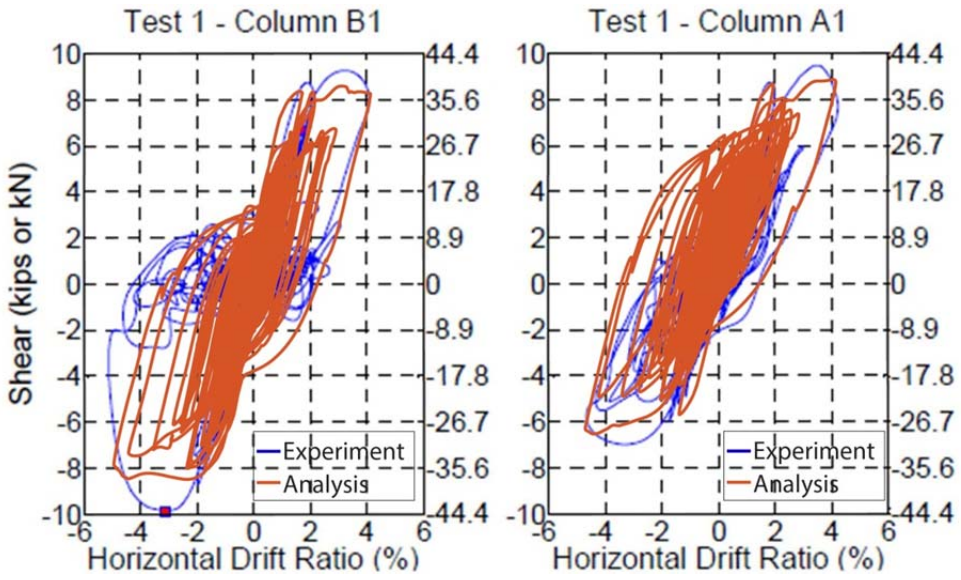

Σχήμα 5.5. Σύγκριση οριζόντιων σχετικών μετακινήσεων με τέμνουσες βάσης

Επιπρόσθετα, σύγκριση πραγματοποιείται για τα δύο υποστυλώματα σε όρους σχετικής μετακίνησης κορυφής ως προς τη στροφή χορδής στη βάση τους και παρουσιάζεται στο Σχήμα 5.6. Ομοίως το εύρος των στροφών χορδής υπολογίζεται ικανοποιητικά για το

υποστύλωμα Α1, ενώ υποεκτιμούνται για το υποστύλωμα Β1, καθώς οι πρόσθετες στροφές στερεού σώματος εξαιτίας της ολίσθησης στην αγκύρωση δεν λαμβάνονται υπ' όψη.

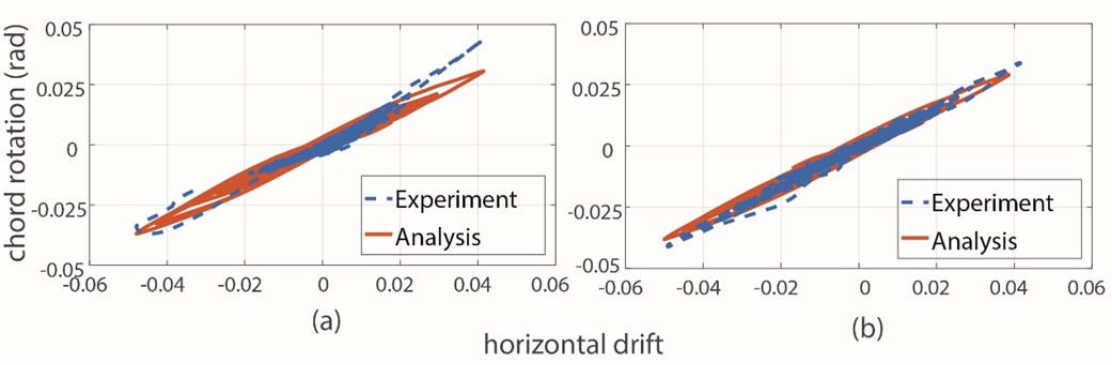

Σχήμα 5.6. Σύγκριση στροφών χορδής: (a) βάση υποστυλώματος Β1, (b) βάση υποστυλώματος Α1

VI. Συμπεράσματα και Μελλοντική Έρευνα

Στην παρούσα διατριβή αναπτύχθηκαν ομαλά καταστατικά προσομοιώματα πλαστικότητας και μηχανικής των βλαβών και ενσωματώθηκαν σε στοιχείο δοκού ινών μικτού ενεργειακού τύπου. Βασικός σκοπός είναι η ακριβής προσομοίωση κατασκευών ΟΣ οι οποίες εκδηλώνουν σημαντικές βλάβες λόγω ισχυρών ανακυκλιζόμενων φορτίσεων. Στο πλαίσιο αυτό αναπτύσσεται το μη-γραμμικό προσομοίωμα του χάλυβα το οποίο συνδυάζει κινηματική και ισοτροπική κράτυνση, ενώ περιγράφει επιτυχώς το πλατό διαρροής, το φαινόμενο Bauschinger και τους σύντομους κλάδους αποφόρτισης-επαναφόρτισης.

Επίσης, αντιμετωπίζεται το φαινόμενο του λυγισμού των διαμήκων ράβδων οπλισμού. Η διατομή της ράβδου επιμερίζεται σε λωρίδες, καθεμία από τις οποίες εκφράζεται μέσω του καταστατικού προσομοιώματος του χάλυβα. Η πλευρική μετακίνηση, η κατανομή των καμπυλοτήτων και η δευτερογενής παραμόρφωση λυγισμού προκύπτουν αναλυτικά από την θεωρία λυγισμού. Η μεθοδολογία αυτή καταλήγει σε μία επαναληπτική διαδικασία όπου επιβάλλονται οι μέσες παραμορφώσεις και οι καμπυλότητες ανανεώνονται μέχρι να ικανοποιηθεί η ισορροπία στο μέσον της ράβδου. Η σύγκριση με πειραματικά δεδομένα της βιβλιογραφία τεκμηριώνει και φανερώνει την ακρίβεια και την αποδοτικότητα του προσομοιώματος.

Παράλληλα, αναπτύσσεται το μονοαξονικό προσομοίωμα του σκυροδέματος με βάση τη θεωρία πλαστικότητας και μηχανικής των βλαβών. Το προσομοίωμα είναι ικανό να περιγράψει μακροσκοπικά εκτός από τη θλιπτική συμπεριφορά, την εφελκυστική θραύση,

τη μη-γραμμική αποφόρτιση και τα φαινόμενα ανοίγματος/κλεισίματος των ρωγμών. Έτσι, αναπαριστά αριθμητικά τις μορφές βλάβης των μελών από ΟΣ, όπως η σύνθλιψη πυρήνα και η αποφλοίωση της επικάλυψης η οποία ενεργοποιεί επίσης και την έναρξη του λυγισμού των διαμήκων ράβδων. Το υπολογιστικό πλεονέκτημα του προσομοιώματος οφείλεται στον άμεσο υπολογισμό των τάσεων μέσω του εφαπτομενικού μέτρου το οποίο ενσωματώνει την πλάστιμη και φθίνουσα συμπεριφορά λόγω βλάβης. Επίσης και σε αυτή την περίπτωση τα εξαγόμενα αποτελέσματα του προσομοιώματος ελέγχονται με βάση πειραματικά δεδομένα σε ανακυκλιζόμενες φορτίσεις δοκιμίων σκυροδέματος.

Στη συνέχεια, τα ξεχωριστά προσομοιώματα της ράβδου οπλισμού και του σκυροδέματος εισάγονται σε ένα στοιχείο δοκού ινών μικτού ενεργειακού τύπου όπου και αλληλοεπιδρούν. Εξάγονται οι εξισώσεις της ισορροπίας και συμβιβαστότητας, ενώ η γραμμικοποίηση τους επιτρέπει την επίλυση τους με αριθμητικές μεθόδους τύπου Newton-Raphson. Το υπολογιστικό πλεονέκτημα της προτεινόμενης μεθοδολογίας έγκειται στο γεγονός ότι οι τάσεις υπολογίζονται ρητά και άμεσα σε κάθε βήμα χωρίς την ανάγκη υιοθέτησης τεχνικών πρόβλεψης-διόρθωσης (predictor-corrector).

Τέλος, το καθολικό προσομοίωμα δοκού-υποστυλώματος συγκρίνεται με τα πειραματικά δεδομένα ενός τριώροφου πλαισίου, τριών ανοιγμάτων στο οποίο επιβάλλεται επιταχυνσιογράφημα βάσης. Η σύγκριση των αριθμητικών με τα πειραματικά αποτελέσματα αποδεικνύει την ακρίβεια και αποδοτικότητα του προτεινόμενου μοντέλου να περιγράφει την ανελαστική, ανακυκλιζόμενη συμπεριφορά κτιρίων από ΟΣ μέχρι του σταδίου ανάπτυξης έντονων τρισδιάστατων καταπονήσεων.

Η παρούσα εργασία αναδεικνύει ενδιαφέροντα θέματα για μελλοντική έρευνα. Ορισμένα προβλήματα που μπορούν να αντιμετωπιστούν είναι τα εξής:

- Η επέκταση της διατύπωσης του λυγισμού των ράβδων, όπου ένας ή περισσότεροι συνδετήρες παραμορφώνονται με συνυπολογισμό της διόγκωσης του πυρήνα
- Ενσωμάτωση του φαινομένου της ολιγοκυκλικής κόπωσης στο προσομοίωμα του χάλυβα.
- Ενσωμάτωση φαινομένων ρυθμού επιβολής της έντασης στο σκυρόδεμα για την αντιμετώπιση κρουστικών φορτίων και εκρήξεων.
- Επέκταση του μονοαξονικού προσομοιώματος του σκυροδέματος ώστε να περιλάβει έμμεσα την επιρροή της διάτμησης.
- Προσομοίωση ενισχυόμενων υποστυλωμάτων ΟΣ με μανδύες σκυροδέματος ή FRP.

Abstract

Modeling Reinforced Concrete Structures under Severe Cyclic Loading Incorporating Plasticity and Damage Models.

By Ilias A. Gkimousis

National Technical University of Athens
School of Civil Engineering
Institute of Structural Analysis and Aseismic Research

Recent advances in the field of computation technology and increased requirements in the field of earthquake engineering have led to the development and implementation of highly efficient beam-column elements capable of tracking the hysteretic behavior of Reinforced Concrete (RC) structures. The aim of this dissertation is to model beam-column behavior in a computationally effective manner, reliably revealing the overall response of RC members subjected to intensive cyclic loading. In this respect, plasticity and damage are considered in the predominant longitudinal direction allowing for the derivation of a fiber finite element model which is formulated on the basis of the two-field Hellinger-Reissner energy principle.

Following this methodology, a uniaxial local stress-strain constitutive relation for steel rebars is developed, which is based on a combined nonlinear kinematic and isotropic hardening law. The model also incorporates Bauschinger effect, yield plateau and is capable of addressing the overshooting problem after short reversals, maintaining full memory of the loading path. In addition, the effect of inelastic buckling of longitudinal rebars, which becomes essential at later stages of intensive cyclic loading, is incorporated. The rebar cross-section is considered discretized into fibers, each one following the derived stress-strain uniaxial law. The buckling curve is analytically determined while equilibrium is imposed on the deformed configuration. Finally, the proposed formulation is verified with existing experimental data of longitudinal rebars under cyclic loading exhibiting inelastic buckling.

In addition, a smooth plasticity-damage model is developed for concrete, accounting for unilateral compressive and tensile behavior, nonlinear unloading and crack-closure phenomena. Softening and stiffness degradation phenomena are handled through a scalar damage-driving variable, which is a function of total strain. Smoothening of the incremental damage behavior is achieved following similar steps to the steel formulation, thus exploiting the common mathematical structure of classical plasticity and damage mechanics. Concrete model is validated in terms of experimental results on concrete specimens under imposed cyclic strain histories and it can efficiently address core crushing and cover spalling failure mechanisms.

The uniaxial models for concrete and rebar are employed to derive a fiber beam-column element which is used to assemble the numerical model of frame structures. Following the two-field mixed approach the state determination of the proposed element is numerically investigated following two alternative methods that provide identical results, i.e. a linearization method and a solution in state-space form. Global solution of the entire system in the linearization method is established using a standard Newton-Raphson numerical scheme, which in the inner loop incorporates the evolution equations of all fibers elevated at section, element and structural level. Also, cover spalling, which triggers the inelastic buckling of longitudinal reinforcing bars, is detected as soon as the damage variable of the adjacent concrete fibers exceeds a threshold value. Numerical results that compare well with existing experimental data on RC structures are presented demonstrating the accuracy and efficacy of the proposed formulation.

Table of Contents

CHAPTER 1 1

1 Introduction 1

1.1 Background and motivation 3

1.2 Modeling reinforced concrete structures, literature review 4

1.2.1 Lumped plasticity models 5

1.2.2 Distributed plasticity models 6

1.2.3 Detailed finite elements 10

1.3 Research objectives 10

1.4 Dissertation outline 11

CHAPTER 2 15

2 Modeling Rebar Cyclic Behavior 15

2.1 Introduction 17

2.2 Uniaxial steel cyclic behavior 20

2.2.1 1D rate independent plasticity 20

2.2.2 Smoothening of the constitutive equations 23

2.2.3 Modifications for steel cyclic behavior 24

2.2.4 Pseudo-code for the steel model 29

2.2.5 Validation with experimental data 30

2.2.6 Nonlinear hardening investigation 32

2.2.7 A special case: linear kinematic hardening 35

2.2.8 Comparison with existing well-known models 37

2.3 Buckling of longitudinal rebars 39

2.3.1 Single rebar model 39

2.3.2 Pseudo-code for rebar buckling model 41

2.3.3 Comparison with corotational formulation 42

2.3.4 Verification with experimental data 44

2.4 Appendix I 49
2.4.1 Menegotto-Pinto model 49
2.4.2 Dodd and Restrepo-Posada model 50
CHAPTER 3 53
3 Modeling Concrete Cyclic Behavior 53
3.1 Introduction 55
3.2 Uniaxial concrete cyclic behavior 59
3.2.1 Plastic behavior 59
3.2.2 Damage behavior 61
3.2.3 Smoothening of the damage equations 64
3.2.4 Nonlinear unloading 66
3.2.5 Crack closure 68
3.2.6 Pseudo-code for concrete model 69
3.3 Influence of model parameters 71
3.3.1 Compressive behavior 71
3.3.2 Tensile behavior 74
3.3.3 Range of model parameters 75
3.4 Verification with experimental data 76
3.4.1 Compressive behavior 76
3.4.2 Tensile behavior 80
3.4.3 Confined concrete behavior 82
3.5 Comparison with existing well-known models 83
3.6 Appendix I. 87
3.6.1 Modified Mander et al. model 87
3.6.2 Konstantinidis and Kappos model 89
3.6.3 La Borderie damage model 90
CHAPTER 4 93
4 Beam-Column Fiber Element 93

4.1 Introduction 95
4.2 Cross-sectional constitutive relations 98
4.3 Element state determination 100
4.4 Displacement based formulation 101
4.4.1 Variational derivation 101
4.4.2 Solution via linearization 104
4.4.3 Solution in state space form 106
4.5 Two field beam element variational formulation 107
4.5.1 Variational derivation 107
4.5.2 Solution via linearization 111
4.5.3 Solution in state space form 113
4.6 Numerical integration and localization 116
4.7 Comparative examples 117
4.7.1 Cantilever column with hardening response 117
4.7.2 Cantilever column with softening response 119
4.7.3 Continuous beam under cyclic vertical load 122
4.8 Incorporation of rebar buckling 124
CHAPTER 5 127
5 Numerical Examples 127
5.1 Introduction 129
5.2 Cantilever column under pseudo-static cyclic excitation 129
5.2.1 Experimental setting description and input data 129
5.2.2 Numerical analysis and comparison 131
5.3 Column-stub system under pseudo-static cyclic excitation 133
5.3.1 Experimental setting description and input data 133
5.3.2 Numerical analysis and comparison 134
5.4 3-storey, 3-bay frame under seismic time history ground acceleration 140
5.4.1 Experimental setting description and input data 140

5.4.2 Numerical analysis and comparison 143

CHAPTER 6 153

6 Conclusions and Future Research 153

6.1 Summary and concluding remarks 155

6.2 Future research 156

References 159

List of Figures

Figure 1.1. Lumped plasticity models: (a) Clough et al. (1965), (b) Giberson (1967) 6
Figure 1.2. Distributed plasticity fiber beam element 7
Figure 2.1: Tension monotonic curve for typical steel reinforcing bar (Leonhardt 1980) 17
Figure 2.2: representation of the σ-ε, back stress evolution b-ε and $rsgn(\sigma)$-ε curve 23
Figure 2.3: Experimental data on Bauschinger effect transition curve by Bate and Wilson, (a) high carbon steel, (b) low carbon steel 25
Figure 2.4: Effect of parameter n_2 in the transition curve of the Bauschinger effect 26
Figure 2.5. Treatment of short reversals in the proposed formulation 27
Figure 2.6: Original and modified steel model including treatment of reversals 28
Figure 2.7: Presentation of the proposed uniaxial steel model 28
Figure 2.8. Comparison with experiment (Thompson and Park 1978) 31
Figure 2.9. Comparison with experimental data of Ma et al. (a) Specimen 3 (b) Specimen 2 32
Figure 2.10: Influence of various nonlinear hardening models in the proposed formulation. Comparison with experimental data from Ma et al. 34
Figure 2.11. Uniaxial bilinear constitutive law in terms of a) total strain and b) plastic strain 35
Figure 2.12: Comparison between linear and nonlinear kinematic hardening 36
Figure 2.13. Comparison between the proposed and Menegotto-Pinto model 38
Figure 2.14. Comparison between the proposed and Dodd and Restrepo-Posada model 39
Figure 2.15. Local buckling physical and computational model 40
Figure 2.16. Axial force vs axial displacement comparison between the proposed model and corotational formulation 43
Figure 2.17. Mid-length lateral displacement comparison between the proposed model and corotational formulation 44
Figure 2.18. Comparison with experimental data S-series of Monti and Nuti: (a) L/D=5, (b) L/D=8, (c) L/D=11 46
Figure 2.19. Comparison with experimental data of Monti and Nuti (C1, C2 specimens, L/d=11) 47
Figure 2.20. Comparison with experimental data of Monti and Nuti (C5 specimen, L/d=11) 48
Figure 2.21: Menegotto-Pinto steel model 50
Figure 2.22: Dodd-Restrepo steel model 52
Figure 3.1 Behavior of concrete in monotonic compression (Chen 1982) 55
Figure 3.2. Behavior of concrete in monotonic tension (Peterson 1981) 57
Figure 3.3. Plastic component considering nonlinear isotropic hardening 60
Figure 3.4. Plastic component considering asymmetric yield stress 61
Figure 3.5. Effective stress concept of damage 62
Figure 3.6. Combination of plasticity and damage theory 62

Figure 3.7. Concrete model with damage contribution only. 65
Figure 3.8. Plastic-damage concrete model 66
Figure 3.9. Schematic representation of concrete nonlinear unloading 67
Figure 3.10. Concrete stiffness recovery representation 68
Figure 3.11. Schematic representation of the proposed concrete model. 69
Figure 3.12. Influence of plasticity parameters in compression 72
Figure 3.13. Influence of damage parameters in compression 73
Figure 3.14. Influence of unloading-reloading and stiffness recovery parameters in compression. 74
Figure 3.15. Influence of tensile parameters 75
Figure 3.16. Comparison with experimental data of Sinha et al. 77
Figure 3.17. Comparison with experimental data of Karsan and Jirsa. 77
Figure 3.18. Comparison with experimental data of Okamoto et al. 78
Figure 3.19. Comparison with experimental data of Muguruma et al. 78
Figure 3.20. Comparison with experimental data of Bahn and Hsu. 79
Figure 3.21. Comparison of model's tensile behavior with experimental data of Gopalaratnam and Shah. 80
Figure 3.22. Comparison of model's tensile behavior with experimental data of Reinhardt and Cornelissen. 81
Figure 3.23. Comparison of confined and unconfined behavior with experimental data of Choi et al. 82
Figure 3.24. Comparison with Martinez-Rueda and Elnashai concrete model 83
Figure 3.25. Comparison with Konstantinidis and Kappos concrete model 85
Figure 3.26. Comparison with the La Borderie concrete model. 86
Figure 3.27. Martinez-Rueda and Elnashai concrete model 89
Figure 3.28. Konstantinidis and Kappos high strength concrete model 90
Figure 3.29. La Borderier concrete model 92
Figure 4.1. Fiber beam element schematic representation 97
Figure 4.2 Cross-sectional local axis and layer definition 98
Figure 4.3. Basic forces, displacements, deformations and distributed loads on the beam element 100
Figure 4.4. Displacements and deformations of beam element i 101
Figure 4.5. Base shear vs top displacement of a cantilever column, comparison with displacement based formulation. 118
Figure 4.6. Base shear vs top displacement of a cantilever column, comparison with mixed formulations. 119
Figure 4.7. Comparison of Base shear vs top displacement for mixed element and displacement based element 120

Figure 4.8. Moment curvature diagrams, (a) mixed formulation vs (b) displacement based formulation 120
Figure 4.9. Moment diagrams, (a) mixed formulation vs (b) displacement based formulation 121
Figure 4.10. localization effect at cantilever column 121
Figure 4.11. Base shear vs top displacement, convergence of displacement based formulation 122
Figure 4.12. Continuous beam under vertical dynamic excitation. 123
Figure 4.13. Vertical load input 123
Figure 4.14. Comparison of vertical mid-span displacement vs external loading history 124
Figure 4.15. Concrete fibers for cover spalling identification. 125
Figure 4.16. Numerical discretization of an RC column with local rebar buckling 126
Figure 5.1. Column geometry and cross-section. 130
Figure 5.2. Input lateral displacement history 130
Figure 5.3. Base shear vs lateral displacement comparison between experimental and analytical behavior for Qiu et al. experiment 132
Figure 5.4. (a) moment-curvature, (b) moment-chord rotation diagrams at column base for Qiu et al. experiment. 132
Figure 5.5. (a) rebar stress-strain and (b) concrete stress-strain histories for Qiu et al. experiment 133
Figure 5.6. Experimental setting of Bayrack and Sheikh 134
Figure 5.7. Imposed displacement history for specimen AS-2H 135
Figure 5.8. Comparison with Bayrak and Sheikh specimen AS-2HT. 135
Figure 5.9. (a) Upper steel rebar stress-strain history, (b) Confined and unconfined concrete stress-strain histories for Bayrak and Sheikh specimen AS-3HT 136
Figure 5.10. Comparison between analysis with and without rebar buckling for specimen AS-2HT 137
Figure 5.11. Imposed displacement history for specimen AS-3HT 138
Figure 5.12. Comparison with Bayrak and Sheikh specimen AS-3HT 138
Figure 5.13. (a) Upper steel rebar stress-strain history, (b) Confined and unconfined concrete stress-strain histories for Bayrak and Sheikh specimen AS-3HT 139
Figure 5.14. Comparison between analysis with and without rebar buckling for specimen AS-3HT 140
Figure 5.15. 3-storey, 3-bay frame dimensions and reinforcing details 141
Figure 5.16. Ground motion input (Chile Valparaio 1985 Llolleo x 4.06) 142
Figure 5.17. Input ground motion and EC8 elastic spectra comparison. 142
Figure 5.18. 1st storey drift comparison 144
Figure 5.19. Base shear comparison 145
Figure 5.20. Horizontal drift vs column shear comparison 146
Figure 5.21. Chord rotations comparison: (a) column B1 bottom, (b) column A1 bottom 146

Figure 5.22. Moment-curvature diagrams of column B1 at the base during cyclic failure..... 148
Figure 5.23. Cyclic loops of column B1 top rebars at the base 149
Figure 5.24. Axial load histories at columns B1, C1 150
Figure 5.25. Base moment-chord rotation loops and EC8-3 capacity limit, (a) column A1, (b) column B1, (c) column C1, (d) column D1..... 151

List of Tables

Table 2.1: Strain history values for steel model presentation 29
Table 2.2. Model parameters for rebar analysis with Thompson and Park experimental data 31
Table 2.3: Model parameters for rebar analysis with Ma Et al. experimental data 32
Table 2.4: Strain history for comparison with Menegotto-Pinto model 38
Table 2.5. Strain history for comparison with Dodd and Restrepo-Posada model 39
Table 2.6. Axial displacement history for inelastic rebar analysis 42
Table 2.7. Steel model parameters for Monti and Nuti S-series experimental data 46
Table 2.8. Steel model parameters for Monti and Nuti experimental data (C1, C2 specimens) 47
Table 2.9. Steel model parameters for Monti and Nuti experimental data (C5 specimens) 48
Table 3.1. Damage concrete parameters 65
Table 3.2. Plastic and damage concrete parameters 65
Table 3.3. Concrete model parameters 69
Table 3.4. Reference compressive parameters 71
Table 3.5. Reference tensile parameters 74
Table 3.6. Range of model parameters values 76
Table 3.7. Concrete compressive parameters for comparison with experimental data. 79
Table 3.8. Concrete tension model parameters for Gopalaratnam and Shah experiment analysis. 81
Table 3.9. Concrete tension and stress recovery model parameters for Reinhardt and Cornelissen experiment analysis. 81
Table 3.10. Confined and unconfined concrete parameters 83
Table 3.11. Strain history for comparison with Martinez-Rueda and Elnashai concrete model 84
Table 3.12. Strain history for comparison with Konstantinidis and Kappos concrete model 85
Table 3.13. Strain history for comparison with La Borderie concrete model. 86
Table 4.1. Vertical load values 123
Table 5.1. Rebar model parameters 130
Table 5.2. Confined and unconfined concrete model parameters 131
Table 5.3. Model parameters for longitudinal rebars 134
Table 5.4. Model parameters for confined and unconfined concrete 134
Table 5.5. Rebar model parameters 143
Table 5.6. Confined and unconfined concrete model parameters 143
Table 5.7. Ultimate capacity ratios for columns A1, B1, C1, D1 according to Eurocode 8-3 151

CHAPTER 1

Introduction

1.1 Background and motivation

Reinforced Concrete (RC) skeletal structures constitute the vast majority of the built environment at seismically prone regions. An outburst in the construction of multi-storey residential and office buildings occurred during the 1960s and 1970s, hence, nowadays these structures have already exceeded or approached their life expectancy. Consequently, there is urgency for seismic assessment and retrofitting of these structures in order to adapt to modern code provisions and contemporary knowledge on seismic-resistant technology. Linear elastic analysis is still considered adequate for performing structural design of new RC buildings as increased safety factors, detailing requirements and capacity design procedures ensure seismic protection. However, in the case of existing buildings, the complete or even partial knowledge of the geometry and reinforcing details renders the possibility of estimating seismic response in a highly reliable way. To achieve that, nonlinear modeling implementing inelastic material behavior is necessary for predicting the true behavior of the structure under ground motion excitation. Realistic seismic evaluation leads to the proper retrofitting and strengthening strategies, a decision making procedure which has significant life-cost and economic consequences.

In this context, modern design codes such as the European Norm for the design of structures for earthquake resistance (EN 1998), the Greek Code for the Seismic Retrofit of existing buildings (ΚΑΝ.ΕΠΕ 2013), and the ASCE standard for the Seismic Rehabilitation of Existing Buildings (ASCE 41-13 2013) offer specific guidelines for the evaluation of the nonlinear properties of RC members and the estimation of the nonlinear structural response. The concept of the performance based design, which demands a given structure to withstand various levels of loading intensity with adequate damage levels, is the basic core of modern codes (Fardis 2010). One of the performance levels is the requirement to prevent structural collapse, namely Near Collapse (NC) in Eurocode 8-3 and ΚΑΝ.ΕΠΕ and Collapse Prevention (CP) in ASCE 41-13. It is therefore evident that proper modeling of structural response should include all inelastic phases such as initial crack formation and expansion until total failure of RC members.

Generally, RC column failure modes are classified into the following three main categories according to the PEER structural performance database (Berry et al. 2004), which includes over 400 tests on rectangular and spiral reinforced columns:

- Flexure critical, if no diagonal shear damage is observed

- Shear critical, if displacement ductility at failure is $\mu_{fail} \leq 2$, or actual maximum load capacity is less than the 95% of the load capacity calculated analytically at the strain value of 0.004, $F_{eff} \leq 0.95F_{0.004}$.
- Flexure-shear critical, if flexure and shear critical criteria are not satisfied

Also, damage observation due to cyclic loading in RC columns is distinguished in the following categories:

- Concrete crushing
- Significant cover spalling
- Longitudinal bar buckling
- Longitudinal bar or spiral fracture
- Loss of axial load capacity

Therefore, it becomes evident that refined modeling of RC members should be able to describe all the above features, while at the same time being computationally effective in the context of the computational power available nowadays for real-life structural engineering simulations. This need for keeping the computational aspects under control is intensified by the record to record variability of the seismic action and the uncertainty regarding live loads and respective masses distribution. Consequently, all codes require at least three Time History (TH) analyses with varying seismic intensity to account for every of the 3 performance levels, considering also 4 displaced mass positions due to accidental eccentricity (i.e. *3x3x4=36 TH analyses*). Also, recent advances in the area of uncertainty quantification like the Incremental Dynamic Analysis (IDA) (Vamvatsikos and Cornell 2004) and fragility assessment are based on statistical evaluation of large amount of response data resulting from many nonlinear numerical analyses (Haselton et al. 2008; Gkimousis and Koumousis 2013).

1.2 Modeling reinforced concrete structures, literature review

During the last fifty years, numerous reinforced concrete models and Finite Element Method (FEM) techniques have been developed for the analysis of RC structures behavior. Beam-column finite element models for the nonlinear analysis of RC structures can be divided in three main categories i.e., the lumped plasticity models, the distributed plasticity models and the detailed ones.

1.2.1 Lumped plasticity models

In the first category, nonlinearity is expressed in stress resultant terms and is expected to develop in predefined regions at the element ends, forming the so called plastic hinges. In these areas rotational springs are used to model nonlinear behavior in terms of moment-curvature relationship. The parallel model by Clough et al. (1965) that was later modified by Takizawa (1976) and the series model by Giberson (1967) are frequently utilized among others (Figure 1.1). The model of Clough et al. (1965) is subdivided in two parallel elements, the first one being elastic and the second elastic-perfectly plastic. Hence, the yield point is defined by the second element, while the first element describes hardening effect. The advantage of the parallel modeling is that element stiffness is calculated by simply adding every element stiffness contribution. Next, Takizawa (1976) proposed a general version of the parallel model where multilinear monotonic constitutive laws are implemented, describing in such way cracking phenomenon. On the other hand, the first series model proposed by Giberson (1967) consists of one linear elastic element and two nonlinear springs placed at both ends, where nonlinear deformations are lumped. The series model is generally more efficient than the parallel one while it can describe complex hysteretic responses by implementing the proper moment-curvature relations at the springs. Recent advances in the field include the hysteretic Euler and Timoshenko beam models by Triantafyllou and Koumousis (2011a,b) where a Bouc-Wen type model is implemented. The overal response is decomposed in an elastic and hysteretic part enabling the explicit numerical solution of the constitutive equations without the need of internal predictor corrector techniques.

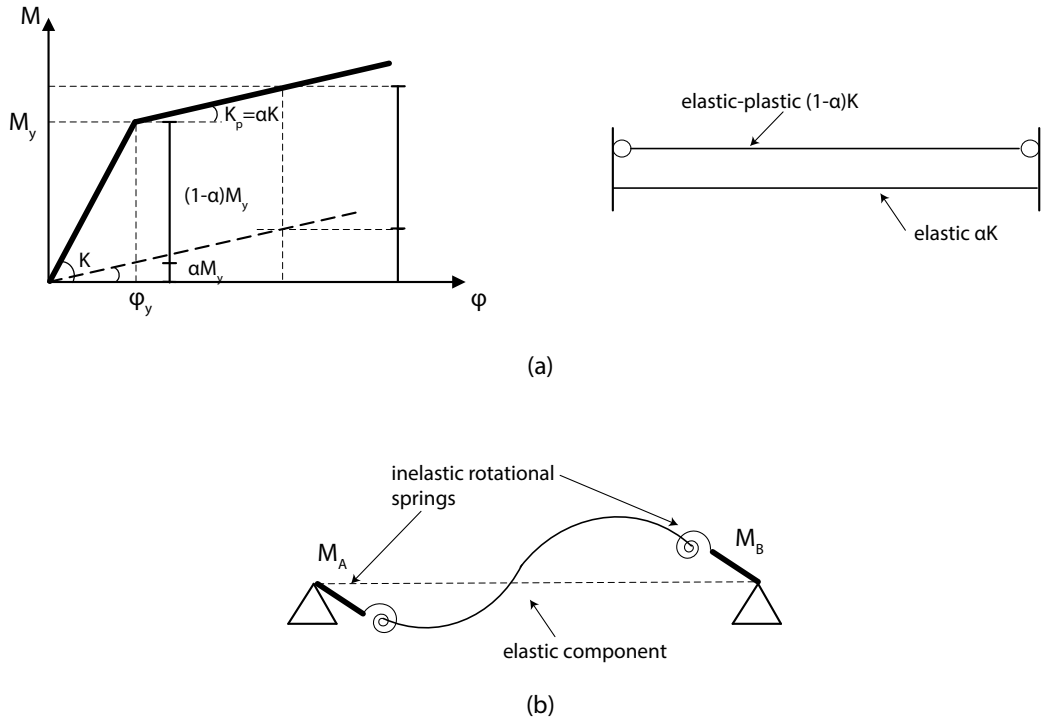

Figure 1.1. Lumped plasticity models: (a) Clough et al. (1965), (b) Giberson (1967)

Generally, lumped phenomenological models depend on a number of parameters like cross-sectional geometry and loading conditions that are predefined, influencing considerably the structure's response. Also, biaxial bending with axial force is addressed with the notion of yield surface and flow rule, which are mainly developed for plastic behavior of metals and have limited application in the case of RC cross sections. In fact, even modeling concrete on the basis of classical nonassociated plasticity (Hu and Schnobrich 1989), local discontinuities in the distribution of stresses in the section are still not considered. However, the main drawback of lumped plasticity elements is that they limit inelastic response in predefined regions and fail to describe the spread of nonlinearity along the element length.

1.2.2 Distributed plasticity models

The second category corresponds to the distributed plasticity elements that monitor nonlinearity in more than two selected regions inside the length of the element. These control sections are described by constitutive relations of classic plasticity in terms of stress resultants, or they are subdivided in longitudinal fibers representing a uniaxial stress-strain law (Figure 1.2). Cross-sectional fiber discretization has the advantage of adjusting the neutral axis location as a function of curvature and axial deformation, offering a direct representation of the combined axial-flexural interaction.

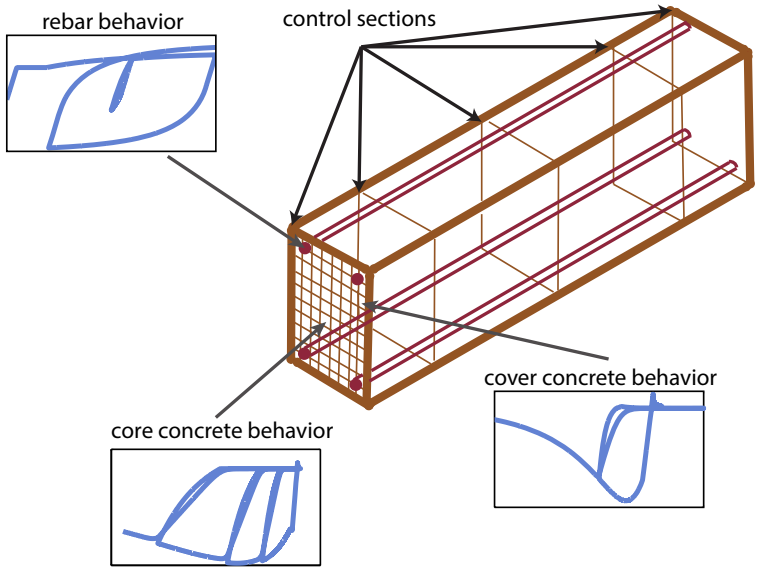

Figure 1.2. Distributed plasticity fiber beam element

Generally, the numerical solution procedure in the context of fiber distributed plasticity elements consists of four levels:

1. **Fiber level**, where given axial strains and material parameters, concrete and rebar fiber uniaxial stress and tangent Young modulus are derived.
2. **Cross-section level**, where fiber stresses and tangent moduli are summed up over the cross-section and stress resultants (axial force, bending moment), while also cross-sectional stiffness matrix are derived.
3. **Element level**, where element state determination takes place, namely the calculation of nodal internal forces and element tangent stiffness matrix.
4. **Structure level**, where every element residual is summed up together by applying continuity at nodes, and global equilibrium is enforced in terms of external and internal nodal forces.

The state determination problem of the first distributed plasticity elements (Keshavarzian and Schnobrich 1984) was based on the classical finite elements method (Bathe 2007) where the displacement field along the element is expressed with cubic polynomials. This methodology only describes constant axial force and linear curvature, which is not accurate in the plastic region where curvature is distributed nonlinearly along the element. Consequently, inner nodes have to be introduced in the element to increase accuracy which in turn increases the computational cost. To address this problem, force based models that interpolate nodal forces inside the element maintaining equilibrium have been proposed.

Mahasuverachai and Powell (1982), Kaba and Mahin (1984) and Zeris and Mahin (1991) suggested different formulations and identified the advantages of the force method in the analysis of nonlinear RC frames. The thorough investigation of these models, making them computationally attractive, was performed by Spacone et al. (1996 a,b). They suggested an iterative procedure under constant displacements for the element state determination establishing compatibility. Soon after, Neuenhofer and Filippou (1997) showed that elemental iterations are not necessary, as the element stresses gradually converge while the whole structure is in equilibrium. Although these early force based elements have a robust and efficient numerical procedure, doubts had arisen on their variational consistency. The issue was raised by Hjelmstad and Taciroglu (2005) who showed that it is possible to provide non-variationally consistent force-based elements within the "nonlinear flexibility" framework by enforcing equilibrium directly, proving in such way that not all force-based elements have a variational base. The same authors had previously (Hjelmstad and Taciroglu 2002) developed mixed beam elements based on two or three field energy principles that present a variationally consistent structure. Variationally consistent algorithms for the state determination process were also proposed by Nukala and White (2004) and Saritas and Soydas (2012). Thereafter, mixed methods seem to dominate the research field of nonlinear distributed plasticity analysis of RC structures as a lot of research has recently been produced in the field (Hjelmstad and Taciroglu 2003; Taylor et al. 2003; Alemdar and White 2005; Alsafadie et al. 2011; Correia et al. 2015).

In the general formulation of fiber beam-column elements uniaxial material laws are implemented for steel rebar and concrete fibers. These models are expressed by analytical relations and are usually derived by interpreting cyclic experimental results on rebar and concrete specimens. The Menegotto-Pinto (1973) and Dodd and Restrepo-Posada (1995) are some of the most frequently used models to describe steel cyclic behavior, while Monti-Nuti (1992) and Dhakal and Maekawa (2002) models incorporate also rebar inelastic buckling. Considering uniaxial concrete behavior, the Kent-Scott-Park (1982) and the Mander et al. (1988) models later improved by Martinez-Rueda and Elnashai (1997) and Chang and Mander (1994) are frequently encountered among others in academic and commercial software, while high strength concrete cyclic behavior is also addressed. (Konstantinidis and Kappos 2007)

The basic drawback of distributed plasticity fiber beam elements is their inefficiency to explicitly incorporate local 3D interaction effects on transverse rebars and concrete, i.e. the

confinement effect. In addition, the weak point of the force based elements is that although they fit perfectly in the Euler-Bernoulli flexural framework, their extension to accommodate shear effects is not straightforward. However, some authors have provided numerical models based on various modeling strategies that try to address the axial-shear-flexural interaction. Martinelli (2000) developed a fiber column element based on Timoshenko beam theory coupled with a strut and tie truss model that accounts for shear deformations by considering the transverse reinforcement with the compressive and tensile concrete diagonals. In such way different shear resistance mechanisms are taken into account as the arch action, truss mechanism, aggregate interlock, and compressive concrete are all described. While Martinelli (2000) used the displacement based approach and uniaxial constitutive laws for concrete, Petrangeli et al. (1999) developed a force based fiber beam element by introducing a biaxial constitutive law based on a modified microplane approach (Bazant and Oh 1985) for modeling monotonic and cyclic loading. Later, Bairan and Marie (2006) proposed a nonlinear fiber sectional model for concrete structures capable of simulating the total interaction between all six internal forces addressing also flexural-torsional interaction problem with warping-distortion phenomena included. Also, Stramandinoli and Rovere (2008) developed a three node and Ceresa et al. (2009) developed a two node Timoshenko fiber beam element by implementing the Modified Compression Field Theory (Vecchio 1999) to account for a robust response under cyclic loading. On the other hand Mazars et al. (2006) and Saritas and Filippou (2009) incorporated general damage theory models in the context of the multi-fiber modeling to describe the axial-shear-flexure interaction.

Furthermore, special treatment is required to account for modeling the bonding interface between longitudinal reinforcing bars and adjacent concrete fibers at beam-column joints and foundation elements. Bar-slip generates rigid body rotations at the ends of frame elements that can substantially increase member flexibility (Sezen and Moehle 2006). Limkatanyu S and Spacone (2002) incorporated the bonding interfaces in the framework of displacement and force based beam-column elements. Also, Berry (2006) and Zhao and Sritharan (2007) models use a zero-length fiber section in connection with the standard fiber beam-column element to account for the bar-slip effect. Later, Ghannoum and Moehle (2012b) improved these models by avoiding discontinuities in rebar stresses and neutral axis location between the bar-slip and adjacent beam-column fiber sections.

Moreover an inherent deficiency of the force-based elements is that they produce unrealistic behavior in softening-strain cases as they result different elemental responses for different number of control sections as described by Coleman and Spacone (2001). In the same work a solution to this problem is proposed by introducing a constant fracture energy regularization technique. Later, a more robust solution was given by Scott and Fenves (2006) where a new constant length plastic hinge integration method based on the modified Gauss-Radau quadrature was developed. Moreover, Almeida and Pinho (2012) tried to expand this concept showing an adaptive algorithm where the plastic hinge length can be modified during the analysis depending on the load conditions.

1.2.3 Detailed finite elements

In the detailed approach the concrete domain is discretized with 3D solid elements while longitudinal rebars are usually modeled with embedded rod elements (Hartl and Ch 2002; Spiliopoulos and Lykidis 2006; Cervenka and Papanikolaou 2008; Cotsovos 2013). However, even if this modeling appears to provide the highest possible accuracy, it lacks numerical consistency and robustness due to the high complexity of triaxial concrete models (Markou and Papadrakakis 2012), i.e. the smeared crack approach. Another modeling approach for the 3D concrete behavior is based on the coupled plastic-damage mechanics theory (Lubliner et al. 1989; Lee and Fenves 1998; Grassl and Jirasec 2006; Richard et al. 2010) that utilizes the concepts of plastic surface and damage surface interaction able to model yielding, softening as well as stiffness degradation cyclic phenomena. To address the numerical instabilities of the complex constitutive models high order finite elements and integration techniques are utilized. For this reason the application of such models in real-life structural engineering applications seem to be impractical at the time being, considering also the large amount of time history analyses needed due to record to record variability. Towards this direction, efforts have been made to combine the distributed plasticity and detailed 3D approach in a hybrid simulation where the clear span of RC members is modeled with beam elements and joints are modeled with solid elements. (Mata et al. 2008; Markou and Papadrakakis 2015).

1.3 Research objectives

The aim of this thesis is to propose a fiber beam-column element able to model skeletal RC structures exhibiting severe cyclic loading. Fiber modeling is selected as the appropriate method to achieve such a purpose, as it combines both computational efficiency and stability with accuracy to describe the physical problem. The main focus is on the numerical

modeling of the flexural critical failure mechanisms that RC members undergo during intensive seismic loading i.e. cover spalling, core crushing and longitudinal rebar buckling. On the level of material modeling, the thesis makes an effort to develop uniaxial steel and concrete constitutive laws based on the solid theoretical background of the general continuum plastic and damage models. On the level of the finite element modeling, the thesis explores the variational consistency of the two-field mixed fiber beam elements and offers efficient numerical solution methods by implementing the proposed material models. More specifically, the dissertation aims to:

- Develop a uniaxial rate steel cyclic model for longitudinal rebars incorporating nonlinear kinematic and isotropic hardening while it can also simulate yield plateau and Bauschinger effect.

- Address reinforcing bar local inelastic buckling by iteratively satisfying equilibrium in the deformed configuration of a single rebar.

- Develop a uniaxial rate coupled plastic-damage concrete model able to simulate core crushing and cover spalling that triggers rebar buckling mechanism. The concrete model can describe softening and stiffness degradation behavior, while it is also enriched with nonlinear unloading and crack closure phenomena.

- Formulate a two-field mixed beam-column finite element that takes advantage of the rate structure of the material constitutive models and propose two different numerical solution schemes i.e. solution via linearization of the element equations and solution in state-space form.

1.4 Dissertation outline

The dissertation is organized as follows:

In Chapter 2 the formulation of the uniaxial steel model solely based on plasticity considerations is presented. Plasticity rate equations are combined together and are smoothed following the notions of hysteresis. In addition, some phenomenological modifications are introduced making the model able to describe yield plateau, Bauschinger effect, correcting also its incompatibility with Drucker's or Ilyushin's postulates of plasticity for partial unloading-reloading in the nonlinear path. Then, the model rate equations are

linearized following a simple backward Euler scheme and a solution algorithm is presented. In addition the inelastic buckling phenomenon of the single rebar is addressed. The rebar is discretized in layers each one represented by the local uniaxial cyclic steel model developed. An iterative procedure is implemented where the buckling curve is determined analytically and equilibrium is imposed on the deformed configuration by updating the curvature field of the rebar cross-section. The accuracy of the proposed steel model is verified in terms of experimental data and the advantages in comparison with other existing uniaxial rebar models are demonstrated.

Chapter 3 deals with the formulation of the uniaxial rate concrete model. The model is based on the combination of continuum damage theory that describes softening and stiffness degradation phenomena and plasticity theory necessary for the expression of permanent inelastic strains. The basic model is also enhanced with the phenomenological additions of nonlinear unloading and crack closure phenomena. The linearization of the rate equations leads to the solution algorithm of the model, while its accuracy is validated on the basis of experimental data and other existing concrete models on both compressive and tensile behavior. Special emphasis is also laid on the influence of model parameters on the outcome response, while also the appropriate range of parameters is notified.

Chapter 4 describes the state-determination process of the proposed RC fiber beam-column element. Cross-sectional internal forces and stiffness are derived from midpoint fiber integration rule, while two basic procedures are investigated, namely the displacement based and the two-field mixed principle approach. Detailed state determination algorithms based on the linearization of the element equilibrium and compatibility equations are described for both methodologies. In addition, a novel state space approach is developed in any case by taking into account the rate form of the constitutive equations and solving theme simultaneously with the global equations of motion. Finally, the superiority of the mixed formulation over the displacement based approach, is demonstrated through comparative examples.

In Chapter 5, examples are presented that demonstrate the validity and accuracy of the proposed formulations. The proposed numerical procedure is compared with experimental results of cyclic tests on RC structures available in literature. Complexity of the experimental tests ranges from a single RC column under pseudo-static cyclic response to seismic time history analysis of a one third scaled 3-storey, 3-bay frame.

Chapter 6, finally, summarizes the conclusions drawn in this work while highlighting some important results obtained. At the same time the directions for future research are outlined.

CHAPTER 2

Modeling Rebar Cyclic Behavior

2.1 Introduction

Stress-strain $\sigma_s - \varepsilon_s$ curve for mild steel rebars in tension until failure is well documented from experiments (Leonhardt 1980). It is typically represented by four regions which are presented in Figure 2.1 and they are listed below:

-Linear elastic region

-Yield plateau

-Strain-hardening region

-Post-ultimate stress region

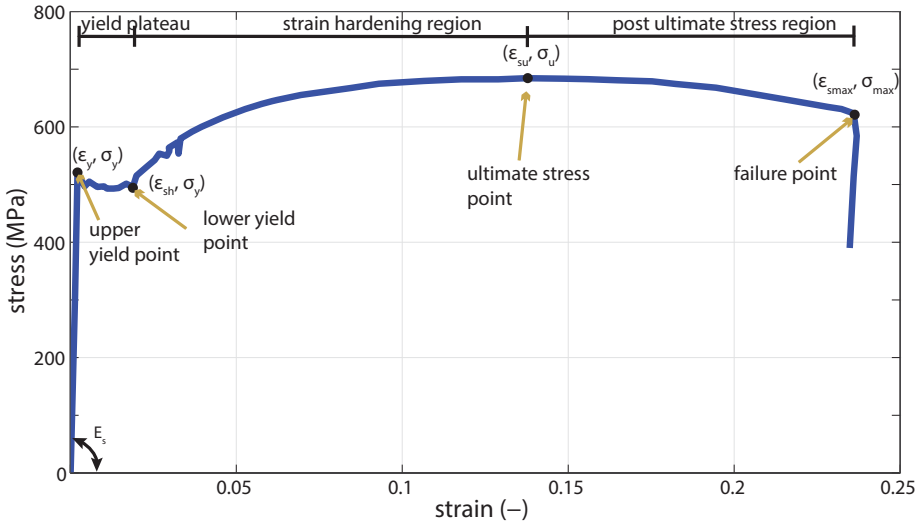

Figure 2.1: Tension monotonic curve for typical steel reinforcing bar (Leonhardt 1980)

The linear elastic region $\left(0 \le \varepsilon_s \le \varepsilon_y\right)$ is described by Hook's law $\sigma_s = E_s \cdot \varepsilon_s$, where E_s is The Young's modulus of elasticity. Elastic branch ends to the yield point (ε_y, σ_y) which is generally higher that the yield plateau but for engineering purposes lower yield stress and yield plateau stress are considered the same.

Similarly, Luders or yield plateau $\left(\varepsilon_y \le \varepsilon_s \le \varepsilon_{sh}\right)$ is typically assumed to be horizontal, although this is not actually the case as fluctuations arise.. The point at which the yield plateau ends and strain hardening begins is not obvious, although generally a dip is preceded, followed by a steep increase that suddenly changes slope into the relatively smooth hardening region. Generally, yield stress σ_y is defined conservatively by the lower yield point. However, high strength rebars do not exhibit this defined plateau.

The strain-hardening region $\left(\varepsilon_{sh} \le \varepsilon_s \le \varepsilon_{su}\right)$ ranges from the idealized coordinates at which strain hardening begins $\left(\varepsilon_{sh}, \sigma_y\right)$ to the ultimate coordinates $\left(\varepsilon_u, \sigma_u\right)$, which correspond to the point at which the maximum tensile load is resisted and necking begins. At this point the stress-strain curve has zero slope.

In the post-ultimate region $\left(\varepsilon_{su} \le \varepsilon_s \le \varepsilon_{s\max}\right)$, localization of damage is achieved, hence the softening branch is related to the location and gauge length over which the experiment is monitored (Marin 1962). This softening behavior of longitudinal rebars is omitted in the analysis of RC members as it is very unlikely to be manifested due to preceding buckling, bond-slip, or failure of neighboring concrete.

Measured data on reinforcing bars show some difference in the responses in tension and compression although it is commonly assumed that the monotonic stress-strain compression and tension curves are identical. For this reason Spurr and Paulay (1984) propose that the compressive stress at a given strain can be defined as the corresponding tension stress multiplied by $\left(1-2\varepsilon_s\right)$. The difference is attributed to the change of the rebar cross-sectional area during loading and it is revealed if engineering coordinates are used for the representation of stress-strain curve. Alternatively, if the natural or true coordinate system is used, then any differences disappear. Natural stress $\bar{\sigma}_s$ is related to engineering stress with relation $\bar{\sigma}_s = \sigma_s\left(1+\varepsilon_s\right)$

However, reinforcing bars in reinforced concrete members that undergo high compressive strains at intense cyclic loading are unlike to exhibit a stable loading path. This is due to buckling that appears in the form of large lateral deformations between adjacent stirrups, or into a length including one or more drifted stirrups. Buckling of longitudinal rebars constitutes a common failure mode of RC columns undergoing cyclic loading along with significant spalling, concrete crushing and rebar fracture. Due to geometrical nonlinearity, the average compressive stress carried by reinforcing bars decreases in the post-buckling range, while point-wise steel stress-strain relations over the rebar's cross-section remain the same. This behavior characterizes buckling as a local phenomenon. On the contrary, the average tensile stress-strain relationship over the specified control volume remains the same as the point wise stress-strain relationship.

To model the elastoplastic piecewise steel cyclic behavior various models have been proposed among which the widely used Menegotto-Pinto model (1973). The advantage of

this model is its explicit formulation enabling the direct derivation of stresses given strains. A lot of preceding steel models are based on the Menegotto-Pinto equations to describe the steel cyclic behavior (Chang and Mander 1994; Balan et al. 1998; Hoehler and Stanton 2006; Kunnath et al. 2009). These models are efficient to capture steel hysteretic loops but generally fail when short reversals take place (see also §2.2.8). Another very common model is the Dodd and Restrepo-Posada model (1995) which resolves the issue of short reversals by keeping in memory only 3 reversal branches, but it is computationally unstable and inefficient as it requires iterations for the reversal curves. A solution to this drawback has recently been proposed by Kim and Koutromanos (2016) by using b-splines to describe reversals. Moreover, high strength steel is addressed experimentally and analytically in Shi et al. (2012) and Wang et al. (2015).

Considering rebar buckling, the Monti-Nuti model (1992) is commonly used as an enhancement of the Menegotto-Pinto model, which accounts for four different hardening rules. Furthermore, a number of average stress-strain relations have been proposed (Gomes and Appleton 1997; Dhakal and Maekawa 2002b; Bae et al. 2005; Berry and Eberhard 2005; Kashani et al. 2013; Zong et al. 2014) that point-wise modify steel cyclic behavior in the compressive region by phenomenologically interpreting extensive experimental and detailed numerical parametric studies. On the other hand Feng et al. (2014) developed a more elaborate hybrid finite-element method to accurately predict rebar buckling in RC members. In this model a fiber model follows the strain history at the local region and a finite element model with solid elements simulates the potential buckling region of a bar and the boundary condition from adjacent transverse reinforcement and concrete, i.e. stirrups.

Generally, reinforcing bars buckle following two distinct buckling modes. The first is a local mode where buckling length is the distance between two adjacent stirrups and is more common in rectangular columns with closed stirrups. The second is a global mode where buckling length includes one or more stirrups that are expanded by the lateral deformation of the rebar and is mostly encountered in circular columns with spiral reinforcement. Typically global buckling models are an extension of the local models, where hoops or spirals are simulated with springs to restrain the expansion (Zong et al. 2013; Massone and López 2014; Su et al. 2015; Kashani et al. 2016).

Generally, using the point wise steel stress-strain law, the lateral deformation of compressed longitudinal reinforcing bars can be addressed provided that the control volume, over which the average stress-strain relationship is computed, is very small.

However, in the finite element analysis of structures such small element size is not feasible because of the enormous computational cost and large memory demand. Hence, for RC members that are generally not susceptible to large geometrical nonlinear effects, a suitable formulation is the one that treats rebar buckling locally in the affected RC region.

The aim of this chapter is twofold; first, to develop the uniaxial piece-wise steel cyclic constitutive law and second to incorporate the proposed model to the inelastic rebar buckling model. The buckling mechanism used is based on the works of Massone and Moroder (2009), Urmson and Mander (2012) and Kim and Koutromanos (2016) and is extended to cyclic inelastic buckling. Steel rebar is simulated as a beam element where average strains are the problem's input and average stresses are the problem's output. Buckling curve and curvature distribution are derived analytically and the numerical procedure results in an incremental scheme where mid-length curvature is updated until equilibrium at the deformed state is achieved. Considering steel model, a combination of nonlinear and isotropic hardening with yield plateau is incorporated, rendering the proposed rebar model capable of expressing various cyclic responses. Verification of the proposed model is performed in terms of comparison with experimental data concerning either the piece-wise steel cyclic behavior or the global rebar cyclic behavior including inelastic buckling.

2.2 Uniaxial steel cyclic behavior

2.2.1 1D rate independent plasticity

The purpose of this chapter is to develop a hysteretic model which incorporates the entire inelastic loading of steel rebar, namely elastic loading, yielding, hardening and unloading in a single nonlinear differential equation that embodies both the yield surface and hardening rule. Mathematically this addresses the entire evolution process without the need of incremental consideration. In this context Sivaselvan and Reinhorn (2003), based on Bouc-Wen model (Wen 1976) proposed a hysteretic model in stress resultant terms derived explicitly from classical plasticity theory. The same approach is generalized herein as a combination of nonlinear kinematic hardening and isotropic hardening is considered. Indeed, it has been observed in various tests that steel rebars exhibit a nonlinear post-yield branch after yield plateau that triggers a ratcheting effect under repeated constant stress reversals with non-zero mean (Dafalias et al. 2008). Also, isotropic hardening has been notified experimentally at higher loading cycles.

Following the fundamentals of classical plasticity (Lubliner 2008; Borja 2013), stress-strain law is expressed according to the strain decomposition rule in rate form as:

$$\dot{\sigma} = E\left(\dot{\varepsilon} - \dot{\varepsilon}^{p}\right) \tag{2.1}$$

where $\dot{\sigma}$ is the rate of normal stress, $\dot{\varepsilon}$ is the rate of total strain and $\dot{\varepsilon}^{p}$ is the rate of plastic strain. This relation indicates that stresses evolve proportionally to the evolution of the elastic strains. Considering the combination of kinematic and isotropic hardening, yield function is expressed as follows:

$$\Phi\left(\sigma, b, r\right) = \left|\sigma - b\right| - r \le 0 \tag{2.2}$$

with b being the back stress and *r* being the reserve between the back stress and the yield stress in tension or compression with initial value σ_{y0} . The rate of the reserve is given as:

$$\dot{r} = m \cdot H \cdot \dot{\lambda} \tag{2.3}$$

where $\dot{\lambda} \ge 0$ is the plastic multiplier which is actually the magnitude of the strain rate. Scalar variable *m* is the percent of isotropic hardening which affects the reserve r, with *(1-m)* being the percent of kinematic hardening which affects the back stress b, i.e., *m=0* indicates full kinematic hardening while *m=1* defines full isotropic hardening.

Also, the flow rule offers the plastic strain rate $\dot{\varepsilon}^{p}$ as:

$$\dot{\varepsilon}^{p} = \dot{\lambda} \cdot \frac{\partial \Phi}{\partial \sigma} = \dot{\lambda} \cdot sgn(\sigma - b) \tag{2.4}$$

There is no restriction in the selection of the nonlinear hardening model in the proposed model (see also section 2.2.6). Herein though, Armstrong-Frederick (1966) evolution equation of the back stress is implemented for the uniaxial stress-strain state:

$$\begin{aligned} \dot{b} &= (1-m)\left(H_0 \cdot \dot{\varepsilon}^{p} - q \cdot \left|\dot{\varepsilon}^{p}\right| \cdot b\right) \\ &= (1-m) \cdot \; q \cdot \dot{\varepsilon}^{p} \cdot \left[\frac{H_0}{q} - \mathrm{sgn}(\dot{\varepsilon}^{p}) \cdot b\right] = \; (1-m) \cdot H \cdot \dot{\varepsilon}^{p} \; = \; (1-m) \cdot H \cdot \dot{\lambda} \cdot sgn(\sigma - b) \end{aligned} \tag{2.5}$$

where, *H* is the nonlinear hardening modulus depending on the real positive parameter *q,* with initial value H_0.

$$H = H_0 - q \cdot \mathrm{sgn}(\dot{\varepsilon}^{pl}) \cdot b \tag{2.6}$$

Hardening modulus can also be expressed in terms of the post to pre-yield hardening ratio *a* $a = E_t / E$ as:

$$H = \frac{E_t}{1 - E_t / E} = \frac{a}{1-a} \cdot E \tag{2.7}$$

Normal stress and plastic multiplier are restricted by unilateral constrains representing restrictions that signify whether the material has yielded or not, resulting from Karush-Kuhn-Tucker (KKT) optimality conditions. These are expressed in the following form:

$$\dot{\lambda} \cdot \Phi(\sigma, b, r) = 0 \tag{2.8}$$

During plastic response ($\dot{\lambda} > 0,\ \Phi(\sigma, b, r) = 0$) the consistency condition is derived by differentiating equation (2.8):

$$\dot{\Phi}(\sigma, b, r) = 0 \Rightarrow \left(\dot{\sigma} - \dot{b}\right) \cdot sgn\left(\sigma - b\right) - \dot{r} = 0 \tag{2.9}$$

Substituting equations (2.1), (2.3) and (2.5) in equation (2.9) plastic multiplier is obtained as:

$$\dot{\lambda} = sgn(\sigma - b) \cdot \frac{E}{E + H} \cdot \dot{\varepsilon} = (1 - a) \cdot sgn(\sigma - b) \cdot \dot{\varepsilon} \tag{2.10}$$

Then, substituting relation (2.10) into equation (2.4) the following relation is derived:

$$\dot{\varepsilon}^p = (1 - a) \cdot \dot{\varepsilon} \tag{2.11}$$

where the current post to pre-yield stiffness ratio *a* is given according to relations (2.6) and (2.7) as:

$$a = \frac{E_{pl}}{E} = \frac{H}{E + H} = \frac{H_0 - q \cdot \mathrm{sgn}(\dot{\varepsilon}^{pl}) \cdot b}{E + H_0 - q \cdot \mathrm{sgn}(\dot{\varepsilon}^{pl}) \cdot b} \tag{2.12}$$

In Figure 2.2 the evolution of the total stress σ, back stress *b* and the stress due to isotropic hardening *r* are presented graphically.

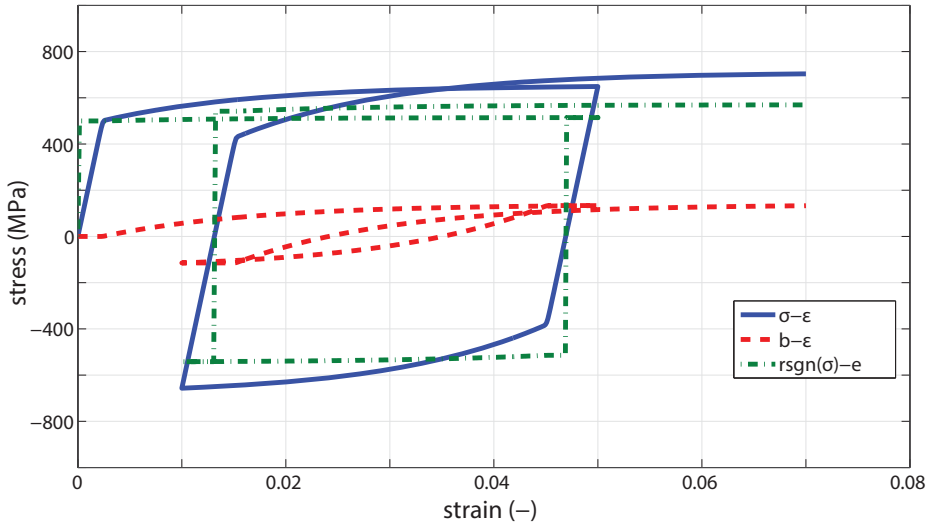

Figure 2.2: representation of the *σ-ε*, back stress evolution *b-ε* and *rsgn(σ)-ε* curve

The reserve r is plotted in terms of the signum value of the stress variable σ for better understanding its role. Indeed, the sum of the back stress and the reserve is the yield surface, which is the point from where plastic strains start to develop. Hence, during plastic flow the $\sigma-\varepsilon$ curve coincides with the curve $\left(b+r\,\mathrm{sgn}(\sigma)\right)-\varepsilon$.

2.2.2 Smoothening of the constitutive equations

All above equations hold for the case where the material is deformed in the plastic region. During elastic loading or unloading plastic strain is not considered as $\dot{\lambda}=0$. To include all loading phases in a single relation, equation (2.11) is extended by considering two Heaviside type functions acting as switches:

$$\dot{\varepsilon}^{p}=H_{1}\cdot H_{2}\cdot(1-a)\cdot\dot{\varepsilon} \tag{2.13}$$

Function H_1 controls yielding while H_2 controls loading/unloading state.

$$H_{1}=\begin{cases}0, & \textit{elastic deformation}\left(\dot{\varepsilon}^{p}=0\right)\\ 1, & \textit{plastic flow}\left(\dot{\varepsilon}^{p}=H_{2}\cdot(1-a)\cdot\dot{\varepsilon}\right)\end{cases} \tag{2.14}$$

$$H_{2}=\begin{cases}0, & \textit{unloading}\left(\dot{\varepsilon}^{p}=0\right)\\ 1, & \textit{loading}\left(\dot{\varepsilon}^{p}=H_{1}\cdot(1-a)\cdot\dot{\varepsilon}\right)\end{cases} \tag{2.15}$$

Consequently, H_1 emerges from the smoothening of the yield function. This is accomplished by raising the absolute value to the nth power approximating in a smooth way the step function with discrete values [0,1] as $n\to\infty$. Consequently, the following relation holds:

$$H_1 = \left| \frac{\sigma - b}{r} \right|^n = \left| \frac{\sigma_h}{r} \right|^n \tag{2.16}$$

Parameter n controls the form of transition from the elastic to plastic branch of the stress-strain law, which is smoother for lower values, approaching a bilinear behavior for higher ones $(n \geq 8)$. Also the expression $(\sigma_h = \sigma - b)$ refers to the hysteretic part of the normal stress, i.e. the part of the stress without kinematic hardening.

In addition, function H_2 aims at controlling loading and unloading following the sign of the yield function rate with positive sign indicating loading while negative sign unloading. Furthermore, the modification of the Heaviside function to yield zero value when unloading occurs and unity when loading occurs is handled as follows:

$$\begin{aligned} H_2 &= 0.5 \cdot \left(1 + sgn\left(\frac{d\Phi}{d\sigma} \cdot \dot{\sigma} \right) \right) \\ &= 0.5 + 0.5 \cdot sgn\left((\sigma - b) \cdot \dot{\varepsilon} \right) \end{aligned} \tag{2.17}$$

After defining functions H_1 and H_2 equation (2.13) is substituted in equation (2.1) and the final form of the constitutive relation in rate form is obtained:

$$\dot{\sigma} = \left[1 - (1 - \alpha) \cdot H_1 \cdot H_2 \right] \cdot E \cdot \dot{\varepsilon} = E_t \cdot \dot{\varepsilon} \tag{2.18}$$

where E_t is the tangent modulus in the stress rate-strain rate relationship.

2.2.3 Modifications for steel cyclic behavior

Steel stress-strain relation under cyclic loading primarily aims at expressing the linear elastic and hardening branches in the first excursion together with the Bauschinger effect for subsequent cycles.

To account for this behavior equation (2.18) along with relations (2.16) and (2.17) for nonlinear kinematic and isotropic hardening are implemented. The initial bilinear constitutive behavior is obtained using a high value for the exponent parameter n $(n_1 \geq 8)$. The bilinear behavior is incorporated just for the initial yield point, while for subsequent yielding in the opposite direction gradual transition in the plastic regime is manifested. In the proposed hysteretic model this is accomplished by subsequently reducing parameter n to lower values n $(n_2 \leq 2)$. Also, Bate and Wilson (1986) have shown experimentally that the shape of the Bauschinger effect depends on the carbon context of steel (Figure 2.3).

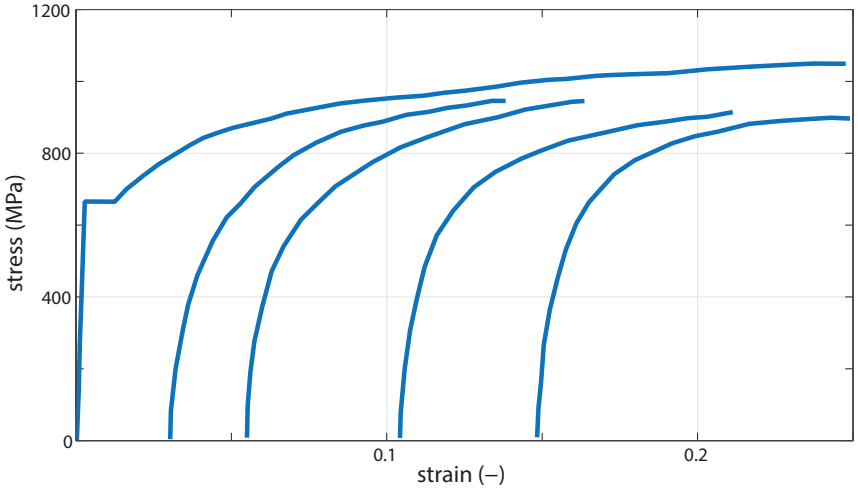

(a)

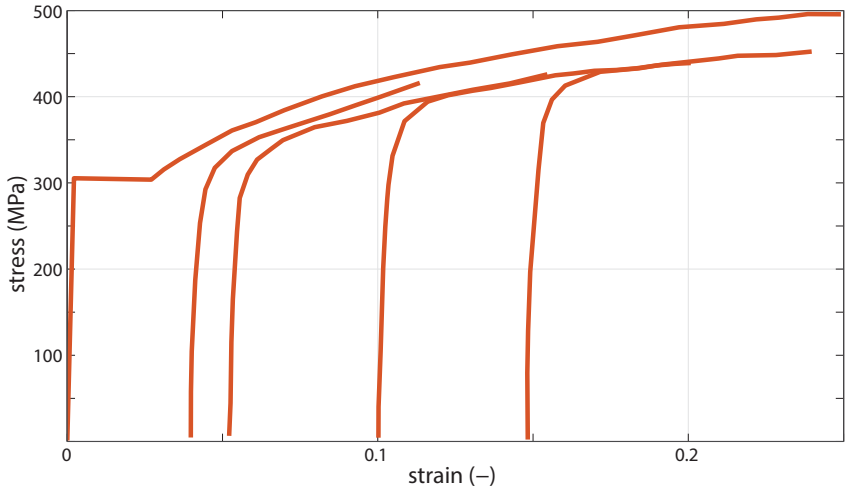

(b)

Figure 2.3: Experimental data on Bauschinger effect transition curve by Bate and Wilson, (a) high carbon steel, (b) low carbon steel

Indeed, low carbon steels tend to have stiffer Bauschinger curve than steels with higher concentrations in carbon. The capability of the proposed model to capture the Bauschinger effect of different steel grades lies on the smoothening exponent n_2. Thus, higher values $(n_2 > 1.5)$ are more suitable to stiffer branches of Bauschinger effect, while lower values $(0.2 \le n_2 \le 1.5)$ simulate a smoother transition. The effect of parameter n_2 is presented graphically in Figure 2.4.

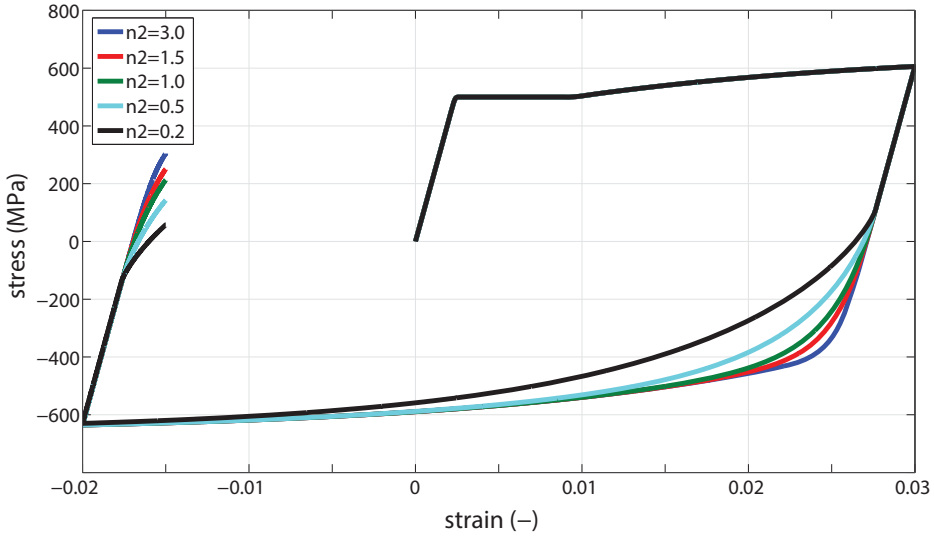

Figure 2.4: Effect of parameter n_2 in the transition curve of the Bauschinger effect

Alongside, many sophisticated models that are based either on the bounding surface theory (Dafalias 1992; Shen et al. 1995; Goto et al. 1998; Peil et al. 2001) or the endochronic theory (Sugiura et al. 1987) are implemented to capture yield plateau. Also, Ucak and Tsopelas (2011, 2012) used a pseudo memory surface in the deviatoric stress space to correctly describe the plateau response. However, yield plateau herein is included simply in the model by setting a plastic strain threshold ε_{plat} where plastic to elastic modulus ratio a obtains its defined value. Consequently, a ratio is initialized with zero value that corresponds to full elastic-plastic behavior and by the time plastic strain ε^p exceeds threshold ε_{plat} value the hardening phase begins $(a > 0)$.

Another modification accounts for the incompatibility with Drucker's or Ilyushin's postulates of plasticity for partial unloading-reloading, i.e. short reversals in the nonlinear path. Generally, hysteretic models have been criticized in the past for their incompatibility with Drucker's or Ilyushin's postulates. Based the work of Wang and Foliente (2001) an accurate solution proposed by Charalampakis and Koumousis (2009) and Kottari et al. (2014) that eliminates the problem by properly modifying the reloading path of the hysteretic spring for the Bouc-Wen model or the Sivaselvan-Reinhorn model respectively. In this work the same approach is utilized, which leads to the modification of the switch function H_2 in the following form:

$$\overline{H}_2 = H_2 \cdot (1 - R) \tag{2.19}$$

where $R\left(\sigma_h,\ \varepsilon,\ \sigma_{y0}\right)$ is a stiffening factor that controls stiffness recovery in the reloading branch, which is expressed as:

$$R = 0.5 \cdot \left[1 + sgn(\sigma_r - \sigma_h) \cdot sgn(\sigma_h)\right] \cdot \left(\frac{\varepsilon_r - \varepsilon_c}{\varepsilon_r - \varepsilon}\right) \tag{2.20}$$

In relation (2.20) σ_h is the hysteretic part of the normal stress $\left(\sigma_h = \sigma - b\right)$, σ_r and ε_r are the stress and strain respectively corresponding to the last observed reversal point and ε_c is the modified strain in the unloading path that corresponds to the given hysteretic stress σ_h:

$$\varepsilon_c = \left(\frac{\sigma_h - \sigma_r}{\sigma_{y0}}\right) \cdot \varepsilon_{y0} + \varepsilon_r \cdot sgn(\sigma_h) \tag{2.21}$$

where also appropriate tracking of the reversal point is needed to accurately handle different types of short reversals as indicated in Charalampakis and Koumousis (2009) and Kottari et al. (2014).

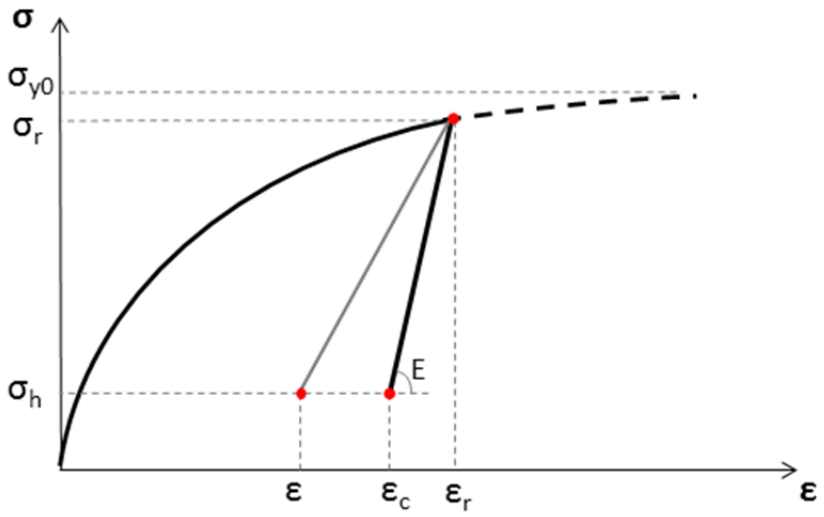

Figure 2.5. Treatment of short reversals in the proposed formulation

The influence of the modification considering Drucker's and Ilyushin's postulate during short reversals is manifested graphically in Figure 2.6.

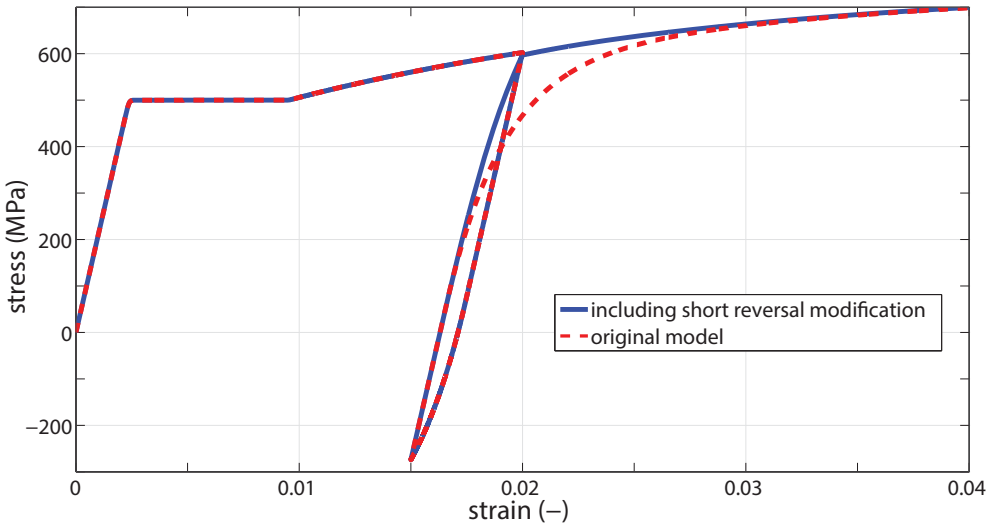

Figure 2.6: Original and modified steel model including treatment of reversals

Finally, the proposed steel model with all the additional features is illustrated in Figure 2.7 with imposed strain history the one presented in Table 2.1. In the figure, the sequence of reversal points while also yield plateau and isotropic hardening effect are marked.

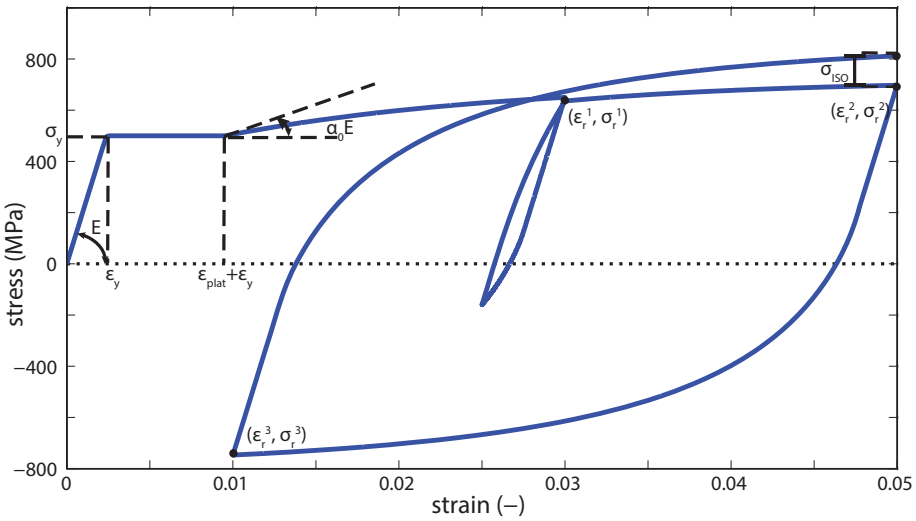

Figure 2.7: Presentation of the proposed uniaxial steel model

Pseudo-Time (sec)	Strain (-)
0	0
1	0.03
2	0.025
3	0.05
4	0.01
5	0.05

Table 2.1: Strain history values for steel model presentation

2.2.4 Pseudo-code for the steel model

Summarizing the described uniaxial steel model, one can apply it to the global solution process as follows:

At any iteration *j* of an outer nonlinear solution process, given variables are the total strain ε_j, strain increment $d\varepsilon_j$ plastic strain $\varepsilon_{p,j}$, back stress b_j, isotropic hardening reserve stress r_j and reversal point $(\varepsilon_r, \sigma_r)$. In order to calculate the updated stress σ_{j+1} and updated elastoplastic tangent modulus $E_{p,j+1}$ the following steps should be calculated:

1. Check if plastic strain is lower than the yield plateau threshold and if this condition holds set initial hardening ratio to zero $(a_0 = 0)$.
2. Calculate hysteretic part of the stress: $(\sigma_{h,j} = \sigma_j - b_j)$.
3. Calculate Heaviside functions H_1 and H_2:

$$H_1^j = \left| \frac{\sigma_{h,j}}{r_j} \right|^n \qquad (2.22)$$
$$H_2^j = 0.5 + 0.5 \cdot \mathrm{sgn}\left[\left(\sigma_j - b_j \right) \cdot d\varepsilon_j \right]$$

4. Update isotropic hardening reserve stress:

$$r_{j+1} = r_j + m \cdot H_j \cdot \left(1 - a_j\right) \cdot \mathrm{sgn}\left(\sigma_{h,j}\right) \cdot H_1^{j+1} \cdot H_2^{j+1} \qquad (2.23)$$

5. Check if yield point has been exceeded $H_1^j \geq 0.99$. If this condition holds then set parameter n_2 as the exponent parameter n.
6. Find last reversal point $(\varepsilon_r, \sigma_r)$ in the plastic region by checking if unloading occurs.
7. Calculate stiffening factor R for short reversals and correct unloading switch H_2^j using equations (2.19)-(2.21).

8. Update current hardening ratio a_{j+1} from equation (2.12)

9. Calculate current plastic strain.

$$\begin{aligned} \varepsilon_{j+1}^{p} &= \varepsilon_{j}^{p} + d\varepsilon_{j}^{p} \\ &= \varepsilon_{j}^{p} + (1-a_{j+1}) \cdot H_{1}^{j} \cdot H_{2}^{j} \cdot d\varepsilon_{j} \end{aligned} \tag{2.24}$$

10. Calculate current back stress.

$$b_{j+1} = b_{j} + (1-m) \cdot d\varepsilon_{j}^{p} \cdot \left(H_{0} - q \cdot \mathrm{sgn}(d\varepsilon_{j}^{p}) \cdot b_{j} \right) \tag{2.25}$$

11. Finally, the requested updated normal stress and elastoplastic modulus are given as:

$$\sigma_{j+1} = \sigma_{j} + E_{0} \cdot \left(\varepsilon_{j} - \varepsilon_{j}^{p} \right) \tag{2.26}$$

$$E_{p}^{j+1} = \left[1 - \left(1 - a_{j+1} \right) \cdot H_{i}^{j} \cdot H_{i}^{j} \right] \cdot E \tag{2.27}$$

As presented in the pseudo - code, the smoothing process permits the direct calculation of the final stress by simply linearizing the rate equations. This feature differentiates the algorithm from the standard return-mapping algorithm (Simo and Hughes 1998) where first an elastic trial stress predictor is obtained by freezing plastic flow and then a plastic stress corrector is applied to the trial stress mapping the trial stress to the actual stress.

2.2.5 Validation with experimental data

Various experiments for steel rebars under cyclic loading have been reported in the literature. For instance, experiments on steel rebars under cyclic response can be found in the work of Thompson and Park (1978). One of these experiments is presented in the following Figure 2.8 along with the predicted response of the proposed model. Steel grade is S275, while post to pre-yield ratio is considered as $a = 0.01$. Model parameters are presented in Table 2.2 to achieve satisfactory agreement with observed experimental behavior.

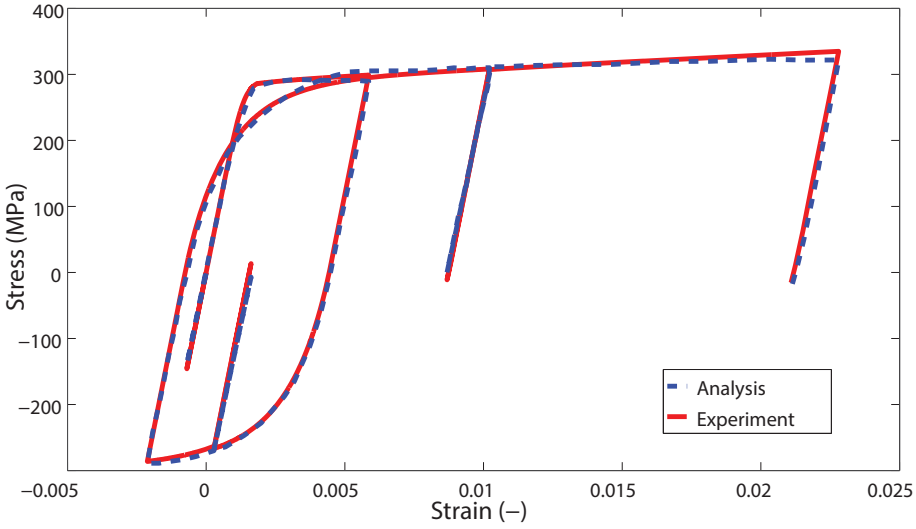

Figure 2.8. Comparison with experiment (Thompson and Park 1978)

σ_y (MPa)	α	n_1	n_2	ε_{plat}	m	q
275	0.01	8	0.9	0	0	0

Table 2.2. Model parameters for rebar analysis with Thompson and Park experimental data

In addition, the proposed model is verified with experiments on 19mm rebars performed by Ma et al. (1976). Both tests were performed on the same specimen but with different strain histories applied. Model parameters are presented in Table 2.3, while in Figure 2.9 the comparison between analysis and experimental test results are presented. The proposed model is proved sufficient enough to capture all phases of inelastic cyclic behavior, namely yield plateau, nonlinear hardening, isotropic hardening and Bauschinger effect.

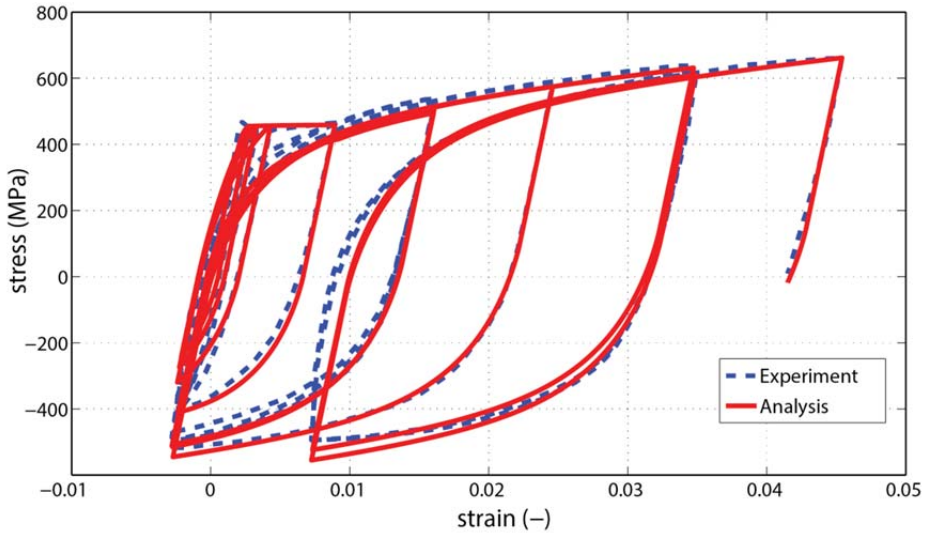

(a)

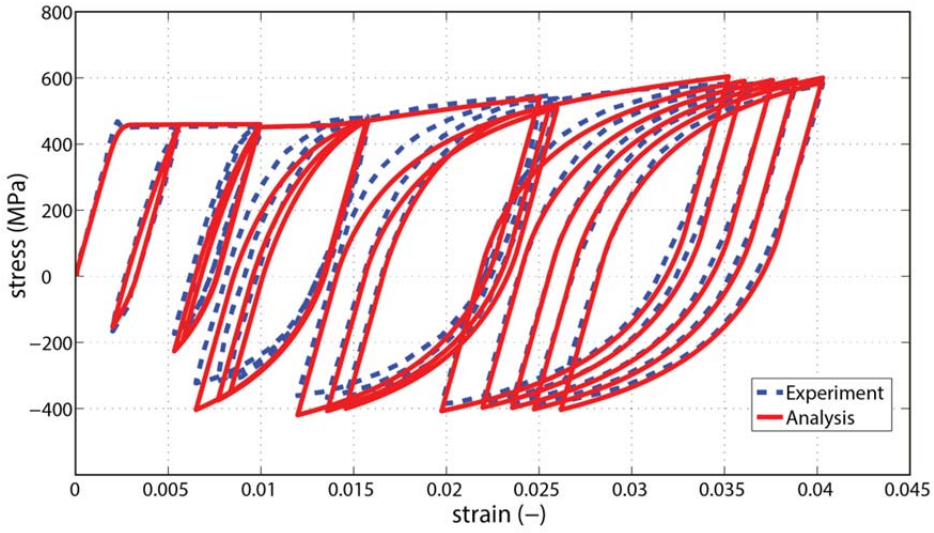

(b)

Figure 2.9. Comparison with experimental data of Ma et al. (a) Specimen 3 (b) Specimen 2

σ_y (MPa)	α	n_1	n_2	ε_{plat}	m	q
460	0.035	10	0.5	$4\varepsilon_y$	0.03	10

Table 2.3: Model parameters for rebar analysis with Ma Et al. experimental data

2.2.6 Nonlinear hardening investigation

In the standard formulation of the uniaxial steel model the Armstrong-Frederick nonlinear kinematic hardening model was used. However, Armstrong-Frederick model has a hidden deficiency as it undershoots the actual stress-plastic strain curve during unloading/reloading from the plastic region (Dafalias 1984). To address this deficiency Chaboche et al. (1979) introduced the additive decomposition rule of the back stress as follows:

$$b = \sum_{i=1}^{M=3} b_i \tag{2.28}$$

where, each component b_i of the back stress obeys the Armstrong-Frederick model with individual parameters $H_{0,i}$ and q_i for the initial hardening ratio and the parameter which controls the steepness of the post-elastic curve respectively.

$$\dot{b}_i = H_{0,i} \cdot \dot{\varepsilon}^p - q_i \cdot \left|\dot{\varepsilon}^p\right| \cdot b_i = q_i \cdot \dot{\varepsilon}^{pl} \cdot \left[\frac{H_{0,i}}{q_i} - \mathrm{sgn}(\dot{\varepsilon}^{pl}) \cdot b_i\right] \tag{2.29}$$

The second term in equation (2.29) is known as the dynamic recovery term which gradually reduces the rate of the evolution of the back stress until it reaches zero values and

the post yield stress-strain curve becomes horizontal (saturation level). By increasing the material parameters of the hardening rule, the Chaboche model is able to simulate a more accurate prediction of ratcheting than the AF model. However, numerical examples indicate that the model is still not suitable to simulate the partial reverse loading/reloading and ratcheting effect (Rezaiee-Pajand and Sinaie 2009). For this reason, Chaboche (1991) further introduced a threshold for the dynamic recovery term, below which it induces a linear response according to a rate equation for the back stress term that in the uniaxial case is written as:

$$\dot{b}_4 = q_4 \cdot \dot{\varepsilon}^{pl} \cdot \left[\frac{H_{0,4}}{q_4} - \text{sgn}(\dot{\varepsilon}^{pl}) \cdot \text{sgn}\left(b_4\right) \cdot \left\langle \left| b_4 \right| - \bar{b} \right\rangle \right] \tag{2.30}$$

where the $\langle\ \rangle$ symbol are the Macauley brackets and $\bar{b}$ is the threshold value for the 4th back stress term, meaning that when $\left|b_4\right|$ is smaller than the threshold variable then the 4th back stress term is evolving linearly, while when it exceeds the threshold an AF rule is activated. It is shown in Bari and Hassan (2000) that when the threshold value is imposed for the 4th term both the partial reverse loading/reloading and the ratcheting improve considerably in comparison not only with a three component decomposition, but also in comparison with the standard four back stress decomposition of the AF type without the concept of the threshold applied to any one of them. The same authors attribute this beneficial effect of the threshold scheme as a result of the combination of linear (at the beginning) and nonlinear (afterwards) evolution of the back stress that allows for a stiff response soon after yield point followed by a smoothly gradual saturation process when the nonlinear part is activated.

The three aforementioned nonlinear hardening models are incorporated in the proposed steel model and their contribution is examined with the experimental data of Ma et al. (1976). The experiment was conducted in terms of imposed strains and consists of an unloading/reloading loop far in the post-yield region and near the saturation level. As it is illustrated in Figure 2.10 the correlation with the experimental curve is improved when the more refined nonlinear hardening models, that treat better the dynamic recovery terms, are used.

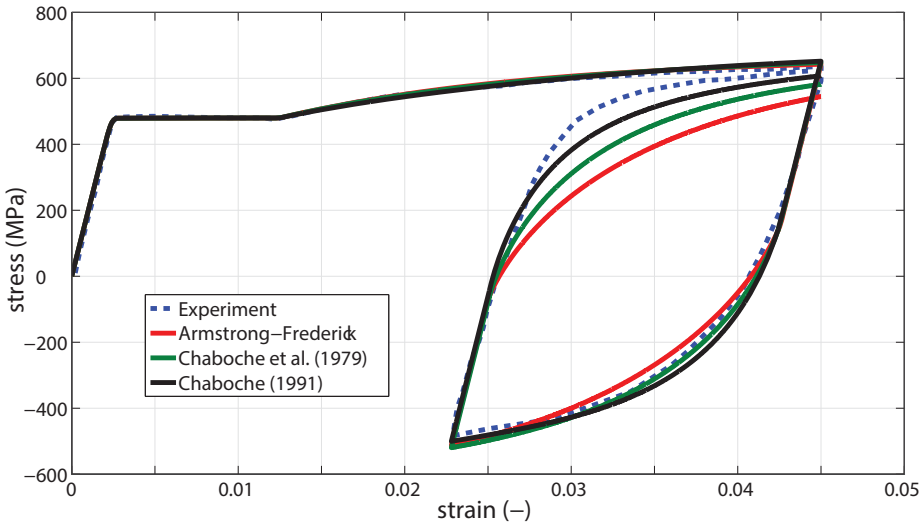

Figure 2.10: Influence of various nonlinear hardening models in the proposed formulation. Comparison with experimental data from Ma et al.

In the analysis, yield stress is σ_y=480 MPa, n_1=20, ε_{plat}=4.2, while no isotropic hardening was considered. For the Armstrong Frederic model n_2 parameter was set to 0.3 and initial hardening ratio and hardening parameter are α_0=0.06 and q=70 respectively. For the Chaboche et al. (1976) three component model n_2=0.4 and model parameters are $\alpha_{0,1}$=0.04, $\alpha_{0,2}$=0.02, $\alpha_{0,3}$=0.004, q_1=100, q_2=30, q_3=1. Finally for the Chaboche (1991) model the respective parameters are $\alpha_{0,1}$=0.03, $\alpha_{0,2}$=0.009, $\alpha_{0,3}$=0.003, $\alpha_{0,4}$=0.0015, q_1=100, q_2=30, q_3=1, q_4=50 while threshold parameters is $\bar{b} = 0.1 \cdot \sigma_{y0} = 48\ MPa$.

Extending this behavior, even more sophisticated models can be emended in the proposed model with similar manner. For example, the model by Henshall et al. (1987) is addressing the dynamic recovery term with a nonlinear power dependence on the back stress, while model by Ohno and Wang (1993) introduces the nonlinear power dependence on non-hardening region. Similarly, Dafalias et al. (2008) proposed the multiplicative AF kinematic hardening rule for the 4th back stress component, while the one of the other 3 components is set to exhibit almost linear response close to the Prager model.

However, even if the accuracy of the proposed model is increased, this happens on the expense of more model parameters, i.e. for the Chaboche (1991) model 8 back stress parameters plus one threshold variable are needed. Not considering the usability of the rebar model, the main purpose of the sophisticated hardening models is to capture ratcheting which is not expected to be critical in earthquake engineering applications of RC

members as other failure phenomena for longitudinal rebars are critical, like inelastic buckling and low cycle fatigue. For these reasons only the Armstrong Frederic model is utilized in the proposed model in the following chapters.

2.2.7 A special case: linear kinematic hardening

A common assumption concerning steel cyclic behavior is the adoption of linear kinematic hardening. This is the case where the stress strain curve becomes bilinear with constant post to pre-yield stiffness ratio a .

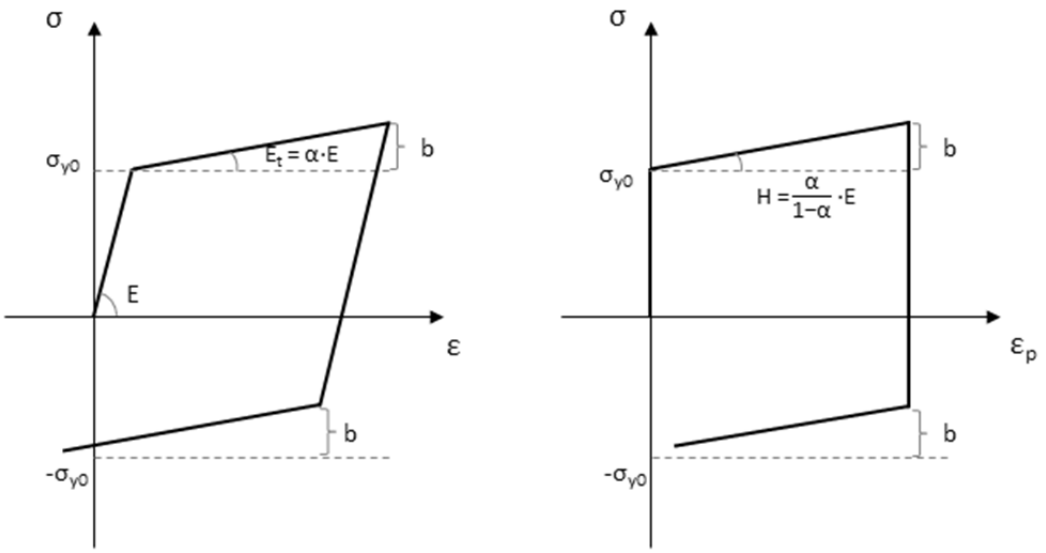

(a) (b)

Figure 2.11. Uniaxial bilinear constitutive law in terms of a) total strain and b) plastic strain

In such case internal parameter r becomes constant and equal to σ_{y0}. Hence, yield function is simplified to:

$$\Phi(\sigma, b, r) = |\sigma - b| - \sigma_{y0} \leq 0 \tag{2.31}$$

In addition, the consistency condition is now given as:

$$\dot{\lambda} \cdot \dot{\Phi}(\sigma, b, \sigma_{y0}) = 0 \Rightarrow \dot{\Phi}(\sigma, b, \sigma_{y0}) = 0 \Rightarrow \dot{\sigma} = \dot{b} \tag{2.32}$$

meaning, that the rate of the back stress is equal to the rate of the total normal stress. Taking into account equation (2.32) the following equation is obtained for the evolution of back stress :

$$\dot{b} = H_0 \cdot \dot{\varepsilon}^p = H_0 \cdot \dot{\lambda} \cdot sgn(\sigma - b) \tag{2.33}$$

Equivalently, the back stress *b* can be algebraically expressed as the mean of current yield stress in tension σ_y^+ and compression σ_y^-:

$$b=\frac{1}{2}\left(\sigma_y^+ +\sigma_y^-\right)=\alpha\cdot\left(E\cdot\varepsilon-\sigma_{y0}\right) \tag{2.34}$$

Taking into account equations (2.31) and (2.34), the yield function can be expressed as follows:

$$\Phi=\left|\frac{\sigma-\alpha\cdot(E\cdot\varepsilon-\sigma_{y0})}{\sigma_{y0}}\right|\le 1 \tag{2.35}$$

Consequently, smoothening Heaviside function H_1 is expressed as:

$$H_1\approx\left|\frac{\sigma-\alpha\cdot(E\cdot\varepsilon-\sigma_{y0})}{\sigma_{y0}}\right|^n=\left|\frac{\sigma-\alpha\cdot E\cdot\varepsilon}{(1-\alpha)\cdot\sigma_{y0}}\right|^n \tag{2.36}$$

while loading/unloading smoothening function remains the same with equation (2.17)

The gain of linear kinematic hardening formulation is that the constitutive law is expressed as a single differential equation which is solved rapidly with a simple backward Euler technique. However, steel models with linear hardening underestimate initial inelastic stages while also they may exaggerate significantly strength capacity of RC members near collapse as large axial strains may develop. For this reason, moderate hardening ratios are advised to be used.

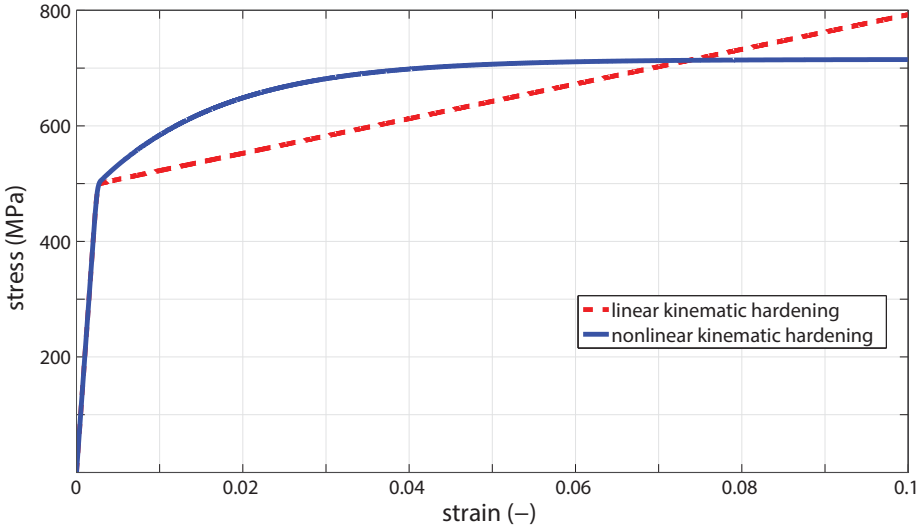

Figure 2.12: Comparison between linear and nonlinear kinematic hardening

2.2.8 Comparison with existing well-known models

In this section two well established and commonly used models are briefly described and their comparison with the proposed formulation is presented. These models are used nowadays in many structural engineering projects and are incorporated in scientific and commercial software packages (OpenSees, Seismostruct).

First, comparison is performed in terms of the well-documented and frequently used Menegotto-Pinto model. Many steel models proposed thereafter are based on the Menegotto-Pinto equations (Chang and Mander 1994; Balan et al. 1998; Hoehler and Stanton 2006; Kunnath et al. 2009). Also, another very common steel model is the Monti-Nuti (1992) which is based on the Menegotto-Pinto model but also incorporates relations to describe inelastic buckling in the compression range. An important drawback of the Menegotto-Pinto model is the inherent overshooting in the reloading curve when short reversals occur. This overshooting originates from its restricted memory as underlined by Filippou et al. (1983), as it doesn't keep in memory all preceding cycles. Kunnath et al. (2009) tried to address this issue by keeping in memory an arbitrary number of reversals, concluding that 16 reversals need to be stored to obtain adequate results, increasing significantly the bookkeeping of the problem. Also, Hoehler and Stanton (2006) tried to fix the overshooting problem by keeping in memory 2 additional points in the stress-strain curve. However, as explained by the authors this solution results in a relaxation phenomenon of the model and does not ensure its validity. In the case of the Monti-Nuti model Fragiadakis et al. (2007) tackled the overshooting problem by adding an additional memory rule, forcing the stress-strain curve to join tangentially the branch defined during the previous strain reversal.

On the other hand the proposed model imposes no restriction on memory returning exactly on the previous loading path. Hence it produces stable loops under short reversals which occur very often in seismic analysis with real or artificial ground motions.

To illustrate the performance of the proposed model, a direct comparison with the Menegotto-Pinto model is performed. For both models an external strain history presented in Table 2.4 is applied and model parameters are selected in such way as to induce similar outcome. More specifically, material modulus is $E=210\ GPa$, yield stress $\sigma_{y0}=235\ MPa$, post-yield to pre-yield ratio $a=0.02$, while for the proposed model the initial exponent is $n_1=10$ and the final exponent is $n_2=0.2$. The parameters of Menegotto-Pinto model are considered as: $R_0=20$, $cR_1=18.5$, $cR_2=0.1$, $a_3=0$, $a_4=1$.

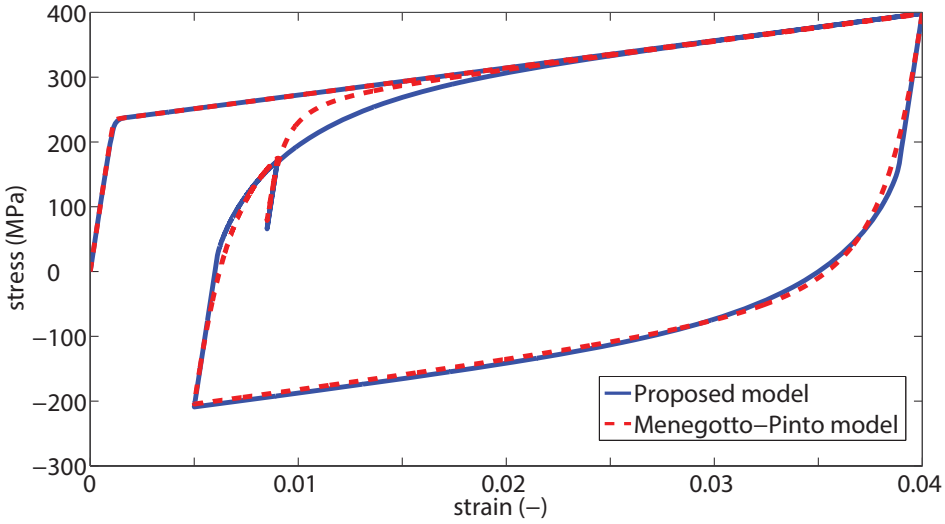

Figure 2.13. Comparison between the proposed and Menegotto-Pinto model

Pseudo-Time (sec)	Strain (-)
0	0
1	0.04
2	0.005
3	0.009
4	0.0085
5	0.04

Table 2.4: Strain history for comparison with Menegotto-Pinto model

In Figure 2.13 it is observed that the proposed model overcomes the overshooting of the Menegotto-Pinto model after the partial unloading branch.

The second well known steel model was proposed by Dodd and Restrepo-Posada (1995) who tried to address the issue of short reversals by distinguishing reversals as major, minor and simple. The model approaches Baussinger effect iteratively, hence it is perplexing, leading to instability issues. Very recently, Kim and Koutromanos (2016) have proposed a modification in the original model, where a non-iterative description for the reversal branches using b-splines is added. Another drawback of the original model is its inaccuracy in describing Bauschinger effect in steel specimens with low carbon context. As it was shown experimentally by Bate and Wilson (1986) low carbon steel rebars manifest steeper while high carbon steel rebars manifest smoother reversal branches. However, the Dodd-Restrepo model doesn't control the smoothness of the transition Bauschinger curve, hence it fails to simulate all types of reversals. On the other hand the proposed model, through parameter

n_2 controls the shape of the Bauschinger effect and presents no restriction in the steel grade. In Figure 2.14 it is shown that the proposed model, for the applied strain history of Table 2.5, is able to capture almost the same post-elastic curve with the Dodd and Restrepo-Posada model, while it has the capability to adjust the smoothness of the Bauschinger transition branch.

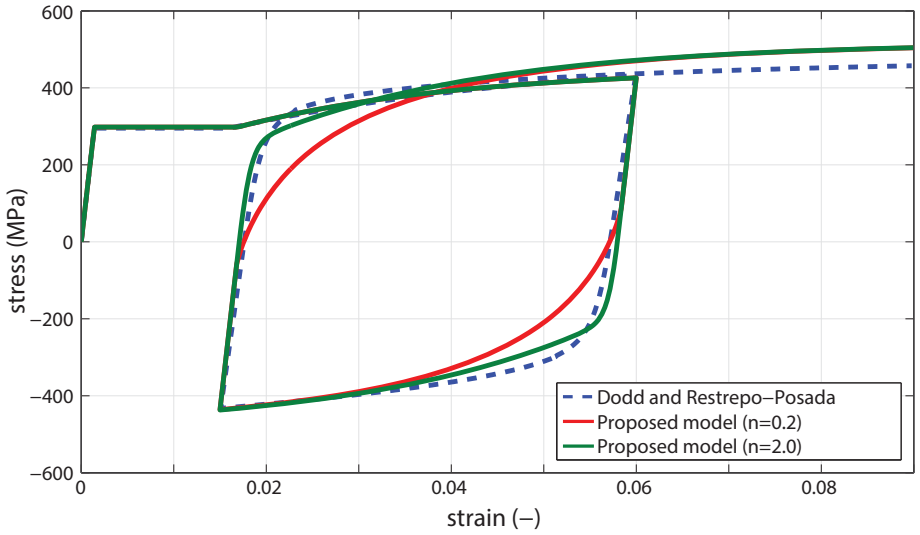

Figure 2.14. Comparison between the proposed and Dodd and Restrepo-Posada model

Pseudo-Time (sec)	Strain (-)
0	0
1	0.06
2	0.015
3	0.09

Table 2.5. Strain history for comparison with Dodd and Restrepo-Posada model

2.3 Buckling of longitudinal rebars

2.3.1 Single rebar model

Rebars in RC columns buckle generally with two different modes, local buckling between two adjacent ties-stirrups and global buckling in a length where one or more ties have yielded or failed due to the lateral deformation of the longitudinal rebar. In this work, only local buckling is addressed considering the assumption that transverse ties are practically rigid and sufficiently anchored in the core. Hence a single longitudinal bar is modeled as fixed end beam under axial force (Figure 2.15). According to Euler elastic buckling theory, that bar deflects laterally following a cosine curve:

$$y(x)=\frac{e}{2}\cdot\left(1-\cos\left(\frac{2\pi x}{L}\right)\right) \tag{2.37}$$

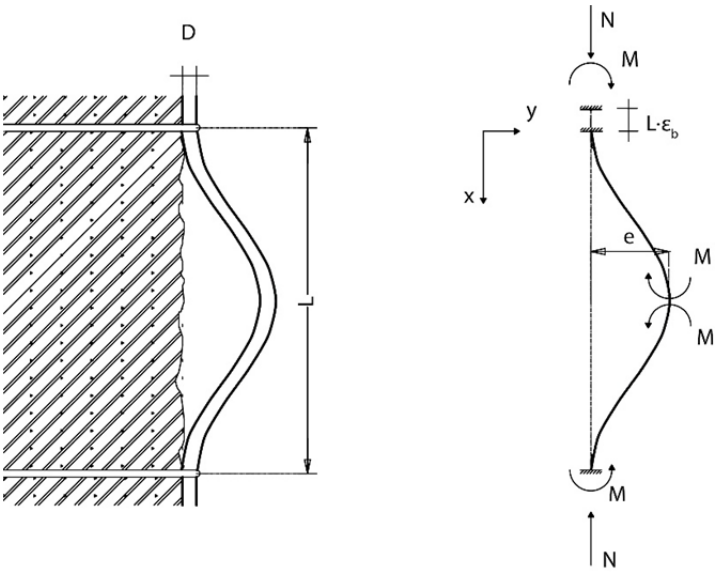

Figure 2.15. Local buckling physical and computational model

Curvature along bar's length $\varphi(x)$ is derived by double differentiation of the displacement field as:

$$\varphi(x)=\frac{2e\pi^2}{L^2}\cdot\cos\left(\frac{2\pi x}{L}\right) \tag{2.38}$$

with maximum mid-length value:

$$\varphi(L/2)=\frac{2e\pi^2}{L^2} \tag{2.39}$$

Total average axial strain ε_{av} of the bar can be decomposed into the sum of the strain ε_0 participating at the internal elastic strain energy of the bar and the buckling strain ε_b caused by the additional shortening of the bar due to lateral deflection:

$$\varepsilon_{av}=\varepsilon_0+\varepsilon_b \tag{2.40}$$

The arc length of the deformed bar can be calculated analytically by the relation proposed by Dhakal and Maekawa (2002) as:

$$L=\int_0^{L(1-\varepsilon_b)}\sqrt{1+\left(\frac{dy}{dz}\right)^2}\,dx=2\cdot\int_0^{L\frac{(1-\varepsilon_b)}{2}}\sqrt{1+\left(\frac{e\pi}{L(1-\varepsilon_b)}\sin\frac{2\pi x}{L(1-\varepsilon_b)}\right)^2}\,dx \tag{2.41}$$

By expanding the square root term in relation (2.41) in Taylor series about *0* and neglecting higher order terms, the following relation for secondary buckling strain is derived:

$$\varepsilon_b = \frac{1}{2}\left(1-\sqrt{1-e^2\pi^2}\right) \tag{2.42}$$

2.3.2 Pseudo-code for rebar buckling model

For the numerical analysis of the buckling problem, rebar section is first discretized in layers, each one represented by the uniaxial steel constitutive law developed is chapter 2.2. Then, the rebar under cyclic axial load subjected to buckling is analyzed incrementally by imposing axial average strains. At any computational increment the following steps are performed:

1. At any given converged step lateral deflection e^i, curvature φ^i, rebar axial force N^i, moment M^i and stiffness $K_{reb}{}^i$ (2x2) are known. For the new step iterations proceed as follows:
2. Updated buckling strain ε_b^i, which is derived from relation (2.42).
3. Material strain ε_0^i is calculated from relation (2.40) and the strain increment is considered: $d\varepsilon_0^i = \varepsilon_0^i - \varepsilon_0^{i-1}$
4. Incremental curvatures at mid-length are calculated from cross-sectional equilibrium equation:

$$d\varphi^i = \frac{dM^i - K_{reb,21}^i \cdot d\varepsilon_0^i}{K_{reb,22}^i} \tag{2.43}$$

5. Updated mid-length deflection is calculated according to relation (2.39):

$$e^i = e^{i-1} + \frac{d\varphi^i \cdot L^2}{2\pi^2} \tag{2.44}$$

6. Total material ε_l^i and incremental $d\varepsilon_l^i$ strains at rebar layers are derived from strain compatibility and respective stresses are calculated by proposed steel model of section 2.
7. Centerline axial force N^{i+1}, moment M^{i+1} and rebar stiffness $K_{reb}{}^{i+1}$ are derived according to layered section analysis.
8. Equilibrium in the deformed configuration gives the residual moment error:

$$dM^i = \frac{N^i \cdot e^i}{2} - M^i \tag{2.45}$$

9. Steps 1-8 are repeated until equilibrium error is lower than a tolerance value: dMi < tol

2.3.3 Comparison with corotational formulation

For the geometrically nonlinear analysis of beam elements the corotational formulation (De Borst et al. 2012) is typically used. This approach is valid for large displacements small deformation problems and permits the use of the same material stress-strain laws used for geometrically linear problems. However, to capture the post-buckling response, rebar should be discretized in a number of elements, making this method computationally prohibitively costly for the buckling analysis of the embedded rebars.

For comparison with the proposed formulation a rebar of D=25mm is considered with L/D ratio L/D=8 and is excited with the imposed displacement history as presented Table 2.6:

Pseudo-time (sec)	**Axial displacement (m)**
0	0
1	-0.002
2	0.002
3	-0.004
4	0.004
5	0.006
6	-0.006
7	0.008
8	-0.008

Table 2.6. Axial displacement history for inelastic rebar analysis

A bilinear stress-strain law is assumed for steel material with yield stress σ_y*=500 MPa* by setting *q, m,* ε_{plat} parameters equals to zero. The hysteretic loops obtained with both methods are compared in Figure 2.16

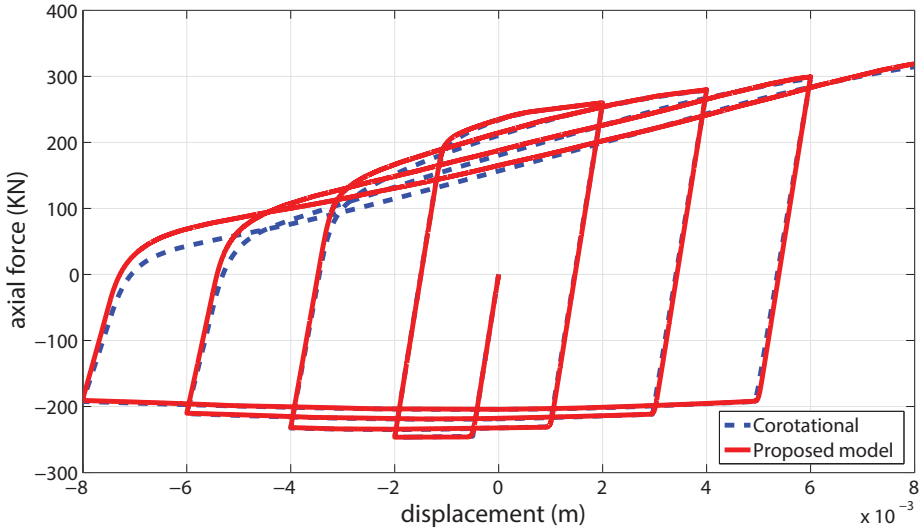

Figure 2.16. Axial force vs axial displacement comparison between the proposed model and corotational formulation

Generally, the proposed formulation is proved adequate to reproduce the same response with the more accurate corotational formulation except from the unloading path at the compressive field. However, the reduction in the computational cost is orders of magnitude lower. Thus considering also the multiple longitudinal rebars at a cross-section, the proposed semi-analytical, semi-numerical method is considered appropriate.

Moreover, in Figure 2.17 the comparison between mid-length lateral displacements of both methods is presented. The difference at the results is attributed to the fact that displacements calculated from the proposed method are due to material deformation only excluding the secondary geometrical nonlinear term. This is indeed the basic concept of the methodology as geometrically nonlinear effects are excluded from total average strain via the buckling strain ε_b from relation (2.42).

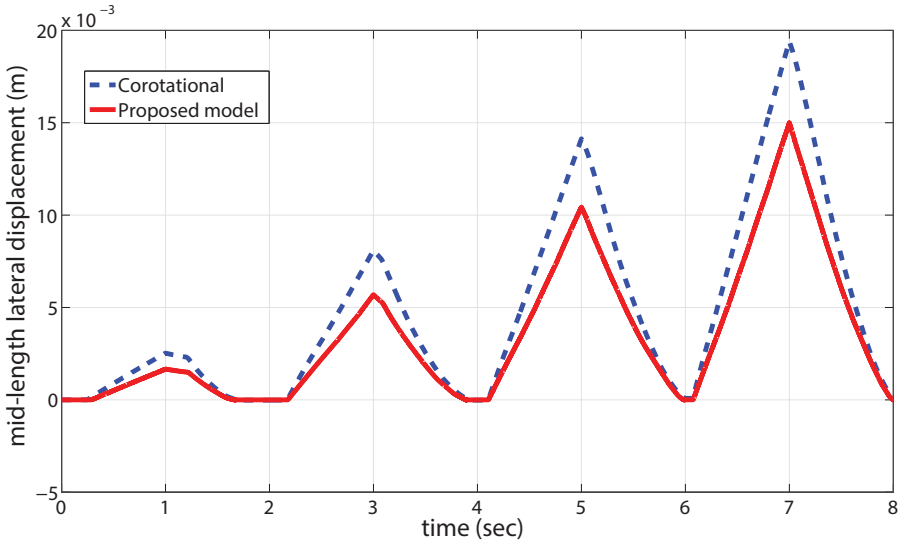

Figure 2.17. Mid-length lateral displacement comparison between the proposed model and corotational formulation

2.3.4 Verification with experimental data

Verification of the proposed cyclic buckling model is also performed with the experiments conducted by Monti and Nuti (1992). In this comparison the S-series rebar experiments are selected, which refer to symmetrical strain histories ranging from (-0.03-0.03). Three different length to diameter (L/D) ratios are tested with model parameters as presented in Table 2.7. Results in Figure 2.18 reveal the capability of the proposed model to capture actual stress-strain behavior at different L/D ratios. It is evident from the results that buckling causes the contraction of hysteretic loops in compression, which for higher levels of buckling length, this contraction is so abrupt that softening of the stress-strain curve is observed.

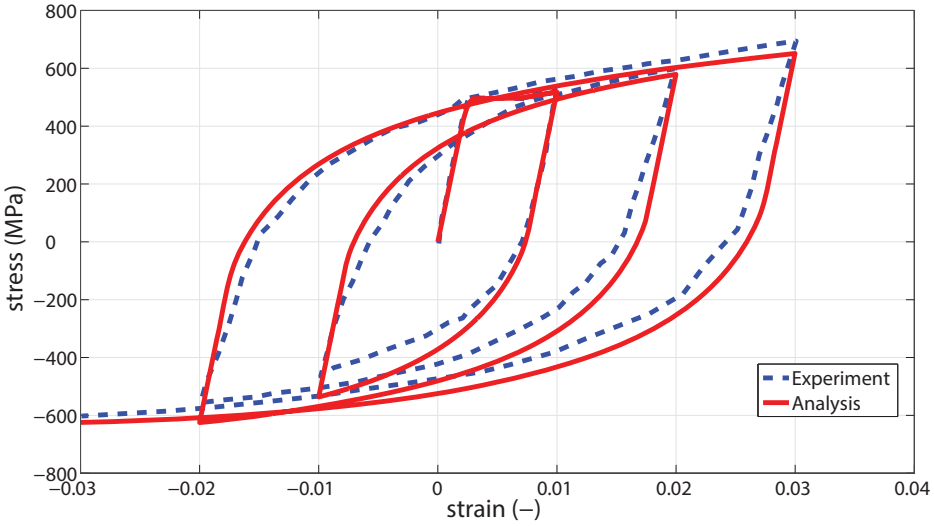
800
600
400
200
0
−200
−400
−600
−800
stress (MPa)
−0.03
−0.02
−0.01
0
0.01
0.02
0.03
0.04
strain (–)
Experiment
Analysis

(a)

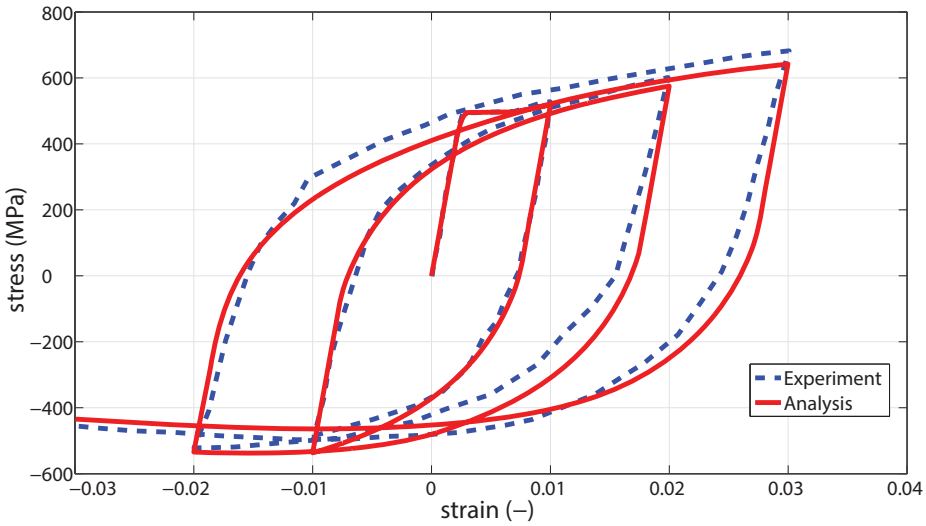
800
600
400
200
0
−200
−400
−600
stress (MPa)
−0.03
−0.02
−0.01
0
0.01
0.02
0.03
0.04
strain (–)
Experiment
Analysis

(b)

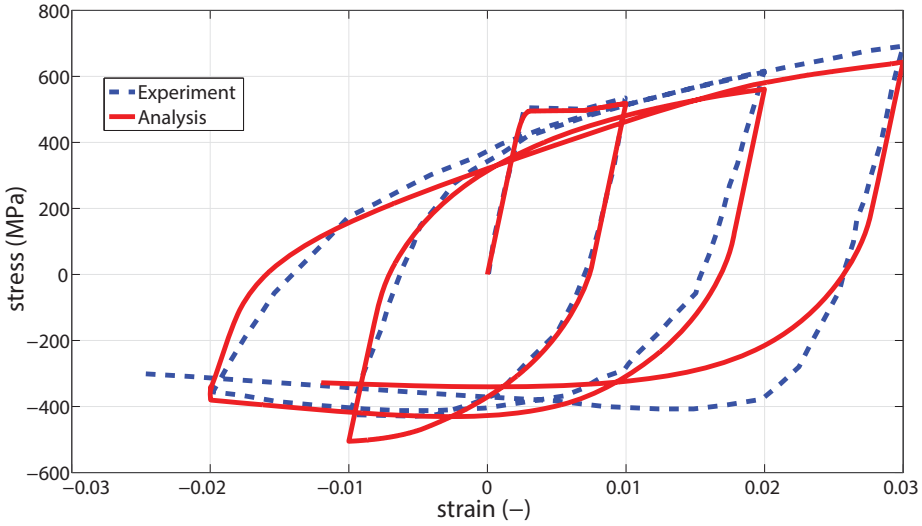

(c)

Figure 2.18. Comparison with experimental data S-series of Monti and Nuti: (a) L/D=5, (b) L/D=8, (c) L/D=11

σ_y (MPa)	α	n_1	n_2	ε_{plat}	m	q
500	0.035	10	0.3	$1.8\varepsilon_y$	0.05	10

Table 2.7. Steel model parameters for Monti and Nuti S-series experimental data

Similarly, the proposed model is verified with the C-series tests of Monti and Nuti (1992) referring to unsymmetrical loading tests. In these tests, slenderness ratio is kept constant and equal to L/D=11, while steel material has slightly different properties. First, in Figure 2.19 steel yield stress is 470 MPa and related model parameters are presented in Table 2.8.

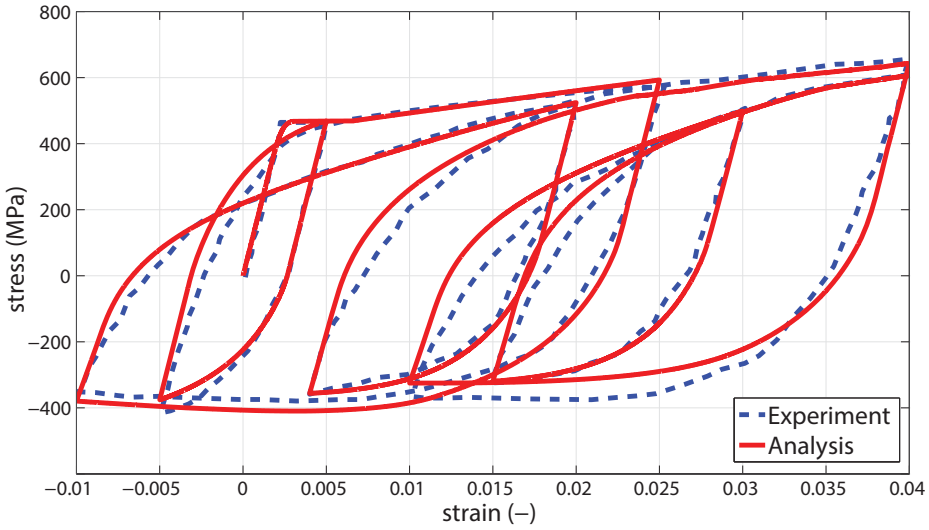

(a)

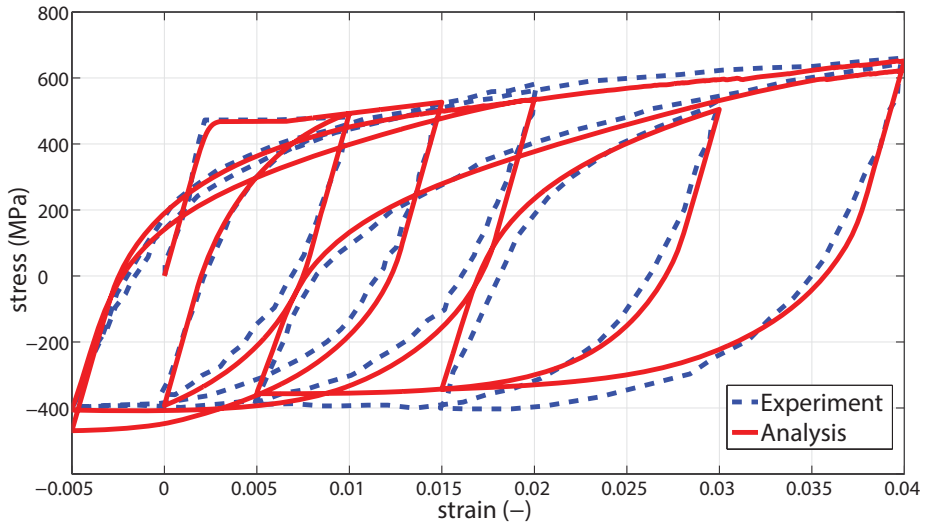

(b)

Figure 2.19. Comparison with experimental data of Monti and Nuti (C1, C2 specimens, L/d=11)

σ_y (MPa)	α	n_1	n_2	ε_{plat}	m	q
470	0.035	10	0.4	$1.8\varepsilon_y$	0.05	5

Table 2.8. Steel model parameters for Monti and Nuti experimental data (C1, C2 specimens)

Finally, the last comparison between proposed model and experimental results is presented in Figure 2.20, while material parameters can be found in Table 2.9. In all figures

there is satisfactory correlation between analysis and experimental results proving the efficiency of the proposed model.

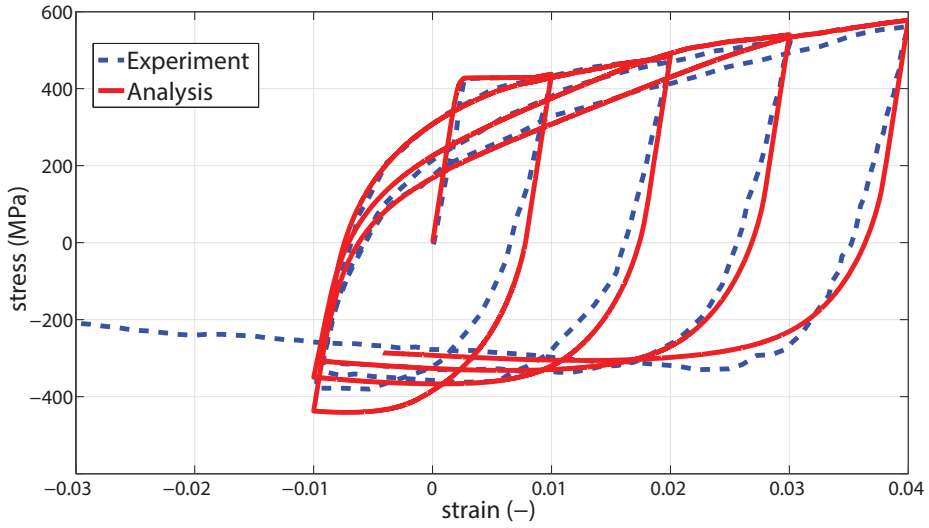

Figure 2.20. Comparison with experimental data of Monti and Nuti (C5 specimen, L/d=11)

σ_y (MPa)	α	n_1	n_2	ε_{plat}	m	q
430	0.03	10	0.4	$3\varepsilon_y$	0.05	10

Table 2.9. Steel model parameters for Monti and Nuti experimental data (C5 specimens)

Moreover, numerical results of the proposed model capture successfully the so-called tension-based buckling mechanism of Moyer and Kowalsky (2003). They observed the influence of tension strains on the eventual buckling of longitudinal bars and described a tension-based buckling mechanism which is summarized with 3 distinct phases. First, buckling of reinforcement rebars requires loading reversals with significant tensile strains. Then, the accumulation of tensile strains over multiple loading cycles impacts longitudinal bar buckling which eventually occurs under compression.

2.4 Appendix I

2.4.1 Menegotto-Pinto model

The Menegotto-Pinto model consists of an explicit algebraic equation of the form $\sigma = f(\varepsilon)$, which holds for the loading phase between two reversal points, while model's parameters are updated after each reversal point. The model was originally proposed by Giuffre and Pinto and implemented later by Menegotto and Pinto (1973). The main characteristic is its numerical efficiency, while the agreement with experimental results from cyclic tests on reinforcing steel bars is satisfactory. The model, as presented by Menegotto and Pinto (1973), takes the form:

$$\sigma^* = b\varepsilon^* + \frac{(1-b)\varepsilon^*}{\left(1+\left|\varepsilon^*\right|^R\right)^{1/R}} \tag{2.46}$$

where

$$\varepsilon^* = \frac{\varepsilon - \varepsilon_r^n}{\varepsilon_y^{n+1} - \varepsilon_r^n},\ \ \sigma^* = \frac{\sigma - \sigma_r^n}{\sigma_y^{n+1} - \sigma_r^n} \tag{2.47}$$

This relation describes a transition between two asymptotes, one with slope E_{s0} and one with $E_s = bE_{s0}$ as presented in Figure 2.21. Point $\left(\varepsilon_y^{n+1},\ \sigma_y^{n+1}\right)$ is the point where the two lines coincide and point $\left(\varepsilon_r^n,\ \sigma_r^n\right)$ refers to the last reversal point. The intersection point is derived from equations:

$$\begin{aligned} \varepsilon_y^n &= \frac{\sigma_{y0} - E_s \cdot \varepsilon_{y0} - \sigma_r + E_{s0} \cdot \varepsilon_r^n}{E_{s0} - E_s} \\ \sigma_y^n &= \sigma_{y0} + E_s\left(\varepsilon_y^n - \varepsilon_{y0}\right) \end{aligned} \tag{2.48}$$

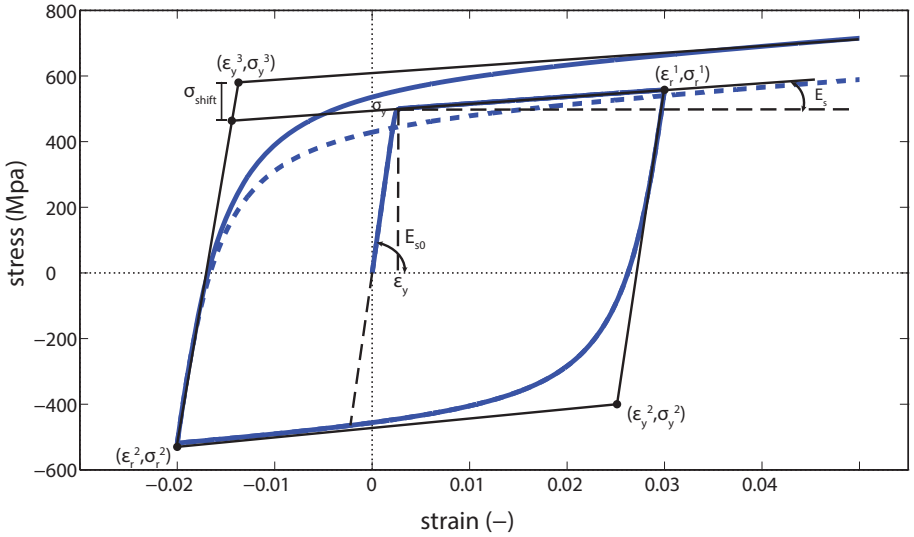

Figure 2.21: Menegotto-Pinto steel model

The plastic part of the total strain is given as:

$$\xi = \left| \frac{\varepsilon_{\max} - \varepsilon_y^n}{\varepsilon_{y0}} \right| \tag{2.49}$$

The transition curve between the two asymptotes is controlled by the expression:

$$R = R_0 \cdot \left(1 - \frac{cR_1 \cdot \xi}{cR_2 + \xi} \right) \tag{2.50}$$

Where R_0, cR_1, cR_1 are model parameters which control the representation of the Bauschinger effect through the transition curve.

In addition, Menegotto-Pinto model can describe isotropic steel softening according to the modification proposed be Filippou et al. (1983), where the hardening asymptote is shifted by the following expression:

$$\sigma_{shift} = \sigma_y^n \cdot a_3 \cdot \left(\frac{\varepsilon_{\max}}{\varepsilon_y^n} - a_4 \right) \tag{2.51}$$

where parameters a_3, a_4 are parameters which define the amount of isotropic hardening and the threshold where the phenomenon commences respectively.

2.4.2 Dodd and Restrepo-Posada model

Dodd and Restrepo-Posada model is expressed in terms of natural space coordinates in order to have the same envelope curve in tension and compression. The basic relations

between the natural stress-strain space and the commonly used engineering counterpart are the following:

$$\begin{aligned} \varepsilon^{'} &= \ln\left(1+\varepsilon\right) \\ \sigma^{'} &= \sigma\left(1+\varepsilon\right) \end{aligned} \tag{2.52}$$

The model distinguishes three regions, elastic loading, yield plateau and strain hardening. The strain-hardening envelope is based on the power curve suggested by Mander et al. (1984) and is given from the following relations:

$$\sigma^{'} = s\left[\sigma_{sh}^{'} + \sigma_{sh}^{'*}\left(\varepsilon_{su}^{'} + \varepsilon_{sh}^{'}\right) - \sigma_{su}^{'}\right]\left\{\frac{\varepsilon_{su}^{'} - s\left[\varepsilon_{s}^{'} - \varepsilon_{0}^{'}(k)\right]}{\varepsilon_{su}^{'} - \varepsilon_{sh}^{'}}\right\}^{P} - \sigma_{sh}^{'*}\left\{s\varepsilon_{su}^{'} - \left[\varepsilon_{s}^{'} - \varepsilon_{0}^{'}(k)\right]\right\} + s\sigma_{su}^{'} \tag{2.53}$$

$$P = \log\left[\frac{\sigma_{sh,1}^{'} + \sigma_{su}^{'*}\left(\varepsilon_{su}^{'} - \varepsilon_{sh,1}^{'}\right) - \sigma_{su}^{'}}{\sigma_{sh}^{'} + \sigma_{su}^{'*}\left(\varepsilon_{su}^{'} - \varepsilon_{sh}^{'}\right) - \sigma_{su}^{'}}\right] / \log\left(\frac{\varepsilon_{su}^{'} - \varepsilon_{sh,1}^{'}}{\varepsilon_{su}^{'} - \varepsilon_{sh}^{'}}\right) \tag{2.54}$$

As it is obvious from equations (2.53) and (2.54) the model includes seven parameters for the description of the post-yield monotonic stress-strain curve in natural coocrdinates, namely, the yield stress $\sigma_{sh}^{'}$, the strain at the onset of hardening $\varepsilon_{sh}^{'}$, the ultimate strength $\sigma_{su}^{'}$, the ultimate strain $\varepsilon_{su}^{'}$, and the stress $s_{sh,1}^{'}$ and strain $\varepsilon_{sh,1}^{'}$ for an intermediate point on the hardening branch of the curve, as shown in Figure 2.22. Also, the term $\varepsilon_{0}^{'}(k)$ is zero for monotonic loading, while its purpose is to shift the skeleton curve when unloading takes inside the yield plateau range.

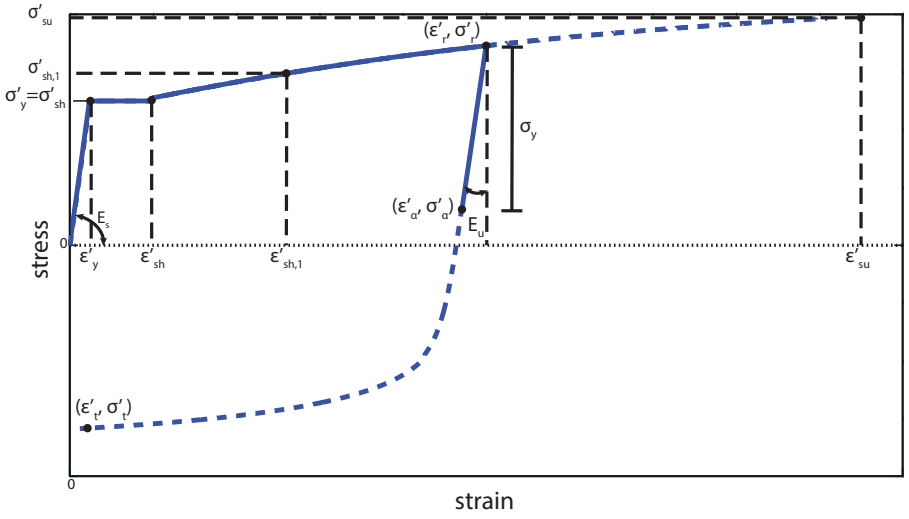

Figure 2.22: Dodd-Restrepo steel model

The unloading branch under cyclic loading conditions is initially linear elastic up to a point $\left(\varepsilon_{\alpha}^{'},\sigma_{\alpha}^{'}\right)$ with vertical length of σ_y with a slope E_u which is a percentage of the initial Young modulus according to the following equation:

$$E_u^{'} = E_s\left(0.82 + \frac{1}{5.55 + \varepsilon_{\max}^{'}}\right) \tag{2.55}$$

where $\varepsilon_{\max}^{'}$ is the maximum natural strain attained. Finally, Bauschinger effect is described by a softening curve extending from point $\left(\varepsilon_{\alpha}^{'},\sigma_{\alpha}^{'}\right)$ until target point $\left(\varepsilon_{t}^{'},\sigma_{t}^{'}\right)$

CHAPTER 3

Modeling Concrete Cyclic Behavior

3.1 Introduction

Modeling plain concrete behavior presents greater uncertainty in comparison with reinforcing steel due to the diversity of its composition. Concrete is a mixture of cement, water and aggregates of various grading, hence its macroscopic behavior is very sensitive to the microstructure. Generally, concrete compressive behavior depends on the formation and propagation of micro cracks inside its volume (Kotsovos and Newman 1977) which macroscopically is manifested as low ductility, nearly zero tensile strength, asymmetric hysteretic loops and brittle failure mechanism.

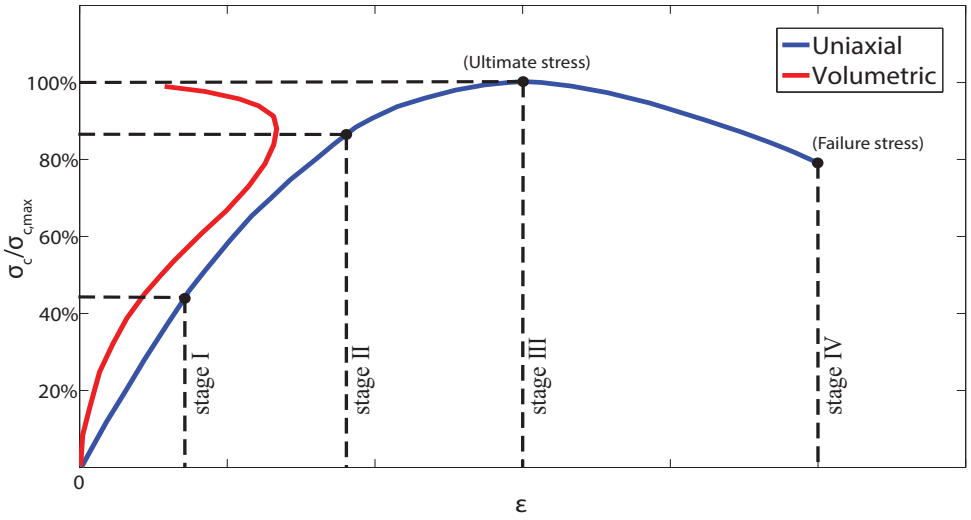

Figure 3.1 Behavior of concrete in monotonic compression (Chen 1982)

Stress-strain $\sigma_c - \varepsilon_c$ curve for plain normal weight concrete until failure is typically represented by four regions which are presented in Figure 3.1 and they are listed below (Chen 1982):

-Linear elastic region

-Stable fracture propagation

-Unstable fracture propagation

-Softening region until failure

The first initial loading stage reaches a loading level of 30-60% of the ultimate compressive strength. Macroscopically concrete material behaves linear elastic as micro cracks that are formed in its volume are not expanding (*stationary cracks*).

The second stage reaches a loading level of 70-90% of the ultimate strength. Cracks now expand and propagate deviating concrete macroscopic behavior from the linear elastic curve. Hence, a reduction in the material stiffness is observed which causes irrecoverable deformation in unloading. Void formation causes increase on the rate of tensile strains normally to the direction of crack propagation with respect to the rate of strains in the direction of branching (Kotsovos and Newman 1977). The start of such deformation behavior is called “onset of stable fracture propagation”.

The third stage expands until the ultimate compressive stress. During this stage, the micro cracks system inside the mortar merges to larger cracks at the surface of the nearby aggregates and form crack zones causing internal damage in the concrete material. The onset of this stage is called “onset of unstable fracture propagation”.

A fourth stage defines the region beyond the ultimate strength. In this softening region which is macroscopically manifested as negative stiffness, the energy released by the propagation of a crack is greater than the energy needed for propagation. The volume of voids increases dramatically causing a rapid dilation of the overall volume of concrete Therefore, the cracks become unstable and self-propagating until complete disruption where failure occurs.

Similarly, monotonic tensile behavior of plain concrete is presented in Figure 3.2. Generally, two distinct phases of monotonic tensile loading are distinguished:

-Linear elastic region

-Softening region

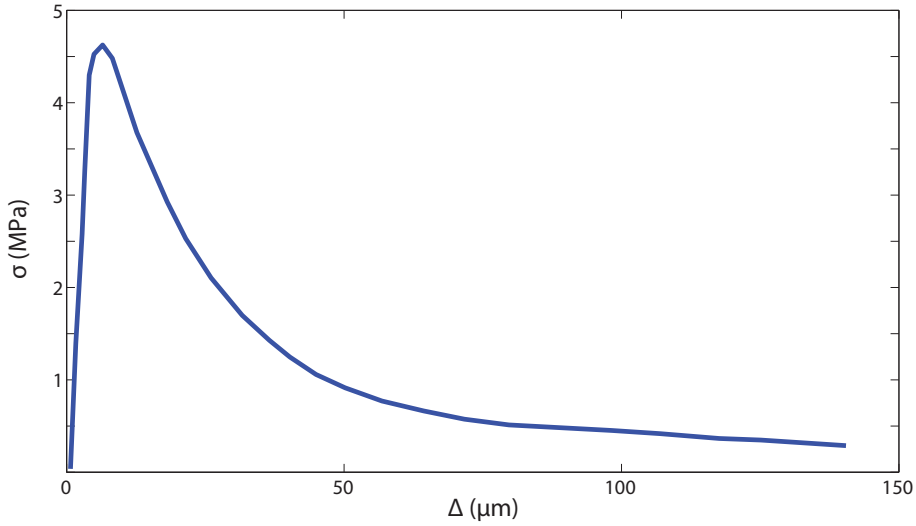

Figure 3.2. Behavior of concrete in monotonic tension (Peterson 1981)

In the end of the linear elastic segment, maximum tensile stress is significantly lower in magnitude than the respective maximum compressive strength. This is due to the significantly lower tensile strength of the aggregate-matrix interface than the matrix alone. Also, the tensile state of stress tends to open cracks much easier than the compressive state of stress, resulting in a more brittle behavior.

Most of the existing concrete numerical models result either from abstractions of well-designed experimental behavior, or theoretical considerations calibrated with experimental data. These are based on either continuous or discontinuous gradient damage and plasticity models (Alessi et al. 2015), as well as multiscale methods (Wu et al. 2014) utilizing also up to molecular dynamic simulations for special aspects of chemical nature (Buyukozturk et al. 2011). Within the phenomenological and macroscopic continuum theories, plasticity theory, continuum damage mechanics and fracture mechanics offer a solid background to address the main features of RC behavior in relatively compact form. The initial consideration of micro-cracks within the material volume that conglomerate into macro-cracks in a changing stress field is quantified on the macroscopic level in terms of internal state variables. More specifically, in isotropic damage mechanics micro-cracks are considered as uniformly distributed within the material and their density is quantified generally by a damage tensor (Kachanov 1986). The result of this process is manifested as degradation of material stiffness with damage mechanics describing the initiation and evolution of cracks growth, while sliding along the crack edges is usually modeled through plasticity theory (Ragueneau et al. 2000). Consequently, damage and plasticity should be taken into account combined in order

to accurately describe the behavior of quasi-brittle materials such as concrete (Lubliner et al. 1989).

On the other hand, a large category of models developed for engineering purposes is the empirical phenomenological category, based solely on analytical expressions developed by matching experimental data (Karsan and Jirsa 1969; Bahn and Hsu 1998; Aslani and Jowkarmeimandi 2012) with no explicit reference to the mechanisms that generate the resulting behavior. Bilinear, trilinear and multilinear models fall in this category, although from engineering perspective are attractive as they point to a piecewise linear behavior. Following the same concept also, analytical models for confined concrete behavior have been introduced (Scott et al. 1982; Mander et al. 1988).

Other models are based on plasticity considerations, mainly adopting nonassociated flow rule (Han and Chen 1985; Pietruszczaks et al. 1988; Hu and Schnobrich 1989) or viscoplasticity (Bicanic and Zienkiewicz 1983). These models use failure surfaces and can describe brittle-ductile transition followed by strain hardening, but generally fail to model damage and concrete compaction (Mazars and Millard 2009). Simple damage models developed for isotropic damage (Mazars 1981; Lemaitre and Chaboche 1985) model stiffness degradation and softening but they cannot describe concrete compaction and sliding. Their deficiencies led to the development of elastoplastic-damage models (Lubliner et al. 1989; Lee and Fenves 1998; Ragueneau et al. 2000; Grassl and Jirasec 2006; Jason et al. 2006; Richard et al. 2010; Ayhan et al. 2013) that utilize the concepts of plastic surface and damage surface interaction able to model yielding, softening as well as stiffness degradation.

Along these lines, a uniaxial smooth concrete model is developed, expressed in rate form combining plastic and damage behavior (Andriotis et al. 2015). The proposed model accounts for the unsymmetrical behavior in tension-compression loading, while addresses concrete features due to cyclic loading, such as nonlinear unloading and crack closure-opening phenomena. The main part refers to smooth damage modeling of concrete behavior developed herein as damage considerations have similar mathematical structure with classical plasticity.

3.2 Uniaxial concrete cyclic behavior

3.2.1 Plastic behavior

Concrete under low stress level exhibits linear elastic behavior but soon after the first cracks appear a nonlinear behavior with irreversible features both in strain and stiffness terms is established. Friction along crack edge prevents the crack from prolonged opening without resistance. In this process energy is dissipated and as a consequence hysteretic behavior is generated. This process is manifested macroscopically as elastoplastic behavior with a nonlinear isotropic hardening branch. Consequently, stress-strain constitutive relation in rate form due to plasticity is expressed according to the decomposition rule as:

$$\dot{\bar{\sigma}}_c = E_c \cdot \dot{\varepsilon}_c^{el} = E_c \cdot \left(\dot{\varepsilon}_c - \dot{\varepsilon}_c^{p} \right) \tag{3.1}$$

where $\bar{\sigma}_c$ is concrete's uniaxial effective (undamaged) stress $\varepsilon_c, \varepsilon_c^p$ are total and plastic axial strain respectively. Plastic strain is given at a compact form combining elastic loading/unloading and plastic phase (chapter 2.2.2)

$$\dot{\varepsilon}_c^{p} = H_{c1} \cdot H_{c2} \cdot (1 - \alpha_c) \cdot \dot{\varepsilon}_c \tag{3.2}$$

where $\alpha_{c,i}$ defines post-yield to pre-yield stiffness ratio and H_{c1}, H_{c2} are Heaviside-type functions acting as switches. More specifically H_{c2} controls loading/unloading condition (0: unloading, 1: loading) and is given as:

$$H_{c2} = 0.5 \cdot \left[1 + \mathrm{sgn}(\bar{\sigma}_c \cdot \dot{\varepsilon}_c) \right] \tag{3.3}$$

while H_{c1} controls yielding condition (0: plastic flow, 1: elastic loading), where in the case of isotropic hardening is expressed as:

$$H_{c1} = \left| \frac{\bar{\sigma}_c}{\sigma_{yc}} \right|^{n_c} \tag{3.4}$$

Parameter n_c controls the transition rate in the post-elastic regime, although generally there is no need for gradual transition, so parameter $n_c \geq 10$. Also, σ_{yc} is the current yield stress that evolves according to the following nonlinear isotropic hardening relation:

$$\dot{\sigma}_{yc} = H_{c1} \cdot H_{c2} \cdot \alpha_c \cdot \mathrm{sgn}(\bar{\sigma}_c) \cdot E_c \cdot \dot{\varepsilon}_c \tag{3.5}$$

Also, isotropic hardening modulus H_c reduces from the initial value H_{c0} in the plastic regime following relation:

$$H_c = H_{c0} - q_c\left(\sigma_{yc} - \sigma_{yc,0}\right) \tag{3.6}$$

where q_c is the nonlinear hardening term and $\sigma_{yc,0}$ is the initial yield stress. Considering relation (3.6) the current post to pre yield ratio α_c is defined as follows

$$a_c = \frac{E_{c,pl}}{E_c} = \frac{H_c}{H_c + E_c} = \frac{H_{c0} - q_C \cdot \left(\sigma_{yc} - \sigma_{yc0}\right)}{E_c + H_{c0} - q_c \cdot \left(\sigma_{yc} - \sigma_{yc0}\right)} \tag{3.7}$$

Finally, the rate of effective stress $\dot{\sigma}_c$ can be calculated with the use of relations (3.1), (3.2), (3.5) and (3.7) as

$$\dot{\bar{\sigma}}_c = \left(1 - (1-\alpha_c)\cdot H_{c1}\cdot H_{c2}\right)\cdot E_c \cdot \dot{\varepsilon}_c \tag{3.8}$$

The concrete behavior due to plasticity only is presented in the following Figure 3.3

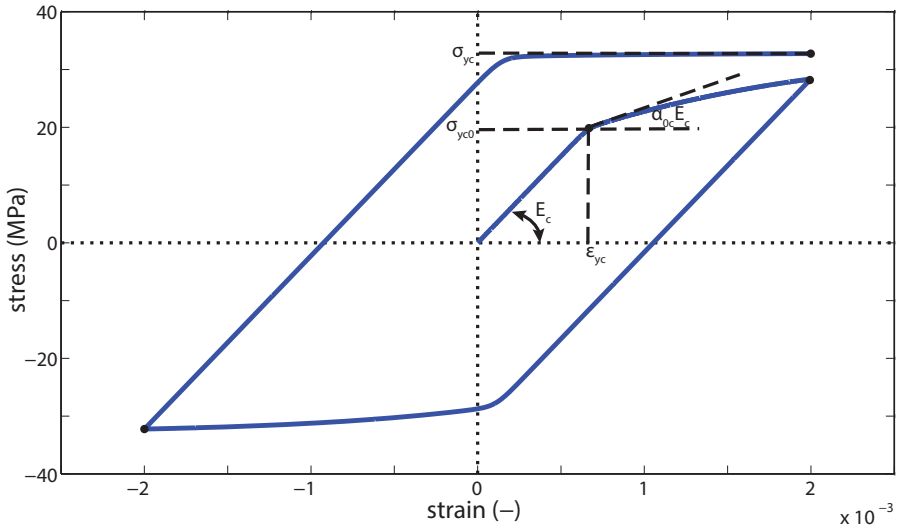

Figure 3.3. Plastic component considering nonlinear isotropic hardening

However, as it will be described in the following chapter (§3.2.2) tensile cracks open at lower stress level in tension. When unloading in tension permanent strains appear at zero stress level due to misfits at crack edges. Similar to compression, this behavior can be macroscopically described with plasticity theory, considering as yield point the stress where crack opening occurs. Moreover, different yield stress levels in tension and compression result in an asymmetry in hysteretic loop, while distinct yield stress is derived according to the following relation:

$$\sigma_{yc0,i} = \left(1 - H_{c3}\right)\cdot \sigma_{yc0}^{+} + H_{c3}\cdot \sigma_{yc0}^{-} \tag{3.9}$$

where σ_{yc0}^{+} is the initial yield stress in tension and σ_{yc0}^{-} the initial yield stress in compression. Heaviside-type term H_{c3} defines the state of tension/compression (0: tension, 1: compression) and is defined as follows:

$$H_{c3} = 0.5\left(1 - \mathrm{sgn}(\bar{\sigma}_c)\right) \tag{3.10}$$

The asymmetric cyclic behavior is presented in Figure 3.4 where different yield points are attributed in tension and compression respectively $\left(\sigma_{yc0}^{+} = 4\ MPa,\ \sigma_{yc0}^{-} = 20\ MPa\right)$. It should be noted that isotropic hardening effect is distinct and independent for every state, i.e. initial yield stress at compression is not affected from any previous yielding in tension.

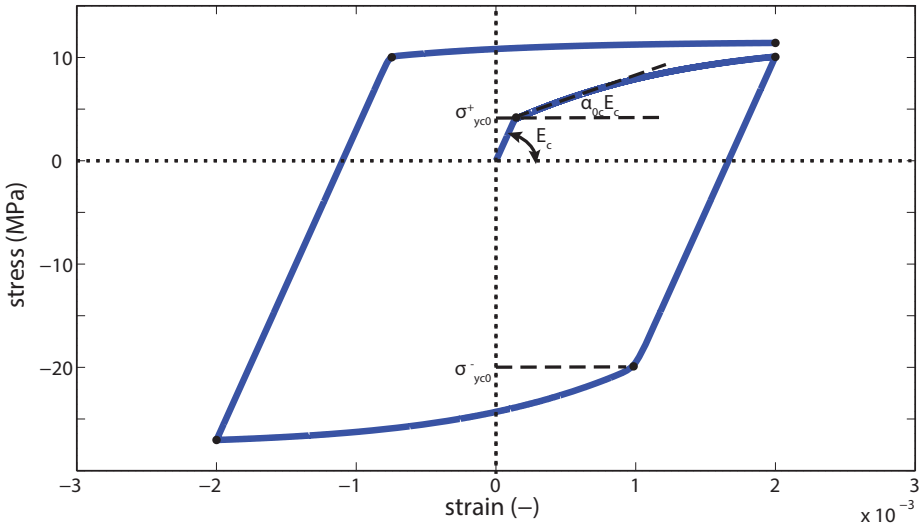

Figure 3.4. Plastic component considering asymmetric yield stress

3.2.2 Damage behavior

Soon after initial loading, cracks are formed and the effective reference volume is reduced. However, hysteresis alone cannot express softening and stiffness degradation phenomena which are attributed to damage due to cracking. The damage concept adopted herein follows the notions introduced by Kachanov (1986) based on macroscopic considerations of the damaged state according to the effective stress concept (Figure 3.5). Following this notion, reference strain is considered the same between the original and the damaged material, while damage stress is reduced due to the increase in the reference area with the presence of voids.

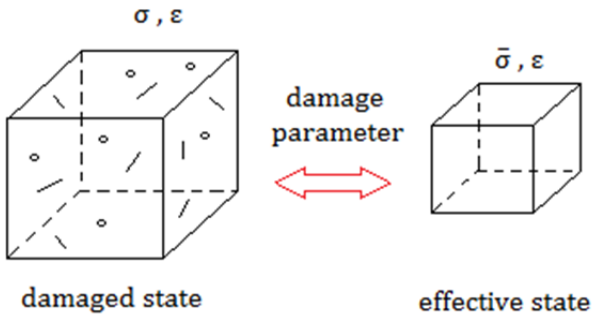

Figure 3.5. Effective stress concept of damage

Subsequent work by Lubliner et al. (1989) and other researchers (Ragueneau et al. 2000; Grassl and Jirasec 2006; Jason et al. 2006), aim at combining damage and plasticity allowing for significant benefits in realistic modeling of brittle materials. Damage theory alone, does not provide permanent strains as it considers the complete and perfect closure of cracks after unloading from a damaged state. However, sliding at cracks edges and incomplete closure of cracks due to misfits at crack lips, result in permanent strains that can be described macroscopically with plasticity theory (Figure 3.6).

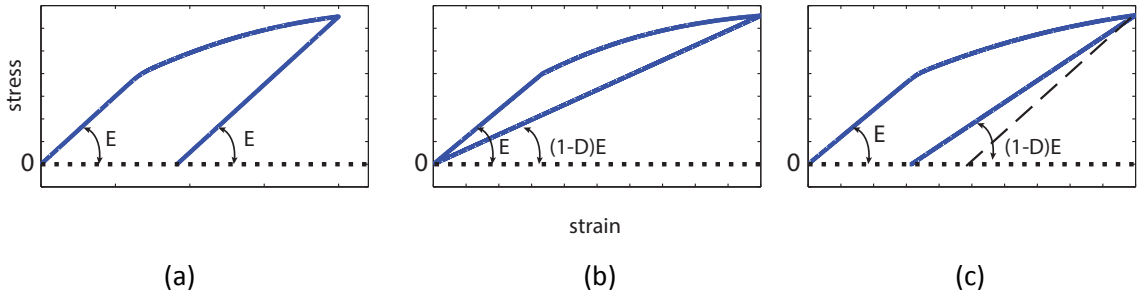

Figure 3.6. Combination of plasticity and damage theory

Within this approach, the initially undamaged volume of the material, starts degrading beyond a certain strain limit. The effective skeleton keeps weakening whenever maximum strain criterion is exceeded, exhibiting in parallel a hysteretic behavior. In this way, cracks, voids and sliding are manifested and phenomenologically can be taken into account. By applying the strain equivalent damage theory the true concrete stress is calculated from the effective undamaged stress with the following relation:

$$\sigma_c = (1-D)\cdot\bar{\sigma}_c \tag{3.11}$$

where D is the time dependent damage parameter which quantifies damage caused in tension and compression field according to the following relation:

$$(1-D)=(1-H_{c3}D_{-})\cdot\left[1-(1-H_{c3})D_{+}\right] \tag{3.12}$$

while D_{-} and D_{+} describe the damage caused within compression and tension fields respectively. These two indices do not interact as they are controlled by the Heaviside-type term H_{c3} of relation (3.10) that prevents a simultaneous activation.

In rate form, relation (3.12) expresses the damage evolution as:

$$\dot{D}=H_{c3}\dot{D}_{-}\left[1-(1-H_{c3})D_{-}\right]+(1-H_{c3})\dot{D}_{+}\left[1-H_{c3}D_{-}\right] \tag{3.13}$$

Moreover, differentiating relation (3.11) with respect to time, a rate expression relating stress with damage parameter and strain is obtained as follows:

$$\dot{\sigma}_c=(1-D)\dot{\bar{\sigma}}_c-\dot{D}\bar{\sigma}_c \tag{3.14}$$

Generally damage state in tension D_{+} differs from the respective damage state in compression D_{-}. The appearance of the first tensile cracks in the tension region results in the immediate loss of strength, while is evolving gradually in the compression field damage. So to distinguish both distinct phases, all damage model parameters employed are denoted with subscript i in the following sections.

Damage parameter either in tension or compression $D_i=D_i\left(k_i\left(\varepsilon_i\right)\right)$ is controlled herein by the damage-driving variable k_i and is given analytically from the following exponential relation:

$$D_i=1-e^{-\left(\frac{k_i-k_{0,i}}{b_i k_{0,i}}\right)^{p_i}} \tag{3.15}$$

where b_i and p_i are model parameter that control damage evolution and are typically calibrated by experimental data. Damage-driving variable k_i is a function of distinct strain ε_i in compression or tension while it starts evolving from the damage threshold strain value $k_{0,i}$ that defines the onset of damage.

$$k_i\left(\varepsilon_i\right)=\max_{\tau\le t}\left(\varepsilon_i\left(\tau\right),k_{0,i}\right) \tag{3.16}$$

When k_i resides within a damage surface it results no damage evolution. The damage surface for a uniaxial problem that delimits the undamaged region is specified as (Grassl and Jirasec 2006):

$$g_i\left(k_i,\varepsilon_i\right)=\varepsilon_i-k_i\left(\varepsilon_i\right) \tag{3.17}$$

Damage evolution is controlled by the Kuhn-Tucker optimality conditions associated with the principle of maximum damage dissipation (Simo and Ju 1987). They are given in the form:

$$g_i \le 0 \ , \ \dot{k}_i \ge 0 \ , \ \dot{k}_i \cdot g_i = 0 \tag{3.18}$$

and designate that if function g_i is negative, remains constant and no damage evolution occurs, whereas if g_i is zero, $\dot{k}_i > 0$ and damage develops.

3.2.3 Smoothening of the damage equations

The above relations describing damage have a similar structure as those of classical plasticity and thus a similar unified smooth expression (§2.2.2) can be also introduced. Hence, relations (3.17) and (3.18) can be expressed via a Heaviside step function H_{c4} and the loading-unloading switch function H_{c2} (3.3), as follows:

$$\dot{k}_i = H_{c4} \cdot H_{c2} \cdot \dot{\varepsilon}_{c,i} \tag{3.19}$$

$$H_{c4} = \begin{cases} 0, \ g < 0 \\ 1, \ g = 0 \end{cases} \tag{3.20}$$

where $\varepsilon_{c,i}$ is the distinct concrete strain in tension/compression and H_{C4} activates damage evolution (0: undamaged phase, 1: damage evolution), while it can be smoothened as follows:

$$H_{c4} = \left| \frac{\varepsilon_{c,i}}{k_i} \right|^m \tag{3.21}$$

Parameter m controls the smooth transition of constant damage to damage evolution, even though for simplicity reasons it is suggested this parameter to obtain large values $m \ge 10$ as immediate damage transition is advised.

Applying the chain rule for the damage parameter D_i, damage evolution law is given as:

$$\dot{D}_i = \frac{dD_i}{dk_i} \dot{k}_i \tag{3.22}$$

Substituting relations (3.19), (3.21) and (3.22) in relation (3.13) the following equation is derived:

$$\dot{D}_i = \frac{dD_i}{dk_i} \dot{k}_i = H_{c4} \cdot H_{c2} \cdot \frac{dD_i}{dk_i} \cdot \dot{\varepsilon}_{c,i} \tag{3.23}$$

which embodies the entire damage evolution. Concrete damage model without any plastic behavior contributing is illustrated in Figure 3.7. Model parameters in tension and compression are presented in Table 3.1.

E_c (GPa)	$k_{0,c}$	$k_{0,t}$	b_c	b_t	p_c	p_t
30	0.000833	0.000167	2.5	0.5	0.9	0.5

Table 3.1. Damage concrete parameters

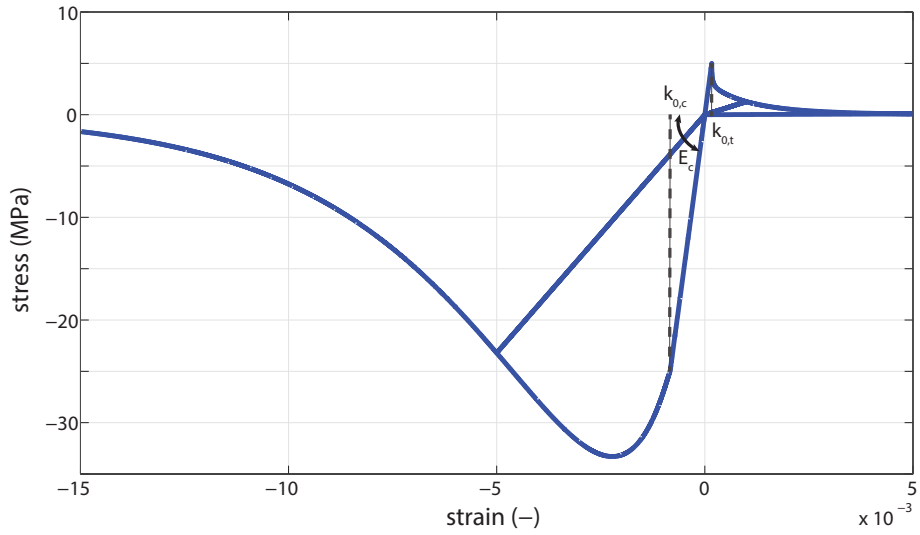

Figure 3.7. Concrete model with damage contribution only.

Finally, substituting relations (3.8) and (3.23) into (3.14) results into the following compact expressions:

$$\dot{\sigma}_c = E_{c,t}\,\dot{\varepsilon}_c \tag{3.24}$$

$$E_{c,t} = \left\{ (1-D)\left[1-(1-a_c)\cdot H_{c1}\cdot H_{c2}\right] - \left(H_{c4}\cdot H_{c2}\cdot \frac{dD_i}{dk_i}\cdot \frac{\bar{\sigma}_c}{E_c} \right) \right\} E_c \tag{3.25}$$

where, E_t is the tangential Young modulus incorporating both plasticity and damage effects. Concrete model when the combined plastic and damage behavior is attributed is illustrated in Figure 3.8 with model parameters those of Table 3.2.

	E_c (GPa)	σ_{yc} (MPa)	a_c	q_c	$k_{0,i}$	b_i	p_c
Compression	30	25000	0.5	1000	0.000833	6.5	1.0
Tension		5000	-	-	0.000167	0.5	0.5

Table 3.2. Plastic and damage concrete parameters

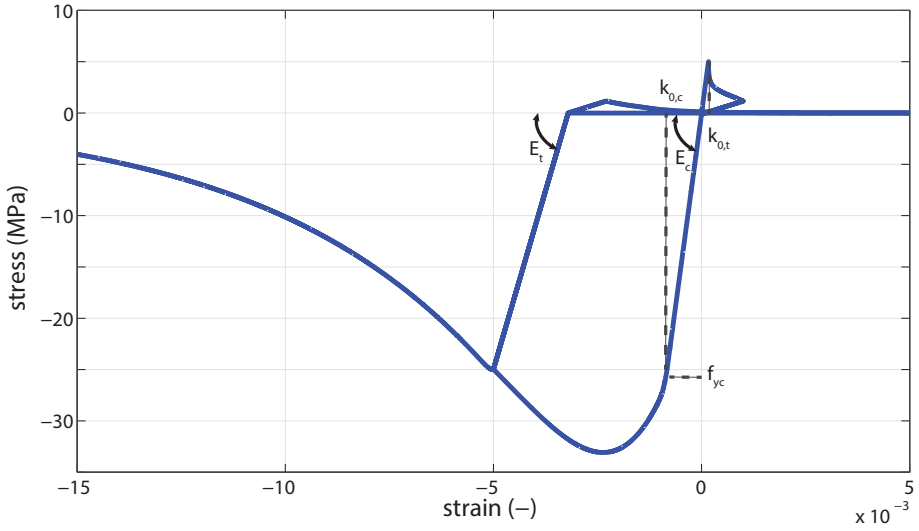

Figure 3.8. Plastic-damage concrete model

As it is obvious, while model is in the compression range it unloads with stiffness E_t which is smaller than the elastic stiffness E_c and permanent compressive strains evoke. Also, after the first excursion in the tensile field a small reserve remains, hence in the subsequent reloading in tension tensile stiffness is non-zero.

When unloading from compressive envelope it is obvious from Figure 3.8 that tension envelope is shifted at the point where the unloading compressive curve intersects with the zero stress level axis. This is accomplished by setting in relation (3.21) the tensile part ε_c^+ of the total strain ε_c , evolving as follows:

$$\dot{\varepsilon}_c^+ = \left(1 - H_{c1}\right)\dot{\varepsilon}_c \tag{3.26}$$

3.2.4 Nonlinear unloading

It is evident from experiments that concrete exhibits nonlinear unloading, whereas in reloading it remains linear forming in such way hysteretic loops (Sinha et al. 1964; Karsan and Jirsa 1969; Okamoto et al. 1976; Bahn and Hsu 1998). To incorporate such a behavior an appropriate modification is introduced into the relation of tangential modulus as follows:

$$r_{un} = \left(c_1 \left| \frac{\bar{\sigma}_c}{\bar{\sigma}_{c,r}} \right| + c_2 \right)^{1-H_{c2}} \tag{3.27}$$

where r_{un} designates the function of the nonlinear unloading branch that depends on $\bar{\sigma}_{c,r}$ which is the effective stress at the reversal point. The exponent $1-H_{c2}$ activates the

unloading function only when unloading is detected and c_1, c_2 are model parameters. Consequently the tangent concrete modulus is modified as:

$$E_{c,t} = \left\{ (1-D)\left[1-(1-a_c)\cdot H_{c1}\cdot H_{c2}\right] - \left(H_{c4}\cdot H_{c2}\cdot \frac{dD_i}{dk_i}\cdot \frac{\bar{\sigma}_c}{E_c} \right) \right\} \cdot r_{un} \cdot E_c \tag{3.28}$$

The modified concrete behavior due to nonlinear unloading is illustrated in effective (undamaged) and total stress terms in Figure 3.9

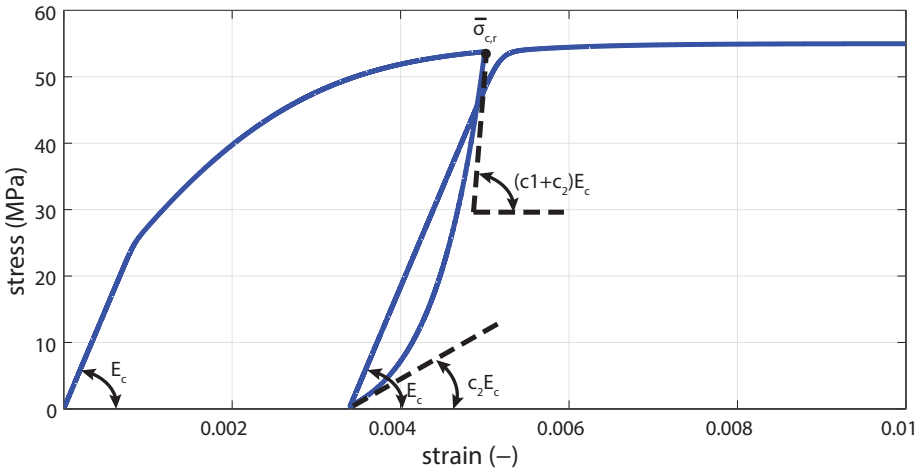

(a)

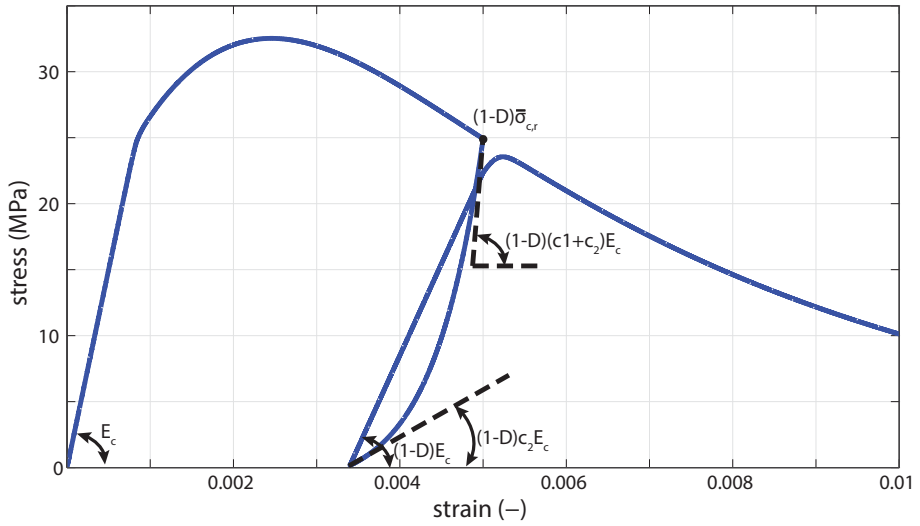

(b)

Figure 3.9. Schematic representation of concrete nonlinear unloading

In the beginning of unloading $\left(H_{c2}=0,\ \sigma_c=\bar{\sigma}_{c,r}\right)$ tangent stiffness obtains value $E_{c,t}=(1-D)(c_1+c_2)E_c$, while if complete unloading takes place, the respective value is

$E_{c,t} = (1-D)c_2 E_c$. Consequently, unloading parameter c_2 controls the percentage of tangent stiffness at zero stress level and the sum of parameters $(c_1 + c_2)$ controls the instant value of tangent stiffness at the reversal point.

3.2.5 Crack closure

When unloading from tensile stresses, at zero stress level, permanent tensile strains appear due to incomplete closure of cracks as misfits at crack edges exist. If loading at compression field follows, stiffness gradually obtains its compressive value as cracks close. This phenomenon is added in the proposed model by the stiffness recover function $r_{rec}(\varepsilon_{rec}, \varepsilon_c^-)$

$$r_{rec} = 1 - \left(1 - \frac{E_c}{E_{c,t}^+}\right) \cdot \left| \frac{\varepsilon_c^-}{\varepsilon_{rec}} \right|^{n_{rec}} \tag{3.29}$$

$$\dot{\varepsilon}_c^- = \left(1 - \left| \frac{\varepsilon_c^-}{\varepsilon_{rec}} \right|^{n_{rec}}\right) \cdot \left| \dot{\varepsilon}_c \right| \tag{3.30}$$

where $E_{c,t}^+$ is concrete tangent modulus in tension, ε_C^- is compressive strain and ε_{rec} is the strain value where cracks close completely when stiffness recovery phenomenon is omitted (Figure 3.10). Parameter n_{rec} controls the smoothness of the transition with larger values meaning the instantaneous closure of cracks.

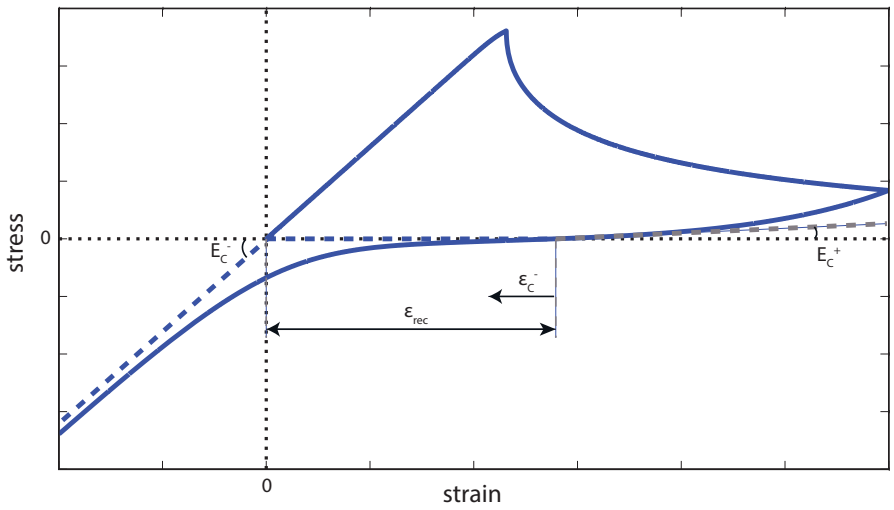

Figure 3.10. Concrete stiffness recovery representation

Finally, combining all previous effects the stress-strain constitutive relation of concrete can be written according to equation (3.31). The 1st part controls loading in either tension or compression and unloading from compression state, while the second part describes unloading from a tension state until compressive stiffness attains its actual value due to stiffness recovery.

$$\dot{\sigma}_c = E_{c,t} \cdot \dot{\varepsilon}_c$$
$$E_{c,t} = \begin{cases} \left\{ (1-D) \cdot \left[1-(1-a) \cdot H_{c1} \cdot H_{c2} \right] - \left(H_{c4} \cdot H_{c2} \cdot \frac{dD_i}{dk_i} \cdot \frac{\bar{\sigma}_c}{E_i} \right) \right\} \cdot r_{un} \cdot E_c \\ r_{rec} \cdot E^{+}_{c,t} \end{cases} \quad (3.31)$$

In Figure 3.11 the proposed concrete model considering the parameters of is presented where all the aforementioned phenomena are illustrated.

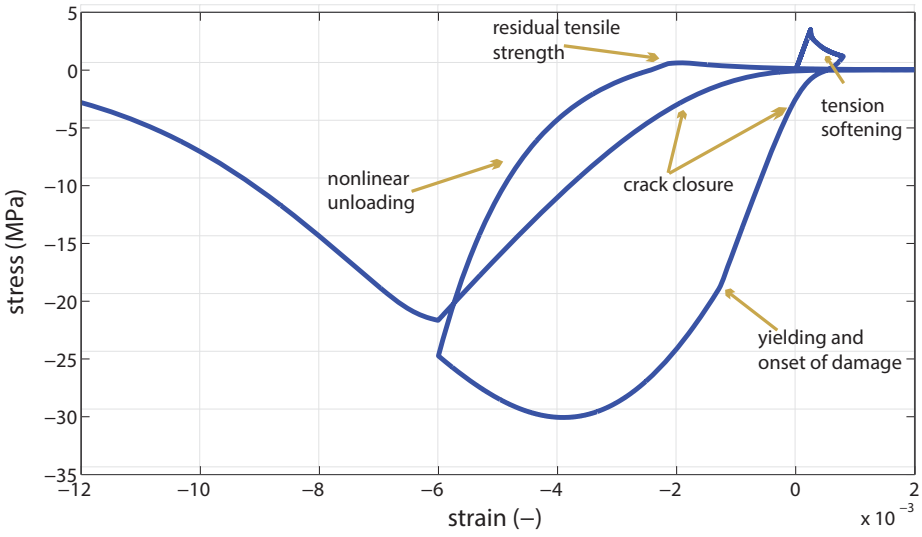

Figure 3.11. Schematic representation of the proposed concrete model.

	E_c (GPa)	σ_{yc} (MPa)	a_c	q_c	$k_{0,i}$	b_i	p_c	c_1	c_2	n_{rec}
Compression	30	25.0	0.5	1000	0.000833	6.5	1.0	3.0	0.2	10
Tension		5.0	-	-	0.000167	0.5	0.5	3.0	0.2	-

Table 3.3. Concrete model parameters

3.2.6 Pseudo-code for concrete model

Summarizing the described uniaxial concrete model, one can apply it to the global solution process as follows. At any iteration *j* of a global incremental numerical scheme the following are performed:

1. Define current tension/compression state by calculating switch function H_{c3}^{j} (3.10) and loading/unloading state by switch function H_{c2}^{j} (3.3).
2. Plastic term
   i. Calculate current post to pre-yield stiffness ratio a_c^j from relation (3.7).
   ii. Derive yield switch function H_{c1}^{j} from relation (3.4).
   iii. Calculate current yield stress by linearizing equation (3.5)

$$\sigma_{yc}^{j+1} = \sigma_{yc}^{j} + H_{c1}^{j} \cdot H_{c2}^{j} \cdot \alpha_c \cdot \mathrm{sgn}(\bar{\sigma}_c^{j}) \cdot E_c \cdot d\varepsilon_c^{j} \tag{3.32}$$

3. Calculate unloading function r_{un} from equation (3.27).
4. Calculate current effective stress from linearization of equation (3.8) as:

$$\bar{\sigma}_c^{j+1} = \bar{\sigma}_c^{j} + \left(1-(1-\alpha_c^{j}) \cdot H_{c1}^{j} \cdot H_{c2}^{j}\right) \cdot E_c \cdot d\varepsilon_c^{j} \tag{3.33}$$

5. Damage term.
   i. Calculate damage threshold function H_{c4}^{j} from relation (3.21) using equation (3.26) for tensile damage.
   ii. Derive damage-driving variable k_i by linearizing equation (3.19) as:

$$k_i^{j+1} = k_i^{j} + H_{c4}^{j} \cdot H_{c2}^{j} \cdot d\varepsilon_{c,i}^{j} \tag{3.34}$$

   iii. Using analytic relation (3.15), calculate the derivative of the damage parameter D_i in terms of k_i. The following relation is obtained:

$$\frac{dD_i}{dk_i} = p_i \cdot \left(\frac{k_i - k_{0,i}}{b_i k_{0,i}}\right)^{p_i - 1} \cdot \frac{1}{b_i k_{0,i}} \cdot e^{\left(-\frac{k_i - k_{0,i}}{b_i k_{0,i}}\right)^{p_i}} \tag{3.35}$$

   iv. Then, calculate the current value of the damage parameter D_i in both tension and compression from equation (3.23):

$$D_i^{j+1} = D_i^{j} + H_{c4}^{j} \cdot H_{c2}^{j} \cdot \frac{dD_i}{dk_i} \cdot d\varepsilon_{c,i}^{j} \tag{3.36}$$

   v. Using relation (3.12), calculate damage coefficient $\left(1-D^{j+1}\right)$ at current distinct loading state (tension or compression).
6. Finally, calculate true stress σ_c and tangent Young modulus. In the regular case they are given as

$$\sigma_c^{j+1} = \sigma_c^{j} + E_{c,t}^{j+1} \cdot d\varepsilon_c^{j} \tag{3.37}$$

$$E_{c,t}^{j+1}=\left\{\left(1-D^{j+1}\right)\cdot\left[1-\left(1-a^{j}\right)\cdot H_{c1}^{j}\cdot H_{c2}^{j}\right]-\left(H_{c4}^{j}\cdot H_{c4}^{j}\cdot\frac{dD_{i}}{dk_{i}}\cdot\frac{\overline{\sigma}_{c}^{j+1}}{E_{c}}\right)\right\}\cdot r_{un}\cdot E_{c} \tag{3.38}$$

7. When unloading from tension envelope and reloading until yield point or damage threshold in compression, relation (3.37) and (3.38) are replaced by the crack closure step by calculating the stress recovery function (3.29). Then the updated total stress is calculated as:

$$\sigma_{c}^{j+1}=\sigma_{c}^{j}+r_{rec}\cdot E_{c,t}^{+}\cdot d\varepsilon_{c}^{j} \tag{3.39}$$

Equations (3.37)-(3.39) trace the full nonlinear concrete path in every time step in a direct way and stresses are determined explicitly. Hence, the residual error in each iteration is due to the inherent error of the Euler numerical scheme used to integrate the differential equations. In the work of Lee and Fenves (2001), as well as in Saritas and Filippou (2009) calculation of effective stress is performed in advance and the contribution of the damage variable is added subsequently (general closest point projection (GCPP) algorithm). As a consequence the consistent tangent stiffness $\left(\sigma_{c}^{j+1}-\sigma_{c}^{j}\right)/\left(d\varepsilon_{c}^{j}\right)$ that ensures the quadratic convergence of the Newton-Raphson numerical strategy should be calculated after the stress determination process. However, this is not the case in the proposed formulation, as tangent stiffness in relation (3.38) is directly used both for stress stiffness and global stiffness matrix offering a more straightforward numerical formulation.

3.3 Influence of model parameters

3.3.1 Compressive behavior

In this section the influence of the parameters that control the proposed concrete model in compression is investigated. The reference values for a parametric study concerning the influence of each parameter variation are presented in Table 3.4:

E_C (GPa)	σ_{yc} (MPa)	α_C	q_C	$k_{0,t}$	b_t	p_t	c_1	c_2	n_{rec}
30	25	0.5	1000	0.00083	6.5	1.0	4.0	0.15	100

Table 3.4. Reference compressive parameters

The sensitivity of the response with respect to the parameters of the model is demonstrated by varying all parameters one at a time while keeping the rest of them as constant. First, the influence of parameters controlling plastic response is demonstrated in Figure 3.12.

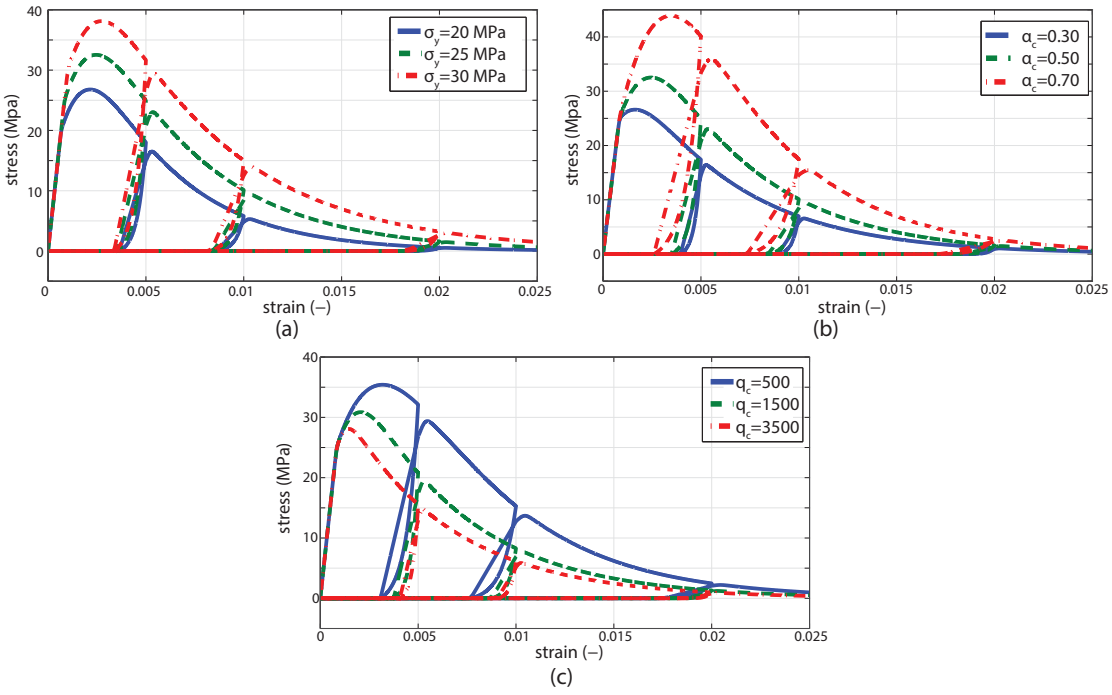

Figure 3.12. Influence of plasticity parameters in compression

For higher values of the initial yield stress σ_{cy} the stress-strain curve rises along the elastic modulus line as it is depicted in Figure 3.12(a). Parameter a_c designates the isotropic hardening modulus in terms of total the strain ε_c. As shown in Figure 3.12(b) this parameter directly affects the compressive strength of concrete, as well as the magnitude of plastic and elastic strain. As a_c approaches unity, plastic deformations tend to disappear. Also, an increase of the hardening parameter q_c (Figure 3.12(c)) approximates an elastic perfectly plastic curve for the plastic term diminishes the plastic response. As it is reflected in the figures plastic parameters affect the initial concrete response after yield point, while post peak response where damage prevails leads asymptotically to the same loading path.

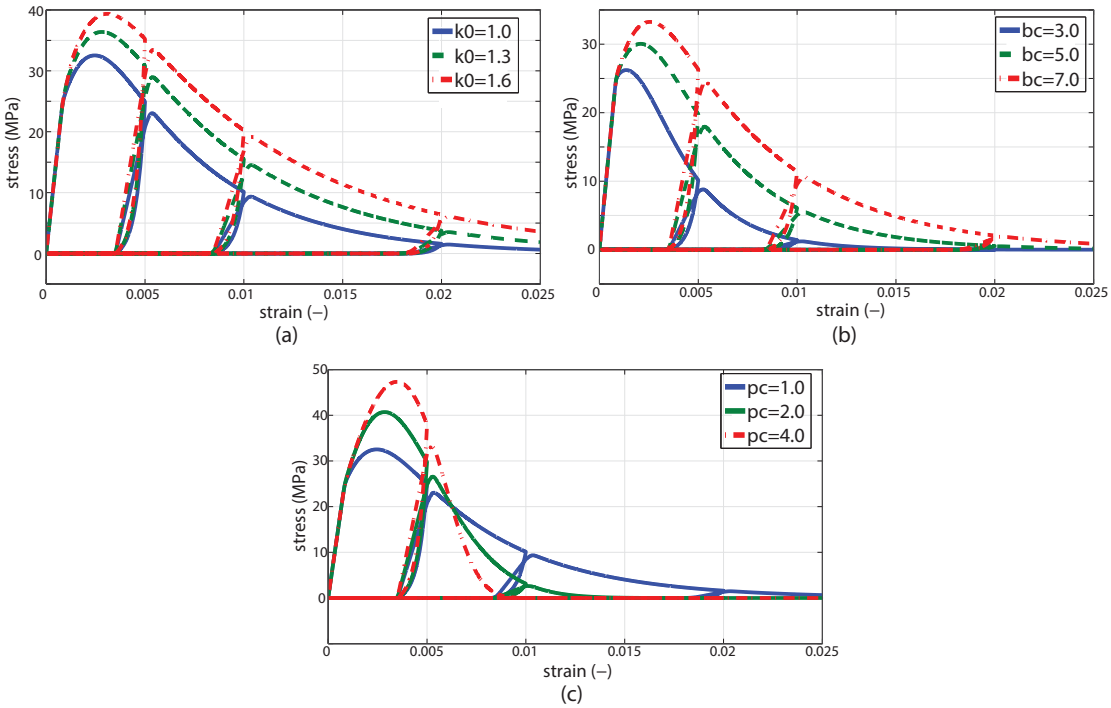

Figure 3.13. Influence of damage parameters in compression

Next, the sensitivity of the model to the damage parameters is presented in Figure 3.13. More specifically, changing the damage threshold k_0 affects the strain point where damage initiates, while for larger values a parallel transition of the softening curve is observed (Figure 3.13(a)). As far as damage parameter b_c is concerned, small values lead to a more rapid softening behavior as depicted in Figure 3.13(b). In addition, parameter p_c controls the slope of the softening curve by affecting the distribution of the released energy in the post damage regime. As p_c increases, damage develops slower at strains near k_0, whereas it evolves faster for higher values of strains, as shown in Figure 3.13(c).

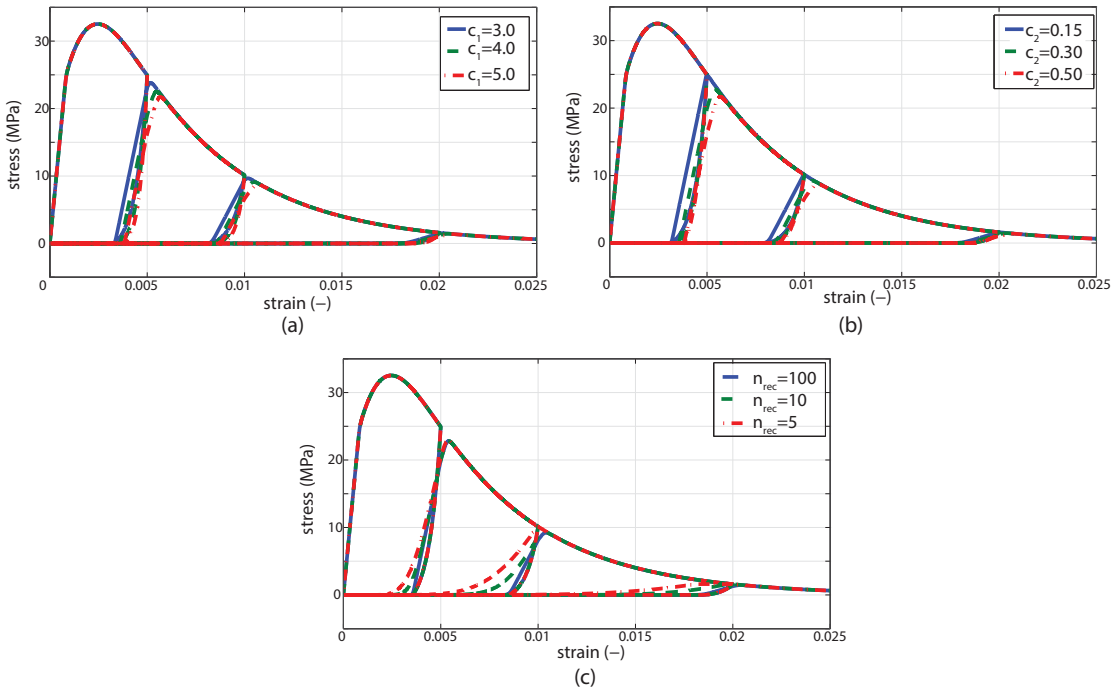

Figure 3.14. Influence of unloading-reloading and stiffness recovery parameters in compression

Finally, the influence of parameters controlling unloading-reloading and crack closure phenomena is investigated. Parameters c_1 and c_2 in Figure 3.14(a)-(b) control the slope at reversal and zero stress point respectively. Thus, during unloading the slope varies between $(1-D)(c_1+c_2)E_c$ at reversal point and $c_2(1-D)E_c$ at zero stress point. For greater values of the ratio c_1/c_2 the unloading-reloading slope range becomes wider. Also, larger stiffness recovery values affect the strain range and the smoothness of the transition from tensile to compressive behavior due to crack closure phenomena (Figure 3.14(c)).

3.3.2 Tensile behavior

Similarly, the influence of parameters in tension is investigated and the parametric comparison is presented in Figure 3.15 with reference values those listed in Table 3.5.

E_C (GPa)	σ_{yt} (MPa)	$k_{0,t}$	b_t	p_t	c_1	c_2
30	5	0.000167	0.5	0.5	3.0	0.3

Table 3.5. Reference tensile parameters

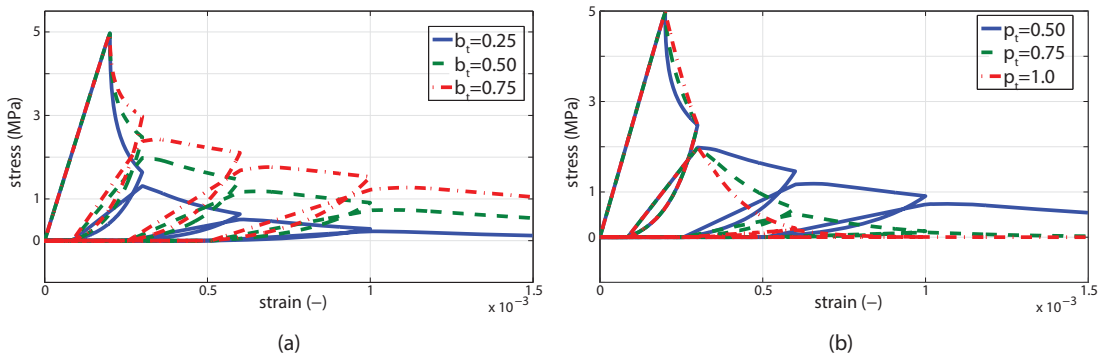

Figure 3.15. Influence of tensile parameters

Generally, to account for tensile behavior with abrupt loss of strength after peak tensile strength, parameters b_t και p_t that control softening branch normally take values lower than *1.0.*

3.3.3 Range of model parameters

The full version of the proposed model includes a number of 9 parameters in compression. However, in the absence of experimental data or even for design purposes the model can be used in a simplified version as some parameters seem to have a similar effect in the nonlinear response. Taking a closer look at Figure 3.12 it appears that all three plasticity parameters affect the initial nonlinear segment with similar manner. For this reason it could be assumed that parameter q_c is redundant and could be excluded from the model if it is assigned a zero value, excluding nonlinear isotropic hardening effect from the model. This reduction can be accompanied with setting damage threshold parameter k_0 equal to the yield strain ε_{cy}. This modification considers a coupled damage-plastic behavior and describes the physical mechanism of cracks formation, as cracks open and slide simultaneously.

As far as tensile behavior is concerned, damage threshold parameter k_0 should obtain the strain value at the peak stress point as damage should evolve rapidly after strength tensile capacity is exceeded $\left(k_0 = \sigma_t / E_c\right)$. Generally, tensile strength is usually considered as the 10% of the compressive strength. Nevertheless, as concrete tensile behavior is of secondary importance and affects usually the initial loading path of RC members, in the absence of experimental data the reference values $b_t = 0.50$, $p_t = 0.50$ are suggested for use.

In conclusion, the following model parameter values in table are suggested for use in the case there is not any experimental data available.

parameters	compression		tension
	unconfined	confined	-
$\sigma_{yc}/\sigma_{c,max}$	0.4-0.8	0.3-0.8	1.0
α_c	0.4-0.9	0.4-0.9	-
q_c	0	10.0-50.0	-
k_o/ε_{cy}	1.0	1.0	1.0
b_c	1.0-10.0	2.0-20.0	0.5
p_c	0.8-1.5	0.4-1.2	0.5
c_1	3.0-4.0	1.5-2.0	3.0
c_2	0.1-0.3	0.3-0.5	0.3

Table 3.6. Range of model parameters values

Together with the previous table, maximum compressive strength $\sigma_{c,\max}$, tensile strength σ_t and 40% secant stiffness E_c are given in any design code depending on the concrete grade.

3.4 Verification with experimental data

The proposed plastic-damage model is verified with various experimental tests that investigate concrete cyclic behavior. The proposed model parameters presented are calibrated heuristically in every case to match the experimental behavior. For better correlation of the numerical with the experimental result proper parameter identification algorithms can be used, however this exceeds the purpose of this thesis. In every case, the normalized recorded strain histories are introduced into the proposed model and the stress outcomes are plotted in conjunction with the actual experimental stresses

3.4.1 Compressive behavior

More specifically, considering compressive behavior, the experimental tests that were used for the comparison and their results are presented in Sinha et al. (1964), Karsan and Jirsa (1969), Bahn and Hsu (1998), Okamoto et al. (1976) and Muguruma et al. (1983). The

results of the comparison are presented in Figure 3.16-Figure 3.20 while normalized model parameters are listed in Table 3.7.

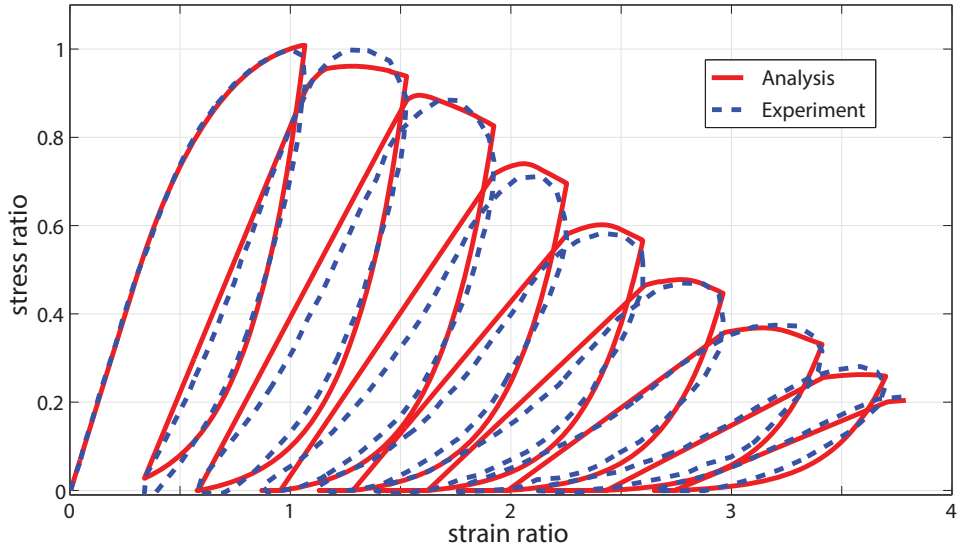

Figure 3.16. Comparison with experimental data of Sinha et al.

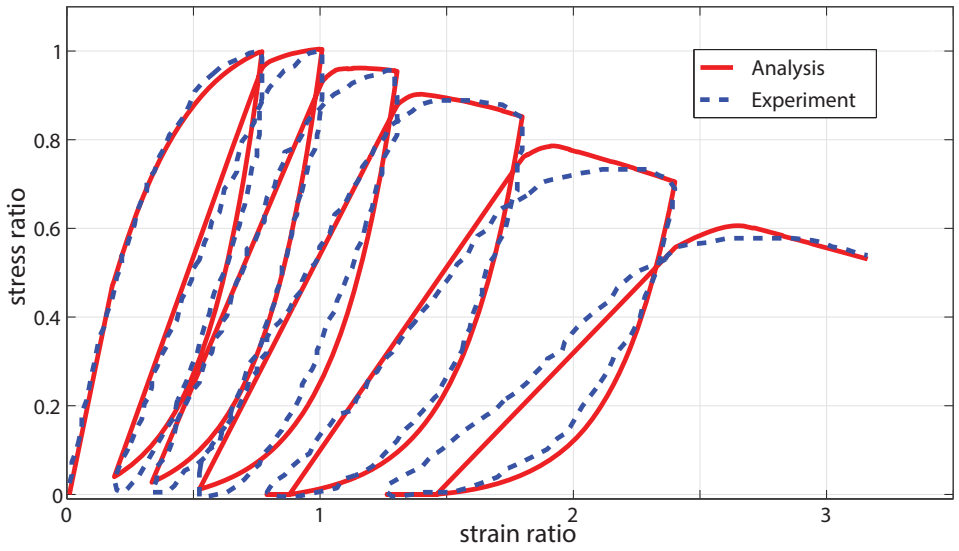

Figure 3.17. Comparison with experimental data of Karsan and Jirsa.

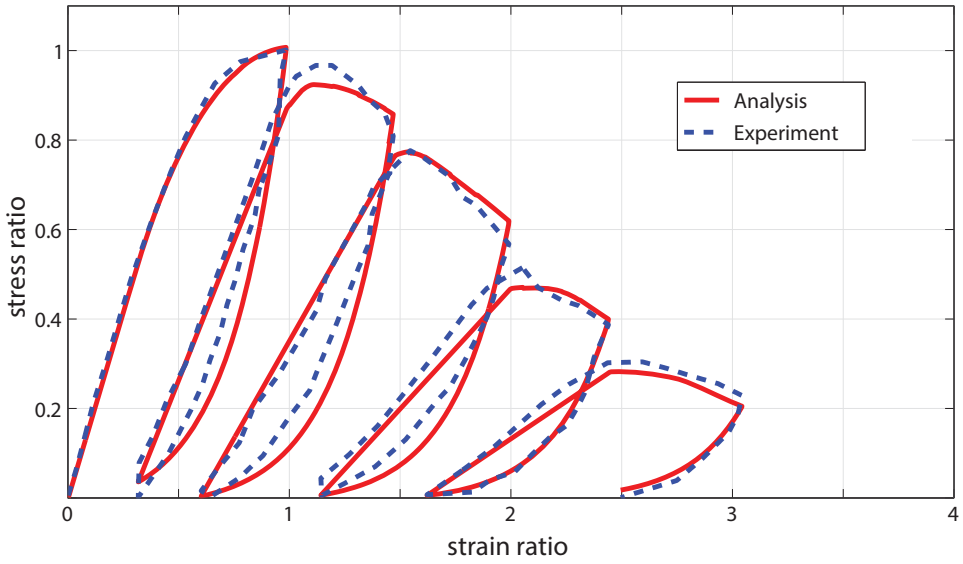

Figure 3.18. Comparison with experimental data of Okamoto et al.

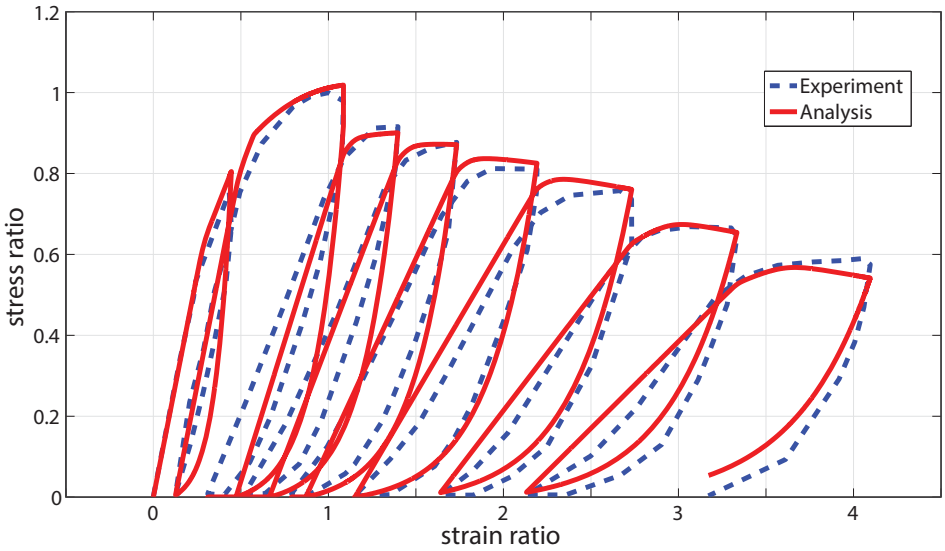

Figure 3.19. Comparison with experimental data of Muguruma et al.

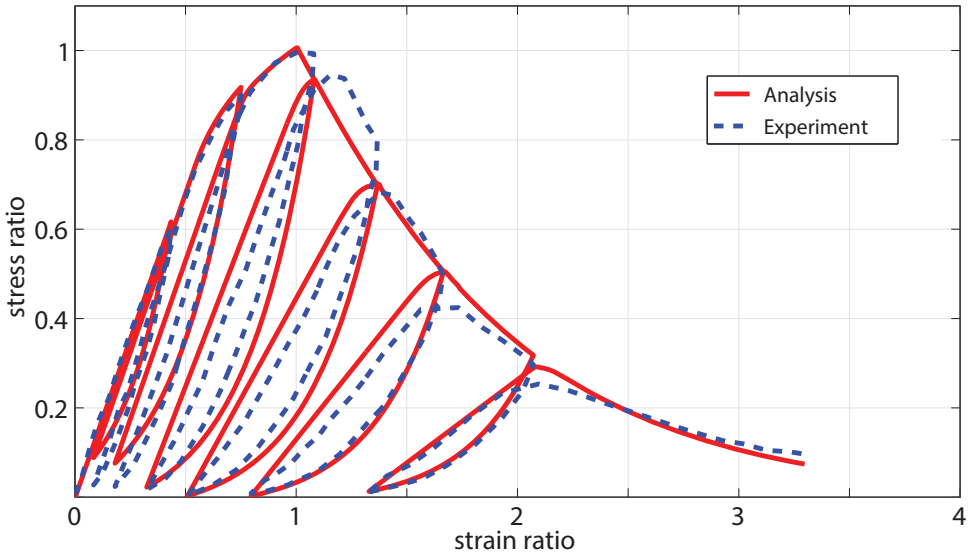

Figure 3.20. Comparison with experimental data of Bahn and Hsu.

normalized parameters	Sinha et al.	Karsan - Jirsa	Okamoto et al.	Muguruma et al.	Bahn-Hsu
$\sigma_{yc}/\sigma_{c,max}$	0.7	0.7	0.7	0.6	0.75
$\varepsilon_{yc}/\varepsilon_{co}$	0.4	0.3	0.4	0.29	0.5
α_c	0.5	0.7	0.6	0.5	0.7
q_c	10	10	5	10	12
k_o/ε_o	0.4	0.3	0.4	0.57	1.0
b_c	4.5	4.5	5.0	2.5	0.9
p_c	1.4	1	1.7	0.75	1.0
c_1	3.8	4.0	3.5	4.0	3.5
c_2	0.1	0.12	0.15	0.1	0.1

Table 3.7. Concrete compressive parameters for comparison with experimental data.

It is evident that the proposed concrete model fits satisfactorily the observed concrete cyclic behavior, demonstrating its flexibility to adapt to a range of different concrete categories. In the experiments performed by Sinha et al. and Okamoto et al. concrete exhibits similar response with peak stress presented in the same strain range and mediocre post-peak envelope stiffness, while in the Karsan and Jirsa experiment post-peak stiffness is less steep. On the contrary, concrete used in Bahn and Hsu experiment demonstrates a more brittle behavior with a steeper softening branch and greater strain at peak stress. This

different concrete cyclic response is reflected in the model parameters. Similar parameter values are used to capture the response of the first three tests while calibration with the Bahn and Hsu experiment corresponds to a different range of parameter values. Finally, Muguruma et al. studied experimentally cyclic behavior of high strength concrete and peak compressive stress in the normalized Figure 3.19 corresponds to *64MPa.* Therefore, it is evident that the proposed concrete model can simulate successfully not only regular strength concrete, but also high strength concrete with the proper set of parameters involved.

3.4.2 Tensile behavior

Similarly, the tensile behavior is verified with cyclic experimental data in the literature. In the first experiment performed by Gopalaratnam and Shah (1985) strain reversals until zero stress level are imposed. As presented in Figure 3.21 permanent tensile strains are manifested and abrupt loss of strength capacity is noticed soon after stress reaches yield limit. This behavior is satisfactorily obtained from the concrete model where both the envelope and the stress reversals are simulated. Concrete model parameters that were used for the analysis comparison can be found in Table 3.8.

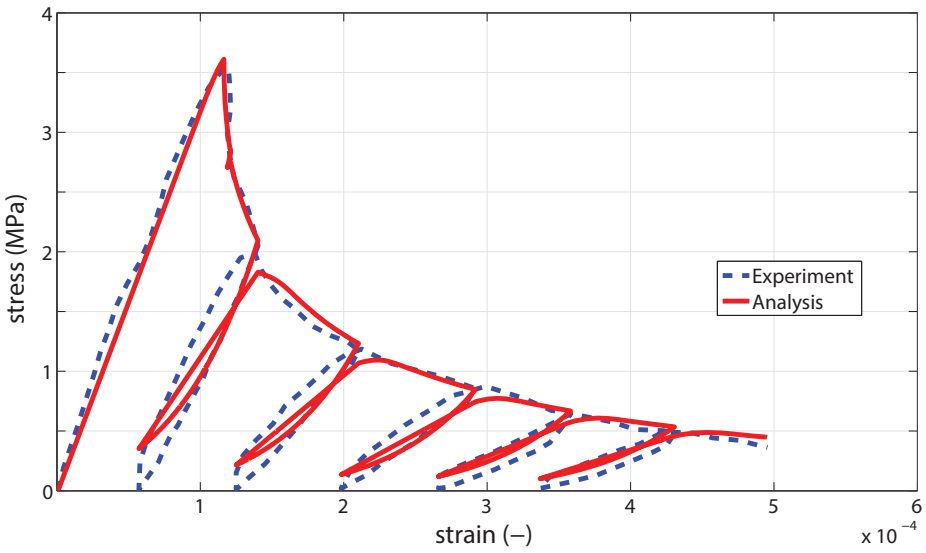

Figure 3.21. Comparison of model's tensile behavior with experimental data of Gopalaratnam and Shah.

E_C (GPa)	σ_{yt} (MPa)	$\alpha_{C,t}$	$q_{C,t}$	$k_{0,t}$	b_t	p_t	c_1	c_2
32	3.7	0.1	0	0.00012	0.6	0.5	2.0	0.2

Table 3.8. Concrete tension model parameters for Gopalaratnam and Shah experiment analysis.

In the next experiment performed by Reinhardt and Cornelissen (1984) concrete specimen is loaded both in tension and compression, thus the crack closure phenomenon is revealed. As it is obvious from Figure 3.22 there is a very good correlation between the analysis model and the recorded outcome, while used model parameters are listed in Table 3.9

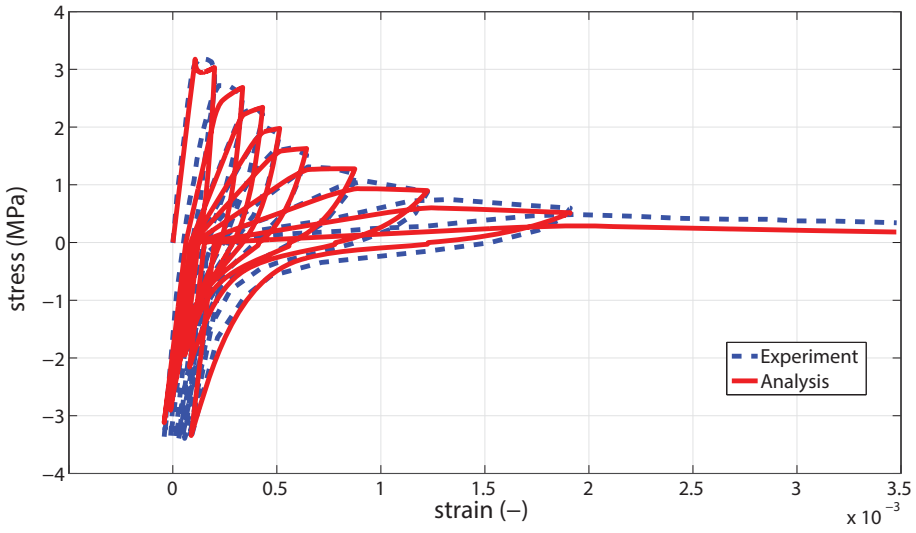

Figure 3.22. Comparison of model's tensile behavior with experimental data of Reinhardt and Cornelissen.

E_C (GPa)	σ_{yt} (MPa)	$\alpha_{C,t}$	$q_{C,t}$	$k_{0,t}$	b_t	p_t	c_1	c_2	n_{rec}
30	3.2	0.6	0	0.00011	3.0	0.7	3.5	0.8	5.0

Table 3.9. Concrete tension and stress recovery model parameters for Reinhardt and Cornelissen experiment analysis.

Nonetheless, in the global analysis of RC structures, tensile phenomena are manifested only at the initial stages of loading as soon after the first cracks appear, tensile strength is lost completely. However, crack closure phenomenon is still active and affects the loading/unloading loops of RC members, so it is advised to be implemented in the analysis.

3.4.3 Confined concrete behavior

Confining pressure offered by the transverse stirrups or hoops increases maximum concrete compressive strength and ductility. In the model, there is not an explicit method to incorporate confining effects as it is by definition a 3D phenomenon that reduces volumetric strain and concrete dilatancy. Nevertheless, Mander et al. (1988) proposed an analytical procedure to account for confinement in a uniaxial constitutive law by considering constant pressure throughout the whole stress-strain curve. This procedure can be adopted herein to derive maximum confined compressive stress and then recalibrate model parameters.

On the other hand experimental data on concrete cylinder specimens confined with circular stainless steel rings are offered in Choi et al. (2013). The experimental results of the unconfined and confined specimens are presented in Figure 3.23. Also, the numerical results of the proposed model under the same imposed strain history are highlighted in the same figure. The comparison reveals the ability of the model to simulate confined cyclic behavior apart from the unconfined one. Finally, the modification of model parameters in order to describe confined behavior is listed in Table 3.10.

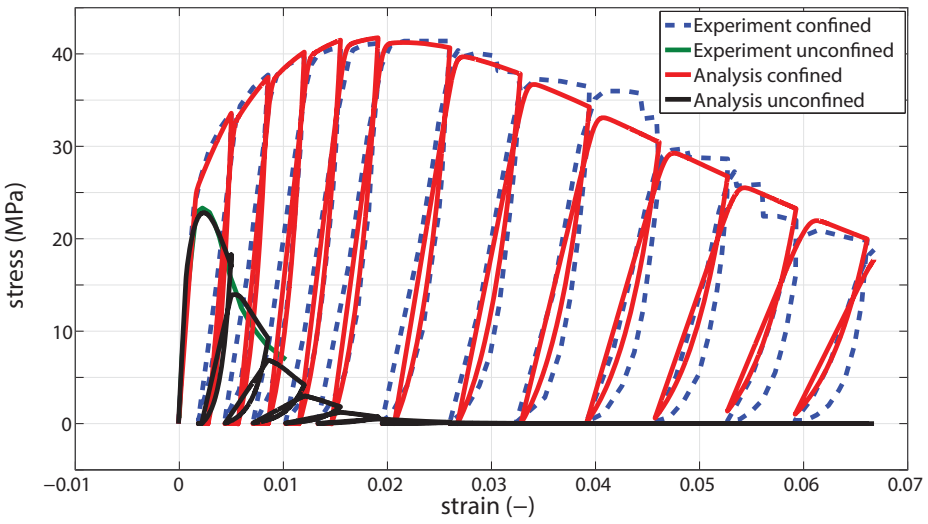

Figure 3.23. Comparison of confined and unconfined behavior with experimental data of Choi et al.

	E_C (GPa)	σ_{yc} (MPa)	α_C	q_C	k_0	b_c	p_c	c_1	c_2
Unconfined	20	15	0.70	0	ε_{yc}	4.0	0.9	4.0	0.2
Confined	20	25	0.25	40	ε_{yc}	19.0	0.9	2.0	0.4

Table 3.10. Confined and unconfined concrete parameters

3.5 Comparison with existing well-known models

In this section well established and commonly used uniaxial concrete model are briefly described and they are compared with the proposed formulation. These models are used nowadays in many structural engineering projects as they are incorporated in scientific and commercial software packages like OpenSees, Seismostruct and Sap2000.

First, a comparison of the proposed model and the model of Mander et. al (1988) as modified by Martinez-Rueda and Elnashai (1997) is performed and the result is presented in Figure 3.24 for the imposed strain history of Table 3.11. Model parameters for both models where selected in such way as to achieve similar response. More specifically Young modulus was set to $E_c = 25\ GPa$, yield stress is $\sigma_{yc,0} = 22\ MPa$, hardening parameters are $a_c = 0.85$, $q_c = 50$, damage parameters are $k_0 = \varepsilon_{cy}$, $b_c = 2.7$, $p_c = 1.0$ and unloading parameters are $c_1 = 4.0$, $c_2 = 0.25$

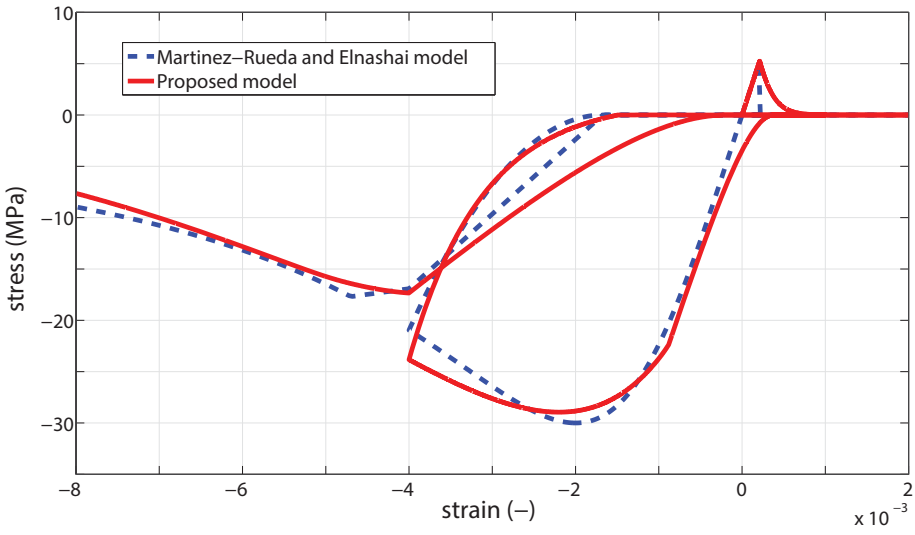

Figure 3.24. Comparison with Martinez-Rueda and Elnashai concrete model

Pseudo-Time (sec)	Strain (-)
0	0
1	0.001
2	-0.004
3	0.002
4	-0.008

Table 3.11. Strain history for comparison with Martinez-Rueda and Elnashai concrete model

First, a difference is spotted in the tension envelope where the model of Martinez-Rueda and Elnashai loses tensile strength instantaneously, while the proposed model describe the tension softening behavior, degrading gradually to zero tensile strength. Another main feature of the proposed model is the crack closure phenomenon, something that is missing from the existing model. On the other hand compressive skeleton appears to be quite similar for both models, but unloading-reloading curves seem to differ. In the proposed model the reloading curve end to a point closer to the reversal point than the existing model. Generally, if nonlinear unloading and crack closure phenomena were excluded from the model the reloading stiffness is the same with the unloading stiffness, while in the model of Martinez-Rueda and Elnashai reloading linear curve has smaller slope than the unloading curve.

In addition, a comparison of the proposed model and the model of Konstantinidis and Kappos (2007) is performed and the result is presented in Figure 3.25 for the imposed strain history of Table 3.12. The purpose of this comparison is to reveal the ability of the model to predict cyclic response of high strength concrete as Konstantinidis and Kappos model results from statistical analysis of experimental data on high strength concrete specimens under cyclic loading. Model parameters for both models where selected to be adequate for high strength concrete feature and to achieve similar response. More specifically Young modulus was set to $E_c = 40\ GPa$, yield stress is $\sigma_{yc,0} = 40\ MPa$, hardening parameters are $a_c = 0.8$, $q_c = 2000$ and damage parameters for $k_0 = -0.002$, $b_c = 2.2$, $p_c = 1.0$ and unloading parameters are $c_1 = 2.0$, $c_2 = 0.2$.

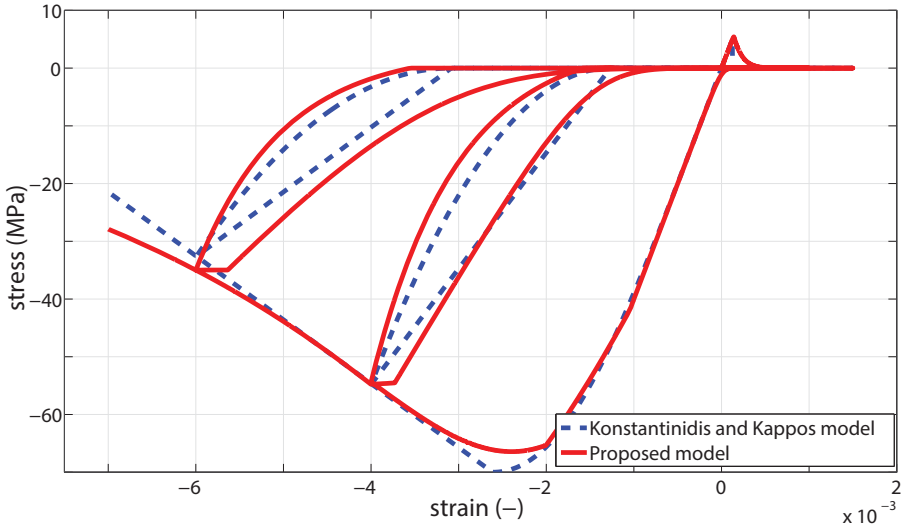

Figure 3.25. Comparison with Konstantinidis and Kappos concrete model

Pseudo-Time (sec)	Strain (-)
0	0
1	0.0005
2	-0.004
3	0.001
4	-0.006
5	0.0015
6	-0.007

Table 3.12. Strain history for comparison with Konstantinidis and Kappos concrete model

Similar to the previous comparison, tension softening behavior is not modeled from the existing model as it loses tensile strength instantaneously, while the proposed model simulates concrete response after peak tensile strength. Also crack closure phenomenon is not included in the existing model perhaps due to lack of experimental data. On the other hand, compressive skeleton appears to be quite similar in both models, even though Konstantinidis and Kappos model describes post peak response with a linear segment, while the proposed model used an exponential law for damage evolution. As expected unloading-reloading curves present the same deviations with the Martinez-Rueda and Elnashai model, as both existing models adopt the same analytical rules with the only difference that in Konstantinidis and Kappos model unloading-reloading loops close completely. Similar closed hysteretic loops can be modeled using the proposed model by properly selecting unloading parameters c_1 and c_2.

Finally, a comparison is performed between the proposed model and the concrete model of La Borderier et al. (1994) which is based on damage theory considerations; hence both models share the same structure. As it is illustrated in Figure 3.26 the proposed model can generate the same stress-strain loop of uniaxial concrete behavior under the imposed strain history of Table 3.13 with the additional feature of nonlinear unloading in compression. Another difference lies on the fact that La Borderie model describes the crack closing/reopening phenomena with a linear segment, while the proposed model uses a smooth transition approach. Nevertheless, all other features of uniaxial concrete cyclic behavior like tension softening, damage state in compression and inelastic strains can be captured from the proposed formulation. To obtain this response the following parameters were used; Young modulus $E_c = 20\ GPa$, yield stress is $\sigma_{yc,0} = 18\ MPa$, hardening parameters are $a_c = 0.6$, $q_c = 10$ and damage parameters that are selected for both compression and tension are $k_{0c} = -0.0013$, $k_{0t} = -0.00025$, $b_c = 4.0$, $b_t = 0.7$, $p_c = 1.75$, $p_t = 0.6$ while unloading parameters are $c_{1c} = c_{1t} = 3.0$, $c_{2c} = 0.25$, $c_{2c} = 1.0$.

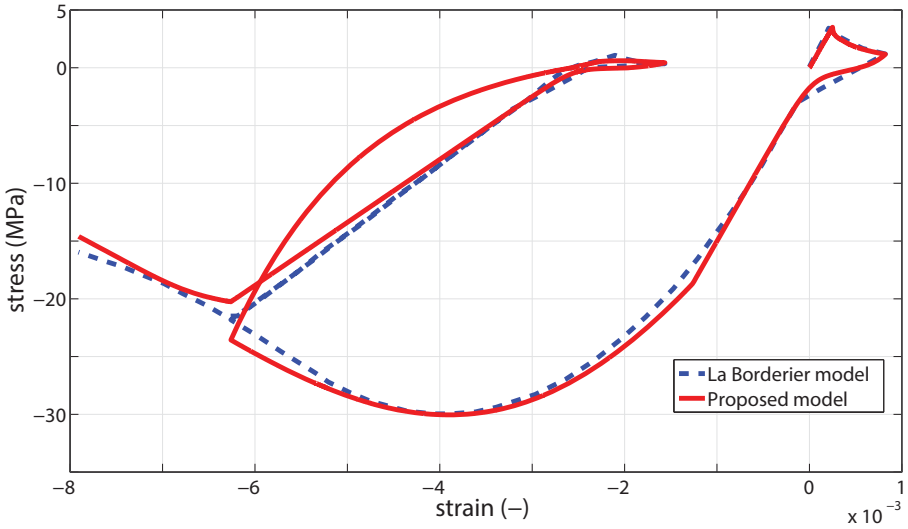

Figure 3.26. Comparison with the La Borderie concrete model.

Pseudo-Time (sec)	Strain (-)
0	0
1	0.008
2	-0.0062
3	-0.0016
4	-0.008

Table 3.13. Strain history for comparison with La Borderie concrete model.

3.6 Appendix I.

3.6.1 Modified Mander et al. model

Mander et al. (1988) proposed a uniaxial model to predict cyclic behavior of concrete, accounting also for the confinement effects. The model distinguishes three distinct phases of hysteretic response, namely the loading envelope curve, unloading and reloading in compression and unloading in tension. Later, model was improved by Martinez-Rueda and Elnashai (1997) to increase numerical stability under large excitations. In another modification of the original Mander et. al model, Chang and Mander (1994) incorporated stiffness recovery phenomenon due to the closing/reopening effect of the crack. The modified Martinez-Rueda and Elnashai model uses the same relations for the envelope $\sigma_c - \varepsilon_c$ curve, but the rules controlling strength and stiffness degradation, inelastic strain and nonlinear unloading are different. More specifically the magnitude of concrete stress under monotonic loading is given from the following relations:

$$\sigma_c = \frac{k f_{c0} \frac{\varepsilon_c}{\varepsilon_{cc}} r}{r - 1 + \left(\frac{\varepsilon_c}{\varepsilon_{cc}} \right)^r} \tag{3.40}$$

$$r = \frac{E_c}{E_c - \frac{\sigma_{cc}}{\varepsilon_{cc}}} \tag{3.41}$$

$$\varepsilon_{cc} = \varepsilon_{c0} \left[1 + 5 \left(\frac{\sigma_{cc}}{\sigma_{c0}} - 1 \right) \right] \tag{3.42}$$

where, σ_{c0} is the compressive maximum strength of the unconfined concrete is, σ_{cc} is the maximum strength of the confined concrete resulting from multiplying σ_{c0} with a scalar parameter k. Strain ε_{c0} is the strain at stress σ_{c0}, ε_{cc} is the strain at maximum concrete stress σ_{cc} and E_c is the initial modulus of elasticity of concrete. Also model assumes that confinement effect is constant throughout the whole range of the stress-strain curve. In tensile loading model behaves elastically $\sigma_c = E_c \cdot \varepsilon_c$ until maximum tensile strength is reached $\sigma_c \le \sigma_t$ and then, instantaneously, it loses total strength $\left(\sigma_c = 0,\ \sigma_c > \sigma_t \right)$.

The unloading curve is described by a second order parabola, starting from the reversal point $\left(\varepsilon_{un}, \sigma_{un} \right)$ and ending up to the point where full stress reversal is attained $\left(\varepsilon_{pl}, 0 \right)$

(Figure 3.27). The permanent inelastic strain depends on the current strain range and is given according to the following relations:

$$\varepsilon_{pl} = \varepsilon_{un} - \frac{\sigma_{un}}{E_c}, \quad 0 \le \varepsilon_{un} \le \varepsilon_{35} \tag{3.43}$$

$$\varepsilon_{pl} = \varepsilon_{un} - \frac{\varepsilon_{un} + \varepsilon_{\alpha}}{\sigma_{un} + E_c \varepsilon_{\alpha}}, \quad \varepsilon_{35} \le \varepsilon_{un} \le 2.5\varepsilon_{cc} \tag{3.44}$$

$$\varepsilon_{pl} = \frac{\sigma_{cr}\varepsilon_{un} - \left|\varepsilon_f\right|}{\sigma_{cr} + \sigma_{un}}, \quad 2.5\varepsilon_{cc} \le \varepsilon_{un} \tag{3.45}$$

where, ε_{35} is the strain corresponding to $0.35\sigma_c$ stress level until where concrete behavior is assumed elastoplastic. Under high strain level a focal point $\left(\varepsilon_f, \sigma_f\right)$ is defined based on the upper limit of the moderate strain range and its coordinates are given as:

$$\left|\varepsilon_f\right| = \frac{\sigma_{cr}\varepsilon_{pl,cr}}{E_c\left(\varepsilon_{cr}\varepsilon_{pl,cr}\right) - \sigma_{cr}} \tag{3.46}$$

$$\left|\sigma_f\right| = E_c\left|\varepsilon_f\right| \tag{3.47}$$

where, $\varepsilon_{cr} = 2.5\varepsilon_{cc}$ and $\varepsilon_{pl,cr}$ is the inelastic strain corresponding to strain $2.5\varepsilon_{cc}$.

Reloading in compression takes place in two steps, first reloading remains linear until point $\left(\varepsilon_{un}, \sigma_{new}\right)$, which is given from the following relation:

$$\sigma_{new} = \frac{0.9 f_{cc}\left(\dfrac{\varepsilon_c}{0.9\varepsilon_{cc}}\right) r}{r - 1 + \left(\dfrac{\varepsilon_c}{0.9\varepsilon_{cc}}\right)^r} \tag{3.48}$$

After reversal strain exceeds unloading strain ε_{un}, a second linear segment between point $\left(\varepsilon_{un}, \sigma_{new}\right)$ and point $\left(\varepsilon_{re}, \sigma_{re}\right)$ is considered, where:

$$\varepsilon_{re} = \frac{\varepsilon_{un}\left(1.00273 + 1.2651\dfrac{\varepsilon_{un}}{\varepsilon_{cc}}\right)}{2} \tag{3.49}$$

The Mander et al. (1988) concrete model with the modifications added from Martinez-Rueda and Elnashai (1997) is presented graphically in the following Figure 3.27

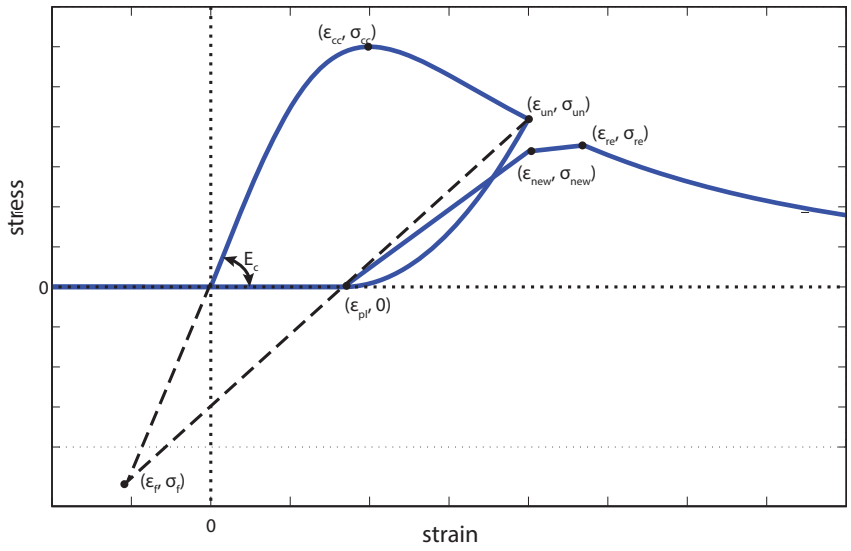

Figure 3.27. Martinez-Rueda and Elnashai concrete model

3.6.2 Konstantinidis and Kappos model

In contrary to previous models that were used to address mainly cyclic behavior of regular strength concrete, Konstantinidis and Kappos (2007) proposed an analytical model to predict cyclic behavior of high strength concrete. They proposed a three-branch envelope curve calibrated with experimental data, while for the unloading-reloading branches they adopted the relations from the Martinez-Rueda and Elnashai model. When strain resides in the ascending branch of the envelope curve stress is evoked from the following relation:

$$\sigma_c = \frac{\sigma_{cc}\dfrac{\varepsilon_c}{\varepsilon_{cc}}\dfrac{E_c}{E_c-\sigma_{cc}/\varepsilon_{cc}}}{\dfrac{E_c}{E_c-\sigma_{cc}/\varepsilon_{cc}}-1+\left(\dfrac{\varepsilon_c}{\varepsilon_{cc}}\right)^{E_c/(E_c-\sigma_{cc}/\varepsilon_{cc})}} \tag{3.50}$$

When strain exceeds strain value ε_{cc} at maximum stress the descending branch of the envelope is defined as:

$$\sigma_c = \sigma_{cc}\left[1-0.5\frac{\varepsilon_c-\varepsilon_{cc}}{\varepsilon_{0.5}-\varepsilon_{cc}}\right] \geq 0.3\sigma_{cc} \tag{3.51}$$

Where the strain at $0.5\sigma_{cc}$ value is calculated as:

$$\varepsilon_{0.5} = \left[\frac{E_c}{\sigma_{cc}/\varepsilon_{cc}}+1+\sqrt{\left(\frac{E_c}{2\sigma_{cc}/\varepsilon_{cc}}+1\right)^2-2}\right]\frac{0.7\sigma_c^{0.31}}{2000} \tag{3.52}$$

The plastic strain ε_{pl} and the loading-unloading rules were adopted from the Martinez-Rueda and Elnashai model and they were presented in equations (3.43)-(3.49) with the simplification that the unloading point $(\varepsilon_{un}, \sigma_{un})$ is considered identical with the point $(\varepsilon_{re}, \sigma_{re})$ where the reloading curve ends. Due to this simplification the loading-reloading loops close at the same point. Finally, the model for high strength concrete proposed by Konstantinidis and Kappos is illustrated in the following Figure 3.28:

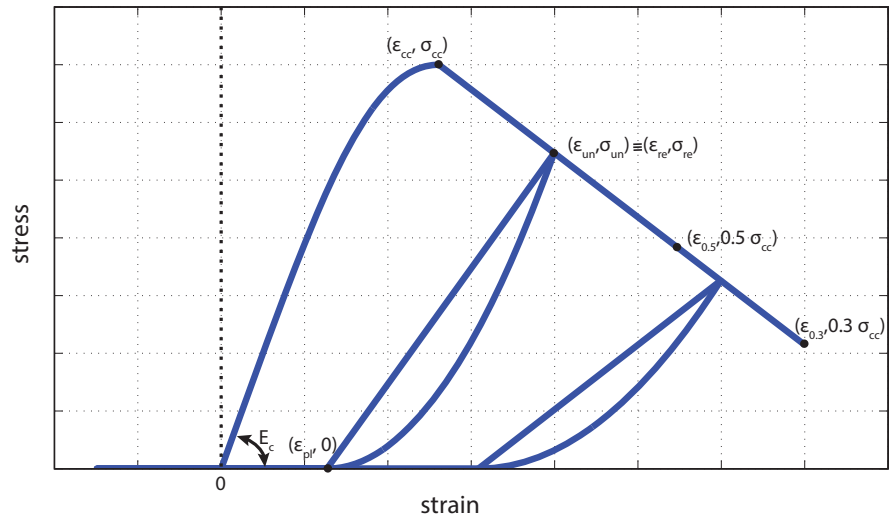

Figure 3.28. Konstantinidis and Kappos high strength concrete model

3.6.3 La Borderie damage model

One of the most well-known concrete models incorporating damage theory is the one proposed by La Borderie et al. (1994). The model takes into account crack opening/ closing phenomena and its general formulation is in the 3D space but only the uniaxial (1D) version is presented herein.

The total strain is presented as the sum of an elastic and an inelastic part:

$$\varepsilon = \varepsilon^e + \varepsilon^\alpha \tag{3.53}$$

$$\varepsilon^e = \frac{\sigma^+}{E(1-D_1)} + \frac{\sigma^-}{E(1-D_2)} \tag{3.54}$$

$$\varepsilon^a = \frac{\beta_1 \cdot D_1}{E(1-D_1)} F'(\sigma) + \frac{\beta_2 \cdot D_2}{E(1-D_2)} \tag{3.55}$$

where, E is the Young modulus, β_1, β_2 are model parameters and σ^+, σ^- are the tensile and compressive stresses respectively, given according to the following relations:

$$\sigma^{+} = \sigma \text{ and } \sigma^{-} = 0 \text{ for } \sigma > 0 \tag{3.56}$$

$$\sigma^{+} = 0 \text{ and } \sigma^{-} = \sigma \text{ for } \sigma < 0 \tag{3.57}$$

Also, $F(\sigma)$ is the function that controls crack opening/closing phenomena and is expressed in terms of the relations:

$$F'(\sigma) = \frac{\delta F}{\delta \sigma}$$

$$F(\sigma) = \begin{cases} \sigma \Rightarrow F'(\sigma) = 1 \text{ for } \sigma \geq 0 \\ \sigma\left(1 + \dfrac{\sigma}{2\sigma_f}\right) \Rightarrow F'(\sigma) = 1 + \dfrac{\sigma}{\sigma_f} \text{ for } \sigma_f \leq \sigma < 0 \\ \dfrac{-\sigma_f}{2} \Rightarrow F'(\sigma) = 0 \text{ for } \sigma < -\sigma_f \end{cases} \tag{3.58}$$

D_1, D_2 are the damage variables in tension and compression respectively, varying from 0 (no damage) to 1 (complete damage).Each variable D_i is driven by Y_i as follows:

$$D_i = 1 - \frac{1}{1 + \left[A_i\left(Y_i - Y_{0i}\right)\right]^{B_i}} \tag{3.59}$$

where, Y_{0i} is the damage threshold and A_i, B_i are model parameters. More specifically, damage driving variables in tension and compression are given from the following relations:

$$Y_1 = \frac{\left(\sigma^{+}\right)^2}{2E\left(1 - D_1\right)^2} + \frac{\beta_1 \cdot F(\sigma)}{E\left(1 - D_1\right)^2} \tag{3.60}$$

$$Y_2 = \frac{\left(\sigma^{-}\right)^2}{2E\left(1 - D_2\right)^2} + \frac{\beta_2 \cdot \sigma}{E\left(1 - D_2\right)^2} \tag{3.61}$$

La Borderie damage model is illustrated graphically in Figure 3.28.

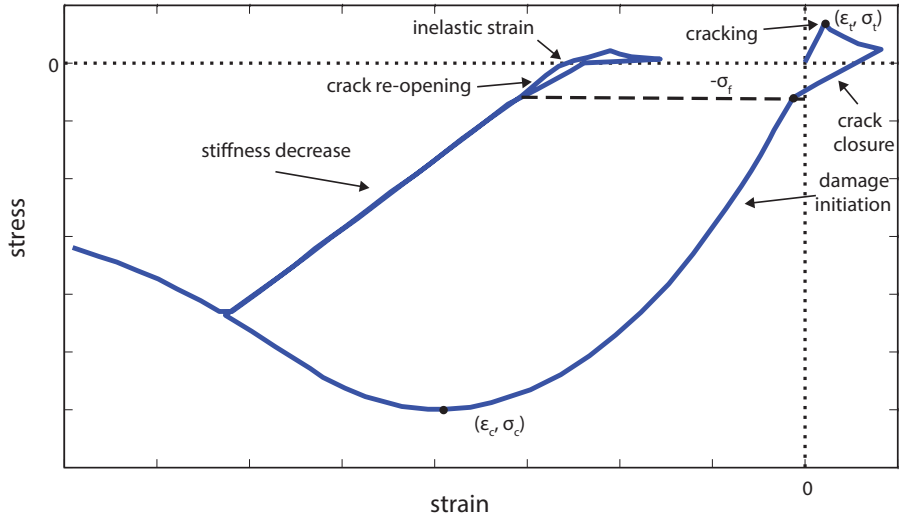

Figure 3.29. La Borderier concrete model

CHAPTER 4

Beam-Column Fiber Element

4.1 Introduction

The state of a deformable body subjected to body forces, tractions and kinematic boundary conditions is considered fully defined when the displacements, stresses and deformations are determined at any point of the body. In particular, for earthquake engineering and structural analysis of skeletal structures, beam elements usually based on the Euler-Bernoulli theory assumption that plane sections remain plane and perpendicular to the deformed axis are typically considered. This facilitates considerably the state determination problem of such elements.

In the context of distributed plasticity analysis, displacement based beam elements were initially utilized following the classical stiffness method in which displacements were the only considered independent field (Bathe 2007). When cubic and linear shape functions are employed for the transverse and axial displacements respectively, the resulting displacement field leads to constant axial deformation and linear curvature, which however is not appropriate when plastic deformations occur. To address this deficiency a structural member should be discretized in more than one element at the expense of increasing computational cost. Also, equilibrium equations are only accurate at element nodes, while within the element they are satisfied in weak form as they are not valid for all possible displacement fields that satisfy essential boundary conditions.

To resolve this problem, force based models were proposed that interpolate nodal forces within the element maintaining equilibrium. A thorough investigation on the advantages of the force based elements over the classic displacement based is presented by Fragiadakis and Papadrakakis (2008) and Calabrese et al. (2010). These models were implemented in the framework of the stiffness method of structural analysis and in that respect they are considered “mixed” as they use both force and displacement fields as independent ones. Zeris and Mahin (1988; 1991) used equilibrium and variable displacement interpolation functions in a linearized event to event context for the state determination problem. Later, one of the first consistent and general force based beam model was proposed by Spacone et al. (1996 a,b) which required element equations to satisfy element equilibrium and compatibility by introducing an internal loop in the element level to minimize deformations unbalance. This methodology was later simplified numerically by Neuenhofer and Filippou (1997) as they pushed element residual to the structural level, eliminating in such way the need for element iterations. Although the force based method proved very efficient and is currently widely used, there were some concerns about its variational consistency that were

resolved by Hjelmstad and Taciroglu (2002). Moreover, the same authors (Hjelmstad and Taciroglu 2005) showed that it is possible to provide non-variationally consistent force-based elements within the "nonlinear flexibility" framework by enforcing equilibrium directly, proving in such way that not all force-based elements have a variational base.

However, the variational structure of the mixed elements is important as it provides various local and global solution strategies to address the numerical solution problem as described by Nukala and White (2004) and Saritas and Soydas (2012). Thereafter, mixed methods seem to have the leading role in the research field of nonlinear beam problems and corresponding numerical procedures as they are proved more efficient. A lot of research work has been produced recently in the field following work of Hjelmstad and Taciroglu (2003), Taylor et al. (2003), Alemdar and White (2005), Alsafadie et al. (2011), Correia et al. (2015) and Gkimousis and Koumousis (2016).

Global solution of beam elements relies significantly on the material models used. Standard concrete and rebar models have an analytical structure, while others, like those that are developed in this dissertation, rely on the notions of yield and damage surface, flow rule and internal parameters. These models are incorporated in the state determination process in linearized form giving rise to the return-mapping algorithm (1985). On the other hand, cyclic behavior can also be modeled using hysteretic evolution differential equations as proposed by Simeonov et al. (2000). In their work a force based element was developed where material constitutive relations are considered in rate form and are solved simultaneously with the global differential equations of motion in state-space form. Also, Jafari et al. (2011) extended this formulation in large displacement analysis following a displacement based formulation. In addition Triantafyllou and Koumousis (2011; 2013) proposed a finite element procedure where material nonlinearity is treated constitutively at the element level through proper implementation of the Bouc-Wen hysteretic rule.

In this chapter both numerical methodologies are utilized by incorporating the proposed concrete and rebar models to a fiber beam-column element. Generally, global solution procedure in the context of distributed plasticity fiber beam elements consists of the following four stages (Figure 4.1).

1. Fiber level, where given axial strains and internal parameters, concrete and rebar fiber uniaxial stress and tangent Young modulus are derived.

2. Cross-section level, where fiber stresses and tangent moduli are summed up over the cross-section and stress resultants (axial force, bending moment), while also cross-sectional stiffness matrix are derived.
3. Element level, where element state determination takes place, namely the calculation of nodal internal forces and element tangent stiffness matrix through integration of cross-sectional stress resultants along element length. Different methodologies for the state determination process arise according to the treatment of element unknown fields, namely, displacement, stress and deformation field.
4. Structure level, where every element residual is summed up together by applying continuity at nodes, and global equilibrium is enforced in terms of external and internal nodal forces.

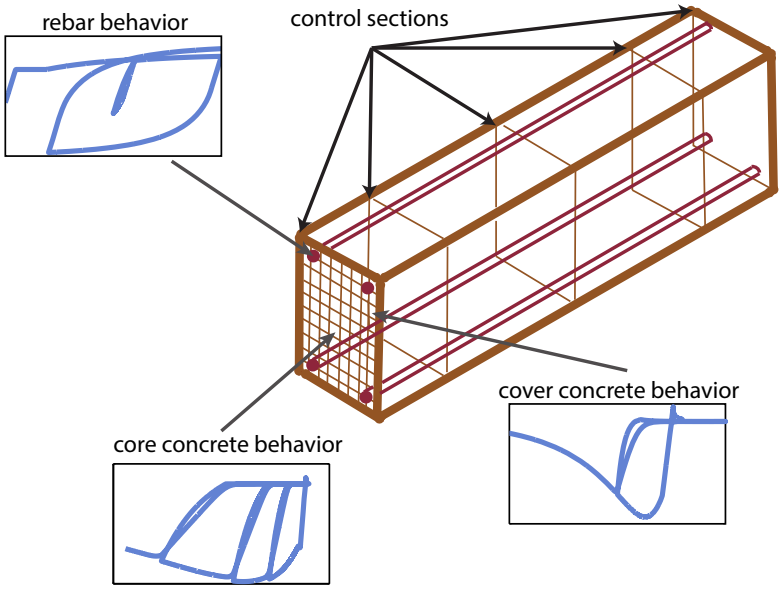

Figure 4.1. Fiber beam element schematic representation

Fiber level has been described rigorously in the previous chapters 2 and 3 for the distinct cases of concrete and steel rebar fibers. In this chapter a new small displacement fiber beam-column element is proposed, which incorporates the uniaxial cyclic concrete and rebar models developed. Cross-sectional stress resultants are derived by mid-point fiber integration, while element state determination is implemented in the general framework of both classical stiffness and mixed two-field Hellinger-Reissner formulation. Element equilibrium and compatibility equations are derived from variational principles which result in well-established state determination algorithms. Finally, advantages of the mixed formulation over the displacement based formulation are revealed both for the hardening and softening material case.

4.2 Cross-sectional constitutive relations

Cross-sectional constitutive relations are derived from integration of the local constitutive equations of all unit length fibers using midpoint integration. Especially for planar analysis and symmetrical cross-sections, fibers can be treated in layers (Figure 4.2). Following the Euler-Bernoulli beam theory the normal stress $\sigma(x,y)$, the axial strain $\varepsilon(x,y)$ and the axial and transverse displacements $u_x(x,y), u_y(x,y)$ are considered.

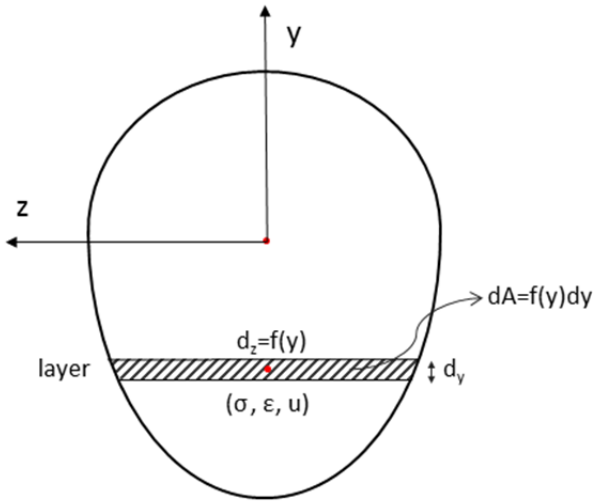

Figure 4.2 Cross-sectional local axis and layer definition

By considering the kinematic assumption that plane sections before deformation remain plane and normal to the elastic line after deformation, the axial displacement $u_x(x,y)$ of any fiber can be expressed in terms of the displacement of the beam reference axis x as:

$$u_x(x,y) = u(x) - y \cdot \frac{\partial w(x)}{\partial x} \tag{4.1}$$

where $u(x)$ and $w(x)$ are the axial and transverse displacements of the cross-section at the reference axis. Thus the following relation holds for the axial strain:

$$\varepsilon(x,y) = \varepsilon_0(x) - y \cdot \varphi(x) = \begin{bmatrix} 1 & -y \end{bmatrix} \cdot \boldsymbol{d}(x) = \boldsymbol{l}^T \cdot \boldsymbol{d}(x) \tag{4.2}$$

where the deformation field $\boldsymbol{d}(x) = \left\{ \varepsilon_0(x),\ \varphi(x) \right\}^T$ consists of the axial strain $\varepsilon_0(x)$ and curvature $\varphi(x)$ at the reference axis. Euler-Bernoulli beam theory considers only the effects of axial stress σ_x, thus by applying equilibrium conditions within the cross-section, the stress resultants are evaluated by integration of stresses over the cross-section areas as follows:

$$N(x)=\int_A \sigma(x,y)dA \quad , \quad M(x)=-\int_A y\cdot\sigma(x,y)dA \tag{4.3}$$

The same relations can be casted in matrix form as:

$$\boldsymbol{D}(x)=\int_A \begin{bmatrix}1 & -y\end{bmatrix}^T\cdot\sigma(x,y)dA \tag{4.4}$$

where $\boldsymbol{D}(x)=\left\{N(x),M(x)\right\}^T$. Also, the axial stress is given with the following relation in rate form (see also chapters 2, 3):

$$\dot{\sigma}(x,y)=E_t\cdot\dot{\varepsilon}(x,y) \tag{4.5}$$

By replacing equation (4.5) along with equation (4.2) in the rate form of equation (4.4) the "cross-sectional constitutive relation" is derived:

$$\dot{\boldsymbol{D}}(x)=\boldsymbol{k}(x)\cdot\dot{\boldsymbol{d}}(x) \tag{4.6}$$

with

$$\begin{aligned}\boldsymbol{k}(x)&=\int_A \begin{bmatrix}1 & -y\end{bmatrix}^T\cdot E_t\cdot\begin{bmatrix}1 & -y\end{bmatrix}dA\\ &=\begin{bmatrix}\sum_{i=1}^{n(x)}\left(E_t\cdot A\right)_i & -\sum_{i=1}^{n(x)}\left(E_t\cdot A\right)_i\cdot y_i\\ -\sum_{i=1}^{n(x)}\left(E_t\cdot A\right)_i\cdot y_i & \sum_{i=1}^{n(x)}\left(E_t\cdot A\right)_i\cdot y_i^2\end{bmatrix}\end{aligned} \tag{4.7}$$

where, $n(x)$ is the number of fibers in the cross-section placed at "x" distance from the element start node. Finally, the flexibility matrix of the cross-section is set as the inverse of the cross-sectional stiffness.

$$\boldsymbol{f}(x)=\boldsymbol{k}(x)^{-1} \tag{4.8}$$

Integrals in relations (4.4) and (4.7) over the cross-section are derived using mid-point fiber integration. This means that a material fiber area A_i over a cross-section is represented by a point at the centroid of the fiber with normal stress σ_i and axial strain ε_i. Fiber integration error reduces rapidly by increasing the number of fibers or layers in the uniaxial case. Generally *20-30* layers for the concrete confined core while *10-15* layers for unconfined cover are adequate for 2D problems. Alternatively, Fafitis (2001) used Green's theorem to convert area to line integration, while Marmo and Rosati (2012; 2013) implemented the so called "fiber-free approach" where stress resultants and stiffness matrix are calculated analytically on a polygonal cross-sectional area.

4.3 Element state determination

A crucial step during a nonlinear numerical procedure is the determination of every element nodal internal forces and tangent stiffness. Having the inelastic constitutive equation for a cross-section via equations (4.6) and (4.7), the next step is to define the overall nonlinear response of the element. This refers to the displacement, deformation and stress fields across the beam length and the tangent stiffness matrix at every point of the nonlinear path during dynamic loading. Moreover, at the boundaries the three fields are interpreted as nodal values. The standard six nodal displacements and rotations for the 2D beam-column element in uniaxial bending $\bar{\boldsymbol{u}} = \{u_1, u_2, r_1, u_4, u_5, r_2\}^T$, are related with deformations $\boldsymbol{q} = \{\delta, \theta_1, \theta_2\}^T$ i.e. axial deformation δ along the reference axis and the chord rotations at both ends. In addition the stress resultants $\boldsymbol{Q} = \{N, M_1, M_2\}^T$ are introduced as presented in Figure 4.3.

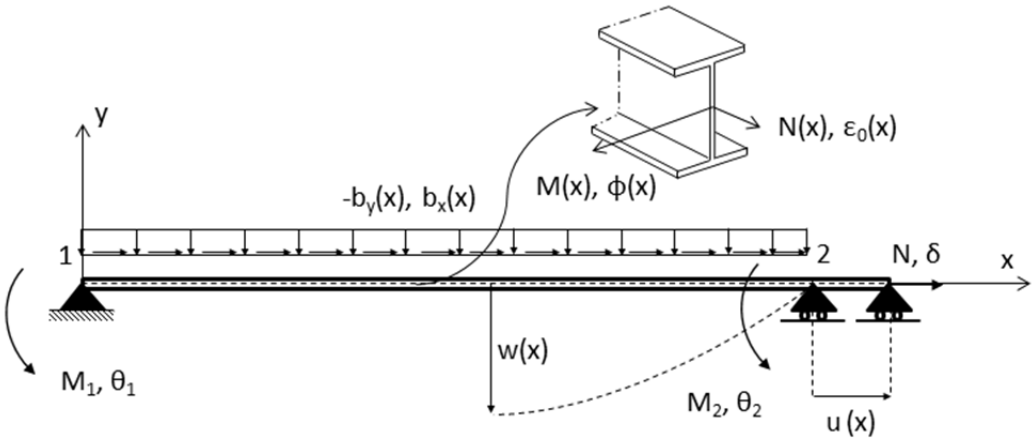

Figure 4.3**.** Basic forces, displacements, deformations and distributed loads on the beam element

The relation between the nodal displacements and member deformations is established with the transformation matrix $\boldsymbol{T}$, which removes rigid body motion as follows (

Figure 4.4):

$$\boldsymbol{q} = \boldsymbol{T} \cdot \bar{\boldsymbol{u}}, \quad \boldsymbol{T} = \begin{bmatrix} 1 & 0 & 0 & -1 & 0 & 0 \\ 0 & 1/L & 1 & 0 & -1/L & 0 \\ 0 & 1/L & 0 & 0 & -1/L & 1 \end{bmatrix} \tag{4.9}$$

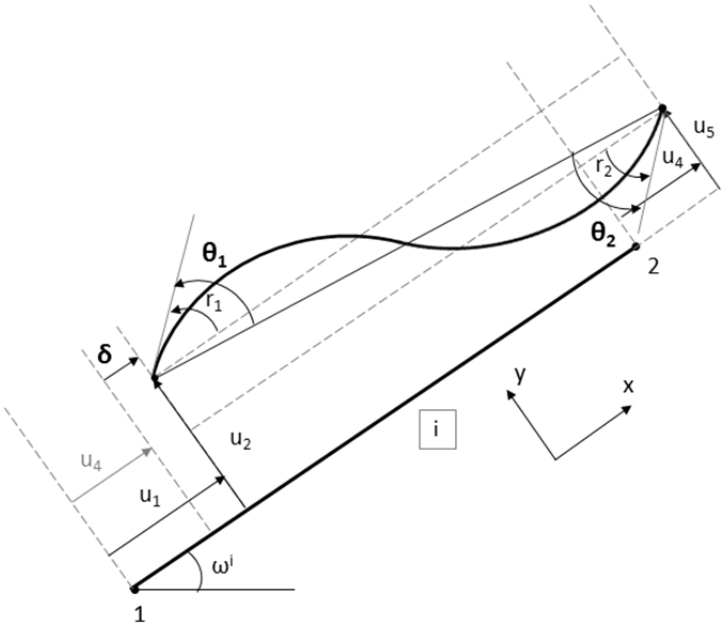

Figure 4.4. Displacements and deformations of beam element i

Also, element equilibrium under distributed applied loads $\boldsymbol{b(x)} = \left[b_x(x), b_y(x) \right]^T$ in both directions x, y requires:

$$\frac{\partial^2 M(x)}{\partial x^2} - b_y(x) = 0$$
$$\frac{\partial N(x)}{\partial x} - b_x(x) = 0 \qquad (4.10)$$

In the following sections, two basic methods for the element state determination process are presented. The first one is the classical stiffness method where the only independent field is the displacement field, while both forces and deformations are derived from displacements. The second approach is a mixed formulation where both displacements and forces are the independent fields.

4.4 Displacement based formulation

4.4.1 Variational derivation

In the displacement based or stiffness based formulation, deformations depend on displacements as they can be calculated from proper differentiations of the displacement field and then stresses are functions of deformations $\sigma(\varepsilon)$ while they are calculated from the strain driven constitutive laws. In the core of the stiffness method the principle of virtual displacements exists, which introduces a virtual displacement field that imposes the equality

between internal and external work. For a fiber Euler-Bernoulli beam the difference of internal and external works gives the following functional:

$$\Pi_u(u) = \int_V \{\varepsilon(u)\cdot\sigma(\varepsilon)\}dV - \Pi_{ext}(u) \tag{4.11}$$

Where, $\Pi_{ext}(\bar{\boldsymbol{u}})$ is the functional of external loading and integration is performed at the undeformed volume V of the element. If the integration over the beam volume V in relation (4.11) is decomposed into integration over the beam length L and cross-sectional area A the following calculations are performed:

$$\begin{aligned}\Pi_u(u) &= \int_0^L \left(\int_A \{\varepsilon(u)\cdot\sigma(\varepsilon)\}dV \right) - \Pi_{ext}(u) \\ &= \int_0^L \boldsymbol{d}^T \left(\int_A \{\boldsymbol{I}^T\cdot\sigma(\varepsilon)\}dA \right) dx - \Pi_{ext}(u) \\ &= \int_0^L \left(\boldsymbol{d}^T\cdot\boldsymbol{D}\right) dx - \Pi_{ext}(u)\end{aligned} \tag{4.12}$$

Axial strains $\varepsilon(x,y)$ at any fiber of the cross-section are expressed in terms of centerline deformations $\boldsymbol{d}(x)$ using relation (4.2). In addition functional $\Pi_{ext}(u)$ for a beam element with distributed applied loads $\boldsymbol{b}(x) = \left[b_x(x), b_y(x)\right]^T$ and nodal external loads $\boldsymbol{F_n}$ is given as:

$$\Pi_{ext}(\bar{\boldsymbol{u}}) = \boldsymbol{q}^T\cdot\boldsymbol{F_n} + \int_0^L \boldsymbol{u}^T(x)\cdot\boldsymbol{b}\, dx \tag{4.13}$$

Consequently, the functional of relation (4.11) is expressed in stress and deformation resultants terms as follows:

$$\Pi_u(\bar{\boldsymbol{u}}) = \int_0^L \left(\boldsymbol{d}^T\cdot\boldsymbol{D}\right) dx - \boldsymbol{q}^T\cdot\boldsymbol{F_n} - \int_0^L \bar{\boldsymbol{u}}^T\cdot\boldsymbol{b}\, dx \tag{4.14}$$

Any deformable beam is in equilibrium when the functional of equation (4.14) obtains its minimum value. This is accomplished by imposing stationarity of the functional by setting its first variation with respect to the displacement field equal to zero.

$$\begin{aligned}\delta\Pi_u = \int_0^L \left(\delta\boldsymbol{d}^T\cdot\boldsymbol{D}\right) dx - \delta\bar{\boldsymbol{u}}^T\cdot\boldsymbol{F_n} - \int_0^L \delta\boldsymbol{u}^T\cdot\boldsymbol{b}\, dx \;= 0 \Rightarrow \\ \int_0^L \left(\delta\boldsymbol{d}^T\cdot\boldsymbol{D}\right) dx \;= \delta\bar{\boldsymbol{u}}^T\cdot\boldsymbol{F_n} + \int_0^L \delta\boldsymbol{u}^T\cdot\boldsymbol{b}\, dx\end{aligned} \tag{4.15}$$

Equation (4.15) is the weak form of the equilibrium equation as equilibrium between external loads and internal forces is satisfied in an average form, while point-wise equilibrium at every beam cross-section is not valid.

To proceed with the formulation, the internal displacement field across the element's length must be expressed as a function of the nodal displacement values $\bar{\boldsymbol{u}}$. This is accomplished in classical FEM with the linear combination of known polynomial shape functions $\boldsymbol{N}_u$.

$$\boldsymbol{u}(x) = \boldsymbol{N}_u(x) \cdot \bar{\boldsymbol{u}} \tag{4.16}$$

where

$$\boldsymbol{N}_u = \begin{bmatrix} N_1(x) & 0 & 0 & N_2(x) & 0 & 0 \\ 0 & N_3(x) & N_4(x) & 0 & N_5(x) & N_6(x) \end{bmatrix}$$

$$\begin{aligned} N_1(x) &= 1 - \frac{x}{L}, & N_2(x) &= \frac{x}{L} \\ N_3(x) &= 2\frac{x^3}{L^3} - 3\frac{x^2}{L^2} + 1, & N_4(x) &= \frac{x^3}{L^2} - 2\frac{x^2}{L} + x \\ N_5(x) &= -2\frac{x^3}{L^3} + 3\frac{x^2}{L^2}, & N_6(x) &= \frac{x^3}{L^2} - \frac{x^2}{L} \end{aligned} \tag{4.17}$$

Also, deformations $\boldsymbol{d}(x)$ along beam length are expressed as derivatives of displacements leading to the following interpolation relations:

$$\boldsymbol{d}(x) = \hat{\partial}\left(\boldsymbol{N}_u(x)\right) \cdot \bar{\boldsymbol{u}} = \boldsymbol{N}_d(x) \cdot \boldsymbol{q} = \boldsymbol{N}_d(x) \cdot \boldsymbol{T} \cdot \bar{\boldsymbol{u}} \tag{4.18}$$

where

$$\boldsymbol{N}_d = \begin{bmatrix} \frac{1}{L} & 0 & 0 \\ 0 & \frac{6x}{L^2} - \frac{4}{L} & \frac{6x}{L^2} - \frac{2}{L} \end{bmatrix} \tag{4.19}$$

Shape functions $\boldsymbol{N}_u$ and $\boldsymbol{N}_d$ account for constant distribution of axial deformation along the element length and linear distribution of curvature, while they are used for any representation of the interpolated displacement and deformation field, namely their normal, virtual or incremental form. This is the source of inaccuracies of the displacement based formulation as the outcome displacement field loses accuracy in the nonlinear case where curvature distribution becomes nonlinear. It should be also noted that equilibrium equation (4.15) is not satisfied for every admissible displacement field that satisfies essential

boundary conditions, but is only satisfied for the applied displacement field described by the shape functions. For this reason equilibrium is not satisfied in a strong form but only in an average sense. By substituting equations (4.6), (4.9), (4.16) and (4.18) in equation (4.15) and after performing some algebraic calculations, we end to the discrete form of the equilibrium equation.

$$\begin{aligned} &\boldsymbol{T}^{T}\cdot\boldsymbol{Q}=\boldsymbol{T}^{T}\cdot\bar{\boldsymbol{P}}_{n}+\int_{0}^{L}\boldsymbol{N}_{u}^{T}\cdot\boldsymbol{b}\;dx\;\Rightarrow \\ &\boldsymbol{P}_{ext}=\left(\boldsymbol{T}^{T}\cdot\boldsymbol{K}\cdot\boldsymbol{T}\right)\cdot\bar{\boldsymbol{u}} \end{aligned} \tag{4.20}$$

where $\boldsymbol{K}$ is the element's tangent stiffness matrix and is calculated as:

$$\boldsymbol{K}=\int_{0}^{L}\left(\boldsymbol{N}_{d}^{T}\cdot\boldsymbol{k}(x)\cdot\boldsymbol{N}_{d}\right)dx \tag{4.21}$$

$\boldsymbol{P}_{ext}$ are the end forces due to element loads. Also, the vector of element's internal nodal forces is derived through integration of cross-sectional forces over its length as:

$$\boldsymbol{Q}=\int_{0}^{L}\left(\boldsymbol{N}_{d}^{T}\cdot\boldsymbol{D}(x)\right)dx \tag{4.22}$$

Equation (4.20) is nonlinear as the cross-sectional tangent stiffness ***k(x)*** is a function of every fiber's material tangent modulus. Linearization of this equation leads to the solution of the problem incrementally by applying for example Newton's method for the global equations and a forward Euler method for the solution of the incremental evolution constitutive equations. Apart from this classic solution process the advantage of expressing the constitutive equations in rate form is exploited further in order to form a DAE system for the static or ODE system for the transient problem which then is solved in state space form.

4.4.2 Solution via linearization

As the displacement field is the only independent field, linearization is performed with respect to displacements. Considering an increment $\Delta\bar{\boldsymbol{u}}^{i}$ in the current configuration i with respect to nodal displacements $\left(\bar{\boldsymbol{u}}^{i+1}=\bar{\boldsymbol{u}}^{i}+\Delta\bar{\boldsymbol{u}}^{i}\right)$, deformation field is updated according to shape functions $\boldsymbol{N}_{d}$:

$$\boldsymbol{d}^{i+1}=\boldsymbol{d}^{i}+\Delta\boldsymbol{d}^{i}=\boldsymbol{d}^{i}+\boldsymbol{N}_{d}\Delta\bar{\boldsymbol{u}}^{i} \tag{4.23}$$

Similarly, internal cross-sectional forces $\boldsymbol{D}(x)$ are linearized with respect to the deformation increment as follows:

$$\boldsymbol{D}(x)^{i+1} = \boldsymbol{D}(x)^{i} + \boldsymbol{k}(x)^{i} \cdot \Delta \boldsymbol{d}(x)^{i} \tag{4.24}$$

where, cross-sectional tangent stiffness $\boldsymbol{k}(x)^{i}$ at current configuration is evaluated from equation (4.7). By substituting relation (4.24) in equation (4.20) the global incremental equilibrium equation is derived as:

$$\begin{aligned} &\boldsymbol{K}^{i} \cdot \Delta \bar{\boldsymbol{u}}^{i} = \boldsymbol{P}_{ext}{}^{i+1} - \boldsymbol{T}^{T} \cdot \boldsymbol{Q}^{i} \;\Rightarrow \\ &\boldsymbol{K}^{i} \cdot \Delta \bar{\boldsymbol{u}}^{i} = \boldsymbol{P}_{ext}{}^{i+1} - \bar{\boldsymbol{Q}}_{int}{}^{i} \end{aligned} \tag{4.25}$$

The basic steps for the solution of the element state determination are briefly described as implemented in structural analysis of frame structures.

1. After solving an incremental step for the whole structure's equilibrium, the vector of incremental nodal displacements is determined. Mapping the global structure's displacements to every element, incremental element's nodal displacements $\Delta \bar{\mathbf{u}}^{i}$ have been defined and the element state determination begins.
2. Cross-sectional incremental deformations are evaluated from interpolation considerations (relation (4.23)) and incremental fiber strains are evaluated from equations (4.2) and (4.23) as:

$$\Delta \varepsilon^{i}(x,y) = [-1 \quad y] \cdot \boldsymbol{N}_{\boldsymbol{d}}(x) \cdot \boldsymbol{T} \cdot \Delta \bar{\boldsymbol{u}}^{i} \tag{4.26}$$

3. In this step updated tangent material modulus E_t^{i+1} and fiber stress σ^{i+1} separately for concrete and rebar fibers are calculated according paragraphs §2.2.4 and §3.2.6. Also internal variables for every fiber are stored in memory.
4. Integration over the cross-sectional area using relations (4.4) and (4.7) provides cross-sectional tangent stiffness $\boldsymbol{k}(x)^{i}$ and internal forces $\boldsymbol{D}(x)^{i+1}$.
5. Integration over the element length using relations (4.21) and (4.22) provides element stiffness $\boldsymbol{K}^{i}$ and nodal forces $\boldsymbol{Q}^{i+1}$.
6. By assembling every element's contribution global structure's stiffness matrix $\boldsymbol{K}_{\boldsymbol{s}}^{i}$ and nodal internal forces $\boldsymbol{P}_{int}^{i+1}$ are derived.
7. Finally, every element's residual is raised at the structural level and tolerance is checked: $\left\| \boldsymbol{P}_{ext}^{i+1} - \boldsymbol{P}_{int}^{i+1} \right\| \le tol$.

4.4.3 Solution in state space form

The formulation of the constitutive equations in rate form provides the opportunity to solve element constitutive relations at the control sections simultaneously with the global equilibrium equations of the structure. Introducing the rate of cross-sectional internal forces $\dot{\boldsymbol{D}}(x)$ of equation (4.6) in equation (4.22), the rate of element nodal forces $\dot{\boldsymbol{Q}}$ are derived as:

$$\begin{aligned} &\dot{\boldsymbol{Q}} = \int_0^L \left(\boldsymbol{N}_{\boldsymbol{d}}^T \cdot \dot{\boldsymbol{D}}(x) \right) dx = \int_0^L \left(\boldsymbol{N}_{\boldsymbol{d}}^T \cdot k(x) \dot{\mathrm{d}}(x) \right) dx = \int_0^L \left(\boldsymbol{N}_{\boldsymbol{d}}^T \cdot k(x) \cdot \boldsymbol{N}_{\boldsymbol{d}} \right) \cdot \dot{\bar{\boldsymbol{u}}}\, dx \Rightarrow \\ &\dot{\boldsymbol{Q}} = \boldsymbol{K} \cdot \dot{\bar{\boldsymbol{u}}} \end{aligned} \tag{4.27}$$

Then the time derivative of the element's equilibrium equation (4.20) offers the following equation:

$$\dot{\boldsymbol{P}}_{\boldsymbol{ext}} = \left(\boldsymbol{T}^T \cdot \boldsymbol{K} \cdot \boldsymbol{T} \right) \cdot \dot{\bar{\boldsymbol{u}}} \tag{4.28}$$

In the dynamic case the 2nd order linear differential equation of motion has the following standard form:

$$\boldsymbol{M}_{\boldsymbol{S}} \cdot \ddot{\boldsymbol{u}}_{\boldsymbol{S}} + \boldsymbol{C}_{\boldsymbol{S}} \cdot \dot{\boldsymbol{u}}_{\boldsymbol{S}} + \boldsymbol{P}_{\boldsymbol{int}} = \boldsymbol{P}_{\boldsymbol{ext}}(t) \tag{4.29}$$

These equations along with the constitutive evolution equations are solved in state space form by adding the velocities as additional unknown vector in the system unknowns $\{\boldsymbol{x}\} = \{\boldsymbol{u}_{\boldsymbol{S}} \quad \dot{\boldsymbol{u}}_{\boldsymbol{S}} \quad \sigma_i\}^T$. Stress vector σ_i contains the stresses at all internal points of all elements where nonlinear material behavior is monitored. In the fiber discretization scheme the dimension of the stress vector is the number of all fibers of the structure. Consequently, the following 1st order ODE system is formed.

$$\{\dot{\boldsymbol{x}}\} = \begin{Bmatrix} \dot{\boldsymbol{u}}_{\boldsymbol{S}} \\ \ddot{\boldsymbol{u}}_{\boldsymbol{S}} \\ \dot{\sigma}_i \end{Bmatrix} = \begin{Bmatrix} \dot{\boldsymbol{u}}_{\boldsymbol{S}} \\ -\boldsymbol{M}_{\boldsymbol{S}}^{-1} \cdot \left(\boldsymbol{C}_{\boldsymbol{S}} \cdot \dot{\boldsymbol{u}}_{\boldsymbol{S}} + \boldsymbol{P}_{\boldsymbol{int}} - \boldsymbol{P}_{\boldsymbol{ext}}(t) \right) \\ E_i \cdot \dot{\varepsilon}_i \,,\ i = 1 \ldots N_{fibs} \end{Bmatrix} \tag{4.30}$$

Where, rate constitutive equation for every material has been derived in chapters 2and 3 for steel rebar and concrete fibers respectively. In every time step of the solution process the global vector of internal forces $\boldsymbol{P}_{\boldsymbol{int}}$ is calculated from every element fiber stresses when equations (4.4) and (4.22) are used and element nodal forces are assembled to the structural level. Additionally, fiber strain rates $\dot{\varepsilon}_i$ are derived from interpolation of nodal element velocities $\dot{\bar{\boldsymbol{u}}}$ using the standard interpolation function in rate form:

$$\dot{\varepsilon}(x,y) = [-1 \quad y] \cdot \boldsymbol{N_d}(x) \cdot \boldsymbol{T} \cdot \Delta\dot{\boldsymbol{u}} \tag{4.31}$$

4.5 Two field beam element variational formulation

4.5.1 Variational derivation

Classical stiffness analysis of frame structures is based on the continuity of the displacement field between elements. This is accomplished explicitly as the cubic interpolation functions satisfy the kinematic boundary conditions at the end nodes. On the other hand, in the pure force formulation based on the principle of virtual forces, only the stress field is independent and interpolation functions based on element equilibrium relate internal and nodal forces. For a single element analysis, force based method is straightforward as interpolation base functions that satisfy essential boundary conditions and external applied loading can easily be defined. However, in a redundant structure a set of redundant forces must be introduced (Hjelmstad and Taciroglu 2002) the selection of which though is difficult to automate. For these reasons stiffness formulation is usually the efficient way to express equilibrium at the structural level. In addition the advantages of the flexibility approach to impose element equilibrium in strong form and derive an exact stiffness matrix in the nonlinear range are explored at the element level. Hence, flexibility approach for the element state determination requires the independency of the stress field, while stiffness based formulation at the structural level suggests the displacement field as independent. Considering the two fields as independent the Hellinger-Reissner energy principle is employed, hence the cross-sectional deformations are expressed in two ways; in terms of displacements ***d(u)*** and as functions of stress resultants ***d(D)*** .

Performance and accuracy of all beam element formulation methods depend primarily on the aspects of mesh refinement and interpolation order (Hjelmstad and Taciroglu 2005). However, for the standard cubic shape function interpolation for the transverse displacements and linear functions for moment distribution, mixed methods appear to dominate the classical displacement based formulation as they satisfy element equilibrium piece-wisely. The equilibrium error is of major importance, as internal forces are overestimated leading to inaccurate structural response. Two or three field methods based on Hellinger-Reissner or Hu-Washizu principles respectively are able to diminish this error successfully. Hellinger-Reissner principle considers the displacement and stress fields as independent and the deformation field expressed in terms of displacements or stresses, hence the size of the problem can be reduced as compared to a three-field formulation.

For a fiber beam under uniaxial deformation with stress σ and strain ε the Hellinger-Reissner functional (1950) can be stated in terms of the two independent sets of variables i.e. the normal stress σ and axial displacement u as follows:

$$\Pi_{HR}(\sigma,u)=\int_V\{\varepsilon(u)\cdot\sigma-\chi(\sigma)\}dV-\Pi_{ext}(u) \tag{4.32}$$

where $\chi(\sigma)$ is the complementary energy density function from which strains can be calculated in terms of stresses, $\Pi_{ext}(u)$ is the functional of external loading and integration is performed at the undeformed volume V of the element. More specifically Hellinger-Reissner functional of equation (4.32) is an energy functional and it exists only under the condition that material constitutive equation is hyperelastic. This means that there exists a stress energy function $\chi(\sigma)$ where strains are derived in terms of stresses such that:

$$\varepsilon=\frac{\partial\chi(\sigma)}{\partial\sigma} \tag{4.33}$$

Similarly to the displacement based method the above functional can be written also in stress resultant and deformation terms omitting for simplicity the argument in the integrals i.e. $\left(\boldsymbol{D}(x)=\boldsymbol{D}\right)$.

$$\Pi_{HR}(\boldsymbol{D},\boldsymbol{u})=\int_0^L\left\{\boldsymbol{d}(\boldsymbol{u})^T\cdot\boldsymbol{D}-\chi(\boldsymbol{D})\right\}dx-\Pi_{ext}(\boldsymbol{u}) \tag{4.34}$$

Complementary energy functional can now be expressed as:

$$d(\boldsymbol{D})=\frac{\partial\chi(\boldsymbol{D})}{\partial\boldsymbol{D}} \tag{4.35}$$

Also, the functional of external loading for nodal loads $\boldsymbol{F_n}$ and distributed loads $\boldsymbol{b}(x)=\left[b_x(x),b_y(x)\right]^T$ obtains the form:

$$\Pi_{ext}=\overline{\boldsymbol{u}}\cdot\boldsymbol{F_n}+\int_0^L\boldsymbol{u}^T\cdot\boldsymbol{b}\,dx \tag{4.36}$$

In order to calculate the state of the element under equilibrium stationarity of the Hellinger-Reissner functional is imposed. This is accomplished by setting its first variation with respect to the two independent fields equal to zero.

$$\delta\Pi_{HR} = \int_0^L \left(\delta \boldsymbol{d}(\boldsymbol{u})^T \cdot \boldsymbol{D}\right) dx + \int_0^L \delta \boldsymbol{D}^T \cdot \left(\boldsymbol{d}(\boldsymbol{u}) - \boldsymbol{d}(\boldsymbol{D})\right) dx - \delta \bar{\boldsymbol{u}}^T \cdot \boldsymbol{F}_n - \int_0^L \delta \boldsymbol{u}^T \cdot \boldsymbol{b}\, dx = 0 \quad (4.37)$$

Then for all variations $\delta\boldsymbol{u}(x)$ and $\delta\boldsymbol{D}(x)$ the state defined by $\left(\boldsymbol{u}(x), \boldsymbol{D}(x)\right)$ satisfies the classical equilibrium (4.38) and strain-displacement compatibility (4.39) equations.

$$\int_0^L \left(\delta \boldsymbol{d}(\boldsymbol{u})^T \cdot \boldsymbol{D}\right) dx - \delta \bar{\boldsymbol{u}}^T \cdot \boldsymbol{F}_n - \int_0^L \delta \boldsymbol{u}^T \cdot \boldsymbol{b}\, dx = 0 \quad (4.38)$$

$$\int_0^L \delta \boldsymbol{D}^T \cdot \left(\boldsymbol{d}(\boldsymbol{u}) - \boldsymbol{d}(\boldsymbol{D})\right) dx = 0 \quad (4.39)$$

Then, in the above relation the independent fields are expressed as linear combinations of shape functions and corresponding nodal values. For the displacement field and the deformations that depend on displacements ***d(u)*** the classical cubic interpolation functions are considered:

$$\begin{aligned} &\boldsymbol{u}(x) = \boldsymbol{N}_u(x) \cdot \bar{\boldsymbol{u}} \\ &\boldsymbol{d}\left(\boldsymbol{u}(x)\right) = \partial\left(\boldsymbol{N}_u(x)\right) \cdot \bar{\boldsymbol{u}} = \boldsymbol{N}_d(x) \cdot \boldsymbol{q} = \boldsymbol{N}_d(x) \cdot \boldsymbol{T} \cdot \bar{\boldsymbol{u}} \end{aligned} \quad (4.40)$$

For the stress field expressed in stress resultant terms, cross-sectional internal forces are calculated from nodal internal forces based on equilibrium considerations. More specifically, equilibrium equations (4.10) are directly integrated and by applying as essential boundary conditions the internal nodal forces, the following interpolation relation is derived.

$$\boldsymbol{D}(x) = \boldsymbol{N}_D(x) \cdot \boldsymbol{Q} + \boldsymbol{D}_p \;,\quad \boldsymbol{N}_D(x) = \begin{bmatrix} 1 & 0 & 0 \\ 0 & \frac{x}{L} - 1 & \frac{x}{L} \end{bmatrix} \quad (4.41)$$

where, $\boldsymbol{D}_p$ is the particular solution of the direct integration and can be completely determined by the applied loads. Also, the interpolation of the variation of the stress field, since $\boldsymbol{D}_p$ is a known function, has the following form:

$$\delta\boldsymbol{D}(x) = \boldsymbol{N}_D(x) \cdot \delta\boldsymbol{Q} \quad (4.42)$$

Substituting equations (4.40), (4.41) and (4.42) into the functional (4.37) the following discrete form is derived:

$$\delta\Pi_{HR} = \delta\bar{\boldsymbol{u}}^{T} \cdot \left\{ \boldsymbol{T}^{T} \cdot \int_{0}^{L} \boldsymbol{N}_{d}^{T} \cdot \left(\boldsymbol{N}_{D} \cdot \boldsymbol{Q} + \boldsymbol{D}_{p} \right) dx - \int_{0}^{L} \boldsymbol{N}_{u}^{T} \cdot \boldsymbol{b}\, dx - \boldsymbol{F}_{n} \right\} + \\ + \delta\boldsymbol{Q}^{T} \cdot \left\{ \int_{0}^{L} \boldsymbol{N}_{D}^{T} \cdot \left(\boldsymbol{N}_{d} \cdot \boldsymbol{T} \cdot \bar{\boldsymbol{u}} - \boldsymbol{d}(\boldsymbol{D}) \right) dx \right\} = 0 \tag{4.43}$$

Since equation (4.43) is valid for any arbitrary variation of the two independent fields, both expressions inside the brackets are set equal to zero. Moreover, the shape functions used are orthogonal i.e. $\int_{0}^{L} \boldsymbol{N}_{d}^{T} \cdot \boldsymbol{N}_{D}\, dx = \boldsymbol{I}$. Thus, the following Euler-Lagrange equations are deduced that describe the state of the element under external loading incorporating the nonlinear material behavior.

$$\boldsymbol{T}^{T} \cdot \left(\boldsymbol{Q} + \boldsymbol{Q}_{p} \right) - \boldsymbol{P}_{ext} = 0 \tag{4.44}$$

$$\boldsymbol{T} \cdot \bar{\boldsymbol{u}} - \int_{0}^{L} \boldsymbol{N}_{D}^{T} \cdot \boldsymbol{d}(\boldsymbol{D})\, dx = 0 \tag{4.45}$$

where the vector of equivalent nodal external actions has the form:

$$\boldsymbol{P}_{ext} = \boldsymbol{F}_{n} + \int_{0}^{L} \boldsymbol{N}_{u}^{T} \cdot \boldsymbol{b}\, dx \tag{4.46}$$

and $\boldsymbol{Q}_{p}$ is the element vector resulting from the additional cross-sectional internal forces due to distributed loading:

$$\boldsymbol{Q}_{p} = \int_{0}^{L} \boldsymbol{N}_{d}^{T} \cdot \boldsymbol{D}_{p}\, dx \tag{4.47}$$

Equation (4.44) stands for the equilibrium equation and (4.45) for the compatibility equation. Interelement continuity is imposed by mapping the structure's global nodal displacements to the element local displacements $\bar{\boldsymbol{u}}$. The only source of nonlinearity in the above equations concerns the derivation of the cross-sectional deformations $\boldsymbol{d}(\boldsymbol{D})$ as functions of stress resultants.

In the following section two approaches are presented for the solution of the nonlinear system of equations. First the classical linearization technique of the nonlinear constitutive equation is presented accompanied with a standard Newton-Raphson solution procedure. Alternatively, taking advantage of the constitutive equations in rate form the element's equilibrium and compatibility equations are solved simultaneously with the global structure's equations as an ODE system in state space form.

4.5.2 Solution via linearization

Various techniques have been proposed for the linearization of the equations that describe the nonlinear problem. Nukala and White (2004) have proposed four different solution procedures investigating all different combinations of linearization. Also, Alemdar and White (2005) have linearized the constitutive law along with equilibrium and compatibility equations in terms of the independent variables for both geometric and material nonlinearity. The four different solution techniques are listed as follows:

- N-N algorithm. It involves solution of the nonlinear equations separately at the element and at the section levels. This is accomplished by performing separate iterations at the cross-section and after that separate iterations at the element level until convergence.
- N-L algorithm. The use of the linearized equations refers to at the section level while the element nonlinear equations are solved iteratively. Hence, the section level iterations are eliminated.
- L-N algorithm. The linearized element compatibility equations are employed, but in which the nonlinear section equations are still utilized.
- L-L algorithm. Both the linearized section and element level equations are employed, meaning that the linearization error is "pushed" at the structural level.

The proposed scheme in this thesis extends the L-L algorithm presented by Hjelmstad and Taciroglu (2005) by implementing the rate material equations describing the constitutive behavior.

Cross-sectional internal forces can result either from nodal internal forces through interpolation or from integration of cross-sectional stresses. To distinguish both derivations, interpolated forces are denoted with $\boldsymbol{D}(x)$ while constitutive forces are denoted with $\hat{\boldsymbol{D}}(x)$. Since cross-sectional constitutive equation is unique the interpolated forces $\boldsymbol{D}(x)$ should be equal to the stress resultants $\hat{\boldsymbol{D}}(x)$ derived from material constitutive laws. This equation is linearized using relations (4.6) and (4.8) as follows:

$$\boldsymbol{D}^{i+1} = \hat{\boldsymbol{D}}^{i+1} \Rightarrow \Delta \boldsymbol{d}^{i} = \boldsymbol{f}^{i} \cdot \left(\boldsymbol{D}^{i+1} - \hat{\boldsymbol{D}}^{i} \right) \tag{4.48}$$

Consequently, updated cross-sectional deformations can be calculated from the following relation:

$$\boldsymbol{d}^{i+1} = \boldsymbol{d}^{i} + \boldsymbol{f}^{i} \cdot \left(\boldsymbol{D}^{i+1} - \hat{\boldsymbol{D}}^{i} \right) \tag{4.49}$$

Substituting equation (4.49) in (4.45) results in the linearized incremental equations:

$$\boldsymbol{T}^{T} \cdot \left(\boldsymbol{Q}^{i+1} + \boldsymbol{Q}_{p}^{i+1} \right) - \boldsymbol{P}_{ext}{}^{i+1} = 0 \tag{4.50}$$

$$\boldsymbol{T} \cdot \bar{\boldsymbol{u}}^{i+1} - \boldsymbol{F}^{i} \cdot \Delta \boldsymbol{Q}^{i} - \boldsymbol{q}^{i} - \boldsymbol{c}^{i} = 0 \tag{4.51}$$

where the element's flexibility, nodal deformations and element's deformations residual are derived integrating over the beam length as:

$$\boldsymbol{F}^{i} = \int_{0}^{L} \left(\boldsymbol{N}_{D}^{T} \cdot \boldsymbol{f}^{i} \cdot \boldsymbol{N}_{D} \right) dx \tag{4.52}$$

$$\boldsymbol{q}^{i} = \int_{0}^{L} \boldsymbol{N}_{D}^{T} \cdot \boldsymbol{d}^{i} \left(\boldsymbol{D}^{i} \right) dx \tag{4.53}$$

$$\boldsymbol{c}^{i} = \int_{0}^{L} \boldsymbol{N}_{D}^{T} \cdot \boldsymbol{f}^{i} \cdot \left(\boldsymbol{D}^{i} - \hat{\boldsymbol{D}}^{i} + \Delta \boldsymbol{D}_{p}^{i} \right) dx \tag{4.54}$$

Considering the incremental expressions for the nodal forces and displacements $\boldsymbol{Q}^{i+1} = \boldsymbol{Q}^{i} + \Delta \boldsymbol{Q}^{i}$, $\bar{\boldsymbol{u}}^{i+1} = \bar{\boldsymbol{u}}^{i} + \Delta \bar{\boldsymbol{u}}^{i}$ and eliminating the increment of nodal forces $\Delta \boldsymbol{Q}^{i}$, the increment of nodal displacements alone $\Delta \bar{\boldsymbol{u}}^{i}$ can be determined, provided that the element flexibility matrix $\boldsymbol{F}^{i}$ is invertible.

$$\boldsymbol{K}^{i} \cdot \Delta \bar{\boldsymbol{u}}^{i} = \boldsymbol{P}_{ext}{}^{i+1} - \bar{\boldsymbol{Q}}_{int}{}^{i} \tag{4.55}$$

$$\bar{\boldsymbol{Q}}_{int}{}^{i} = \boldsymbol{K}^{i} \cdot \bar{\boldsymbol{u}}^{i} + \boldsymbol{T}^{T} \cdot \left[\boldsymbol{Q}^{i} - (\boldsymbol{F}^{i})^{-1} \cdot \left(\boldsymbol{q}^{i} + \boldsymbol{c}^{i} \right) + \boldsymbol{Q}_{p}^{i+1} \right] \tag{4.56}$$

where, $\boldsymbol{K}^{i} = \boldsymbol{T}^{T} \cdot (\boldsymbol{F}^{i})^{-1} \cdot \boldsymbol{T}$ is the element's tangent stiffness matrix. Equation (4.55) has the same form with the standard incremental equations of the displacement based method with the difference that internal element forces and stiffness matrix are exact as they satisfy equilibrium equations in strong form. On the other hand compatibility is satisfied in weak form as nodal deformations are calculated as the weighted average of the cross-sectional deformations. Considering the computational aspects of the formulation, cross-sectional residuals are directed to the element's residuals and then to structure's residuals.

Following a Newton-Raphson procedure for the global equilibrium equations, the procedure of calculating the updated global stiffness matrix and internal nodal forces proceeds as follows:

1. After solving for an incremental step for the whole structure's equilibrium equation, the vector of incremental nodal displacements is evaluated and total nodal displacements are updated. Mapping the global structure's displacements to every element, element's nodal displacements $\bar{\boldsymbol{u}}^{i+1}$ are defined and the element state determination begins.
2. Element incremental nodal forces $\Delta \boldsymbol{Q}^{i}$ are calculated from equation (4.51) and total nodal forces are updated $\left(\boldsymbol{Q}^{i+1} = \boldsymbol{Q}^{i} + \Delta \boldsymbol{Q}^{i}\right)$.
3. Cross-sectional forces are calculated from interpolation:

$$\boldsymbol{D}^{i+1} = \boldsymbol{D}^{i} + \boldsymbol{N}_{\boldsymbol{D}} \cdot \Delta \boldsymbol{Q}^{i} + \Delta \boldsymbol{D}_{\boldsymbol{p}} \tag{4.57}$$

   where $\Delta \boldsymbol{D}_{\boldsymbol{p}}$ is the increment of cross-sectional stress resultants due to distributed loads.
4. Cross-sectional deformations are evaluated from the linearized constitutive equation (4.49) and updated fiber strains ε^{i+1} are derived from equation (4.2).
5. Material constitutive equations for concrete or rebar steel are solved and updated tangent fiber modulus E_t^i and fiber stresses σ^{i+1} are evaluated. Then integration over the cross-section evaluates the updated tangent stiffness $\boldsymbol{k}(x)^{i+1}$ which gives the cross-sectional flexibility $\boldsymbol{f}(x)^{i+1}$ by its inverse.
6. Integration over the length using equations (4.52) and (4.53) provides element flexibility matrix $\boldsymbol{F}^{i+1}$ and element's nodal deformations $\boldsymbol{q}^{i+1}$.
7. Equation (4.56) determines the nodal internal forces $\bar{\boldsymbol{Q}}^{i+1}$ for the next step, while by assembling every element's contribution the global structure's stiffness matrix $\boldsymbol{K}_{\boldsymbol{S}}^{\boldsymbol{i+1}}$ and nodal internal forces $\boldsymbol{P}_{\boldsymbol{int}}^{\boldsymbol{i+1}}$ are derived.
8. Every element's residual is directed to the structural level and tolerance is checked. $\left\| \boldsymbol{P}_{\boldsymbol{ext}}^{\boldsymbol{i+1}} - \boldsymbol{P}_{\boldsymbol{int}}^{\boldsymbol{i+1}} \right\| \leq tol$.

4.5.3 Solution in state space form

Material constitutive equations in rate form enable the solution of the element constitutive relations at the control points simultaneously with the global equilibrium equations of the structure. Following this approach, constitutive rate equations are not linearized but are stated in their original nonlinear form. Taking the rates of equations (4.44) and (4.45) the element's equilibrium and compatibility equations are derived in rate form as:

$$\boldsymbol{T}^{T}\cdot\left(\dot{\boldsymbol{Q}}+\dot{\boldsymbol{Q}}_{\boldsymbol{p}}\right)-\dot{\boldsymbol{P}}_{\boldsymbol{ext}}=\boldsymbol{0} \tag{4.58}$$

$$\boldsymbol{T}\cdot\dot{\bar{\boldsymbol{u}}}-\int_{0}^{L}\boldsymbol{N}_{\boldsymbol{D}}^{T}\cdot\dot{\boldsymbol{d}}(\boldsymbol{D})\,dx=\boldsymbol{0} \tag{4.59}$$

Also, the interpolation equation (4.41) is obtained in rate form as:

$$\dot{\boldsymbol{D}}(x)=\boldsymbol{N}_{\boldsymbol{D}}(x)\cdot\dot{\boldsymbol{Q}}+\dot{\boldsymbol{D}}_{\boldsymbol{p}} \tag{4.60}$$

Substituting equation (4.60) with the rate form of the cross-sectional constitutive equation $\left(\dot{\boldsymbol{d}}(x)=\boldsymbol{f}(x)\cdot\dot{\boldsymbol{D}}(x)\right)$, equation (4.59) is expressed in terms of the rate of internal nodal forces as:

$$\dot{\boldsymbol{Q}}=\boldsymbol{F}^{-1}\cdot\boldsymbol{T}\cdot\dot{\bar{\boldsymbol{u}}}-\dot{\boldsymbol{Q}}_{\boldsymbol{p}} \tag{4.61}$$

In the dynamic case the standard 2nd order linear differential equation of motion has the following standard form:

$$\boldsymbol{M}_{\boldsymbol{S}}\cdot\ddot{\boldsymbol{u}}_{\boldsymbol{S}}+\boldsymbol{C}_{\boldsymbol{S}}\cdot\dot{\boldsymbol{u}}_{\boldsymbol{S}}+\boldsymbol{P}_{\boldsymbol{int}}=\boldsymbol{P}_{\boldsymbol{ext}}(t) \tag{4.62}$$

where $\boldsymbol{M}_{\boldsymbol{s}}$ and $\boldsymbol{C}_{\boldsymbol{s}}$ are the mass and damping stiffness matrices of the structure. Following this approach, equation (4.62) is solved simultaneously with every element's constitutive evolution equations in state-space form. The displacement, stress and strain fields are considered as the system unknowns as presented in equations (4.58) and (4.59). The displacement field is expressed in the form of nodal displacements at the element nodes $\boldsymbol{u}_{\boldsymbol{S}}$ for the whole structure. In relation to the stress field, as cross-sectional forces are calculated from nodal forces through equilibrium considerations, cross-sectional stresses at all fibers cannot uniquely be determined, indicating that there is not a unique stress field that satisfies cross-sectional equilibrium. This leads to the introduction of all fiber stresses $\boldsymbol{\sigma}_{\boldsymbol{i}}$ and strains $\boldsymbol{\varepsilon}_{\boldsymbol{i}}$ in the beam element's unknown vector. Adding also the velocities $\dot{\boldsymbol{u}}_{\boldsymbol{S}}$ as additional unknowns for the dynamical case, the following vector of unknowns for the whole structure $\{\boldsymbol{x}\}=\{\boldsymbol{u}_{\boldsymbol{S}}\quad\dot{\boldsymbol{u}}_{\boldsymbol{S}}\quad\boldsymbol{\sigma}_{\boldsymbol{i}}\quad\boldsymbol{\varepsilon}_{\boldsymbol{i}}\}^{T}$ is determined.

For a structure consisting of N_{el} elements each one having N_{cs} control sections and each control section discretized in N_{fb} fibers, stress and strain vectors $\boldsymbol{\sigma}_{\boldsymbol{i}}$ and $\boldsymbol{\varepsilon}_{\boldsymbol{i}}$ respectively contain all stress and strains at all $\left(N_{el}\cdot N_{cs}\cdot N_{fb}\right)$ fibers of all elements where nonlinear behavior is monitored, i.e. Gauss points. Consequently, the following 1st order ODE system is formed.

$$\dot{x}=\begin{Bmatrix}\dot{\boldsymbol{u}}_S\\ \ddot{\boldsymbol{u}}_S\\ \dot{\boldsymbol{\varepsilon}}_i\\ \dot{\boldsymbol{\sigma}}_i\end{Bmatrix}=\begin{Bmatrix}\dot{\boldsymbol{u}}_S\\ \boldsymbol{M}_S^{-1}\cdot\left(-\boldsymbol{C}_S\cdot\dot{\boldsymbol{u}}_S-\boldsymbol{P}_{int}+\boldsymbol{P}(t)\right)\\ \boldsymbol{I}_j^T\cdot\boldsymbol{f}_j\cdot\left(\boldsymbol{N}_{\boldsymbol{D},i}\cdot\dot{\boldsymbol{Q}}_i+\dot{\boldsymbol{D}}_{\boldsymbol{p},j}\right)\\ E_{t,k}\cdot\dot{\varepsilon}_k\end{Bmatrix}\begin{matrix}\\ \\ \\ \end{matrix}\begin{matrix}, \text{ i}=1...N_{el}, \text{ j}=1...N_{cs}\\ \\ , \ k=1...\left(N_{el}\cdot N_{cs}\cdot N_{fb}\right)\end{matrix} \tag{4.63}$$

where $\boldsymbol{I}_j^T$ is the position matrix that maps cross-sectional deformations at control section j to fiber strains (relation (4.2)), $\boldsymbol{f}_j$ is the flexibility matrix at every control section j and the rate vector of element nodal forces $\dot{\boldsymbol{Q}}_i$ is given from equation (4.61).

In every step of the solution process the global vector of internal nodal forces $\boldsymbol{P}_{int}$, as well as the new tangent fiber modulus $E_{t,k}$ together with cross-sectional $\boldsymbol{f}_j$ and element $\boldsymbol{F}_i$ flexibilities should be evaluated. This is accomplished by the following steps:

1. Given the stress and strain vectors $\boldsymbol{\sigma}_i$ and $\boldsymbol{\varepsilon}_i$ the updated fiber material modulus $E_{t,k}$ is evaluated for each material.
2. Calculate cross-sectional flexibility $\boldsymbol{f}(x)$, as the inverse of cross-sectional stiffness derived from relation (4.7) and cross-sectional stress resultants $\hat{\boldsymbol{D}}(x)$ using equation (4.4).
3. Considering piecewise element equilibrium, element internal nodal forces can be derived directly from cross-sectional stress resultants at both element ends, adding also the contribution of distributed loading $\boldsymbol{Q}_{\boldsymbol{p},i}$.
4. Element flexibility matrix $\boldsymbol{F}_i$ is calculated integrating along element's length according to relation (4.52).
5. Finally, assembling every element's internal forces $\boldsymbol{Q}_{int}$ at a structural level provides the total vector of internal forces $\boldsymbol{P}_{int}$.

Both proposed methods yield identical results, with the solution in state-space form being more compact compared to the linearized one. Its computational efficiency though, relies heavily on the numerical algorithm used for the integration of the ODE system with the most computationally expensive part concerning the evaluation of the Jacobian of the system. For simplicity reasons the numerical examples presented in the following sections are analyzed using the linearization method.

Based on the above it becomes evident that the inelastic constitutive behavior can be directly incorporated into a two-field variational formulation offering a compact and physical

approach to state determination of a fiber beam model. The generic fiber constitutive behavior properly escalated first at cross-sectional level and then at member and structural levels establishes the framework for the solution of framed structures following a linearization scheme or equivalently a state-space approach.

4.6 Numerical integration and localization

The integrals over the element length in both displacement and mixed element formulation are calculated numerically in this work using Gauss-Lobatto quadrature. The method integrates a given function $f(x)$ by transforming a definite integral in a finite sequence as follows:

$$\begin{aligned}\int_a^b f(x)dx &= \frac{b-a}{2}\int_{-1}^{1} f\left(\frac{b-a}{2}\cdot\xi+\frac{a+b}{2}\right)d\xi \\ &= \frac{b-a}{2}\cdot\sum_{i=1}^{n} w_i \cdot f\left(\frac{b-a}{2}\cdot\xi+\frac{a+b}{2}\right)\end{aligned} \tag{4.64}$$

where, $[a\ b]$ is the integration interval, usually $[0\ L]$, w_i is the numerical weight of the quadrature, n is the number of the control points and ξ is the position of the control section on x axis in the non-dimensional system $[-1\ 1]$. This method is preferred over the standard Gauss quadrature as it includes both element ends where nonlinear behavior is usually more pronounced. Alternatively, Newton-Cotes integration scheme places integration points uniformly along the element including both element ends, while fixed location integration places control points at any selected beam locations. In this quadrature weights w_i are computed by the method of undetermined coefficients using Vandermonde matrix (Scott 2011).

$$\sum_{i=1}^{n} x_i^{j-1} w_i = \frac{1}{j} \qquad (j=1,..\mathrm{n}) \tag{4.65}$$

where, n is again the number of integration points and x_i are the defined locations in the natural system [0,1].

Moreover, the *nth* order Gauss-Lobatto integration is exact for polynomials up to $(2n-3)$ degree. Displacement based formulation produces a curvature distribution of *2nd* degree, hence 3 point Gauss Lobatto integration is adequate. However the inherent error in the displacement based methodology demands more than one element discretization in order to capture the higher degree of the curvature distribution. For this reason an efficient

numerical strategy, as far as the stiffness method is concerned, is to keep control points number at three per element, increasing on the same time the number of elements near the member ends.

On the other hand increasing the number of control points in a mixed beam element nonlinear response convergences to a more accurate solution. However, the increase of accuracy is valid only for the hardening material case. In the softening case, inelastic response of force-based elements depends to the number of control points due to loss of objectivity. Damage localizes at the reference volume of the first control point and as a result denser discretization leads to fictitious steeper softening branches. Consequently regularization techniques are necessary to obtain an objective response (Coleman and Spacone 2001; Addessi and Ciampi 2007; Scott and Hamutcuoglu 2008; Almeida et al. 2012). However, in the absence of a proper regularization technique, the objective response can be approximated by selecting the first Gauss point length to be equal to the plastic hinge length (Zeris and Mahin 1988; Calabrese et al. 2010). This suggestion lies on the fact that softening energy is dissipated from the plastic hinge area where damage is profound. A lot of relations have been proposed to estimate plastic-hinge length like the formula proposed by Paulay and Priestley (1992):

$$L_p = 0.08L + 0.022 f_y D_b \ (KN, mm) = 0.19 \ m \tag{4.66}$$

4.7 Comparative examples

4.7.1 Cantilever column with hardening response

In this example the proposed element formulation is validated by solving the problem presented by Saritas and Soydas (2012). In this reference, different numerical procedures and element discretization schemes of a mixed three-field Hu-Washizu element, first proposed by Taylor et al. (2003) are compared.

The problem consists of a non-dimensional cantilever column with height of 120 units and rectangular cross-section of 15x20 units. Material is considered bilinear with elastic modulus of elasticity $E_{el}=29000$, yield stress $\sigma_y=50$ and hardening post-yield to pre-yield ratio $\alpha=0.01$. The cross-section is discretized in 5 layers, each one participating in the overall cross-section response according to mid-point integration. Element behavior is integrated along its length using Gauss-Lobatto integration with 5 control points.

The first step is to validate the displacement based formulation, but implementation of the classical displacement based formulation requires several elements in the discretization to achieve a satisfactory and objective response. For this reason two different discretization schemes were tested consisting of one (1DB) and four elements (4DB) respectively. The results are presented in Figure 4.5 relating base shear and top displacement, with the proposed formulation proven very efficient in generating the accurate response.

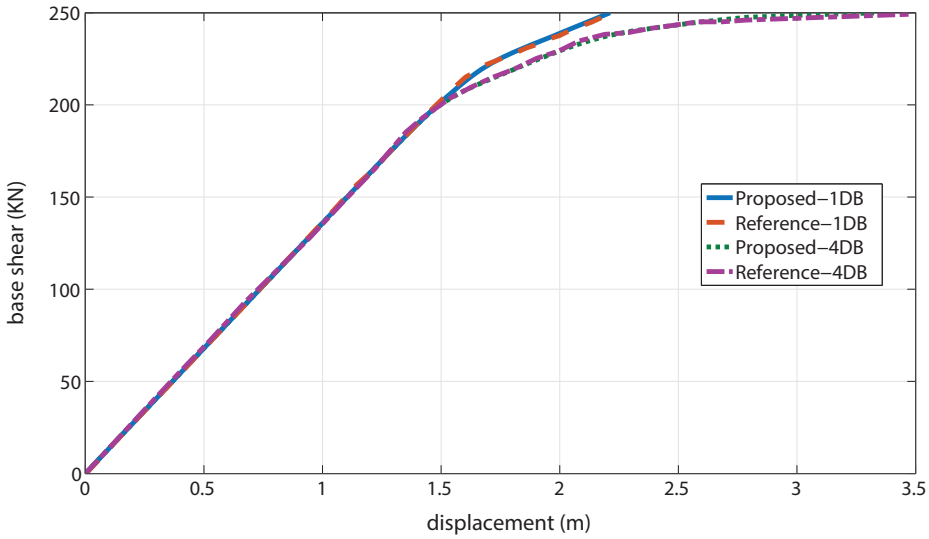

Figure 4.5**.** Base shear vs top displacement of a cantilever column, comparison with displacement based formulation.

Next, the proposed two-field mixed element (Proposed-1HR) is compared for the same example against the three-field force based element of Saritas and Soydas (2012) (Reference-1FB) and the results are quite satisfactory as presented in Figure 4.6.

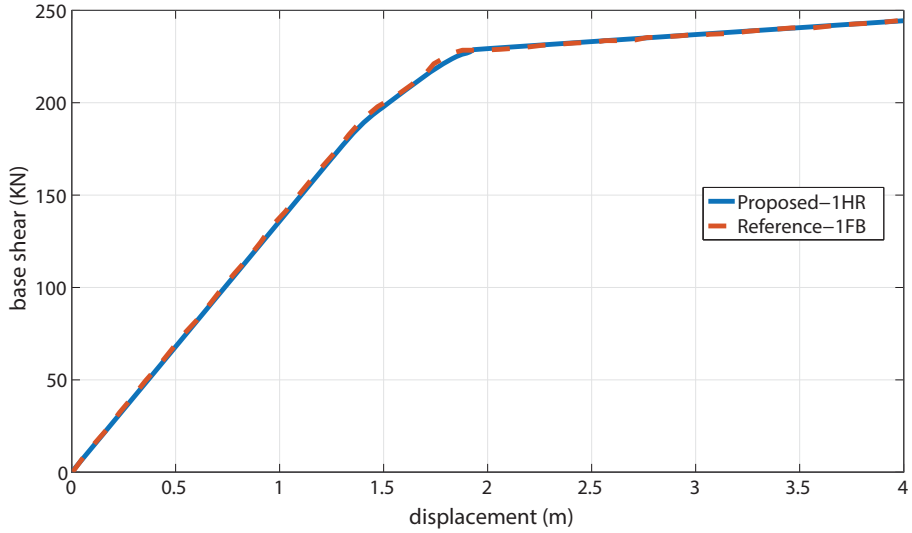

Figure 4.6. Base shear vs top displacement of a cantilever column, comparison with mixed formulations.

4.7.2 Cantilever column with softening response

After the accuracy of the proposed element formulations is validated, attention is focused on RC members with softening response. More specifically, in this example comparison between the mixed and displacement based formulation is performed using a cantilever RC column under incremental static loading. Column is of rectangular 40x40 cross-section with 4Ø18 rebars, while its height is 3m. Column initially resists a vertical point load of 1500KN and is pushed laterally under incremental applied displacements, until tip displacement reaches 0.12m. Also, column discretization scheme consists of 5 Gauss-Lobatto control points, while the number of cross-sectional layers selected to be 30/12/2 for core, cover and reinforcing layers respectively. Figure 4.7 presents the comparison between the mixed and displacement based elements in terms of base shear vs top displacements. It is clear that displacement based formulation overestimates significantly column lateral strength capacity.

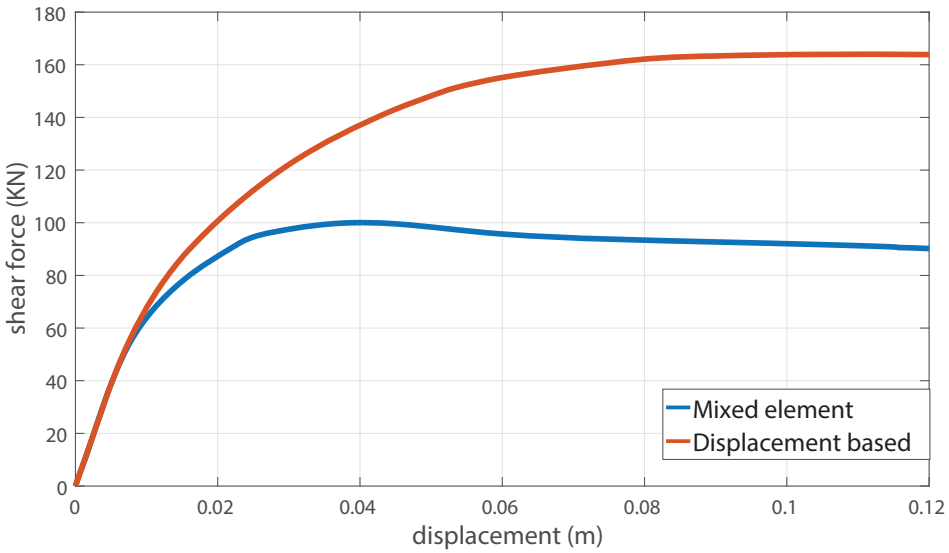

Figure 4.7. Comparison of Base shear vs top displacement for mixed element and displacement based element

The erroneous behavior of 1 element displacement based formulation is due to the lack of point-wise element equilibrium and curvature distribution as manifested in Figure 4.8 and Figure 4.9.

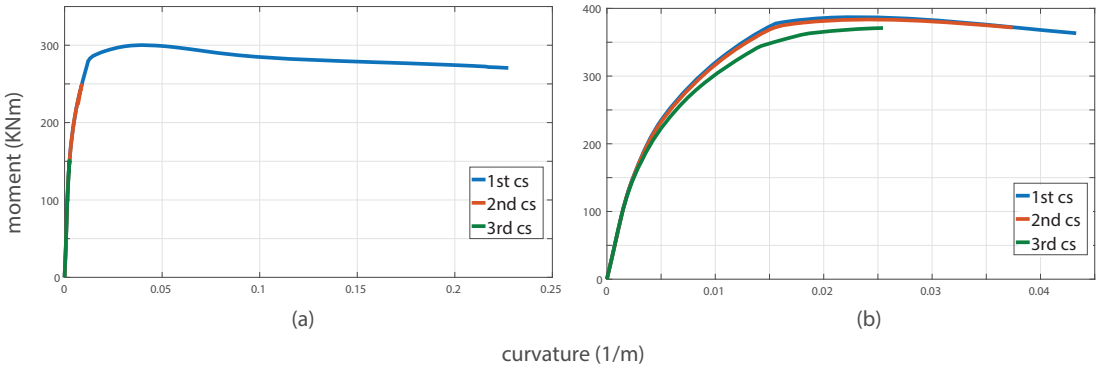

Figure 4.8. Moment curvature diagrams, (a) mixed formulation vs (b) displacement based formulation

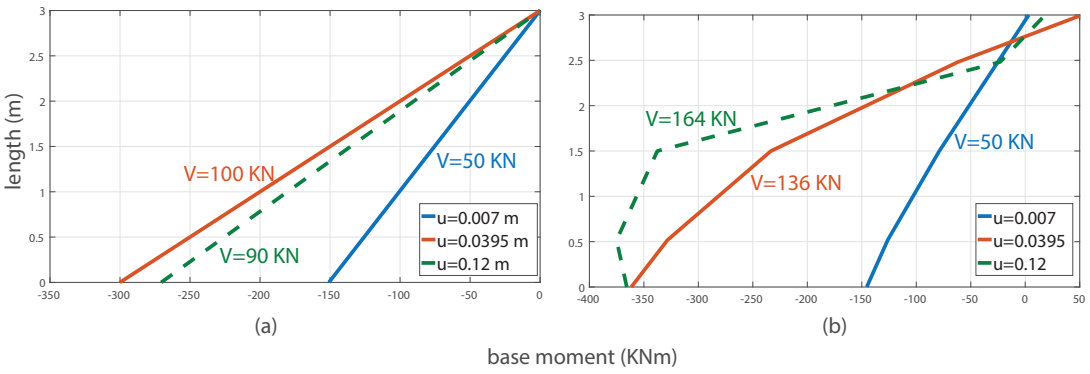

Figure 4.9. Moment diagrams, (a) mixed formulation vs (b) displacement based formulation

Equilibrium condition demands that moment distribution remains linear under any level of lateral loading. After column exceeds maximum strength capacity, softening branch starts as base moment is reduced while curvatures still increase. Equilibrium condition enforces the rest of the element cross-sections to unload satisfying linearity of moment distribution (Figure 4.7(a), Figure 4.8(a)). Consequently, all nonlinear behavior localized at the first cross-section, while all other cross-sections are in an unloading linear state. Localization phenomenon is presented in Figure 4.10, where an increase on the number of control sections has an effect on the softening stiffness of the member. According to relation (4.66) plastic hinge length equals to 0.44 m, hence 3 control sections with *L/6=0.50 m* 1st Gauss-Lobatto length is considered to represent the accurate discretization scheme.

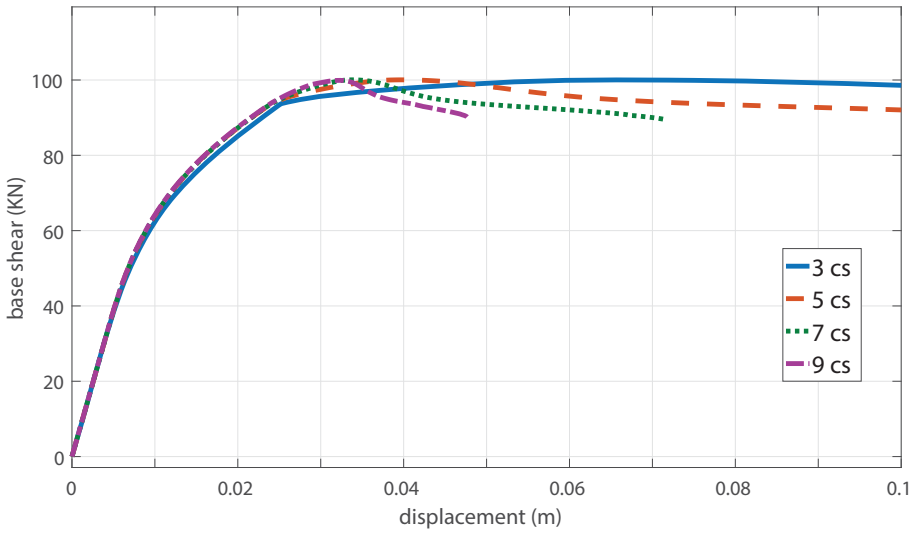

Figure 4.10. localization effect at cantilever column

In displacement based formulation on the other hand, continuous increase of nodal displacements results in increasing curvatures witch on the same time derive greater stresses and cross-sectional moments (Figure 4.8(b)). This produces the fictitious moment diagrams of Figure 4.8(b) where moment value at the free end deviates from zero.

To reduce computational error, denser discretization schemes are tested in Figure 4.11. As it is obvious eight displacement based elements are necessary to approach the reliable mixed element response, while further refinement converges to even better solution.

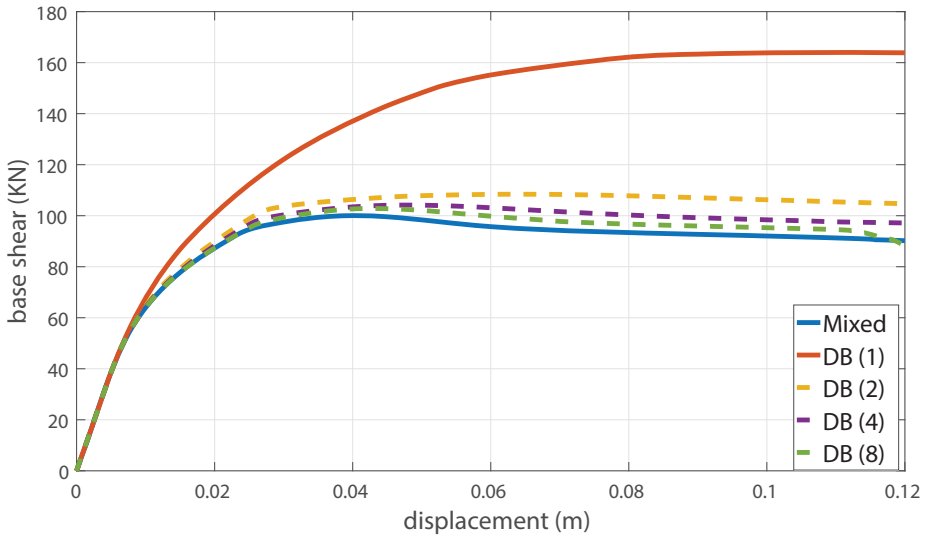

Figure 4.11. Base shear vs top displacement, convergence of displacement based formulation

4.7.3 Continuous beam under cyclic vertical load

In this example the proposed element formulations are employed for the solution of a 2-span continuous beam (Figure 4.12) under a pseudo-static cyclic external loading consisting of a varying concentrated vertical load at the middle of the first span following a piecewise linear pattern presented in Figure 4.13 and Table 2. Also, cross-section is an IPE 300 European steel cross-section which is discretized in 50 layers. Every layer is represented by steel material with yield stress $\sigma_y = 235\ MPa$ and linear kinematic hardening with $a = 0.015$, while n_2 value for Bauschinger effect is $n_2 = 1.0$.

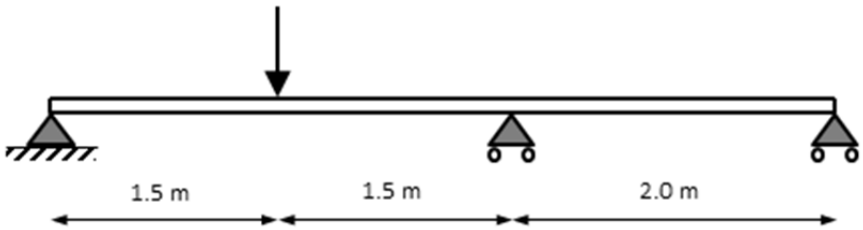

Figure 4.12. Continuous beam under vertical dynamic excitation.

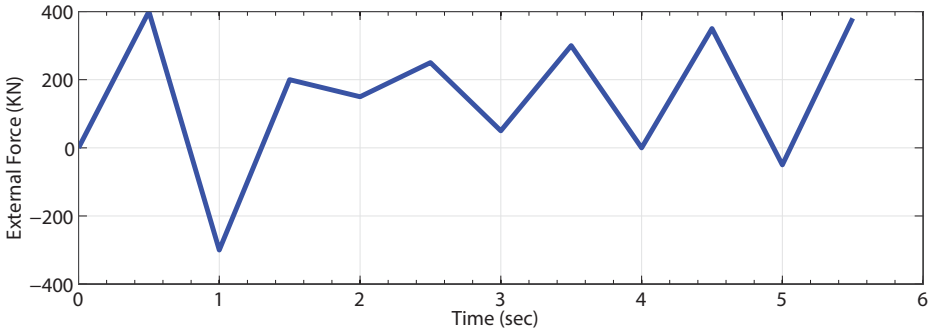

Figure 4.13. Vertical load input

Time (sec)	External Force (KN)
0	0
0.5	400
1	-300
1.5	200
2	150
2.5	250
3	50
3.5	300
4	0
4.5	350
5	-50
5.5	380

Table 4.1. Vertical load values

In Figure 4.14 the two element formulations are compared. For the displacement based formulation two different discretization schemes with 3 control sections are utilized, while for the mixed formulation a single element discretization with 15 control sections is sufficient to yield accurate results. A dense discretization consisting of 40 equal beam elements with 3 Gauss-Lobatto points per element for the total length of the continuous

beam is used to overcome the deficiencies of the classical displacement based stiffness method and serves as the accurate solution where the other two formulations are compared with.

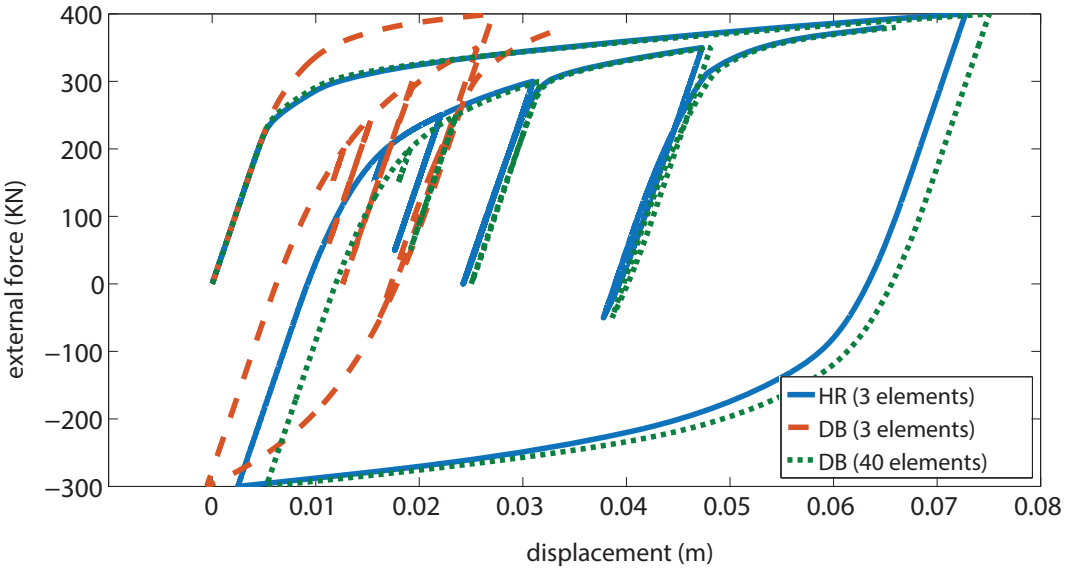

Figure 4.14. Comparison of vertical mid-span displacement vs external loading history

It is evident that the discretization with 3 elements following the stiffness method (DB 3 elements) delivers inaccurate results and is not capable of capturing the real behavior. This inefficiency is magnified for intensive external loading, as overestimation of the maximum strength results into more than 2.5 times decreased plastic deformations compared to a more refined discretization. On the other hand the proposed two-field mixed element (HR 3 elements) satisfies the equilibrium equations in strong form and a single element captures directly the real cyclic response with no need for further refinement.

4.8 Incorporation of rebar buckling

The individual rebar buckling model as developed in chapter §2.3 is further incorporated in the RC fiber column element developed by employing a suitable procedure. Generally, concrete cover between consecutive stirrups prevents longitudinal rebars from buckling at the initial stages of cyclic loading. However, soon after spalling of concrete cover, steel rebars are free to buckle outwards between 2 adjacent stirrups. Spalling for the rebar neighboring concrete fibers (Figure 4.15) is detected by setting a threshold spalling value for the damage parameter D in the concrete model. Reference threshold value can be considered in the range of D_{sp}=*[0.6-0.8].*

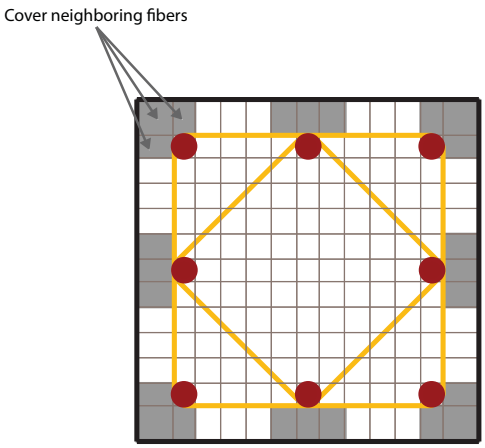

Figure 4.15. Concrete fibers for cover spalling identification.

After the onset of rebar buckling, average axial strains at rebar location continue to evolve obeying the linear distribution due to full bond i.e. compatibility with neighbouring concrete fibers (Pantazopoulou 1998). Compatibility is enforced at the average strain ε_{av}, while buckling strain ε_b begins to increase significantly with progressive rebar lateral displacement.

During cross-sectional analysis inside a global numerical increment, stress and stiffness determination of rebars is performed as follows:

1. Stress determination process is first performed for concrete fibers and damage parameter D_{-} in compression is stored for the neighboring cover fibers of any longitudinal rebar.
2. For the same fibers it is examined whether damage parameter D_{-} exceeds reference spalling parameter D_{sp} that defines the onset of rebar buckling. If buckling model is activated, this is performed in an inner loop as described in section 2.3.1. Average stain ε_{av} at the rebar location is inserted in the model and local variables are updated and kept in memory for the next buckling iteration.
3. The output of this procedure is the total average stress σ^i while tangent axial stiffness is simply calculated as: $E_t^i = \left(\sigma^i - \sigma^{i-1}\right) / \Delta\varepsilon_{av}^i$
4. Subsequently, cross-section and element state determination are continued until convergence at the overall level is achieved.

In a nonlinear force based beam-column element rebar average strain ε_{av} and stress σ are considered constant between Gauss points. Consequently, to accurately model local

buckling between two consecutive stirrups Gauss point's length should be nearly equal to the distance between the adjacent stirrups. For columns with equally spaced stirrups, Newton-Cotes integration scheme appears to be suitable as it places integration points uniformly along the element including both element ends, which may coincide with the position of stirrups. Alternatively, for columns designed with modern codes, which enforce denser stirrup distribution at the end critical zones, fixed location integration may be used.

Herein, for simplicity reasons, as local buckling is expected to occur primarily at the critical zone between the first two stirrups near column base, the commonly used Gauss-Lobatto quadrature may be used as well, by selecting the number of total Gauss-Lobatto points in such way, that the 1st Gauss-Lobatto length is nearly equal to the distance between the first two stirrups (Figure 4.16). This implies the assumption that due to local buckling and extensive spalling, plastic-hinge length is nearly equal to the distance between the two adjacent stirrups.

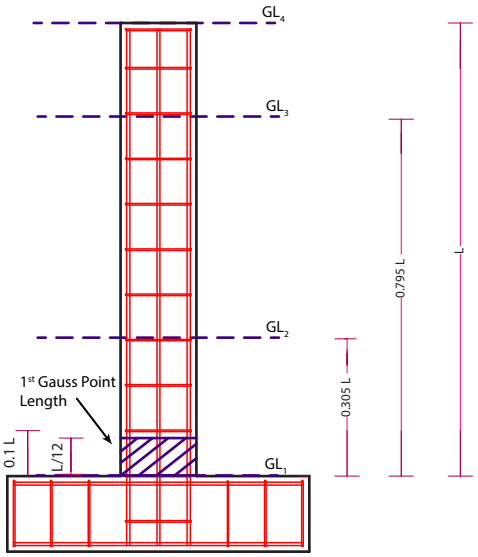

Figure 4.16. Numerical discretization of an RC column with local rebar buckling

CHAPTER 5

Numerical Examples

5.1 Introduction

The proposed fiber beam-column element implementing uniaxial constitutive models for steel and concrete cyclic behavior is validated against experimental tests on RC structural components. The first comparative example is a cantilever column that exhibits pseudostatic cyclic response under imposed displacement history. The second experimental test describes a high strength concrete pier-column system under high compressive load. The system is pushed laterally under imposed displacements until collapse due to concrete spalling and buckling of reinforcing longitudinal bars. Finally, a 3-storey, 3-bay RC frame is tested with a real accelerogram time history analysis. The one half side of the frame presents columns designed with past code provisions, while the other half side columns are designed according to modern codes.

In all experimental examples the mixed beam-column element is utilized for the numerical analysis results due to its computational effectiveness and accuracy. Detailed experimental data for the individual material cyclic behavior are not provided except from their yield and maximum stress values. Hence, model parameters are selected based on the analyses with experimental results on concrete and rebar specimens presented in the previous chapters.

5.2 Cantilever column under pseudo-static cyclic excitation

5.2.1 Experimental setting description and input data

In this section the efficacy of the introduced material models and their incorporation in nonlinear RC element analysis are investigated in comparison with experimental data presented by Qiu et al. (2002) for a series of cantilever columns in uniaxial and biaxial bending. Herein, the uniaxial bending test (specimen label RC-0 in Qiu et al. (2002)) is utilized for comparison purposes. The cantilever column geometry and loading conditions are presented in Figure 5.1. More specifically, column has a *20x20* cross-section with *8Ø12* reinforcing bars and clear cover *1.5 cm*. Also, concrete maximum strength value is $\sigma_c = 39.6\ MPa$.

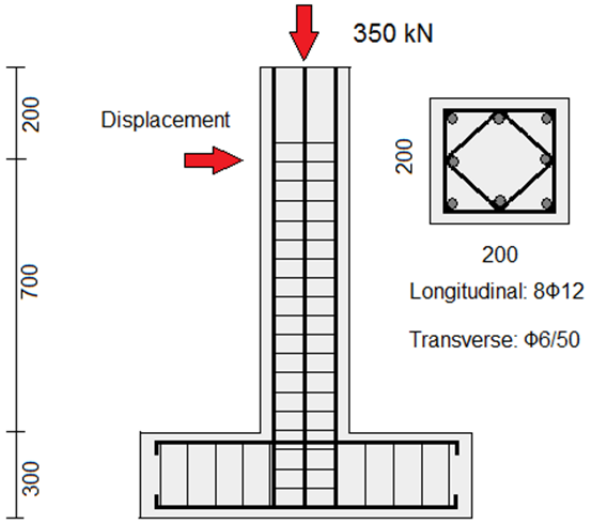

Figure 5.1. Column geometry and cross-section.

The column resists a permanent axial compressive load of *N=350 KN* and is pushed laterally by imposing the displacement history presented in Figure 5.2.

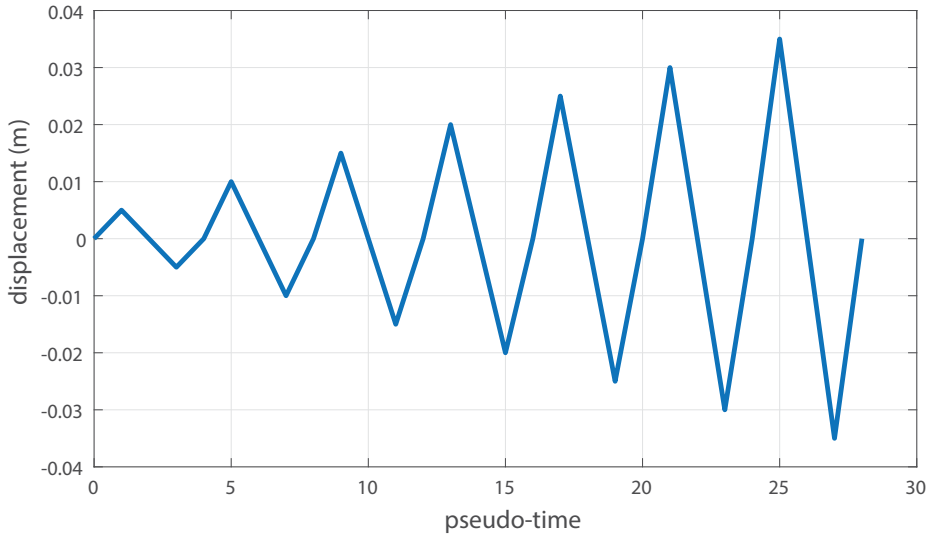

Figure 5.2. Input lateral displacement history

Reinforcing bars yield stress is $\sigma_y = 460\ Mpa$ with nonlinear kinematic hardening as presented in Table 5.1.

σ_y (MPa)	α	n_1	n_2	ε_{plat}	m	q
460	0.03	10	0.5	$3\varepsilon_y$	0	30

Table 5.1. Rebar model parameters

Concrete was modeled in terms of its compressive cyclic behavior and its parameters representing unconfined concrete fibers are presented in Table 5.2. The Mander et al. (1988) model was used to calculate the maximum confined compressive strength in the case of the confined fibers. Confinement factor k obtains value $k=1.4$ for the stirrup setting of Figure 5.1, hence maximum confined strength is $\left(\sigma_{cc}=k\cdot\sigma_{c}=55.4\ MPa\right)$. In this case confined concrete parameters are modified as presented in Table 5.2. It should be noted that the whole area inside the transverse hoops was considered as confined.

Παράμετροι σκυροδέματος									
	E_C (GPa)	**σ_{yc} (MPa)**	**α_C**	**q_C**	**k_0**	**b**	**p**	**c_1**	**c_2**
Confined	35	20	0.8	10	0.00057	8	0.65	2	0.35
Unconfined	35	20	0.65	10	0.00057	6.5	1.1	4	0.1

Table 5.2. Confined and unconfined concrete model parameters

Also, the computational model consists of two mixed elements with 4 Gauss-Lobatto control points each. The first element spans a distance of *0.7m* between fixed end and the node where the displacement history is imposed, while the rest length of *0.2m* until the free end consists the second element.

5.2.2 Numerical analysis and comparison

The global column cyclic analysis is tested against the experimental results in terms of base shear vs lateral displacement. As depicted in Figure 5.3 the overall numerical behavior is quite satisfactory while the maximum and residual strength are captured with sufficient accuracy. Some small discrepancies that can be noticed in the unloading stiffness are attributed to bond-slip and shear effects which are not considered in the present analysis.

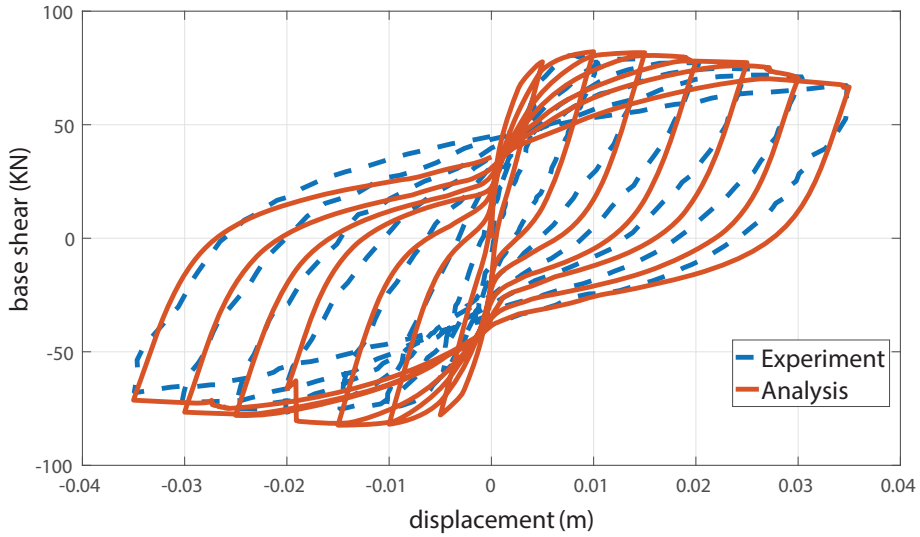

Figure 5.3. Base shear vs lateral displacement comparison between experimental and analytical behavior for Qiu et al. experiment

In addition, moment-curvature and moment-chord rotation results as derived from the analysis are presented in Figure 5.4 to better illustrate the analytical results.

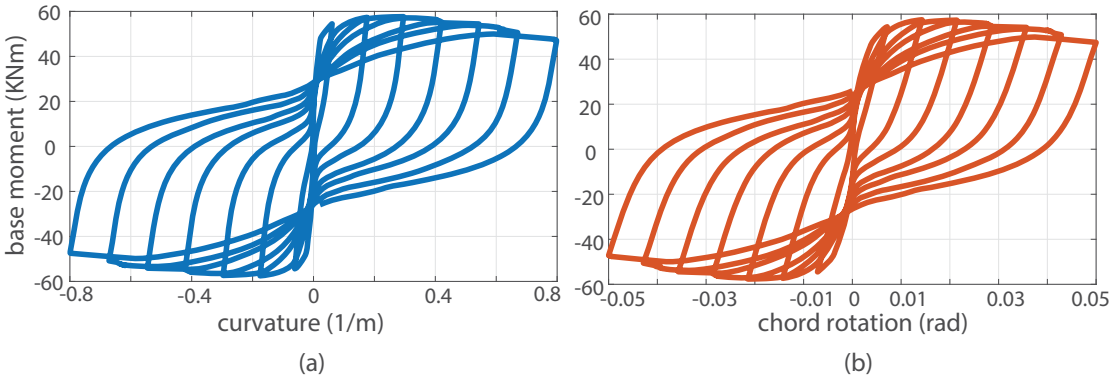

Figure 5.4. (a) moment-curvature, (b) moment-chord rotation diagrams at column base for Qiu et al. experiment.

Finally, the cyclic response of the individual materials is presented in Figure 5.5. In Figure 5.5(a) the stress-strain loops of the top rebars are presented. Also, the stress-strain loops of the confined and unconfined concrete fibers placed at distances 0.092m 0.082m from cross-sectional centroid are plotted in Figure 5.5(b).

To sum up, it seems that complete cover spalling along with core crushing is the critical failure mechanism of the column, while the small distance between stirrups restricts reinforcing bar buckling.

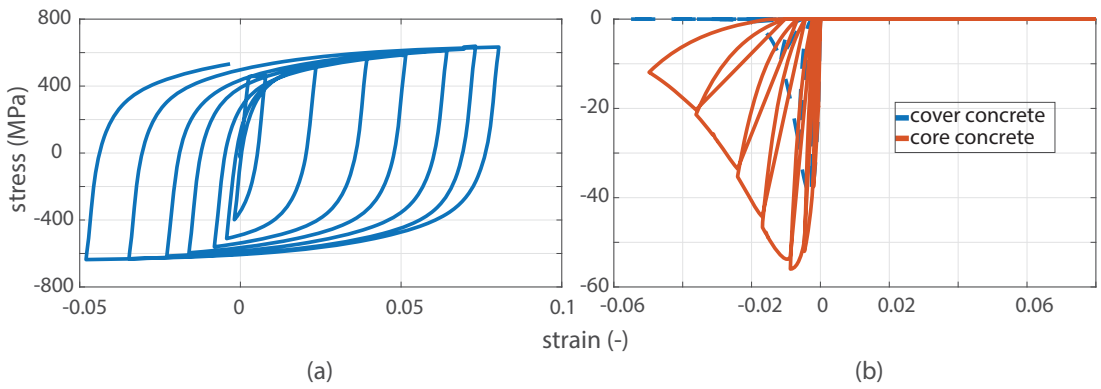

Figure 5.5. (a) rebar stress-strain and (b) concrete stress-strain histories for Qiu et al. experiment

5.3 Column-stub system under pseudo-static cyclic excitation

5.3.1 Experimental setting description and input data

The proposed RC column fiber element is also tested against Bayrack and Sheikh (1996) experiment AS-2HT on RC rectangular columns. Experimental setting and analysis model are presented in Figure 5.6. Column length is *L=1.473m* with rectangular *0.305x0.305m* cross-section and it is connected to a *0.508x0.762x0.813m* stub. The column-stub system is supported with hinges at both ends and a constant axial compressive load is applied. Concrete strength is σ_c *=72 MPa*, steel rebars have a diameter of D_b *=19.5mm* with yield stress σ_y *= 454 MPa*, while stirrup distance to rebar diameter ratio is L/D_b*=4.6*. To verify the local buckling hypothesis, the global buckling length of the rebar calculated according to the methodology proposed by Su et al (2015). It is found that the global buckling lengths are equal to local buckling length for the experimental specimen proving that the local buckling model is applicable. In addition, the reference spalling value for concrete fibers was set to $D_{sp} = 0.6$.

The numerical model is based on the mixed element formulation with 4 Gauss-Lobatto control sections where the length related to the control points at both ends *is L/12= 0.12 m* accounting for the localization effect.

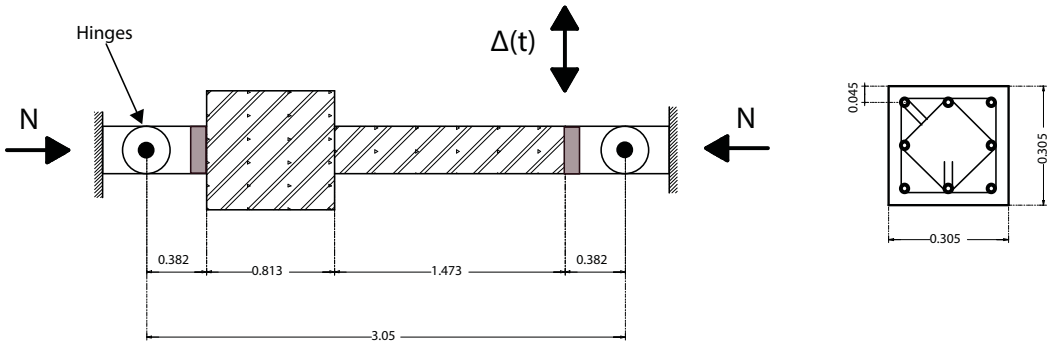

Figure 5.6. Experimental setting of Bayrack and Sheikh

Rebar steel and concrete model parameters are presented in Table 5.3 and Table 5.4 respectively. Especially, unconfined concrete parameters were selected considering the numerical comparison with the Muguruma et al. (1983) experiments on high strength column specimens, which is presented in chapter 3.4.1. Confining parameter *k* obtains value *k=1.12,* hence maximum confining stress is $\sigma_{cc}= k\cdot\sigma_c= 81$ *MPa.*

σ_y (MPa)	α	n_1	n_2	ε_{plat}	m	q
454	0.03	10	0.5	$2\varepsilon_y$	0.05	10

Table 5.3. Model parameters for longitudinal rebars

		E_C (GPa)	σ_{yc} (MPa)	α_C	q_C	k_0	b	p	c_1	c_2	n_{rec}
Confined	**Compression**	40	40	0.5	10	0.0018	2.7	0.45	1.5	0.5	4
	Tension	40	7	0.5	0	0.00018	0.5	0.5	3	0.2	4
Unconfined	**Compression**	40	40	0.5	30	0.0018	2.5	0.75	4	0.1	5
	Tension	40	7	0.5	0	0.00018	0.5	0.5	3	0.2	5

Table 5.4. Model parameters for confined and unconfined concrete

5.3.2 Numerical analysis and comparison

The imposed displacement history of Figure 5.7 is inserted in the numerical model and comparison with the experimental results is presented in Figure 5.8 in terms of column shear force and displacement history. First, the case where the axial force is set to *N=-2400 KN* is tested (specimen AS-2HT). Generally, the proposed model is capable of predicting satisfactorily initial and post buckling hysteretic loops. Larger discrepancies appear at latter stages of loading, which are attributed to the assumptions made for the buckling model,

shear effects, bond-slip of rebars and other reasons that are not accounted in the analysis model.

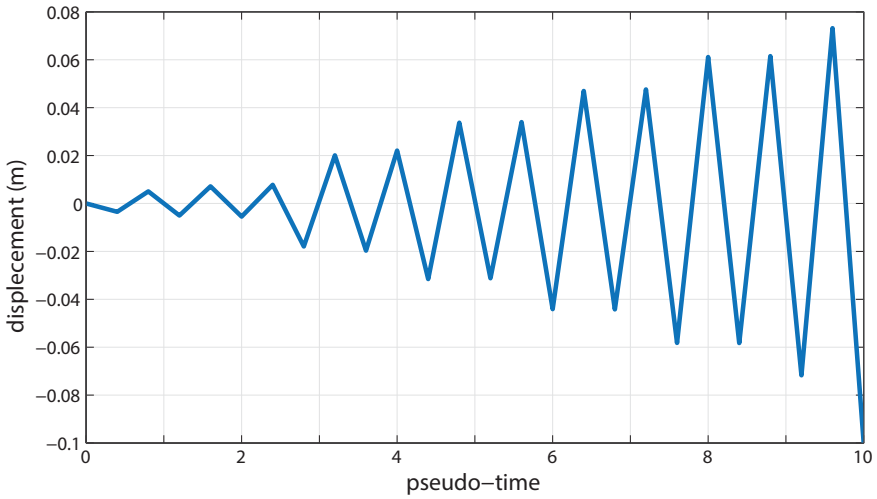

Figure 5.7. Imposed displacement history for specimen AS-2H

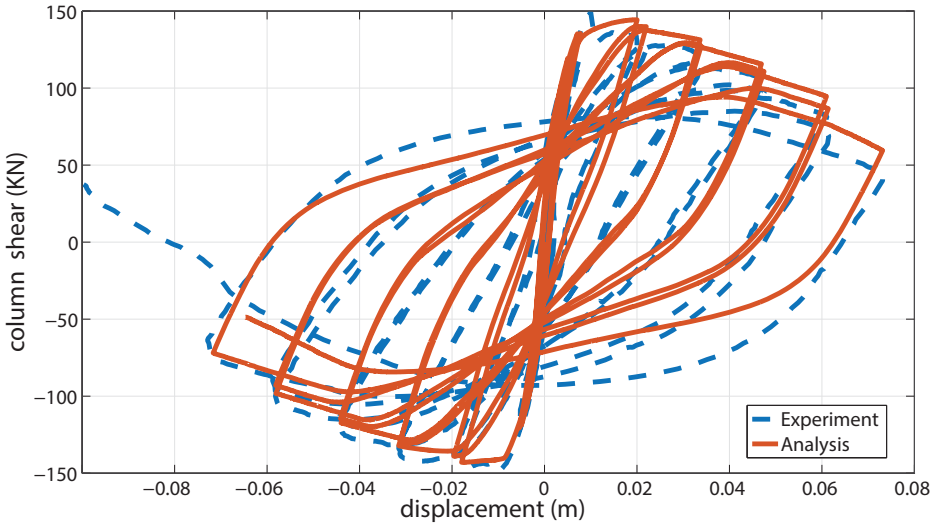

Figure 5.8. Comparison with Bayrak and Sheikh specimen AS-2HT

As reported in the real experiment by Bayrack and Sheikh, cover spalling occurred soon after specimen reached its maximum strength value and significant buckling could be noticed at the final cycle. In Figure 5.9 stress-strain histories of both steel and confined/unconfined concrete fibers at the bottom edge of the cross-section are presented. Unconfined concrete compressive stress is below 10% of maximum strength at strains larger than 0.04 indicating the complete spalling of column cover. This enables the inelastic buckling mechanism of neighboring longitudinal rebars, while their loops are asymmetric

and loading capacity at compressive strains is diminished. This behavior is reflected at the overall column cyclic response of Figure 5.8, where final loop loses strength rapidly, which leads to analysis termination due to convergence errors, while the column specimen collapses soon after.

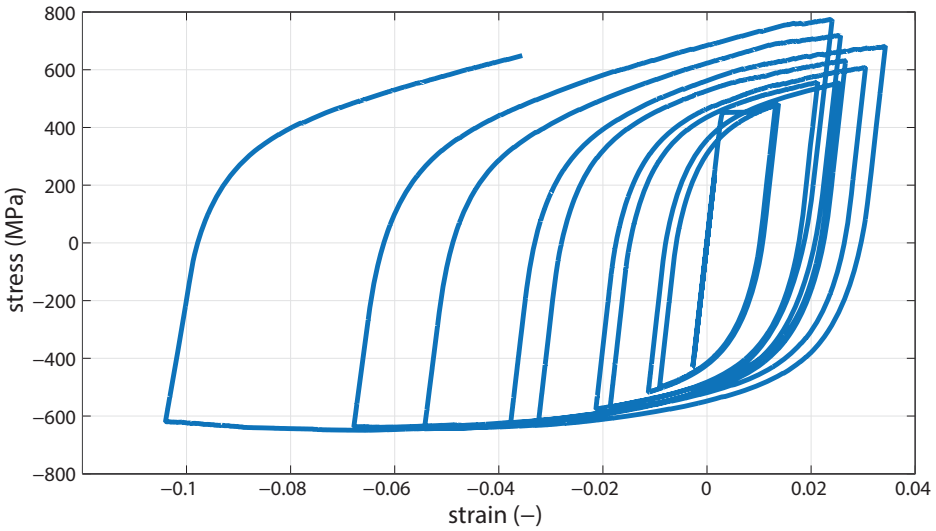

(a)

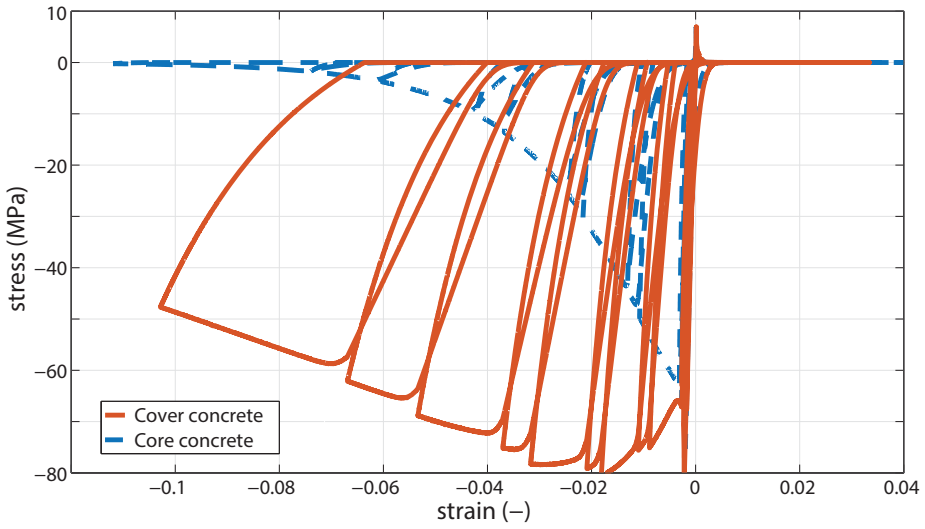

(b)

Figure 5.9. (a) Upper steel rebar stress-strain history, (b) Confined and unconfined concrete stress-strain histories for Bayrak and Sheikh specimen AS-3HT

Finally, the effect of the reinforcing bars inelastic buckling is reflected in Figure 5.10 where both numerical responses with and without rebar buckling are plotted. Incorporation

of the buckling mechanism affects significantly the last cyclic loop where column-stub system numerically "collapses" with residual strength of near *V=-50 KN*. At the same instance the model without rebar buckling effects is numerically stable with shear strength value of *V=-90 KN*.

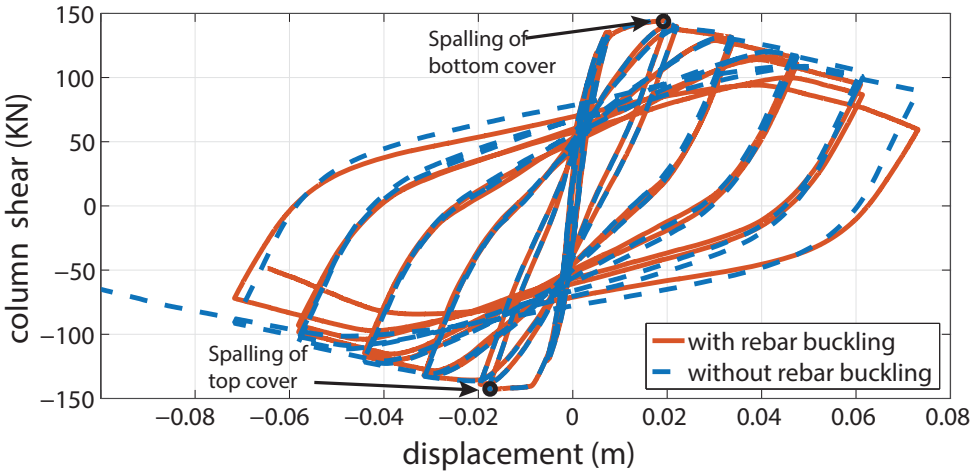

Figure 5.10. Comparison between analysis with and without rebar buckling for specimen AS-2HT

Generally, for regular strength RC columns with high axial loads, concrete usually fails in compression before the initiation of rebar buckling mechanism. However, in this example high strength concrete resists large compressive strains, enabling lateral rebar deformations to evolve which are proved critical for column's structural integrity. To emphasize more one the axial load effect on column's carrying capacity, the same experimental setting is tested with permanent axial force *N=-3340 KN* (specimen AS-3HT) under the imposed displacement history of Figure 5.11. Afterwards, comparison of the hysteretic loops between displacement and shear force is presented in Figure 5.12.

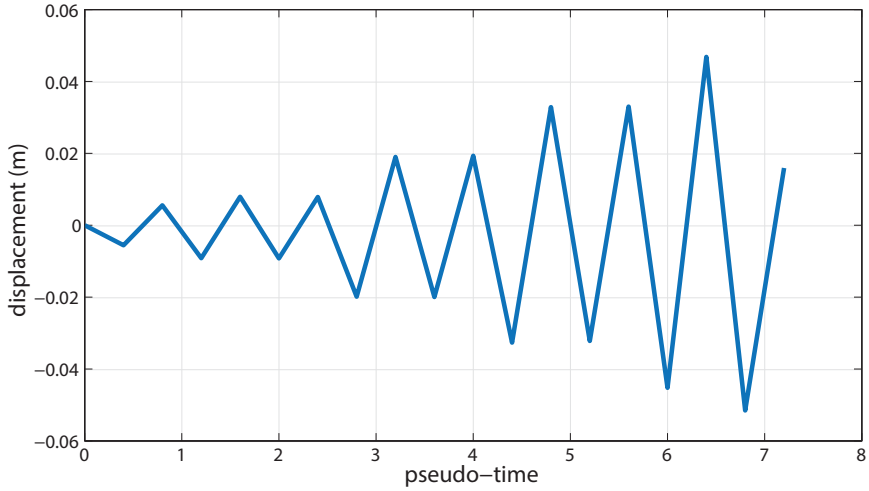

Figure 5.11. Imposed displacement history for specimen AS-3HT

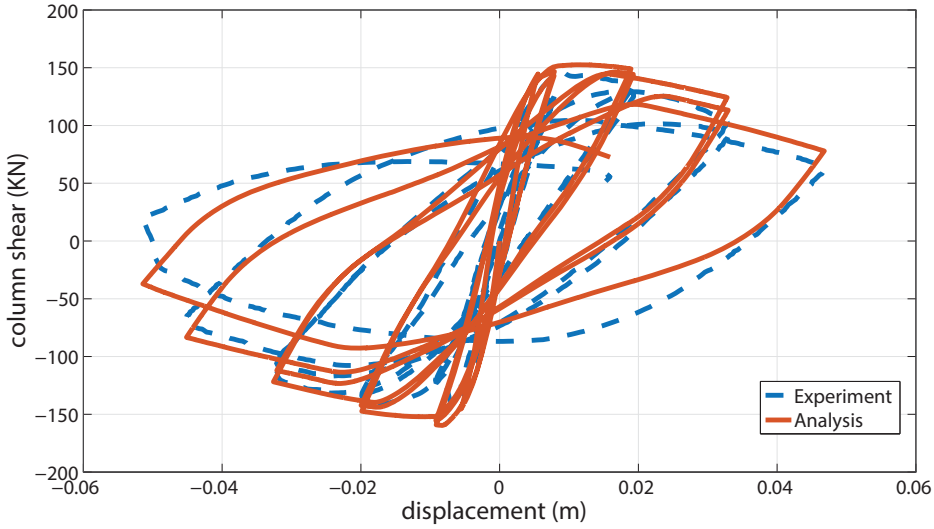

Figure 5.12. Comparison with Bayrak and Sheikh specimen AS-3HT

It is again evident that the analysis model predicts not only the initial stable loops but also the failure mechanism due to inelastic buckling of longitudinal rebars. Indeed, bottom rebars start to loose average stress capacity at compressive strains larger than 0.04 as presented in the stress-strain loops of Figure 5.13(a). At these large strain values cover concrete loses almost all of its strength capacity, which constitutes a spalling failure mode (Figure 5.13(b)).

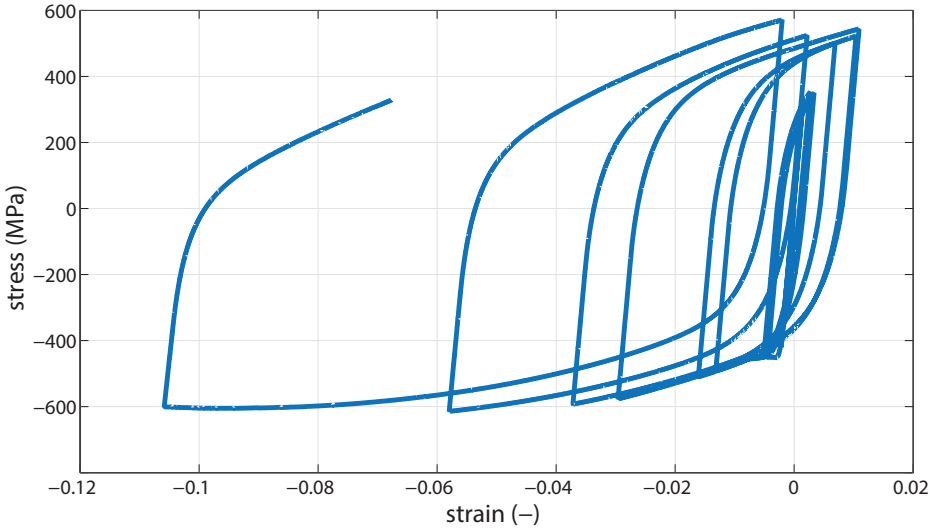

(a)

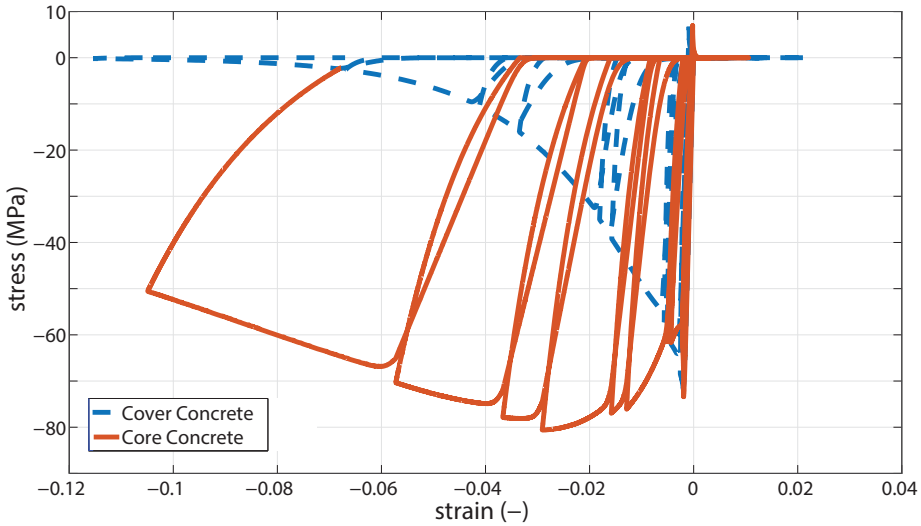

(b)

Figure 5.13. (a) Upper steel rebar stress-strain history, (b) Confined and unconfined concrete stress-strain histories for Bayrak and Sheikh specimen AS-3HT

Finally, the effect of the reinforcing bars inelastic buckling is reflected in Figure 5.14 where both numerical responses with and without rebar buckling are plotted. However, influence of rebar buckling is still important, it has smaller effect than the case of the lower axial load of *N=-2400 KN*. Hence, in the current case with the high axial load of *N=-3340 KN* core crushing is the dominating collapse mechanism of the pier-column system.

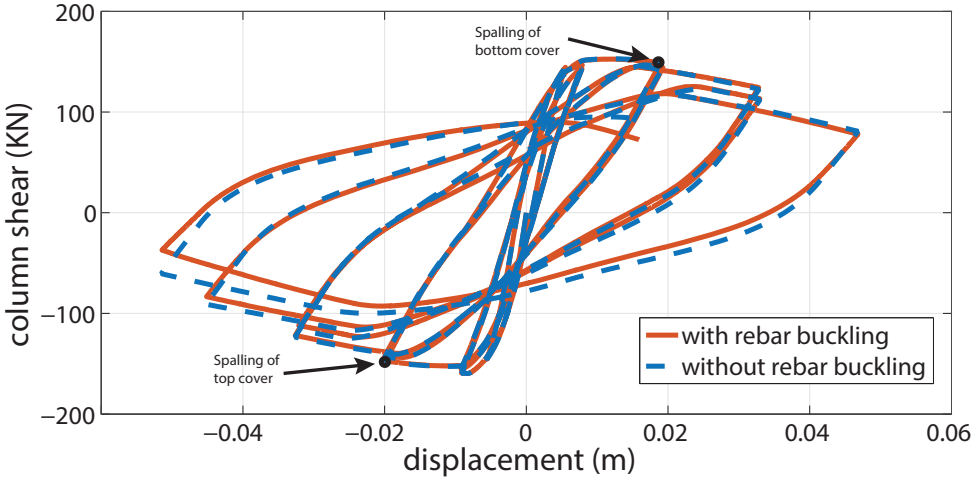

Figure 5.14. Comparison between analysis with and without rebar buckling for specimen AS-3HT

5.4 3-storey, 3-bay frame under seismic time history ground acceleration

5.4.1 Experimental setting description and input data

In this example the numerical model is tested against a 3-storey, 3-bay frame tested dynamically by Ghannoum and Moehle (2008, 2012a) on the University of California, Berkeley shake table. The frame is a one-third scale planar specimen representing a typical strong beam, weak column design office building of the 1960s. Structure's geometry and reinforcing details are presented in Figure 5.15. More specifically, it consists of two different types of column detailing as half left side columns (C1-C3, D1-D3) are designed according to modern design provisions (ACI 318-08) for moment resisting frames with high ductility. On the other hand, the right half side columns (A1-A3, B1-B3) are dimensioned to represent typical columns of the 1960s with widely spaced ties closed with 90 degrees hoops.

Rebars are mentioned in terms of American sizes, hence the ductile columns have *8#2 (50,8 cm^2)* longitudinal reinforcement with *4.8 mm* wire ties spaced every *32 mm* at the column critical regions. On the contrary, older type columns have *8#3 (76,2 cm^2)* longitudinal reinforcement with sparse transverse reinforcement of *3.2 mm* ties equally spaced at *100 mm.* Finally, beams have the same top and bottom reinforcement consisting of *4#3 (38,1 cm^2)* rebars and *4.8 mm* stirrups equally spaced at *89 mm* apart.

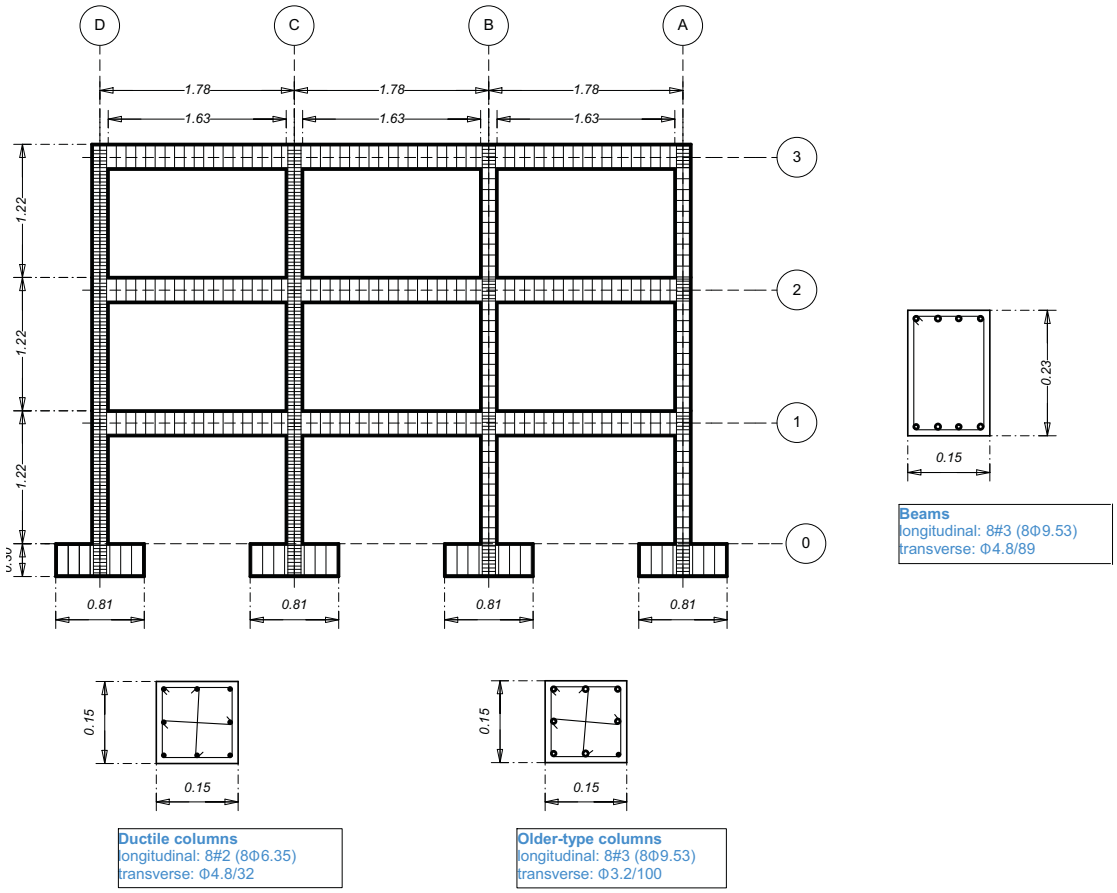

Figure 5.15. 3-storey, 3-bay frame dimensions and reinforcing details

The RC frame is dynamically tested with a record obtained during March 3, 1985, Chile earthquake (Llolleo Station, Component 100) which is presented in Figure 5.16. The original ground motion is amplified with a scale factor of *4.06* in order to enforce the frame RC structure to reach its ultimate strength capacity. The eventual acceleration history recorded on the shake table is reported to differ slightly from the input ground motion due to the bounded frequency range of the shake table. However, the numerical analysis is conducted with the original ground motion data.

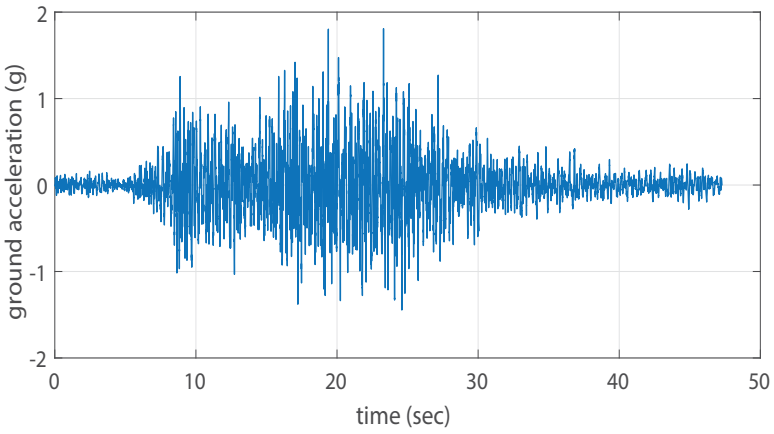

Figure 5.16. Ground motion input (Chile Valparaiso 1985 Llolleo x 4.06)

To obtain a measure of comparison about the intensity of the ground motion, a comparison with the elastic response spectrum of Eurocode 8-1 is presented. Indeed, the scaled ground motion corresponds to the elastic spectrum with a_g=0.53g and probability of appearance 1% in 50 years, if the scaling criteria of Eurocode 8-1 are applied, i.e. the ground motion response spectrum to exceed the 90% of the code's elastic spectrum in the range of periods $0.2T_1$-$2T_1$ (Figure 5.17).

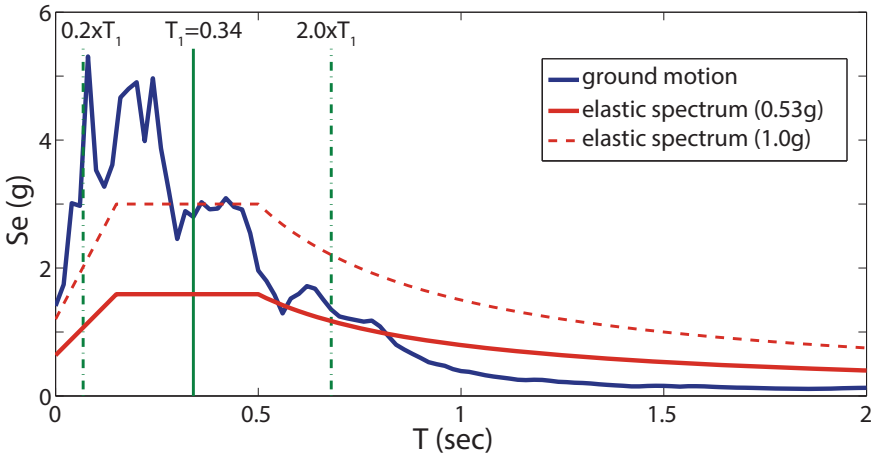

Figure 5.17. Input ground motion and EC8 elastic spectra comparison.

Considering material properties, rebar yield stress is $\sigma_y = 475\ MPa$ as it is offered by the experimental data, while steel rebar parameters are listed in Table 5.5.

σ_y (MPa)	α	n_1	n_2	ε_{plat}	m	q
475	0.03	10	0.5	$3\varepsilon_y$	0.02	20

Table 5.5. Rebar model parameters

Concrete strength was measured to be $\sigma_c = 24.6\ MPa$ at the day of the experiment, while secant modulus at the stress level of $0.4\sigma_c$ is $E_c = 19\ GPa$. In the case of the confined concrete fibers, the Mander et al. (1988) model was used to calculate the maximum confined compressive strength. Confinement factor k obtains value $k = 1.9$ for the confined columns $\left(\sigma_{cc} = k \cdot \sigma_c = 46.7\ MPa\right)$ and $k = 1.1$ for the older-type columns $\left(\sigma_{cc} = k \cdot \sigma_c = 27.1\ MPa\right)$. Finally, model parameters for every column type and every beam are presented in Table 5.6.

	E_C (GPa)	σ_y (MPa)	α_C	q_C	k_0	b	p	c_1	c_2
Confined columns (C1-C3,D1-D3)									
Confined	20	18	0.9	0	0.0009	5	0.7	2	0.35
Unconfined	20	18	0.7	0	0.0009	3	1.2	4	0.1
Old-type columns (A1-A3,B1-B3)									
Confined	20	18	0.8	0	0.0009	3.7	0.8	2	0.35
Unconfined	20	18	0.7	0	0.0009	3	1.2	4	0.1
Beams									
Unconfined	20	18	0.7	0	0.0009	3	1.2	4	0.1

Table 5.6. Confined and unconfined concrete model parameters

Every span of the frame is loaded with a uniformly distributed load of *16.67 KN/m*, considering also its respective mass contribution. The flexibility at the footings was included in the numerical model with rotational springs. Spring stiffness was selected in such way that the fundamental elastic eigenperiod of the numerical model to match the fundamental eigenperiod (T_1*=0.34 sec*) of the frame specimen which was measured experimentally. Following this procedure, spring stiffness value is K_{spring}*=6500 KNm/rad*.

5.4.2 Numerical analysis and comparison

Time history analysis is performed using Newmark numerical integration with $\beta = 0.25$ and $\gamma = 0.50$. Rayleigh viscous damping is also implemented based on the damping ratios

measured experimentally by interpreting the logarithmic decay of accelerations during low-amplitude snapback tests. Hence, damping ratio for the first eigenmode $\left(T_1 = 0.34 \text{ sec}\right)$ is *1.93,* while damping ratio for the second eigenmode $\left(T_2 = 0.12 \text{ sec}\right)$ is *1.85.*

The element discretization scheme consists of *4* Gauss-Lobatto integration points for the columns, resulting in a localization zone of *83 mm* at both column ends. Fiber discretization consists of 12 layers for the sections cover and 30 layers for the section core. Finally, reference spalling value for concrete fibers was set to $D_{sp} = 0.7$.

Initially, comparison with experimental results performed in terms of global frame behavior like interstorey drift and base shear. Indeed, in Figure 5.18 and Figure 5.19 1st storey drift and base shear time histories for both numerical analysis and experiment are plotted for the time period between 10 sec and 35 sec where the significant nonlinear response is observed.

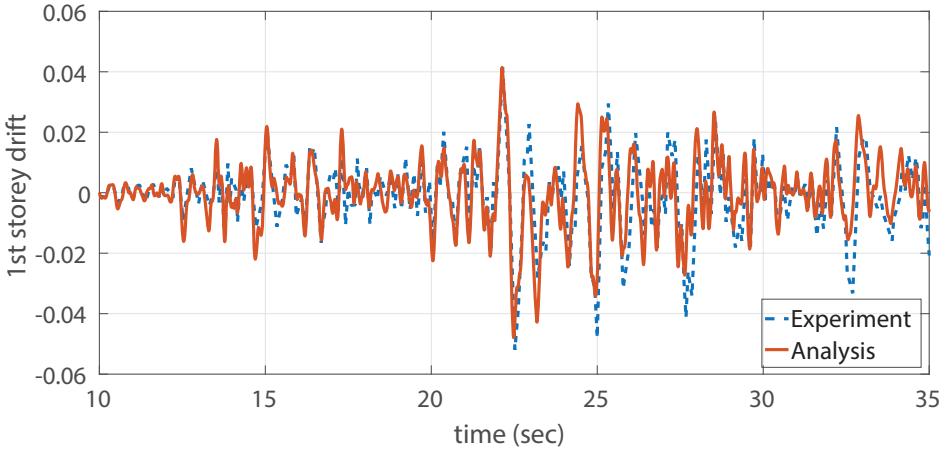

Figure 5.18. 1st storey drift comparison

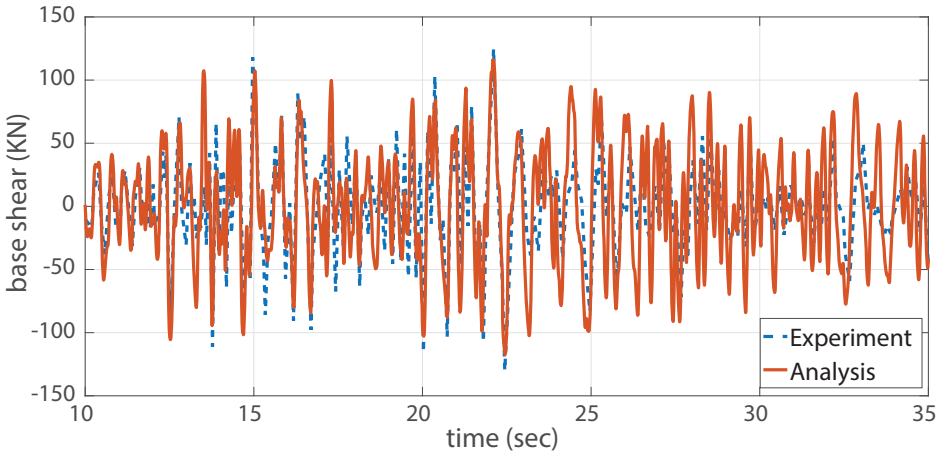

Figure 5.19. Base shear comparison

Initial elastic behavior is matched perfectly by the numerical model until the first nominal yielding occurs for the interior old-type column B1 at nearly 13 sec, followed soon after by yielding of the exterior old-type column A1. After yielding of the older-type columns, some small discrepancies are noticed between the numerical and experimental response. Differences in the responses become larger after the 22nd second where significant damage occurs at column B1. During this time segment of the ground motion, frame exhibits an intense loading cycle where 1st storey drift ratio reaches the value of 5%. The proposed modeling predicts larger base shears after failure of column B1 as its residual strength is overestimated. However, satisfactory correlation in terms of the 1st storey drifts is maintained. In any case, such severe frame damage reaches the proposed modeling strategy at its limitations. For instance, frame nodes are rigidly modeled while diagonal shear cracks are reported by Ghannoum and Moehle (2012a) in the experiment. Also, slip of reinforcement from adjacent anchorage zones at the footings is noticed, while also column D1 experiences uplifting. All these features in conjunction with the co-existence of shear-flexural response exceed the purpose of this dissertation.

After comparison at the global level, the individual column response predicted numerically is tested. In Figure 5.20 horizontal drift ratio versus shear forces at the base of the older type columns A1 and B1 is presented. Numerical modeling is able to capture initial stable cycles of shear response and the drift range for both columns. Correlation with the cyclic loops of column A1 is quite satisfactory, however numerical modeling predicts larger residual shear capacity in the case of column B1 after it is damaged heavily. Nevertheless, some minor underestimation of maximum strength capacity is mainly attributed to rate effects that are not addressed in this thesis. It is interesting that column B1 develops a

symmetric maximum strength in both directions, while column A1 presents reduced shear force in the negative direction. During reloading half-cycle after both columns reach shear force of nearly 40 KN, exterior column A1 experiences tensile axial loading which reduces its compression zone, diminishing on the same time its strength capacity.

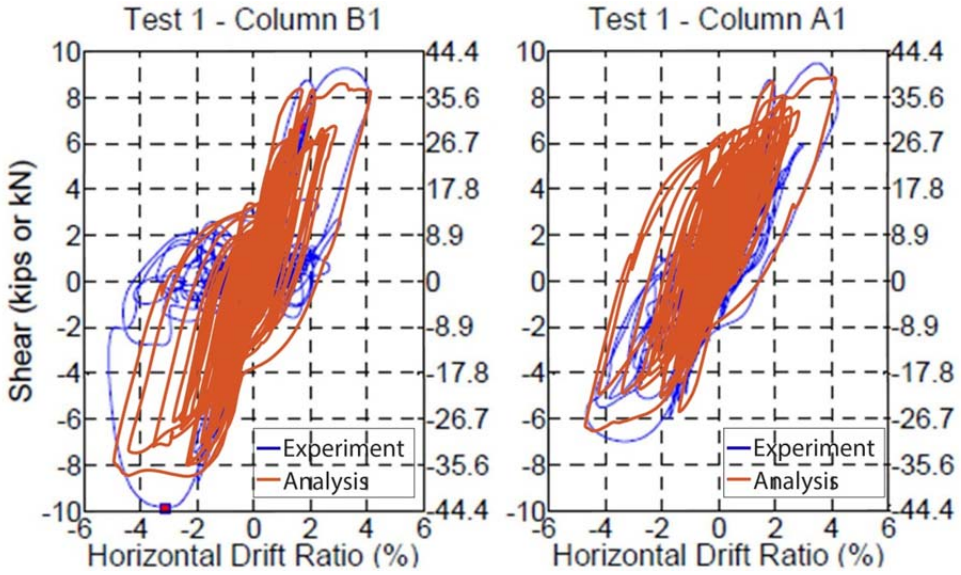

Figure 5.20. Horizontal drift vs column shear comparison

In addition, comparison is performed in terms of chord rotations for columns A1 and B1 and the results are presented in Figure 5.21. Again, the range of chord rotations is almost perfectly predicted for exterior column A1. On the other hand, frame specimen exhibits slightly larger chord rotations at column B1 as additional rigid body rotations due to slippage of longitudinal reinforcement at the footing anchorage zones are omitted in the analysis.

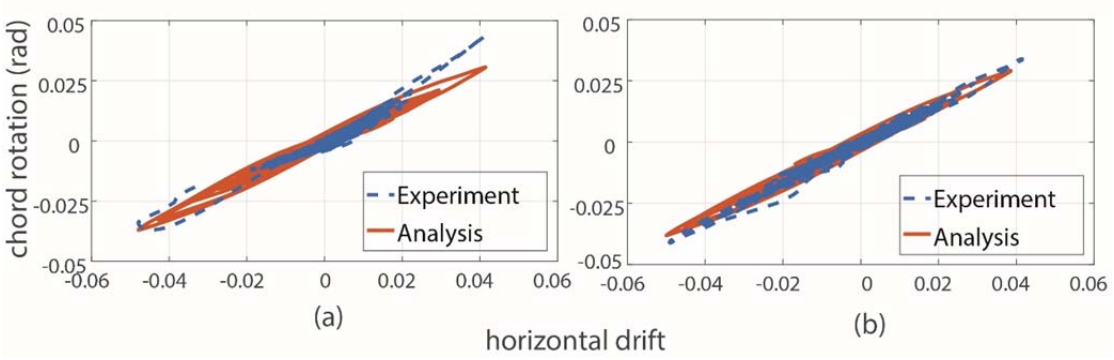

Figure 5.21. Chord rotations comparison: (a) column B1 bottom, (b) column A1 bottom

To emphasize more on the failure of column B1 during the cyclic experiment, the sequence of loading phases during time period between 22.38 sec and 25.11 sec are

presented in Figure 5.22. Photos of column B1 at the base provided by Ghannoum and Moehle (2012a) are listed in Figure 5.22 in companion with the moment-curvature numerical results at the same time instances.

Before failure initiation, column exhibits nonlinear response mainly due to rebar yielding and some small cracks at column cover. At time t_2*=22.45 sec* the first widely open inclined crack appears and column reaches is maximum ductility at the positive direction. During reloading in the opposite direction, column B1 develops its maximum ductility capacity at the opposite direction, where curvature reaches its maximum value of φ*=-0.37 1/m*, while a second visible inclined crack appears, inducing cover spalling initiation. Spalling becomes significant at the time instance of t_4*=25.11 sec* where inelastic buckling of the longitudinal reinforcement is obvious. Buckling mechanism still develops along with core crushing until the end of experiment where large lateral rebar displacements and sever disruption of the core concrete are easily visible.

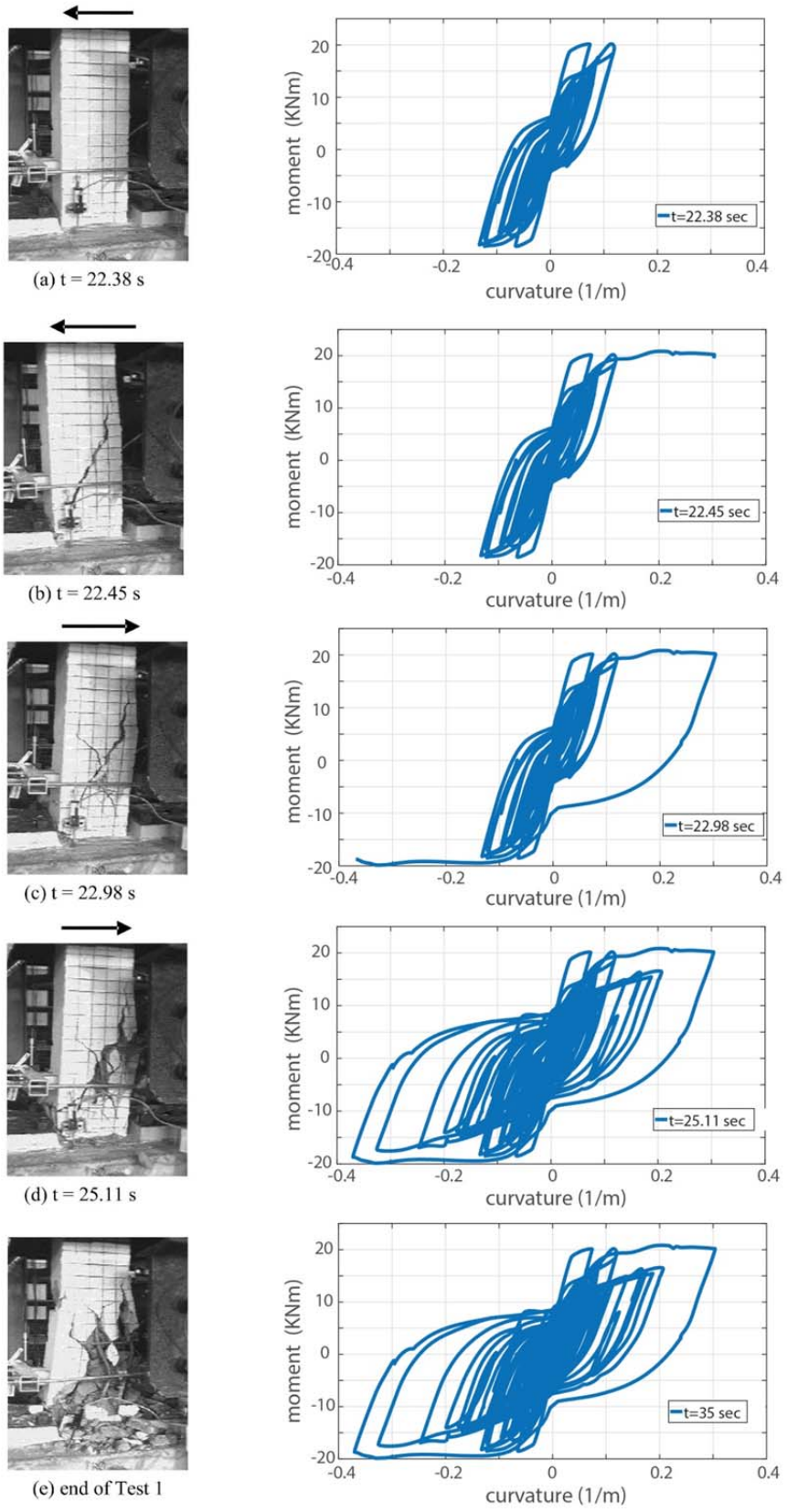

Figure 5.22. Moment-curvature diagrams of column B1 at the base during cyclic failure

The effect of rebar buckling incorporated in the analysis is reflected in Figure 5.23 where stress-strain loops of the top rebars at the column base are presented. Before, cover spalling, cyclic loops are symmetrical in stress, but soon after spalling is detected a significant reductions in compressive stresses is noticed.

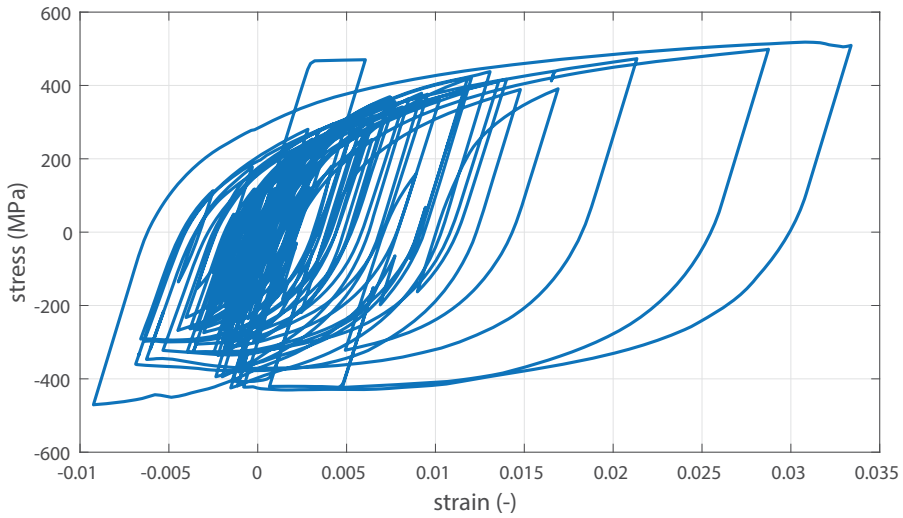

Figure 5.23. Cyclic loops of column B1 top rebars at the base

Also, failure of column B1 provokes axial load redistribution as it is presented in Figure 5.24. The numerical results of Figure 5.24 are in agreement with the experimental ones provided in the paper by Ghannoum and Moehle (2012a). Both interior columns B1 and C1 have the same axial compressive load at the beginning of the experiment, but after sever damage of column B1, it cannot longer sustain its initial axial load, redistributing it in the neighboring columns C1 and A1. It is very interesting however, that even after failure column B1 is able to resists great part of the axial gravitational force.

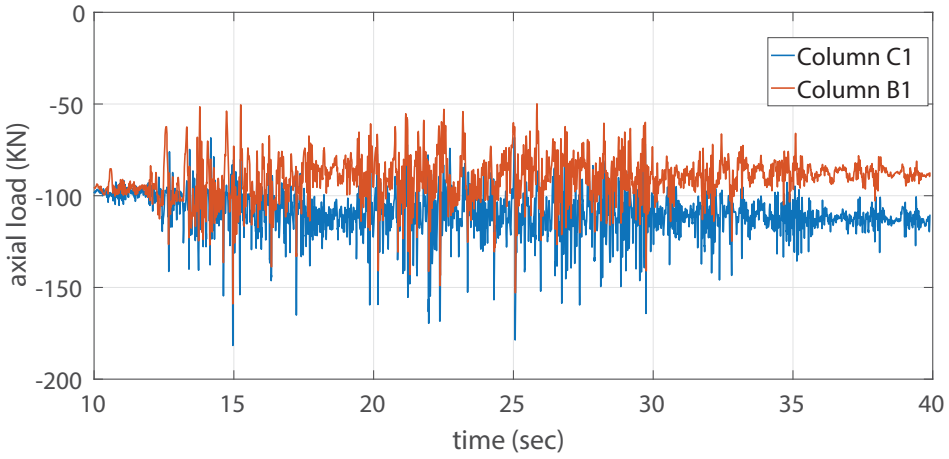

Figure 5.24. Axial load histories at columns B1, C1

Finally, numerical outcome for columns A1, B1, C1 and D1 in terms of base moment-chord rotations are plotted in Figure 5.25. At the same, the ultimate capacity ratio $(\lambda = \theta / \theta_u)$ according to Eurocode 8-3 is calculated at every time step and the maximum values for ever column are listed in Table 5.7. Ultimate chord rotation demand θ_u is calculated in terms of the empirical relation A1 of EC8-3 for RC members under cyclic loading. It is clear that all columns exceed the ultimate capacity limit of Eurocode 8-3 and older type columns have higher capacity ratios than the newer ones. However, exterior columns A1 and D1 present lower capacity than the interior columns B1 and C1 respectively. This feature is contradicting with the experimental and analytical results that invoke that column B1 is the prevalent failing column. A possible explanation is that EC8-3 does not incorporate in the ultimate chord rotation formula potential rebar buckling and strength degradation effects during loading cycles.

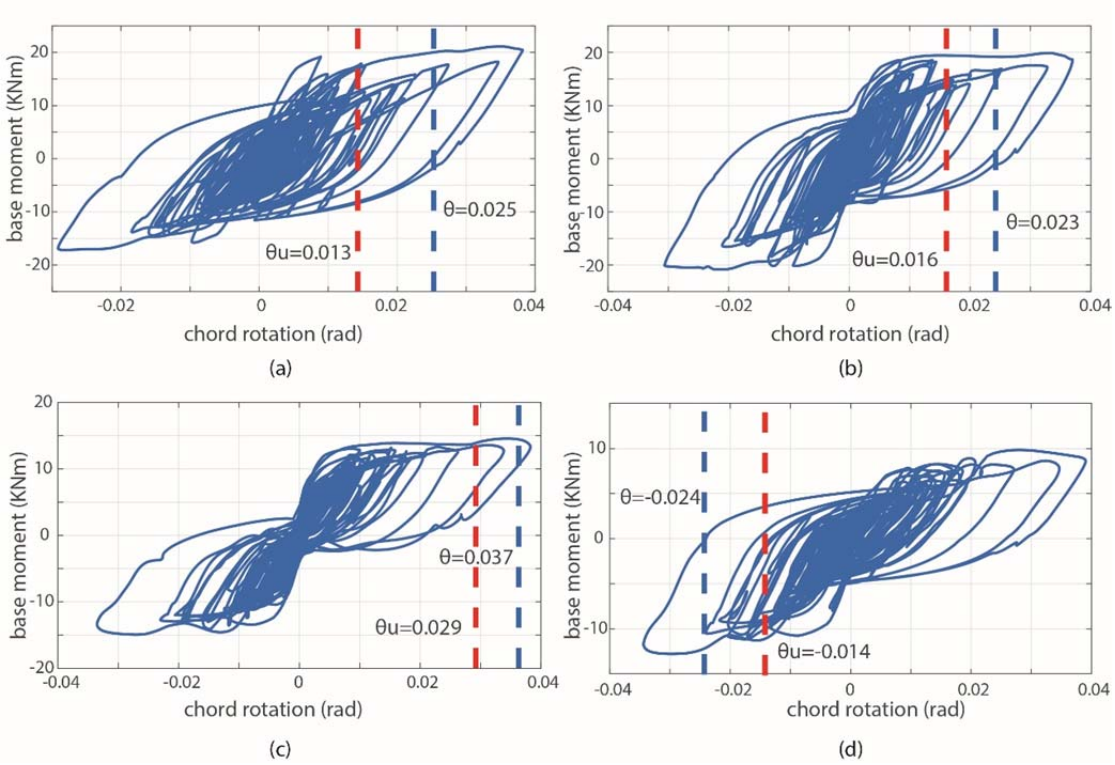

Figure 5.25. Base moment-chord rotation loops and EC8-3 capacity limit, (a) column A1, (b) column B1, (c) column C1, (d) column D1

Column	Capacity ratio (λ)	θ	θ_u
A1	1.91	0.025	0.013
B1	1.44	0.023	0.016
C1	1.25	0.037	0.029
D1	1.73	-0.025	-0.014

Table 5.7. Ultimate capacity ratios for columns A1, B1, C1, D1 according to Eurocode 8-3

It is therefore evident from this example, that the proposed methodology is able to simulate sufficiently cyclic seismic behavior of real RC structures even after failure of some members has occur. The important factor of the proposed modeling is its computational efficiency. Actually, frame time history analysis needed about 1 hour to run in a single processor with 2.20 GHz CPU, while the computer code lacks any optimization techniques and is implemented in Matlab, which is an interpreted computer language.

CHAPTER 6

Conclusions and Future Research

6.1 Summary and concluding remarks

In this dissertation smooth plasticity and damage models based on theoretical considerations are developed and embedded in a two-field mixed fiber beam-column element. The main scope is to accurately model RC skeletal structures cyclic behavior near collapse due to severe cyclic loading. In this context, the nonlinear constitutive model for steel cyclic behavior is introduced based on plasticity considerations. More specifically, the model is capable of expressing a combined nonlinear kinematic and isotropic hardening rule, while it can successfully simulate the yield plateau and the Bauschinger effect while being in compliance with plasticity postulates after short reversals.

Also, cyclic inelastic buckling effect in stress-strain loops is captured by discretizing rebars in layers each one expressed by the proposed uniaxial constitutive law. Lateral displacement, curvature distribution and secondary buckling strain analytically derive from elastic buckling theory. This methodology leads to a numerical scheme where average strains are incrementally imposed and curvatures are updated until equilibrium at mid-length is satisfied. Existing experimental data on steel rebars under cyclic loading validates the proposed rebar model, thus producing accurate results. In addition, it is compared with well documented and frequently used existing steel models like the Menegotto-Pinto and the Dodd Restrepo-Posada model and its efficacy is demonstrated. This stems from the fact that the proposed formulation avoids overshooting after short reversals and it is eligible to describe various smoothing types of the Bauschinger transition curve, while being at the same time computationally effective and low-cost.

Alongside, the proposed uniaxial concrete model incorporates plasticity and damage considerations including along with compressive behavior, tensile softening, nonlinear unloading and crack closure phenomena. Hence, it is able to simulate core crushing and cover spalling that triggers rebar inelastic buckling phenomenon. The smooth damage approach employed enables a unified treatment of damage similar to plasticity. This formulation encapsulates the fundamental features attributed to plasticity and damage in a compact smooth relation that evolves stresses as a function of strains controlled by the selected yield and damage functions. The model is based on nine parameters that affect the behavior and need to be adjusted or formally identified using experimental data. Proper parameter identification enables modeling of a variety of regular and high strength concrete categories ranging from brittle to confined ones. The computational advantage of the proposed concrete model emanates from the direct evaluation of the stresses using the

consistent tangent stiffness incorporating plasticity and damage. This tangent stiffness is explicitly evaluated in every increment from a single relation and subsequently the stresses that correspond to the specific strains are determined. The proposed numerical procedure avoids the separate computation of effective stresses, real stresses and algorithmic tangent stiffness as it compacts these three steps. The concrete model is validated in terms of both experimental and analytical results of other well established models like the Mander et al. model on concrete specimens under cyclic loading.

Furthermore, rebar and concrete models are embedded in a nonlinear two-field RC beam-column element under the plane sections remain plain hypothesis. The introduction of the constitutive equations in the general formulation of mixed beam finite elements, results in two different methods of numerical solution. First, linearization of the differential constitutive equation leads to the standard incremental equilibrium and compatibility equations which are solved using a Newton type iterative numerical scheme. Alternatively, maintaining the constitutive equations in rate form offers the ability of solving them simultaneously with the global differential equations of motion in state space form. Irrelevantly of the solution method, the main beneficial feature of the proposed formulation is that solving the constitutive equation ensures in every time step the explicit and direct calculation of stresses without the need of predictor-corrector schemes. Also local rebar buckling between two adjacent stirrups is included in the cross-sectional level. Spalling of concrete cover that permits the onset of buckling is detected and from that point lateral rebar displacement and curvature start to develop.

Finally, the global fiber beam-column element is tested against experimental results of RC RC structures subassemblies and RC frames under cyclic pseudo-static and time history seismic loading. Numerical results verify the accuracy of the proposed formulation which is proved adequate for earthquake engineering applications. Analysis outcome predicts not only the initial stable cyclic loops of RC members but also the loading region where failure initiates followed by rapid strength deterioration. In conclusion, the proposed scheme can be used in a computationally efficient manner to address the flexural inelastic behavior of RC frame structures subjected to intensive cyclic loading.

6.2 Future research

Interesting problems that on can address in a future work are among others:

- Improve rebar buckling formulation by considering stirrup flexibility and global buckling effect on the model (Kashani et al. 2016). Also, buckling curve has been derived considering only axial rebar deformation. However core concrete lateral expansion applies pressure on the longitudinal rebars, amplifying buckling effect. Hence, incorporating this phenomenon would directly affect model's accuracy.

- Incorporate low cycle fatigue in the uniaxial steel model. Considering the work of Huang and Mahin (2010) for structural steel members, modeling low cycle fatigue follows the concept of damage in brittle materials. It is stated that rupture in the steel material occurs when a scalar damage variable, which depends on the accumulated plastic strain under tensile stresses, exceeds a critical value.

- Include rate effects in concrete model to account for impact and blast loading. Concrete strength depends on rate phenomena which are accounted according to Pontiroli et al. (2010) by considering a dynamic threshold value k_0^d which is deduce from the static value k_0^s through an amplification factor depending on the strain rate $\left(d\varepsilon / dt\right)$.

- Extend the uniaxial concrete model in the triaxial case to allow for shear and torsional effects. In the context of a Timoshenko beam-column element, shear contribution can be addressed if fiber axial and shear stresses are rotated in the principle directions and principle stresses are derived using the 3D concrete constitutive law. Then, rotation back to the original reference system provides fiber stresses.

- Model strengthened RC columns with concrete and FRP jackets. Numerical analysis of strengthened columns with concrete jackets should not be limited to model only the different concrete strengths but it should also simulate the contact interface between the old and new parts (Lampropoulos and Dritsos 2011).

References

[1] Addessi D., Ciampi V. (2007). “A regularized force-based beam element with a damage-plastic section constitutive law” *Int J Numer Methods Eng,* 70 (5), pp. 610-629.

[2] Alemdar B.N., White D.W. (2005). “Displacement, Flexibility and Mixed Beam-Column Finite element Formulations for Distributed Plasticity Analysis.” *Journal of Structural Engineering,* 131:12(1811).

[3] Alessi R., Marigo J.-J., Vidoli S. (2015). “Gradient damage models coupled with plasticity: Variational formulation and main properties.” *Mechanics of Materials,* 80(B), 351-367.

[4] Almeida J.P., Das S., Pinho R. (2012). “Adaptive force-based frame element for regularized softening response.” *Comput Struct,* 102-103:1-13.

[5] Alsafadie R., Hjiaj M., Somja H., Battini J.-M. (2011). “A comparative study of displacement and mixed-based corotational finite element formulations for elasto-plastic, three-dimensional beam analysis”. *Engineering Computations: International Journal for Computer-Aided Engineering and Software,* 28(7):939-982.

[6] Andriotis C., Gkimousis I., Koumousis V. (2015). "Modeling Reinforced Concrete Structures Using Smooth Plasticity and Damage Models." *J. Struct. Eng.,* Volume 142, Issue 2.

[7] Armstrong P.J., Frederick C.O., (1966). “A Mathematical Representation of the Multiaxial Bauschinger Effect.” GEGB Report No. RD/B/ N731.

[8] ASCE. (2013). “Seismic Rehabilitation of Existing Buildings (41-13)”.

[9] Aslani F., Jowkarmeimandi R. (2012). “Stress-strain model for concrete under cyclic loading.” *Magazine of Concrete Research,* 64(8), 673-685.

[10] Ayhan B., Jehel P., Brancherie D., Ibrahimbegovic A. (2013). “Coupled damage-plasticity model for cyclic loading: Theoretical formulation and numerical implementation.” *Engineering Structures,* 50:30-42.

[11] Bae S., Mieses A.M., Bayrak O. (2005). “Inelastic buckling of reinforcing bars.” *J. Struct. Eng., 131:2(314),* pp. 314-321.

[12] Bahn B.Y. and Hsu T.T.C. (1998). “Stress-strain behavior of concrete under cyclic loading.” *ACI Material Journal,* 95(2), 178-193.

[13] Bairan J.M. and Mari, A.R. (2006). “Coupled model for the non-linear analysis of anisotropic sections subjected to general 3D loading. Part 1: Theoretical formulation.” *Computers and Structures,* 84, 2254-2263.

[14] Balan T.A., Filippou F.C., Popov E.P. (1998). “Hysteretic model of ordinary and high-strength reinforcing steel.” *Journal of Structural Engineering,* 124(3):288-297.

[15] Bathe K.J. (2007). “Finite Element Procedures.” Prentice Hall Engineering, Science, Mathematics, New York.

[16] Bari S., Hassan T. (2000). “Anatomy of coupled constitutive models for ratcheting simulation.” *Int. J. Plasticity*, 16, 381-409.

[17] Bate P.S., Wilson D.V. (1986). "Analysis of the Bauschinger effect." *Acta Metal*., 34(6), 1097-1105.

[18] Bayrak O. and Sheikh S. (1996). “Confinement steel requirements for high strength concrete columns.” Proc., 11th World Conf. on Earthquake Engineering, Aculpulco, Mexico, Paper No. 463.

[19] Bazant Z.P. and Oh B.H. (1985). “Microplane model for progressive fracture of concrete and rock,” *Journal of Engineering Mechanics*, ASCE 111(4), 559-582.

[20] Berry M., Parrish M., Eberhard M. (2004). “PEER structural performance database user’s manual (Version 1.0) [R].” CA: University of California: Berkeley.

[21] Berry M.P. (2006). “Performance Modeling Strategies for Modern Reinforced Concrete Bridge Columns.” PhD dissertation, University of Washington, Seattle, WA.

[22] Berry M.P. and Eberhard M.O. (2005). “Practical performance model for bar buckling.” *J. Struct. Eng.*, 131: 7(1060), pp. 1060-1070.

[23] Bicanic N., Zienkiewicz O.C. (1983). “Constitutive model for concrete under dynamic loading.” *Earthquake Engineering and Structural dynamics*, Vol. 11, 689-710.

[24] Borja R.I. (2013). “Plasticity, Modeling & Computation” Springer-Verlag Berlin, Heidelberg.

[25] Buyukozturk O., Buehler M.J., Lau D. and Tuakta, C. (2011). “Structural solution using molecular dynamics: fundamentals and a case study of epoxy-silica interface.” *International Journal of Solids and Structures*, Vol.48, No.14-15, 2131-2140.

[26] Calabrese A., Almeida J.P., Pinho R. (2010). “Numerical issues in distributed inelasticity modeling of RC frame elements for seismic analysis.” *Journal of Earthquake Engineering*. 14, pp.38-68.

[27] Ceresa P., Petrini L., Pinho R. and Sousa R. (2009), “A fiber flexure-shear model for seismic analysis of RC-framed structures”, *Earthquake Engng. Struct. Dyn*., Vol. 38 No. 5, pp. 565-586.

[28] Červenka J. and Papanikolaou V.K. (2008), “Three dimensional combined fracture plastic material model for concrete”, *International Journal of Plasticity*, Vol. 24 No. 12, pp. 2192-2220.

[29] Chaboche J.L., Dang-Van K., Cordier G. (1979). “Modelization of strain memory effect on the cyclic hardening of 316 stainless steel.” Transactions of the 5th International Conference on Structural Mechanics in Reactor Technology. Berlin, no. Div L in 11/3.

[30] Chaboche J.L. (1991). “On some modifications of kinematic hardening to improve the description of ratcheting effects.” *Int. J. Plasticity*. 7, 661-678.

[31] Chang G.A. and Mander J.B. (1994). "Seismic energy based fatigue damage analysis of bridge columns. Part I: Evaluation of seismic capacity." Res. Rep. NCEER-94-0006, Dept. of Civ. Engrg., State Univ. of New York at Buffalo, N.Y.

[32] Charalampakis A.E., Koumousis V.K. (2009). “A Bouc-Wen model compatible with plasticity postulates.” *Journal of Sound and Vibration*, 322(4-5):954-968.

[33] Chen F.W. (1982). “Plasticity in reinforced concrete”. McGraw-Hill, New York.

[34] Choi E., Cho B.S., Chung W., Hui D. (2013) “Monotonic and cyclic behavior of densely confined concrete using stainless steel rings” *KSCE J Civ Eng*, 17 (6), pp. 1403-1412.

[35] Clough R.W., Benuska K.L. and Wilson E.L. (1965). “Inelastic earthquake response of tall buildings.” Proc., 3rd World Conf. on Earthquake Engineering, Wellington, New Zealand.

[36] Coleman J., Spacone E. (2001). “Localization issues in force-based frame elements.” *Journal of Structural Engineering*. 127(11), pp. 1257-1265.

[37] Correia A.A., Almeida J.P., Pinho R. (2015). “Force-based higher-order beam element with flexural-shear-torsional interaction in 3D frames. Part I: Theory.” *Engineering Structures*, 89:04-217.

[38] Cotsovos D. (2013). “Cracking of RC beam/column joints: implications for the analysis of frame-type structures.” *Engineering Structures*, 52:131-139.

[39] Dafalias Y. (1992). “Bounding surface plasticity model under cyclic loading.” Stability and ductility of steel structures under cyclic loading, Y. Fukumoto and G. C. Lee, eds., CRC, Boca Raton, Fla., 25-36.

[40] Dafalias Y.F. (1984). “Modelling Cyclic Plasticity: Simplicity versus Sophistication.” *Mechanics of Engineering Materials*, John Wiley & Sons, pp. 153-178.

[41] Dafalias Y.F., Kourousis K.I., Saridis G.J. (2008). “Multiplicative AF kinematic hardening in plasticity.” *Int. J. Solids Struct*., 45, pp. 2861-2880.

[42] De Borst R., Crisfield M., Remmers J., and Verhoosel C. (2012). “Non-linear finite element analysis of solids and structures.” 2nd edition, Wiley, New York.

[43] Dhakal R.P. and Maekawa K. (2002). “Reinforcement stability and fracture of cover concrete in reinforced concrete members.” *J. Struct. Eng.*, 128(10), pp. 1253-1262.

[44] Dhakal R.P. and Maekawa K. (2002). “Path-dependent cyclic stress strain relationship of reinforcing bar including buckling.” *Eng. Struct.*, 24(11), pp. 1383-1396.

[45] Dodd L.L., Restrepo-Posada J.I. (1995). “Model for Predicting Cyclic Behavior of Reinforcing Steel.” *Journal of Structural Engineering*, ASCE 1995; 121(3):433-445.

[46] EN 1998 Eurocode 8 Earthquake, Part 3: Strengthening and repair of buildings.

[47] Fafitis A. (2001). “Interaction surfaces of reinforced-concrete sections in biaxial bending.” ASCE J *Struct Eng*; 127(7):840–6.

[48] Fardis M. (2010). “Advances in Performance-Based Earthquake Engineering”, Springer, Berlin

[49] Feng Y., Kowalsky M., Nau J. (2014). "Finite-Element Method to Predict Reinforcing Bar Buckling in RC Structures." *J. Struct. Eng.*, Volume 141, Issue 5.

[50] Filippou F.C., Popov E.P., Bertero V.V. (1983). “Efects of bond deterioration on hysteretic behavior of reinforced concrete joints.” Report, Earthquake Engineering Research Centre, University of California, Berkeley, UCB/EERC-83/19.

[51] Fragiadakis M., Pinho, R. and Antoniou S. (2007). “Modeling inelastic buckling of reinforcing bars under earthquake loading.” ECCOMAS Thematic Conference on Computational Methods in Structural Dynamics and Earthquake Engineering, Greece.

[52] Fragiadakis M. and Papadrakakis, M. (2008). ‘‘Modeling, analysis and reliability of seismically excited structures: Computational issues,’’ *International Journal of Computational Methods*, 5 (4), 483-511.

[53] Ghannoum W.M., and Moehle, J.P. (2008). "Experimental Collapse of a Lightly Reinforced Concrete Frame Subjected to High Intensity Ground Motions." The 14 th World Conference on Earthquake Engineering October 12-17, 2008, Beijing, China.

[54] Ghannoum W.M. and Moehle J.P. (2012a). "Shake-Table Tests of a Concrete Frame Sustaining Column Axial Failures." *ACI Structural Journal*, 109(3), 393-402.

[55] Ghannoum W.M and Moehle J.P. (2012b), "Dynamic collapse analysis of a concrete frame sustaining column axial failures", *ACI Struct. J.*, 109(3), 403-412.

[56] Giberson, M.F. (1967) “The response of nonlinear multistory structures subjected to earthquake excitation.” PhD thesis, California Institute of Technology, Pasadena, Calif.

[57] Gkimousis I.A., Koumousis V.K. (2013). “Collapse Fragility Curves of RC Frames with Varying Design Parameters.” In book: Computational Methods in Earthquake Engineering, pp.297-316.

[58] Gkimousis I.A., Koumousis V.K. (2016). “Inelastic mixed fiber beam finite element for steel cyclic behavior.” *Engineering Structures*, 106, pp. 399-409.

[59] Gomes A. and Appleton, J. (1997). “Nonlinear cyclic stress-strain relationship of reinforcing bars including buckling.” *Eng. Struct.*, 19(10), pp. 822-826.

[60] Gopalaratnam V.S. and Shah S.P., (1985). “Softening response of plain concrete in direct tension.” *ACI Journal*, 82, pp. 310-323.

[61] Goto Y., Wang Q.Y. and Obata M. (1998). “FEM analysis for hysteretic behavior of thin-walled steel columns.” *J. Struct. Eng*., 12411, 1290-1301.

[62] Grassl P. Jirasec M. (2006). “Damage-plastic model for concrete failure.” *International Journal of Solids and Structures*, Vol. 43, 22-23, 7166-7196.

[63] Han D.J., Chen W.F. (1985). “A non-uniform hardening plasticity model for concrete materials.” *Mechanics of Materials*, 4, 283-302.

[64] Hartl H. and Ch H. (2002), “3D finite element modeling of reinforced concrete structures”, fib 2002 Congress, 13-19 October, Osaka.

[65] Haselton C.B., Goulet C.A., Mitrani-Reiser J., Beck J.L., Deierlein G.G., Porter KA, et al. (2008). “An assessment to benchmark the seismic performance of a code-conforming reinforced-concrete moment-frame building.” Report No. 2007/12, Pacific Earthquake Engineering Research Center,PEER. Berkeley, California: University of California.

[66] Henshall G.A., Miller A.K., Tanaka J.G. (1987). “Modeling cyclic deformation with the Matmod-Bssol unified constitutive equations.” 2nd International Conference on Low-cycle Fatigue and Elasto-plastic Behavior of Materials, Munich.

[67] Hjelmstad K.D., Taciroglu E. (2002). “Mixed methods and flexibility approaches for nonlinear frame analysis.” *Journal of Constructional Steel Research*, 58:967-993.

[68] Hjelmstad K.D., Taciroglu E. (2003). “Mixed variational methods for finite element analysis of geometrically non-linear, inelastic Bernoulli-Euler beams.” *Communications in Numerical Methods in Engineering*, 19(10):809-832

[69] Hjelmstad K.D., Taciroglu E. (2005). “Variational Basis of Nonlinear Flexibility Methods for Structural Analysis of frames.” *Journal of Engineering Mechanics,* 131(11):1157-1169.

[70] Hoehler M.S. and Stanton, J.F. (2006). “Simple phenomenological model for reinforcing steel under arbitrary load.” J*. Struct. Eng*., 10.1061/ (ASCE)0733-9445(2006)132:7(1061), 1061-1069.

[71] Hu H.T., Schnobrich W.C. (1989). “Constitutive Modeling of Concrete by Using Nonassociated Plasticity.” *Journal of Materials in Civil Engineering,* Vol. 1, No. 4, ©ASCE.

[72] Huang Y. and Mahin S.A. (2010). “Simulating the inelastic seismic behavior of steel braced frames including the effects of low-cycle fatigue.” PEER Rep. No. 2010/104, Pacific Earthquake Engineering Center, Univ. of California, Berkeley, CA.

[73] Jafari V, Rahimian M, Vahdan S.H. (2011). “Improved Formulation in Mixed-based State-Space Approach for large Displacement Inelastic Analysis of Frames.” *Journal of Engineering Mechanics*, 137(3):196-204.

[74] Jason L., Huerta A., Pijaudier-Cabot G., Ghavamian S. (2006). “An elastic plastic damage formulation for concrete: Application to elementary tests and comparison with an isotropic damage model.” *Computer Methods in Applied Mechanics and Engineering,* 195 (52), 7077-7092.

[75] Kaba S. and Mahin S.A. (1984). “ Refined modeling of reinforced concrete columns for seismic analysis.” EERC Report No. 84/03, Earthquake Engineering Research Center, University of California, Berkeley, CA.

[76] Kachanov L. (1986). “Introduction to Continuum Damage Mechanics.” Martinus Nijhoff Publishers, Dordrecht, The Netherlands.

[77] Karsan I.D. and Jirsa J.O. (1969). “Behavior of concrete under compressive loadings.” *ASCE Journal of Structural Engineering*, 95(12), 2543-2563.

[78] Kashani M.M., Crewe A.J., Alexander N.A. (2013). “Nonlinear stress-strain behavior of corrosion-damaged reinforcing bars including inelastic buckling.” *Engineering Structures*, 48:417-429.

[79] Kashani M.M., Lowes L.N., Crewe A.J., Alexander N.A. (2016), “Nonlinear fiber element modelling of RC bridge piers considering inelastic buckling of reinforcement.” *Engineering Structures*, (116) 163-177.

[80] Keshavarzian M. and Schnobrich W.C. (1984). "Computed nonlinear seismic response of R/C wall-frame structures." Technical Report, University of Illinois Engineering Experiment Station. College of Engineering, University of Illinois at Urbana-Champaign

[81] Kim S.H., Koutromanos I. (2016). "Constitutive model for reinforcing steel under cyclic loading". *Journal of Structural Engineering*, 10.1061/(ASCE)ST.1943-541X.0001593 , 04016133.

[82] Konstantinidis D.K., Kappos A.J., Izzuddin B.A. (2007). "Analytical Stress-Strain Model for High-Strength Concrete Members under Cyclic Loading." *Journal of Structural Engineering*, Vol. 133, No. 4.

[83] Kottari A.K., Charalampakis A.E., Koumousis V.K. (2014). "A consistent degrading Bouc-Wen model." *Engineering Structures*, 60:235-240.

[84] Kotsovos M.D. and Newman, J.B. (1977). "Behavior of concrete under multiaxial stress". *ACI*, 74(9), 443-444.

[85] Kunnath S., Heo Y., Mohle J. (2009). "Nonlinear Uniaxial Material Model for Reinforcing Steel Bars." *J. Struct. Eng.,* 135(4):335-343.

[86] La Borderie C., Mazars J., Pijaudier-Cabot G. (1994). "Damage mechanics model for reinforced concrete structures under cyclic loading." *A.C.I*, vol. 134; 1994. p. 147–172.

[87] Lampropoulos A.P., Dritsos S.E. (2011). "Modeling of RC columns strengthened with RC jackets." *Earthquake Eng Struct Dyn*, 40, pp. 1689-1705

[88] Lee J., Fenves G.L. (1998). "Plastic-damage model for cyclic loading of concrete structures." *J. Eng. Mech.*, 124, 892-900.

[89] Lee J., Fenves G.L. (2001). "A return-mapping algorithm for plastic-damage models: 3-D and plane stress formulation." *Int. J. Numer. Methods Eng*., 50(2), 487-506.

[90] Lemaitre J., Chaboche J.L. (1985). "Mécanique des matériaux solides." Dunod, Paris.

[91] Leonhardt F. (1980). "Vorlesungen aber Massivbau." Vol. 1-6. Springer, Berlin, Germany.

[92] Limkatanyu S., Spacone E. (2002). "Reinforced concrete frame element with bond interfaces. I: Displacement-based, force-based and mixed formulations." *Journal of Structural Engineering*, 128:346-355.

[93] Lubliner J. (2008). "Plasticity Theory." Dover Publications, Inc. New York.

[94] Lubliner J., Oliver J., Oller S., Oñate E. (1989). "A plastic-damage model for concrete." *International Journal of Solids and Structures*, 25 (3), 299-326.

[95] Ma S.-Y.M., Bertero V.V., Popov E.P. (1976). "Experimental and analytical studies on the hysteretic behavior of reinforced concrete rectangular and T-beams." EERC Rep. 76-02. Earthquake Engrg. Res. Ctr., University of California. Berkeley, Calif.

[96] Mahasuverachai M. and Powell G.H. (1982). "Inelastic analysis of piping and tubular structures", EERC Report No. 82/27, Earthquake Engineering Research Center, University of California, Berkeley, CA.

[97] Mander J.B., Priestley M.J.N. and Park R. (1984). "Seismic design of bridge piers." Res. Rep. 84-2. Dept. of Civ. Engrg.. Univ. of Canterbury. Christchurch. New Zealand.

[98] Mander J.B., Priestley M.J.N. and Park R. (1988) "Theoretical stress-strain model for confined concrete," *Journal of Structural Engineering,* ASCE, Vol. 114, No. 8, pp. 1804-1826.

[99] Marin J. (1962). "Mechanical behavior of engineering materials." Prentice-Hall Inc., Englewood Cliffs, N. J.

[100] Markou G. and Papadrakakis M. (2012). "An efficient generation method of embedded reinforcement in hexahedral elements for reinforced concrete simulations" *Advances in Engineering Software*, ADES, Vol. 45 No. 1, pp. 175-187.

[101] Markou G., Papadrakakis M. (2015). "A simplified and efficient hybrid finite element model (HYMOD) for non-linear 3D simulation of RC structures." *Engineering Computations*, 32(5):1477-1524.

[102] Marmo F., Rosati L. (2012). "Analytical integration of elasto-plastic uniaxial constitutive laws over arbitrary sections." *International Journal for Numerical Methods in Engineering*, 91(9):990-1022.

[103] Marmo F., Rosati L. (2013). "The fiber-free approach in the evaluation of the tangent stiffness matrix for elastoplastic uniaxial constitutive laws." *Int J Numer Methods Eng,* 94(9):868-894.

[104] Martinelli L. (2000). "The behavior of reinforced concrete piers under strong seismic actions." Proceedings of the 12th Word Conference on Earthquake Engineering, Auckland, New Zealand.

[105] Martinez-Rueda J.E. and Einashai A.S. (1997). "Confined concrete model under cyclic load," *Materials and Structures*, Vol. 30, April 1997, pp. 139-147.

[106] Massone L., Moroder D. (2009). "Buckling modeling of reinforcing bars with imperfections." *Eng Struct*, 31(3), pp. 758-67.

[107] Massone L.M., López E.E. (2014). "Modeling of reinforcement global buckling in RC elements." *Eng Struct*, 59, pp. 484-494.

[108] Mata P., Barbat A.H., Oller S.(2008). “Two-scale approach for the nonlinear dynamic analysis of RC structures with local non-prismatic parts.” *Engineering Structures*, 30(12):3667-3680.

[109] Mazars, J. (1981). “Mechanical damage and fracture of concrete structures.” In: Proceedings of the ICF-5, Advances in Fracture Research, Cannes, France, 4, 1499-1506.

[110] Mazars J., Kotronis P., Ragueneau F., and Casaux G. (2006). “Using multifiber beams to account for shear and torsion. Applications to concrete structural elements.” *Computers Methods in Applied Mechanics and Engineering*, 195(52), 7264-7281.

[111] Mazars J. and Millard A. (2009). “Dynamic Behavior of Concrete and Seismic Engineering.” ISTE Ltd, UK, John Wiley & Sons, Inc., USA.

[112] Menegotto M., Pinto P.E. (1973). “Method of analysis for cyclically loaded R.C. plane frames including changes in geometry and non-elastic behavior of elements under combined normal force and bending.” Symposium on the Resistance and Ultimate Deformability of Structures Acted on by Well Defined Repeated Loads, International Association for Bridge and Structural Engineering, (IABSE) Lisbon, Portugal: 15-22.

[113] Monti G., Nuti C. (1992). “Nonlinear cyclic behavior of reinforcing bars including buckling.” *J Struct Eng*, ASCE, 118, pp. 3268-84.

[114] Moyer M.J. and Kowalsky M.J. (2003). “Influence of tension strain on buckling of reinforcement in concrete columns.” *ACI Struct*. J., 3(2), pp.75-85.

[115] Muguruma H., Watanabe F., Iwashimizu T., and Mitsueda R. (1983). “Ductility improvement of high strength concrete by lateral confinement.” Trans. Jpn. Concr. Inst., 5, 403-410.

[116] Neuenhofer A., Filippou F.C. (1997). “Evaluation of nonlinear frame finite-element models.” *J. Struct. Eng*., 123(7):958-966.

[117] Nukala P.K., White D.W. (2004). “Variationally Consistent State Determination Algorithms for Nonlinear Mixed Beam Finite Elements.” *Computer Methods in Applied Mechanics and Engineering*, 193:3647-3666.

[118] Ohno N., Wang J.D., (1993). “Kinematic hardening rules with critical state of dynamic recovery, Part I: formulations and basic features for ratcheting behavior.” *Int. J. Plasticity*, 9, 375-390.

[119] Okamoto S., Shiomi S. and Yamabe K. (1976). “Earthquake resistance of prestressed concrete structures.” Proceedings of Annual Architectural Institute of Japan (AIJ) Convention, Japan, 1251-1252.

[120] Opensees version 2.4.4 [Computer software]. Pacific Earthquake Engineering Research Center, Berkeley, CA.

[121] Pantazopoulou S.J. (1998). ”Detailing for reinforcement stability in RC members.” *J Struct Eng*, ASCE; 124, pp.623-32.

[122] Paulay T. and Priestley M.J.N. (1992). “Seismic Design of Reinforced Concrete and Masonry Buildings”, John Wiley & Sons, New York.

[123] Peil U., Scheer J., and Scheibe H. Reininghaus, M., Kuck, D., and Dannemeyer, S. (2001). “On the behavior of mild steel Fe 510 under complex cyclic loading.” Plasticity of metals: Experiments, models, computation.” E. Steck, R. Ritter, U. Peil, and A. Ziegenbein, eds., Collaborative Research Centers, Wiley-VCH Verlag GmhH, Weinheim, Germany, 218-252.

[124] Peterson P.E. (1981). “Crack growth and development of fracture zones in plain concrete and similar materials”. Rep. No. TVBM-11-6, Division of Building Materials, University of Lund, Lund, Sweden.

[125] Petrangeli M., Pinto, P.E. and Ciampi V. (1999). “Fiber element for cyclic bending and shear of RC structures. I: theory.” *Journal of Engineering Mechanics*, 125 (9), 994, 1001.

[126] Pietruszczaks S., Jlang J., Mirza, F.A. (1988). “An elastoplastic constitutive model for concrete.” *Int. J. Solids Structures*, 24, 7, 705-722.

[127] Pontiroli C., Rouquand A., Mazars J. (2010). “Predicting concrete behaviour from quasi-static loading to hypervelocity impact.” *Eur J Environ Civil Eng* 14(6–7):703–727.

[128] Qiu F., Li W., Pan P. and Qian J. (2002). “Experimental tests on reinforced concrete columns under biaxial quasi-static loading.” *Engineering Structures*, 24, pp. 419-428.

[129] Ragueneau F., La Borderie Ch., Mazars J. (2000). “Damage model for concrete-like materials coupling cracking and friction, contribution towards structural damping: first uniaxial applications.” *Mechanics of Cohesive-Frictional Materials,* 5 (8), 607-625.

[130] Reinhardt H.W. and Cornelissen H.A.W. (1984). “Post-peak cyclic behavior of concrete in uniaxial tensile and alternating tensile and compressive loading”. *Cement and concrete research*, 14(2), pp.263-270.

[131] Reissner E. (1950). “On a variational theorem in elasticity.” *Journal of Mathematical Physics*, 29:90-95.

[132] Rezaiee-Pajand M., Sinaie S. (2009). “On the calibration of the Chaboche hardening model and a modified hardening rule for uniaxial ratcheting prediction”. *Int J Solids Struct.*, 46, pp. 3009-3017.

[133] Richard B., Ragueneau F., Cremona C., Adelaide L. (2010). "Isotropic continuum damage mechanics for concrete under cyclic loading: stiffness recovery, inelastic strains and frictional sliding." *Engineering Fracture Mechanics*, Volume 77, Issue 8, May 2010, Pages 1203-1223

[134] Sap2000 version 18.1 [Computer software]. Computers and Structures, Inc.

[135] Saritas A., Soydas O. (2012). "Variational base and solution stradegies for the non-linear force-based beam finite elements." *International Journal of non-linear Mechanics*, 47:54-64).

[136] Saritas A., Filippou F.C. (2009). "Numerical integration of a class of 3d plastic-damage concrete models and condensation of 3d stress-strain relations for use in beam finite elements." *Engineering Structures,* 31 (10), 2327-2336.

[137] Scott B.D., Park R. and Priestley M.J.N. (1982). "Stress-Strain Behavior of Concrete Confined by Overlapping Hoops at Low and High Strain Rates." *ACI Journal*, Vol. 79, No. 1, 13-27.

[138] Scott M.H., Fenves G.L. (2006). "Plastic hinge integration methods for force-based beam-column elements." *ASCE Journal of Structural Engineering,* 132*(2):*244-252.

[139] Scott H.M. and Hamutcuoglu O.M. (2008). "Numerically consistent regularization of force-based frame elements." *International Journal for Numerical Methods in Engineering*, 76(10), pp. 1612-1631.

[140] Seismostruct version 7.1 [Computer software]. Seismosoft Ltd.

[141] Sezen H., and Moehle J.P. (2006). "Seismic Tests of Concrete Columns with Light Transverse Reinforcement." *ACI Structural Journal*, V. 103, No. 6, Nov.-Dec., pp. 842-849.

[142] Shen C., Mamaghani I.H.P., Mizuno E. and Usami, T. (1995). "Cyclic behavior of structural steels. II: Theory." *J. Eng. Mech.*, 12111, 1165-1172.

[143] Shi G., Wang M., Bai Y., Wang F., Shi Y.J., Wang Y.Q. (2012). "Experimental and modeling study of high-strength structural steel under cyclic loading." *Engineering Structures*, 37:1-13.

[144] Simeonov V.K., Sivaselvan M.V., Reinhorn A.M. (2000). "Nonlinear Analysis of Structural frame Systems by the State-Space Approach." *Computer aided Civil and Infrastructure Engineering*, 15:76-89.

[145] Simo J.C., Hughes T.J.R. (1998). "Computational Inelasticity." Springer, New York.

[146] Simo J.C. and Ju J.W. (1987). "Strain and stress-based continuum damage models-I. Formulation." *Int. J. Solids Structures*, Vol. 23. No. 7. 821-840.

[147] Sinha B.P., Gerstle K.H. and Tulin L.G. (1964). “Stress-strain relations for concrete under cyclic loading.” *ACI Structural Journal*, 61(2), 195-211.

[148] Sivaselvan M.V., Reinhorn A.M. (2003). “Nonlinear structural analysis towards collapse simulation-a dynamical systems approach.” Buffalo, New York.

[149] Spacone E., Ciampi V. and Filippou F.C. (1996a). “Mixed formulation of nonlinear beam element.” *Computers and Structures*, Vol. 58 No. 1, pp. 71-83.

[150] Spacone E., Filippou F.C. and Taucer F.F. (1996b). “Fiber beam column model for nonlinear analysis of R/C frames. I: Formulation.” *Earthquake Eng. and Struct. Dyn.,* 25(7), 711-725.

[151] Spiliopoulos K.V., Lykidis G. (2006). “An efficient three-dimensional solid finite element dynamic analysis of reinforced concrete structures.” *Earthquake Engng Struct*., 35(2): 137-157

[152] Spurr S.D. and Paulay T. (1984). ‘‘Post-elastic behavior of reinforced concrete frame-wall components and assemblages subjected to simu-lated seismic loading.’’ Rep. 84-19, Dept. of Civ. Engrg., University of Canterbury, Christchurch, New Zealand.

[153] Stramandinoli R.S.B., Rovere H.L.L. (2008). “An efficient tension-stiffening model for nonlinear analysis of reinforced concrete members.” *Eng Struct*, 30, pp. 2069-2080

[154] Su J., Wang J., Bai Z., Wang W., Zhao D. (2015). “Influence of reinforcement buckling on the seismic performance of reinforced concrete columns.” *Engineering Structures*, 103, pp. 174-188.

[155] Sugiura K., Lee G.C. and Chang K.C. (1987). “Endochronic theory for structural steel under non proportional loading.” *J. Eng. Mech.*, 11312, 1901-1971.

[156] Takizawa H. (1976), “Notes on Some Problems in Inelastic Analysis of Planar RC Structures,” *Trans. Of Arch. Inst. Of Japan*, 240, Part I in February, pp.51-62, Part II in March, pp. 65-77.

[157] Taylor R.L., Filippou F.C., Saritas A., Auricchio F. (2003). “A mixed finite element method for beam and frame problems.” *Computational Mechanics*, 31:192-203.

[158] Thompson K.J., Park R. (1978). “Stress-strain model for grade 275 reinforcing steel with cyclic loading.” *Bulletin of the New Zealand national society for earthquake engineering*, 11(2).

[159] Triantafyllou S.P., Koumousis V.K. (2011a). “Small and Large Displacement Dynamic Analysis of Frame Structures Based on Hysteretic beam Element.” *Journal of Engineering Mechanics*, Vol. 138, 1, 36-49.S.P.

[160] Triantafyllou S.P., Koumousis V.K. (2011b). "An inelastic Timoshenko beam element with axial-shear-flexural interaction." *Comput Mech.* 48 (2011), pp. 713-727.

[161] Triantafyllou S.P., Koumousis V.K. (2014). "Hysteretic Finite Elements for the Nonlinear Static and Dynamic Analysis of Structures." *Journal of Engineering Mechanics*, Vol. 140, 6.

[162] Ucak A., Tsopelas P. (2011). "Constitutive model for cyclic response of structural steels with yield plateau." *Journal of Structural Engineering*, 137 (2), pp. 195-206.

[163] Ucak A, Tsopelas P. (2012). "Accurate modeling of the cyclic response of structural components constructed of steel with yield plateau." *Engineering Structures*, 35:272-280.

[164] Urmson C.R. and Mander J.B. (2012). "Local buckling analysis of longitudinal reinforcing bars." *Journal of Structural Engineering*, 138 (1), pp. 62-71.

[165] Vamvatsikos D. and Cornell C.A. (2004). "Applied Incremental Dynamic Analysis." *Earthquake Spectra*, 20(2): 523-553.

[166] Vecchio, F.J. (1999). "Towards cyclic load modelling of reinforced concrete," *ACI Structural Journal,* 96(2), 193-202.

[167] Wang C.H., Foliente G.C. (2001). "Discussion on hysteretic models for deteriorating inelastic structures." *J Eng Mech-ASCE*, 127 (11):1200-1202.

[168] Wang Y.B., Li G.Q., Cui W., Chen S.W. (2015). "Experimental investigation and modeling of cyclic behavior of high strength steel." *Journal of Constructional Steel Research*, 104:37-48.

[169] Wen Y.K. (1976). "Method of random vibration of hysteretic systems." *Journal of Engineering Mechanics Division*, 102, 249-263.

[170] Wu T., Temizer I., Wriggers P. (2014). "Multiscale hydro-thermo-chemo-mechanical coupling: Application to alkali-silica reaction." *Computational Materials Science*, Vol. 84, 381-395.

[171] Zeris C.A. and Mahin S.A. (1988). "Analysis of reinforced concrete beam-columns under uniaxial excitation." *J. Struct. Eng.* ASCE 114(ST4): 804–820.

[172] Zeris C.A. and Mahin S.A. (1991). "Behavior of reinforced concrete structures excitation." *Journal of Structural Engineering*, ASCE, Vol. 117 No. ST9, pp. 2657-2673.

[173] Zhao J. and Sritharan S. (2007). "Modeling of Strain Penetration Effects in Fiber-Based Analysis of Reinforced Concrete Structures." *ACI Structural Journal*, V. 104, No. 2, Mar.-Apr., pp. 133-141.

[174] Zong Z., Kunnath S. and Monti G. (2013). “Simulation of reinforcing bar buckling in circular reinforced concrete columns.” *ACI Struct. J.*, 110, 607-616.

[175] Zong Z., Kunnath S., Monti G. (2014). “Material Model Incorporating Buckling of Reinforcing Bars in RC Columns.” *J. Struct. Eng*, 140(1).

[176] ΟΑΣΠ. (2013). «Κανονισμός Επεμβάσεων (ΚΑΝ.ΕΠΕ.)», ΟΑΣΠ, Αθήνα. (in greek).